SEISMIC RETROFITS FOR SQUARE REINFORCED CONCRETE COLUMNS USING TITANIUM ALLOY BARS

Final Report

PROJECT SPR-784

RESEARCH

Oregon Department of Transportation

SEISMIC RETROFITS FOR SQUARE REINFORCED CONCRETE COLUMNS USING TITANIUM ALLOY BARS

Final Report

PROJECT SPR-784

by

Christopher Higgins, Ph.D., Andre Barbosa, Ph.D.
Sharoo Shrestha, Mackenzie Lostra, and Andre Belejo

School of Civil and Construction Engineering
Oregon State University

for

Oregon Department of Transportation
Research Section
555 13th Street NE, Suite 1
Salem OR 97301

and

Federal Highway Administration
1200 New Jersey Avenue SE
Washington, DC 20590

May 2020

1. Report No. FHWA-OR-RD-20-05	2. Government Accession No.	3. Recipient’s Catalog No.

4. Title and Subtitle Seismic Retrofits of Reinforced Concrete Columns Using Titanium Alloy Bars	5. Report Date May 2020
	6. Performing Organization Code
7. Author(s) Christopher Higgins, Ph.D., https://orcid.org/0000-0002-2853-3648 Andre Barbosa, Ph.D. - https://orcid.org/0000-0003-4547-531X Sharoo Shrestha, Mackenzie Lostra, Andre Belejo	8. Performing Organization Report No.
9. Performing Organization Name and Address Oregon State University School of Civil and Construction Engineering 101 Kearney Hall Corvallis, Oregon 97331	10. Work Unit No. (TRAIS)
	11. Contract or Grant No.
12. Sponsoring Agency Name and Address Oregon Dept. of Transportation Research Section 555 13th Street NE, Suite 1 Salem, OR 97301 Federal Highway Admin. 1200 New Jersey Avenue SE Washington, DC 20590	13. Type of Report and Period Covered Final Report 2015-2018
	14. Sponsoring Agency Code

15. Supplementary Notes

16. Abstract

To explore their potential for seismic retrofitting of seismically deficient RC columns using titanium alloy bars (TiABs), experimental tests were undertaken in the laboratory using full-scale specimens. The specimens were designed to have vintage details and proportions that are widely recognized as being seismically deficient. Some specimens were retrofitted with TiABs to increase the confinement and provide alternate load paths for flexural resistance. Soil-structure interactions were considered for spread footing and timber pile supported footing. Specimens were subjected to reversed cyclic lateral loading and the results of these experiments are reported. Analytical methods were used to predict the individual specimen response and to conduct nonlinear time-history response analyses of bridge models with and without TiAB retrofits. The results and studies indicate that TiAB retrofits do effectively improve the seismic performance of poorly detailed RC columns. This information can be used to develop design recommendations.

17. Key Words Seismic, Reinforced Concrete, Columns, Titanium Alloy, Retrofit, Tests	18. Distribution Statement Copies available from NTIS and online at http://www.oregon.gov//ODOT/TD/TP_RES/

19. Security Classification (of this report) Unclassified	20. Security Classification (of this page) Unclassified	21. No. of Pages 279	22. Price

SI* (MODERN METRIC) CONVERSION FACTORS

APPROXIMATE CONVERSIONS TO SI UNITS

Symbol	When You Know	Multiply By	To Find	Symbol
		LENGTH		
in	inches	25.4	millimeters	mm
ft	feet	0.305	meters	m
yd	yards	0.914	meters	m
mi	miles	1.61	kilometers	km
		AREA		
in^2	square inches	645.2	millimeters squared	mm^2
ft^2	square feet	0.093	meters squared	m^2
yd^2	square yards	0.836	meters squared	m^2
ac	acres	0.405	hectares	ha
mi^2	square miles	2.59	kilometers squared	km^2
		VOLUME		
fl oz	fluid ounces	29.57	milliliters	mL
gal	gallons	3.785	liters	L
ft^3	cubic feet	0.028	meters cubed	m^3
yd^3	cubic yards	0.765	meters cubed	m^3
NOTE: Volumes greater than 1000 L shall be shown in m^3.				
		MASS		
oz	ounces	28.35	grams	g
lb	pounds	0.454	kilograms	kg
T	short tons (2000 lb)	0.907	megagrams	Mg
		TEMPERATURE (exact)		
°F	Fahrenheit temperature	5(F-32)/9	Celsius temperature	°C

APPROXIMATE CONVERSIONS FROM SI UNITS

Symbol	When You Know	Multiply By	To Find	Symbol
		LENGTH		
mm	millimeters	0.039	inches	in
m	meters	3.28	feet	ft
m	meters	1.09	yards	yd
km	kilometers	0.621	miles	mi
		AREA		
mm^2	millimeters squared	0.0016	square inches	in^2
m^2	meters squared	10.764	square feet	ft^2
ha	hectares	2.47	acres	ac
km^2	kilometers squared	0.386	square miles	mi^2
		VOLUME		
mL	milliliters	0.034	fluid ounces	fl oz
L	liters	0.264	gallons	gal
m^3	meters cubed	35.315	cubic feet	ft^3
m^3	meters cubed	1.308	cubic yards	yd^3
		MASS		
g	grams	0.035	ounces	oz
kg	kilograms	2.205	pounds	lb
Mg	megagrams	1.102	short tons (2000 lb)	T
		TEMPERATURE (exact)		
°C	Celsius temperature	1.8 + 32	Fahrenheit	°F

* SI is the symbol for the International System of Measurement

(4-7-94 jbp)

ACKNOWLEDGEMENTS

The authors would like to thank Dr. Matthew Mabey of the ODOT Research Section for shepherding this project, and the Technical Advisory Committee, consisting of Dr. Tanarat Potisuk, Mr. Albert Nako, Mr. Ray Bottenberg, Mr. Paul Strauser, Mr. Bert Hartman of ODOT, and Mr. Tim Rogers of FHWA for their interest and suggestions.

The authors would like to thank Mr. Jeff Gent, OSU Faculty Research Assistant, for his technical support of the experiments. We would also like to thank the team of undergraduate research assistants: Kyle Logan, Jonathon Roy, Aléxia Ribeiro, Lance Parson, Hunter Anderson, Kyle Sonnevile, John Huntoon, Glen Galant, Corey Groshong, James Kemp, and Spenser Maunu who assisted in construction and testing of specimens in the laboratory.

Construction and testing of four tall columns included in this report were funded as a proof-of-concept study by Perryman Company, Houston, PA. The support of Mr. Jim Perryman Sr., Rose Perryman, Frank Perryman, Jim Perryman Jr., and Jill Adkins is gratefully acknowledged. Mr. Warren George helped coordinate the initial efforts of the proof-of-concept studies.

DISCLAIMER

TABLE OF CONTENTS

LIST OF FIGURES

LIST OF TABLES

1 INTRODUCTION

Large numbers of reinforced concrete (RC) bridges were built in the past that are now recognized as seismically deficient. Two of the most common causes of seismic deficiencies in older RC columns are inadequate transverse reinforcing steel and poorly detailed lap lengths at the footing to column joint location. Seismic hazards are a threat to the resiliency of these bridge lifelines; however, complete replacement of seismically deficient bridges is not practical due to limited resources. Alternatively, rehabilitation and renewal of aging and deficient infrastructure is a most feasible approach. Many alternative materials and techniques are available to retrofit deficient RC columns and each has advantages and disadvantages. A new material for civil infrastructure that offers unique potential for seismic retrofitting is titanium alloy bars (TiABs). However, no experimental data are available to support the implementation of the material for such seismic strengthening applications. To explore their potential for seismic retrofitting of seismically deficient RC columns, experimental tests were undertaken in the laboratory using full-scale specimens. The specimens were designed to have vintage details and proportions that are widely recognized as being seismically deficient. Some specimens were retrofitted with TiABs to increase the confinement and provide alternate load paths for flexural resistance. Soil-structure interactions were considered for spread footing and timber pile supported footing. Specimens were subjected to reversed cyclic lateral loading and the results of these experiments are reported. Analytical methods were used to predict the individual specimen response and to conduct nonlinear time-history response analyses of bridge models with and without TiAB retrofits. The results and studies can be used to develop design recommendations.

1.1 MOTIVATION AND BACKGROUND

The Cascadia Subduction Zone (Cascadia fault) is a megathrust fault located off the Western United States coastline, where the Juan de Fuca Plate has been gradually sliding beneath the North America Plate. The fault spans nearly 620 miles (998 km) along the Pacific Ocean, with the northern end beginning at Vancouver Island, Canada and stretching to the south near Cape Mendocino in Northern California. The full earthquake potential of the Cascadia Subduction Zone was only fully recognized at the end of the last century. Now, paleoseismic research has estimated that the Pacific Northwest region of the United States has a 15 percent probability of experiencing an event exceeding M9.0 in the next 50 years (Goldfinger et al. 2012). Prior bridge design codes did not recognize the seismic hazard and as a result, many older existing bridges in the region are not adequately designed for the current level of expected seismic hazard.

Based upon review of the Oregon Department of Transportation bridge database, it was observed that many bridges built in the 1950s, 1960s, and 1970s contained reinforced concrete columns with flexural and shear reinforcing steel inadequate to resist expected seismic demands. In particular, these columns contain widely spaced and low strength ties with small hooks that provide low confinement of the concrete, inadequate support of the flexural steel, and have short lap splices without supplemental confinement that are located above the footing in the plastic hinge region of the column. Along Interstate-5 in Oregon, 69 bridges were identified that were built prior to 1970 and contained rectangular reinforced concrete columns. The columns most commonly consisted of #11 Intermediate Grade (Grade 40) reinforcing steel, lap splice lengths above the footing averaged 30db, and #3 Intermediate Grade reinforcing steel ties spaced at 12 in (305 mm) on-center.

Poorly detailed lap splice lengths and inadequate transverse reinforcing steel are the primary sources for insufficient ductility and poor performance of vintage columns subjected to cyclic loads (Cairns and Arthur, 1979; ElGawady, Endeshaw, McLean, & Sack, 2010; Girard and Bastien, 2002; Lukose, Gergely, & White, 1982; Melek and Wallace, 2004; Paulay, 1982). Although the plastic hinge zone of columns coincides with the column ends where the lap splices were placed, designers placed the splices at this location for ease of construction. It is now recognized that the lap lengths are insufficient to fully develop the column reinforcing steel before the lap splice bond strength is exceeded and this creates a bond-slip failure mode (or lap splice failure) in which the starter bars anchored in the footing and the column bars slide relative to each other, reducing the stiffness, displacement capacity, ductility, and strength of the columns when subjected to cyclic lateral loading. Secondly, inadequate transverse reinforcing steel permits buckling of the longitudinal reinforcing steel bars between tie locations and insufficient concrete confinement, resulting in loss of compressive axial load capacity and non-ductile plastic hinge behavior. Widely spaced transverse ties in rectangular reinforced concrete columns make them a particular concern because of their naturally low confining capabilities compared to circular columns.

Removal and replacement of these types of bridges would be the most effective solution, however, the large numbers of structures needing replacement is simply too high and resources are too limited. Not only are these bridges now being used beyond their originally intended design life, but they are being required to resist a hazard for which they were not designed. These considerations lead to rehabilitation as the most practical solution. The objective of any retrofit approach is to provide the desired level of seismic performance in the most economical way. This research presents full-scale laboratory test results on the performance of seismically deficient square reinforced concrete columns retrofitted with externally mounted TiABs.

TiABs have well-defined material properties including high strength, low stiffness, and negligible inelastic strain hardening compared to conventional reinforcing steel. They are lightweight (which make them easy to work with in construction), fully impervious to conventional sources of corrosion (long-term exposure to the environment is not a concern), and have a coefficient of thermal expansion that is closer to concrete than reinforcing steel. The high cost of TiABs is a concern, however small diameter bars can be used because of the high strength and durability and simplified details allow for economical installation. The construction details reported here allow for visual inspection of the materials within the retrofit for condition assessment after a seismic event.

The proposed seismic retrofit using TiABs consisted of two parts and aimed to compensate for the common inadequate flexural and transverse reinforcing steel details that are observed in vintage RC columns. Vertical TiABs were embedded into epoxy-filled drilled holes in the footings and columns to provide an alternative flexural tension load path and self-centering or restoring mechanism to the column. A spiral TiAB reinforced concrete shell was added to provide confinement to the column core and bracing of the vertical TiABs that were unbonded along their length. The spiral TiAB reinforced shell was formed without concrete cover. The combined effects were intended to improve ductility and deformation capacity while controlling column flexural strength to preclude other undesirable failure modes. These features can produce more resilient bridges and offer designers an alternative seismic retrofitting method to economically achieve seismic performance objectives in vintage substructures.

1.2 RESEARCH SIGNIFICANCE

Presently available retrofitting techniques all have some drawbacks that provide incentive to develop economical alternatives. The well-defined material properties of TiABs are advantageous for retrofitting RC columns with seismic deficiencies, but there are no experimental data on the use of TiABs for seismic retrofitting of RC columns. The goal of this research was to provide experimental data and analytical tools to evaluate the effectiveness of externally mounted TiABs for rehabilitating bridge columns to enhance seismic performance of existing bridges. This research reports on the experimental testing of fourteen (14) square RC columns constructed and retrofitted in a manner so as to simulate the application of TiAB retrofits on vintage bridges that are seismically deficient. The performances of the TiAB retrofitted specimens are compared to reference RC columns. All of the columns consisted of the same cross sectional dimensions and were detailed according to mid-20th century design standards that included short lap splices and widely spaced transverse steel. Two column heights were considered and three different footing connections were investigated to consider soil-structure influences on the performance of the retrofits. The results help develop design recommendations for seismic retrofitting of deficient reinforced concrete columns.

Analytical models of RC columns retrofitted with TiABs were developed based on a phenomenological modeling approach of the measured experimental response. The individual column model was validated using the experimental results and was adapted in a bridge bent system to study the system behavior in regular and irregular bridges. Column bases were fixed to simulate rigid foundations. The retrofit was applied uniformly to all columns in a bridge system regardless of their height and the performance was compared with that of a similar bridge model with non-retrofitted columns. The results of this study demonstrate the improvements to seismic performance for retrofitted bridges with poorly detailed RC columns in bridge substructures.

2.0 LITERATURE REVIEW

This chapter presents a review of relevant literature where the main research topics are addressed. The main topics under this work are: (1) Lap splice behavior, (2) Confinement and ductility, (3) Effect of axial load and lateral load direction on lateral load capacity, (4) Alternative retrofit strategies, (5) Titanium applications in civil engineering, (6) Soil-foundation interaction, (7) Analytical modeling, and (8) Retrofit design approach.

2.1 LAP SPLICE BEHAVIOR

In reinforced concrete (RC) bridges, the most critical region prone to bond failure include the base of bridge piers or columns, especially for vintage RC bridge columns where the longitudinal reinforcing steel is spliced with starter bars for ease of construction at the base of the column, above the foundation. Presence of splices at the region of highest flexural demands in columns (i.e. above the footing level) could be acceptable in case of buildings as long as the "strong column-weak beam" design philosophy is adopted (Paulay, 1982). However, the base of bridge piers or columns supporting the superstructure are deliberately designed to develop plastic hinges during a major earthquake and bridge structures exhibit less redundancy than buildings. Several studies have attributed poor performance of these bridge columns to short lap-splice lengths and inadequate transverse reinforcing steel (Cairns & Arthur, 1979; Lukose, Gergely, & White, 1982; Girard & Bastien, 2002; Melek & Wallace, 2004; ElGawady, Endeshaw, McLean, & Sack, 2010). Thus, researchers (Lynn, Moehle, Mahin, & Holmes, 1996; Paulay, 1982; Chai, Priestley, & Seible, 1994) argue that lap-splices in these regions should be avoided or at least be properly detailed with proper confinement and adequate development length to ensure lateral load capacity and ductility.

The performance of RC columns with lap-spliced bars depends largely on different factors including splice length, longitudinal reinforcement ratio, bar size, yield strength of longitudinal reinforcing steel, spacing between vertical bars, lateral confinement, and applied axial load (Priestley, Seible, & Calvi, 1996). Other parameters contributing to the onset of concrete splitting such as thickness of concrete cover, distance between spliced bars, strength of the concrete, however, are believed to have minimal influence in a seismic environment (Paulay, 1982).

Lukose et al. (1982) studied the behavior of lap-splices under repeated monotonic and reversed cyclic loading and assessed the effect of different parameters in their performance. They found that the reversed cyclic loading is more detrimental to the performance of spliced bars due to the increase in crossing concrete cracks and damage penetration as compared to monotonic loading. They also noticed higher bond stress in tension lap-splices compared to compression lap-splices followed by considerable relative bar-slip under tension compared to compression. Bar-slip in compression was more pronounced once the cover concrete was lost due to longitudinal splitting of the concrete over the spliced reinforcing bars. In either case, they emphasize the importance of well distributed and adequate transverse reinforcing steel along the splice, and extension beyond the high moment splice end to control bond deterioration thereby increasing strength and ductility of the splice region.

Lap-splice lengths of 20 to 30 times the diameter of bar (d_b) were popularly adopted in vintage bridge columns as compression lap-splices and are characteristic of columns with large diameter reinforcing bars (Lukose et al., 1982). These lap-splices have been shown to be inadequate to transfer the full tensile force of the longitudinal reinforcing steel to the starter bars of the foundation in both rectangular and circular columns and are found to be responsible for rapid degradation of flexural strength (Chai et al., 1994; Xiao & Ma, 1997; Breña & Schlick, 2007; Harajli, 2008; Chai, Priestley, & Seible, 2008).

Valluvan, Kreger, and Jirsa (1993) tested twelve (12) 2/3 scale column specimens to examine retrofitted-splice behavior. Their test specimens were scaled from the prototype reinforced concrete column of 18 in x 18 in (457 mm x 457 mm) dimension with four #9 (#29M) longitudinal bars and #3 (#10M) ties. Their actual specimens were 12 in x 12 in (305 mm x 305 mm), 6 ft. (1829 mm) tall with four #6 (#19M) longitudinal bars and #2 (#6M) ties at 12 in (305 mm) spacing and had splice of length 24 times longitudinal bar diameters located at mid-height. One of the specimens was a control specimen, two were strengthened by welding the spliced bars together with an additional tie near the end of the outer spliced bar on one of them, and the remaining nine specimens were retrofitted by confining the splice region. Confinement was provided by three different mechanisms: (1) steel angles and straps along the splice region, (2) external steel reinforcing bars ties, and (3) additional internal ties in the splice region. Different grouting conditions were also explored when using supplemental confinement. They found that welding the splice bars provided continuity in the load path and caused yielding during cyclic loading when additional ties were provided internally around the outer spliced bars. They also concluded that external confinement of the splice region was effective in increasing the splice strength when steel elements and ties were added along with the grout. They, however, found that adding internal ties by removing cover concrete was even more detrimental to the splice strength as it created micro-cracking in the core concrete. This research supports the contribution of confinement in increasing splice strength when done properly without any intrusion to the existing column. Although welding the splice bars created continuity in the load path, if not controlled, welding can severely change the chemical properties of the reinforcing bars and cause brittle failures. In addition, chipping through the cover concrete is not preferred as it can cause micro-cracking in the core concrete and create stress concentrations.

Melek and Wallace (2004) tested six (6) full-scale reinforced concrete cantilevered columns with deficient lap-splices ($20d_b$) under axial and reversed cyclic loading. They studied the behavior of the columns with insufficient lap-splices under different axial loads, shear demands and loading history. The specimens tested were of similar proportions as those tested by Lynn et al. (1996) who studied the behavior of columns with lap-splices and continuous longitudinal reinforcing steel bars. Comparing both test results revealed that inadequate lap-splice lengths caused lateral strength degradation. They observed that the rotation caused by the slippage of the longitudinal bars accounted for a major portion of the total rotation especially after the bond deterioration. They emphasized the importance of characterizing the column rigid body rotation due to slip over the splice length which can help to calibrate moment versus slip-rotation springs in modeling splice behavior. They also observed that ACI 318-02 (ACI Committee 318, 2004) underestimated the bond stresses in the lap-spliced bars, which could lead to column shear failures. They found that the magnitude of axial load maintained during testing and the shear strength ratios had negligible impact on normalized moment versus lateral drift behavior. However, peak lateral load capacity was higher with higher axial load and the rate of lateral strength degradation increased slightly with increasing shear level.

Harries, Ricles, Pessiki, and Sause (2006) investigated the use of carbon-fiber-reinforced polymer (CFRP) composite jackets to retrofit non-ductile square reinforced concrete columns with inadequately detailed lap-splices. They were successful in increasing the lap-splice capacity of those columns to develop the nominal flexural capacity of columns with continuous longitudinal reinforcing steel bars. They noticed that the external confinement using CFRP jackets could delay the beginning of significant slip by limiting the transverse strains and thus the splitting of concrete along the splice. However, the ductility capacity was limited by the eventual occurrence of significant slip after which the confinement has negligible effect on the residual splice capacity. These results suggest the necessity of alternate load path or alternate measure (in addition to confinement) to control the slip in spliced bars once there is significant slip in the lap-spliced bars, and the inefficiency of using reinforcing plating for confinement on square and rectangular columns. The studies reviewed above emphasize the importance of proper detailing of the lap-spliced bars in potential plastic hinge regions including proper confinement and provision of alternate load path after splice failure. The retrofit developed and presented subsequently in this report offers an alternate load path through external ligaments to bridge the poor reinforcing steel bar lap-splice. In addition, the retrofit developed provides circular confinement to square columns thereby providing near uniform confining pressure throughout the section.

2.2 CONFINEMENT AND DUCTILITY

The available ductility in RC columns is directly related to the longitudinal and transverse reinforcing steel details especially in the critical plastic hinge regions (Daudey & Filiatrault, 2000). Inadequate confinement of RC columns tends to limit the ultimate curvature corresponding to the compressive strain in the range of 0.005 and may lead to bond failure between reinforcing steel bars and concrete in a brittle splitting mode, resulting in the relatively low ductility capacity of these members (Chai et al., 1994; Harajli, 2009). Under inelastic cyclic loading, as in the case of a strong seismic shaking, degradation of concrete results in the decrease of shear capacity in the plastic hinge region. RC columns, thus, need to be detailed for sufficient ductility through effective confinement of these critical regions to sustain the likely inelastic displacements without significant degradation of strength.

Ozcebe and Saatcioglu (1987) tested four (4) full-scale square reinforced concrete columns under constant axial load and reversed cyclic loading to study the behavior of columns with different confinement configuration. The specimens were identical in terms of column cross-section (350 mm x 350 mm square) and longitudinal reinforcing steel detailing with 8-#8 (#25M) diameter reinforcing bars uniformly distributed. The first and second specimens were confined with square hoops with 135˚ hooks with the second one having hoops spaced at two-third the spacing of the first one. The third and fourth specimens had additional cross-ties spaced at the spacing as that of the first specimen. The cross-ties in the third specimen had 135˚ hooks whereas the fourth had 135˚ and 90˚ hooks. The performance of the columns with cross-ties were superior to the ones with only square ties. Although the specimen with closely spaced square ties performed better than the one with wide spacing, the performance enhancement was not as significant as the ones with the cross-ties. Hence, the authors suggested that the proper selection of confinement configuration is more efficient in improving confinement than increasing the transverse reinforcement ratio, which fails to engage the unsupported longitudinal reinforcing steel bars. They also compared the performance with the analytical prediction using the "Kent and Park model" (Kent & Park, 1971) and the "Sheikh and Uzumeri model" (Sheikh & Uzumeri, 1982). Results indicated that the analytical prediction underestimated column performance when the unconfined concrete model was used and reinforcing steel strain hardening was not considered in the modeling.

Saatcioglu and Ozcebe (1989) tested fourteen (14) full-scale square RC column specimens to study the effect of confinement by transverse reinforcing steel on their response. The specimens tested had the same layout of transverse reinforcing steel at varying spacing. The one with 2 in (51 mm) spacing most effectively enhanced the column behavior by confining the core than the ones with more than 2 in (51 mm) spacing. Analyses of these results in combination with the ones from the specimens with different transverse reinforcing steel configuration indicated that a proper choice of transverse steel arrangement could be more feasible than reducing the tie spacing to achieve the same level of confinement. The increase in shear capacity associated with increased transverse steel, over and above the shear capacity corresponding to the peak shear force, is believed to have little effect on improved response.

Mander, Priestley, and Park (1988) developed a theoretical stress-strain model for concrete confined by different arrangement of transverse reinforcing steel bars. The stress-strain model was validated through the correlation with experimental tests of 31 nearly full-scale column specimens. They developed a single equation for confined compressive strength for tied and continuously confined sections with different values of effective confinement coefficient, k_e, based on the type of transverse reinforcing steel bars used. Typical values of k_e were 0.95 for sections confined by spirals, 0.75 for sections with ties, and as low as 0.6 for tied sections with large aspect ratios; circular hoops lay somewhere in between. The high confinement coefficient for continuously confined or circular geometries reflects the greater efficiency of circular transverse reinforcement to achieve confinement in concrete columns compared to rectangular ties. The equation proposed directly relates compression strength of the confined concrete to the effective lateral confining stress, $f_{l'}$ (a function of k_e), that could be developed at yield of the transverse reinforcing steel. The theoretical expression for lateral confining pressure, f_l, shows that it is inversely proportional to the longitudinal spacing of the ties or spiral.

Watson, Zahn, and Park (1994) developed design charts using previously derived stress-strain relationships for confined concrete. These design charts allow for the determination of the quantity of transverse reinforcing steel required for specified curvature-ductility factors in the potential plastic-hinge regions of reinforced concrete columns.

Razvi and Shaikh (2018) tested nine (9) 1/3 scale square reinforced concrete columns to study the confinement contribution of ferro-mesh jacketing. Their test specimens consisted of three groups: (1) three specimens with stirrups as confinement, (2) three specimens with stirrups as well as ferro-mesh jacketing for confinement, and (3) three specimens having only ferro-mesh jacketing for confinement. All the specimens were subjected to concentric compressive load and their behavior in terms of axial load carrying capacity, energy dissipation and ductility in terms of lateral deformation were studied. They observed that the specimens with just the stirrups or just the ferro-mesh jacketing had similar axial load carrying capacities and the specimens with both as confinement were better than the other two and showed 20% increase in the axial load carrying capacity. The specimens with ferro-mesh jacketing also showed higher energy dissipation as compared to the conventional design.

2.3 EFFECT OF AXIAL LOAD AND LATERAL LOAD DIRECTION ON LATERAL LOAD CAPACITY

Axial loads can be both detrimental and beneficial depending on the magnitude of axial load and the drift level. While the column axial load can have adverse effects in terms of crushing force and additional overturning moments due to P-Delta effects, it can also help increase the shear strength by arch action forming an inclined compression strut thereby resisting the applied shear force directly through its horizontal component (Priestley, Verma, & Xiao, 1995).

Saatcioglu and Ozcebe (1989) tested 14 full-scale square RC columns to study the effect of variation in axial load, transverse reinforcing steel and bidirectional loading in the hysteretic behavior of reinforced concrete columns. The axial load was varied linearly between 500 kN (112 kips) tension when the column was displaced horizontally 6 percent of the column height in one direction and 500 kN (112 kips) (approximately 15% of $f_c'A_g$) compression when the specimen was displaced the same amount in the opposite direction. This loading was selected to simulate an axial load couple resulting from lateral loading in a bent frame. Hysteretic response results indicated that the yield moment is affected by the level of concurrent axial load. The specimens showed early inelastic response but delay in strength degradation beyond the initial yield when accompanied by axial tension, whereas, when accompanied by axial compression, the specimens showed higher yield strength but early strength degradation. In addition, the behavior under increasing axial compression was similar to that of the specimens tested under constant axial compression.

Saatcioglu and Ozcebe (1989) also compared the response of columns subjected to different lateral loading direction. They noticed that the response of the columns loaded parallel to the principal axis in terms of strength, stiffness and ductility was similar to those loaded parallel to the section diagonal. However, when the columns were subjected to simultaneously varying bidirectional load reversals, the post-yield response was characterized by severe strength and stiffness degradation as compared to unidirectional load response.

Columns with rectangular and square cross sections in bridge structures are often subjected to biaxial bending owing to earthquake-induced lateral load acting along directions other than the principal axis (Zahn, Park, & Priestley, 1989). This led Zahn et al. (1989) to conduct experimental tests on 400 mm (15.7 in) square RC columns with code-specified transverse reinforcing steel and subjecting them to axial load and to cyclic lateral load acting along a section diagonal. The choice of the direction of lateral load application was to allow bending about the diagonal rather than the axis parallel to the face of the column. Results indicated that for the same quantity of confining steel and level of axial load, there was no significant difference between the flexural strength and ductility for bending about a section diagonal and for a bending about a principal axis.

Wang, Wang, Yu, and Li (2018) tested ten (10) full-scale rectangular reinforced concrete columns with aspect ratio of 1.5 to study the effect of lateral loading direction on lateral load capacity, ductility, stiffness, and energy dissipation capacity of CFRP retrofitted columns. Five of their specimens were unretrofitted and five were retrofitted with 3 layers of CFRP along the theoretical plastic hinge region. The main test variable was the lateral loading angle, which varied from 0˚ (strong axis) to 90˚ (weak axis). Results indicated that the lateral drift, shear resistance and energy dissipation capacities generally decrease with the increase in lateral loading angle (highest in strong axis and lower as the angle increased). Results also indicated that the performance of both unretrofitted and retrofitted column loaded at 60˚ angle was even worse than the weak axis loading. CFRP retrofit was seen to enhance the seismic performance of the columns irrespective of the loading direction with their efficiency decreasing with the increase in the lateral loading direction angle. The failure of unretrofitted control columns generally varied from brittle shear failure mode to ductile flexural failure mode for the variation of lateral loading direction from strong to weak direction. The retrofitted columns exhibited ductile failure mode despite the direction of lateral loading. Results also indicated that the lateral strength of both unretrofitted and retrofitted columns in non-principal loading directions can be reasonably predicted from that in the principal directions by an elliptical relationship. It is worth noting, however, that the columns had continuous longitudinal reinforcing steel that were properly anchored to the footing block and extended along the length of the column and the stirrups were provided at half the spacing of 100 mm (4 in) on center along the plastic hinge length which was the same as the CFRP retrofit height.

2.4 ALTERNATIVE RETROFIT STRATEGIES

Various techniques have been developed to seismically retrofit and strengthen deficient RC columns. Previous work includes experimental and analytical studies. The most popular retrofit solutions in practice are steel jacketing, composite material jacketing, and wire prestressing. Some of the relevant studies are discussed in this section.

Xiao and Ma (1997) studied the behavior of reinforced concrete circular columns with poor lap-splice details retrofitted using prefabricated composite jacketing. Of the tested column specimens, the as-built column suffered brittle failure due to lap-splice failure. However, the two retrofitted specimens and the failed as-built column after repair showed significant enhancement in flexural capacity and ductility. They also developed an analytical model to assess the seismic behavior and retrofit design taking into consideration the bond-slip deterioration of lap-spliced longitudinal bars. They claim that the gradual bond-slip mechanism is acceptable for seismic retrofit as long as the retrofitted column develops the required load carrying capacity and ductility. The authors hypothesized that this gradual bond-slip failure mechanism of the lap-splice can avoid rupture of the longitudinal bars and therefore, could even be beneficial.

Mirmiran et al. (1998) studied the effect of different parameters in FRP-confined columns under uniaxial compression. They found that square sections are less effective in confinement than the circular ones and even in circular FRP-confined columns, mechanical bond using shear connectors were preferred over adhesive bond alone. The mechanical anchors distributed confinement pressure effectively around the circumference of the circular FRP-jacket which helped improve the performance of the section.

Goksu, Yilmaz, Chowdhury, Orakcal, and Ilki (2014) tested eight (8) reinforced concrete rectangular columns to study the behavior of non-ductile columns retrofitted with carbon fiber reinforced polymer (CFRP). Their specimens were 7.9 in x 11.8 in (200 mm x 300 mm) with 4 – 0.55 in (14 mm) diameter plain bars which were continuous for four of the specimens and the rest had lap-splice length of 40 times the diameter of the bars. For the other four specimens, transverse reinforcement was provided at 7.9 in (200 mm) on center. Their results indicated that CFRP jackets were effective in increasing the ductility of the columns with continuous longitudinal reinforcement but not as much for the case of columns with inadequate lap-splices. The increase in ductility for the columns with continuous longitudinal bars was attributed to the prevention of buckling of the bars through effective confinement whereas, in the columns with lap-splice, bond slip failure occurred and caused significant loss in strength. These results indicate that along with effective confinement, an alternate load path is required after the lap-splice fails, which was not provided by CFRP jackets alone.

Haroun and Elsanadedy (2005) performed lateral cyclic loading tests on thirteen (13) ½ scale reinforced concrete bridge columns with insufficient lap-splice length to study the effect of fiber-reinforced plastic jackets on ductility of circular and rectangular columns. The circular columns were 24 in (609 mm) in diameter and the square columns were 24 in x 24 in (609 mm x 609 mm) and 135 in (3429 mm) tall. The circular columns had 20 #6 (#19M) longitudinal bars with #2 (#6M) circular hoops at 5 in (127 mm) on center and the square ones had 28 #6 (#19M) longitudinal bars with #2 (#6M) square ties at 5 in (127 mm) on center. In addition, 2 in (50.8 mm) circular radius was provided at the corners of the square columns. Based on the results, the authors noted that the jacketing was effective in improving the cyclic performance of the circular columns but not in case of square columns. Even with the circular columns, the effectiveness of jacketing depended on the jacket strain, which had to be controlled during their manufacture. Failure to provide the intended jacket strain could severely affect their efficiency in improving ductility. Although all retrofitted square columns failed to meet their target ductility demand, one of the square columns that was retrofitted by adding pre-mold mortar blocks to provide a quasi-circular section with continuous confinement showed improved performance over the square jackets. Results indicate that a circular profile is better than square profile in providing effective confinement, as it provides uniform hoop stress.

Galal et al. (2005) tested seven (7) 2/3-scale square reinforced concrete short columns with two different quantities of transverse reinforcement under reversed cyclic lateral and constant axial load to study the effect of retrofitting using different materials in each group. Five (5) columns were designed according to the current Canadian Reinforced Concrete Design Code with higher transverse reinforcement and two (2) columns had pre-1970s details with low transverse reinforcement. They only had one control specimen with higher transverse reinforcement and the remaining specimens were either retrofitted with CFRP or GFRP over the entire height with and without anchors to study the effect of different FRP materials and the contribution of anchors. Results indicated that anchored CFRP sheets were more effective in increasing both shear force and energy dissipation capacity in short square RC columns than anchored GFRP. Anchoring of the FRP jackets and increasing the number of FRP layers were both seen to improve the confinement of the concrete as shown by the decrease in strains in both transverse reinforcement as well as the fiber materials. Providing anchors even increased column shear forces and energy dissipation capacities. They were able to change the failure mode from brittle shear failure in the control specimens to ductile behavior with plastic hinging at top and bottom of the columns in retrofitted specimens.

Ozcan, Binici, and Ozcebe (2008) tested five (5) reinforced concrete columns under constant axial load and reversed cyclic lateral loading to study the effectiveness of CFRP to retrofit non-ductile square reinforced concrete columns with low strength concrete and continuous plain reinforcing bars and investigate the effect of presence and absence of axial load during the strengthening process. One of their specimens was a control specimen, two of the specimens were retrofitted with 1-ply CFRP and the other two with 2-ply CFRP. The axial load on one specimen each of the retrofitted group was maintained constant from the time of retrofitting till the end of test whereas, the remaining were axially loaded only during testing. It was observed that the CFRP retrofit improved the column ductility significantly with negligible lateral load carrying capacity enhancement. Increasing the number of CFRP layers improved the column drift capacity irrespective of the presence of axial load during strengthening, however, the enhancement was not proportional to the number of added layers. The effect of having the axial load during FRP wrapping on the ultimate drift ratios was also observed to be negligible. The authors suggested additional studies were needed with higher loads to generalize the observation. It is important to note that all the specimens had continuous longitudinal bars whose behavior and failure mechanism can be different from specimens with lap-spliced bars.

Chai et al. (2008) investigated the use of steel jacketing to retrofit circular columns with insufficient flexural strength and ductility. They tested six 0.4-scale circular columns that included as-built and retrofitted columns and compared their behavior under lateral load with analytical predictions. The columns were all 24 in (610 mm) in diameter and 12 ft (3.657 m) high and reinforced with 2.53% longitudinal reinforcement (26-#6 (#19M) Gr. 40 deformed bars) and circular hoops (# 2 (#6M) Gr. 40 plain bars) placed at 5 in (127 mm) on center. Two columns were built with 1960's footing design using only straight reinforcement (two orthogonal layers of 24 #6 (#19M) bars each) in the bottom region of the footing. The footing was supported on 1 in (25.4 mm) high rigid pile-blocks. A strong footing detail was used in the remaining four columns. The columns were subjected to lateral loading reversals while keeping a vertical load of 400 kips (1779 kN) ($0.18f'_cA_g$) constant throughout the testing. The control specimen was repaired after the damage and tested again. Results indicated that the lap length of 20 times the longitudinal bar diameter was insufficient to develop yield stress of the longitudinal bar and that rapid strength degradation due to bond failure was observed. Steel jacketing was effective in increasing the lateral strength and ductility. The lateral stiffness increased about 10 to 20% in case of fully grouted steel jacket. The results also highlighted the importance of ensuring comparable footing strength before retrofitting the columns with steel jacketing as full grouting of the jacket can create inelastic strain penetration into the footing which can cause brittle footing shear failures.

Abedi, Afshin, and Shirazi (2010) observed that conventional steel jacketing using "bellow tube" method suffered from unavoidable stress transfer in the longitudinal direction. This stress transfer caused reduced efficiency due to initial yielding of the tube from bending or axial loading. In addition, this retrofit method was found to be challenging in areas with space constraints. Rectangular steel jackets was favored in areas with space constraints but they suffered from out-of-plane bulging.

ElGawady et al. (2010) tested eight (8) 0.4-scale rectangular reinforced concrete columns with aspect ratios of 1.5 and 2.0 having deficient lap-splice details to study the contribution of different retrofit jacketing techniques in improving the cyclic behavior of these columns. The columns tested had lap-splice length of $35d_b$, vertical reinforcement ratio of 1.2% and were tested under constant axial load of 7% of the column axial capacity ($0.07f_c'A_g$). The axial load was applied using a hydraulic jack mounted on a low-friction trolley and the horizontal force component was neglected. The test results revealed that the control specimens having $35d_b$ lap-splice length without any retrofit performed relatively better than the columns with lap-splices shorter than $35d_b$ when compared to the studies done in the past. Retrofitting the columns using CFRP wraps increased the displacement ductility about 10% to 14% and the failure mechanism was mostly low-cycle fatigue rupture of the longitudinal bars except one of the control specimens where lap-splice bond failure was observed in addition to low-cycle fatigue rupture of the longitudinal bars. The specimen retrofitted with steel jacketing performed worse than the control specimens which was attributed to the crushing of the concrete in the gap provided between the jacket and footing which eventually lead to buckling of the longitudinal bars within the gap. It was observed that retrofitting did not change the initial stiffness of the specimens. Overall, all specimens had stable hysteretic response with reduced pinching in case of retrofitted specimens. It was also observed that the axial strains in the rectangular CFRP jackets was significantly higher than the oval-shaped jacket. The authors, however, indicated that the full-scale specimens might have performed worse than the scaled specimens and suggested caution when applying the test conclusions to all the existing rectangular bridge columns.

Overall, most of the retrofitting techniques focus on lateral confinement only, whereas, a column retrofitted to increase shear capacity also requires enhanced flexural ductility, which they often lack. There are few studies that explored the provision of flexural load paths through the use of NSM bars. Bournas and Triantafillou (2009) studied three (3) different types of near-surface-mounted reinforcing materials (carbon or glass fiber-reinforced polymers (CFRP or GFRP)) versus stainless steel) with different configuration and amount of NSM material and bonding agents for flexural strengthening of reinforced concrete (RC) square columns. The retrofitting scheme consisted of the combination of epoxy-bonded NSM bars with local confining jackets of textile-reinforced mortars (TRM). All bare column specimens were 250 mm x 250 mm (9.84 in x 9.84 in) in cross-section with cantilever column height of 1.6 m (63 in) and reinforced with four 14 mm (0.55 in) diameter smooth bars (except for one specimen, which had 12 mm (0.47 in) smooth bars) along with 8 mm (0.32 in) diameter smooth stirrups, closed with 90° hooks at both ends at a spacing of 200 mm (7.87 in) on center. The columns were subjected to lateral loading cycles while maintaining constant axial load of $0.2f_c'A_g$ applied to the columns throughout the cyclic tests. Stainless steel and FRP NSM bonded bar with epoxy resin were most effective in enhancing the flexural resistance as well as displacement ductility. Local TRM jacketing helped control buckling of the NSM reinforcement to some extent. The failure modes ranged from fracture and debonding of NSM FRP strips to buckling, fracture and extraction of NSM stainless steel bars. Failures could be attributed to inadequate confinement, as the jacket was provided in a square geometry. Moreover, the method was deemed challenging since there are a lot of technical construction nuances such as surface preparation and NSM grooving associated with this method.

Most of the notable research involving seismic retrofit using externally bonded FRP jacketing are cited in an ACI special publication (ACI 440.2R-17, ACI Committee 440 (2017)). One of the recognized problems in the external confinement of rectangular columns with FRP sheets is delamination between the FRP and concrete, which is accelerated by concrete cracking. Moreover, wrapping in rectangular jacketing is found to only be effective in confining the corners leaving the column sides vulnerable to bulging due to concrete cracking when the column is subjected to lateral loads. In addition, FRP performance under harsh environment and extreme temperatures had been studied to a limited extent. Many complicated installations such as tie rods, mechanical or fiber anchors have been developed have been shown to be effective in improving distribution of confinement pressure, but they are believed to increase the cost of rehabilitation scheme by 20% (Galal et al., 2005).

Circular and elliptical steel jackets with grout infill were popularly used in the past to retrofit RC bridge columns due to their potential for providing uniform confinement in the case of square and rectangular columns. However, the increase in the section with infill grout bonded to the bare column has the tendency to increase the lateral stiffness of the column depending upon the dimension of the jacket and the bond strength between the jacket and grout infill. Depending on the structure, this increase in stiffness can increase seismic demand in these columns making them even more vulnerable. The use of steel jackets also tend to concentrate the plastic hinge length and therefore increase curvature demands which can result in low-cycle fatigue fracture of the longitudinal reinforcing steel bars (Chai et al., 1994).

Review of the literature indicates that there is still a need for an economic, efficient and environmentally durable retrofit solution to improve the performance of deficient square RC columns. The proposed method intends to overcome these gaps by providing a novel retrofit solution using high-performance materials and conventional construction methods. This retrofit technique offers uniform confinement through circular profile of TiABs spirals with a provision of a supplemental and alternative flexural load path through external ligaments at the column surface, along with an infill grout unbonded from the bare columns to prevent stiffness increase.

2.5 TITANIUM IN CIVIL ENGINEERING

Takahashi, Muto, Hitoshi, Tadokoro, and Tagomori (1994) talks about the application of titanium to construction and civil engineering. Titanium alloys have been popular for their remarkable corrosion resistance characteristics, which makes it suitable for use in marine environments. They argue that titanium is an ideal metallic material for construction owing to its properties such as lightweight, flexibility, and slight dimensional change with heat. They also claim that it is as strong as carbon steel, nonmagnetic and nontoxic, does not easily ionize and does not pollute the environment, which makes it an even better alternative for construction underwater and in marine environments.

Adkins and George (2017) argue that titanium alloy bars have a lot to offer in the field of civil engineering. The material provides favorable properties for design including high tensile strength, ductility, environmental durability, high shear strength, resistance to mechanical damage, high maximum service temperature, and thermal expansion compatibility with concrete.

TiABs have also been successfully implemented for flexural and shear strengthening of prototype and full-scale bridge girders using Near Surface Mounted (NSM) technique (Barker, 2014; Amneus, 2014; Knudtsen, 2016; Vavra, 2016; Higgins, Knudtsen, Amneus, & Barker, 2017). After successful testing in a laboratory setting, NSM TiABs were used in an overpass (Mosier Bridge on Oregon's main East-West Route I-84) to rehabilitate girders that were found to be deficient after observing severe cracks with vertical deformations along the crack faces. The rehabilitation work was completed in a couple of weeks in 2014 and the bridge remains in service since. ODOT determined that the overall cost for the titanium strengthening for the Mosier Bridge was less than 3% of the estimated cost for bridge replacement and 30% lower than rehabilitation costs using alternative materials.

Recently, an ASTM standard specification for titanium alloy bars (TiABs) near surface mounts in civil structures (ASTM standard B1009-18, ASTM Committee B10 (2018)) was published. This specification provides standard material properties and requirements of TiABs with surface deformations and 90˚ anchorage hooks for use in NSM technique.

2.6 SOIL-FOUNDATION INTERACTION

The interaction between soil and foundation and the contribution of footing deformations to the overall structural response in a seismic event is an important concern to fully understand the seismic effect on structures. Kawashima and Nagai (2006) and Apostolou, Gazetas, and Garini (2007) indicated the uplift of spread footing foundations in events of past earthquakes such as Alaska 1964, San Fernando 1971, Kocaeli 1999, and Athens 1999. In general, the authors argue that provided spread footings are supported on the soil only through gravity loading, foundation rocking in the case of severe earthquake conditions is inevitable. While neglecting the effect of foundation rocking could be conservative in seismic design, thereby overestimating the seismic forces applied to the structures, the possible impacts due to rocking such as large lateral displacements of the deck and permanent settlement in soils can lead to catastrophic results.

Hung, Liu, Ho, and Chang (2011) tested three (3) circular reinforced concrete columns with spread foundations to study the effect of rocking behavior for columns with lap-spliced longitudinal reinforcement and inefficient transverse confinement and columns retrofitted with steel jacket representing column with sufficient ductility. Two specimens represented as-built columns with inadequate ductility and the third was retrofitted. One of the as-built columns was tested with its foundation constrained to the strong floor to serve as a benchmark column and the rest were rested on the neoprene pad allowing footing rocking. The specimens were tested under pseudo-dynamic loading and cyclic loading under constant axial load of $0.15\mathrm{f}_\mathrm{c}'\mathrm{A}_\mathrm{g}$. The comparison of results for specimens with restrained and rocking spread footing supported the isolation effect of rocking which reduced the ductility demand on the columns. However, the authors claimed that the reduction in the local ductility demand can only be achieved as long as the system has sufficient ductility to ensure that the isolation effect of the rocking mechanism can be achieved.

The studies involving soil-foundation interaction of RC bridge columns under seismic loading are limited and the existing ones are also limited to scaled models. Most of the experimental tests on RC bridge columns have restrained footings that do not reflect realistic foundation scenarios observed in the field. The contribution of foundation rocking to the overall lateral displacement is, therefore, not well understood. This calls for experimental and analytical study of RC column behavior with real footing and foundation conditions. This is even important when studying the behavior of retrofitted columns to ensure that column strengthening does not cause unintended damage in the footings, which is much more difficult to inspect and repair

The current study includes experimental tests of two full-scale retrofitted columns with realistic footing details (vintage spread footing and timber pile footing) to compare their behavior with that of common laboratory footing anchorage conditions. The experimental results can be used for development and validation of analytical models to assess the performance of control and retrofitted columns with soil-structure interactions.

2.7 ANALYTICAL MODELING

One of the important steps in developing a numerical model is to understand how the structure or different elements of the structure behave under specific loading condition. This includes properly understanding different components that contribute to the overall structural performance characteristics. Inelastic deformation of reinforced concrete columns subjected to cyclic lateral loads comprise mainly from deformations due to flexure, shear and anchorage slip or strain penetration Saatcioglu and Ozcebe (1989). Depending upon shear span ratios, flexural deformations, and reinforcement details, shear deformations can either be significant or insignificant. In addition, deformation due to strain penetration or anchorage slip can also contribute substantially to the overall deformation response. Modeling each of these parameters is essential to develop a coherent analytical model that is able to best represent the structural behavior under different loading conditions.

Several studies have suggested modeling approaches to characterize the behavior of bond-slip that is particularly important when modeling short lap-splices in RC columns (Harajli, Rteil, & Hamad, 2004; Zhao & Sritharan, 2007; Harajli, 2009; Chowdhury & Orakcal, 2012). A local bond stress-slip monotonic relationship was proposed by Harajli et al. (2004) that was later enhanced by Harajli (2009) to account for cyclic response. The latter model considers the level of confinement of concrete and the effect of critical bond parameters such as the diameter of steel bars, the ratio of concrete cover to bar diameter, the concrete compressive strength, the type of confinement and the area or contact of confining reinforcement. Zhao and Sritharan (2007) integrated a reinforcing bar stress-slip response into fiber-based analysis of concrete structures using a zero-length element to develop a model to address the slip and strain penetration effects. Chowdhury and Orakcal (2012) developed a fiber-based macro model to capture the local bond slip deformations along the lap-splice region in either splitting or pull-out bond failures under cyclic loading conditions.

Chai et al. (1994) developed an analytical model to simulate flexural response of circular steel jacketed column. They included the contribution of effective bond transfer between steel jacket and column in increasing the stiffness of the column. They assessed enhanced ultimate compressive strains of concrete due to confinement by steel jacket using an energy balance method for the ultimate limit state. They also used an energy-based damage model to assess the potential for a low-cycle fatigue fracture of the longitudinal reinforcement.

Yalcin and Saatcioglu (2000) developed the Column Analysis (COLA) software to provide sectional moment-curvature analysis, anchorage slip analysis, and member analysis, including P-Delta effects. The limiting condition of the sectional analysis was either the ultimate fracturing stress of the tension steel or the extreme concrete compressive fiber strain reaching the ultimate specified value whichever was reached first.

Isaković and Fischinger (2011) developed and analyzed a bridge model in OpenSees to study the applicability of pushover methods for seismic analysis of RC bridges. The superstructure was modeled using elastic beam-column elements. The columns were modeled using an inelastic lumped plasticity model for flexural behavior in the transverse direction of the bridge and an elastic model was used for flexural response in the longitudinal direction and shear response in both directions. The inelastic model comprised of zero length elements with non-linear behavior defined by Takeda's hysteretic rules that were linked by elastic beam column elements. They used guidelines by Priestley et al. (1996) to calculate the plastic hinge length. They employed three pushover methods to analyze the bridge: (a) the N2 method, as a standard single-mode pushover method; (b) the MPA (Modal Pushover Analysis) method, as a typical, non-adaptive multimode pushover method; and (c) the IRSA (Incremental Response Spectrum Analysis) method, as an adaptive multimode pushover method. Experimental results showed best correlation to the IRSA method as it was successful in adapting to the change in mode shapes. The N2 method was, however, the least effective in case of the higher intensities followed by the MPA method, since they could not consider the changes of the predominant mode at different seismic intensities.

Simulation of full nonlinear degrading behavior of structural elements is important in assessing seismic collapse vulnerability. Ignoring damage progression in structural elements can lead to erroneous failure progression predictions (Yavari, Elwood, & Wu, 2009). A calibrated analytical element was developed in LeBorgne and Ghannoum (2014) for reinforced concrete columns with functionalities implemented to allow coupling of degrees of freedom and allow deformations in flexural elements to trigger degradation in the proposed element. The element only requires users to input column geometry and material properties to define the analytical behavior.

Belejo, Barbosa, and Higgins (2019) developed analytical column models based on a phenomenological approach in OpenSees by calibrating the column responses to measured experimental response by Lostra (2016). The columns under study were 24 in x 24 in (609 mm x 609 mm) and 12 ft (3.66 m) tall, and reinforced with 4 – #10 (#32M) ASTM Gr. 60 reinforcing steel bars along with 3.3 ksi (22.7 MPa) concrete. The column models were developed for unretrofitted and TiAB retrofitted columns using phenomenological bond-slip model adapted from Harajli et al. (2004) and Harajli (2009), and TiAB model defined using Pinching4 material model in OpenSees. The column models were defined with fiber-based displacement beam column elements and TiAB ligaments were assigned as truss elements. The column models were able to estimate the overall expected force-deformation response well up to the peak capacity, however, the strength degradation and pinching effect was not estimated well for the retrofitted columns. These models were adapted into a bridge bent system to study the system behavior in regular and irregular bridges. Column bases were fixed to simulate rigid foundations. The retrofit was applied uniformly to all columns in a bridge system regardless of the column height and the performance was compared with that of a similar bridge model with unretrofitted columns.

2.8 RETROFIT DESIGN APPROACH

Many seismic evaluation and retrofit design provisions such as ASCE 41-13 (2013) and Eurocode 8-1 (2004) were established in the past based on numerous experimental studies on various seismic retrofitting and strengthening techniques for buildings. These provisions are not inclusive of newly immerging retrofit methods and are, therefore, limited to the retrofit techniques used in the past. ASCE 41-13 (2013), for example, does not include modeling parameters necessary to establish nonlinear load-deformation curves for concrete columns after retrofit.

Seismic Design Criteria Version 1.7 (Caltrans, 2013) provides minimum seismic design requirements for Ordinary bridges under design seismic hazard scenario. Seismic Retrofitting Manual for Highway Structures : Part 1 – Bridges (2006) provides design recommendations for seismic retrofitting of bridges based on performance based design principles.

ACI 440.2R-17 (2017) was recently developed to serve as a guide for the selection, design, and installation of externally bonded FRP systems for strengthening concrete structures which is the most popular retrofit method for existing concrete structures. This document is based on hundreds of research publications on the FRP retrofit system and is limited to the use for this particular retrofit method only, which relies on the performance enhancement by means of external confinement.

Each retrofit application is unique and a failure to recognize the characteristic difference in terms of performance and role of each element when using a design provision could result in an unexpected performance and lead to failure in unanticipated locations. Therefore, each retrofit solution should be followed by design guidelines to ensure the expected performance. This research, thus, provides design guidelines and recommendations for practicing engineers and professionals specific to the proposed retrofit method.

3.0 EXPERIMENTAL PROGRAM

An experimental program was developed to evaluate the performance of RC columns retrofitted with TiABs subjected to cyclic lateral loading. The program consisted of tests on full-scale square RC bridge columns constructed in the laboratory. The dimensions and loading of the column specimens was selected after analysis of geometrical, material, and detailing information for vintage RC columns in the Oregon Department of Transportation bridge database. The specimens were configured in the laboratory as cantilever columns on a footing that was attached to the laboratory floor.

The structural behaviors of 14 full-scale column specimens were investigated to study the effect of the proposed seismic retrofit on their cyclic performance. The program consisted of design, construction, and reverse cyclic lateral loading of column specimens under constant axial load. The main test variables were the column height, lateral loading direction, height of the retrofit shell, presence and absence of vertical ligaments, hook angle of vertical ligaments, type of materials used for vertical ligaments, and the foundation details and restraints.

The specimens were grouped based on the height of the column stubs: 12 ft (3657 mm) high “tall columns” and 8 ft (2438 mm) high “short columns.” The height of column stubs (measured from the top of the footing to the point of lateral load application) was chosen to represent lower half of the columns assuming the point of inflection at mid-height of these columns. The bare column design and details before retrofit application for all specimens reflected pre-1970’s bridge construction details and were constant except for the height of column stubs for two different groups. Four of the “tall columns” were tested as a preliminary part of the research (Lostra, Higgins, & Barbosa, 2016) and an additional “tall column” was tested later to complete the test matrix of that group. The parameters for the “tall columns” were taken from a bridge along I-5 (Mackenzie River Bridge) and the column stub height was 12 ft (3657 mm). The column parameters including the height of the columns for “short columns” group are based on a statistical study of the detailed structural drawings of the bridges along I-5, US-97, and OR-58 from the Oregon Department of Transportation bridge database.

3.1 OREGON DENPARTMENT OF TRANSPORTATION (ODOT) BRIDGE INVENTORY REVIEW

A statistical study of the detailed structural drawings of the bridges along I-5, US-97, and OR-58 in the state of Oregon from the Oregon Department of Transportation (ODOT) bridge database was performed to establish the typical construction details that would reflect the pre-1970 bridge column design. On I-5 in Oregon alone, 223 bridges were built prior to 1970s (i.e. before the adoption of modern seismic design provisions), out of this population 69 bridges are supported on poorly detailed reinforced concrete (RC) square columns (most of them solely supported on square columns and some in combination with RC circular and rectangular columns). The number of these RC square columns was approximately 600.

The RC square columns were then sorted and characterized in terms of their geometries (column dimension and clear height from footing top to the base of bent beam), material properties (concrete and reinforcing steel grade), longitudinal and transverse reinforcement details (reinforcing steel quantity, bar size, and bar type), details of bar splice at the column base (lap-splice length in terms of diameter of bar), axial load supported by each column (tributary weight from the super structure) and foundation details (size, depth, and reinforcing steel details). These characteristic details are summarized in the following sections.

3.1.1 Column Dimensions

The most common column size is 24 in x 24 in (610 mm x 610 mm) square having a frequency of 55%, the second being 20 in x 20 in (508 mm x 508 mm) square with 25% frequency. The distribution of column section dimensions was grouped together using a bin size of 2 in (50.8 mm) and is shown in Figure 3.1.

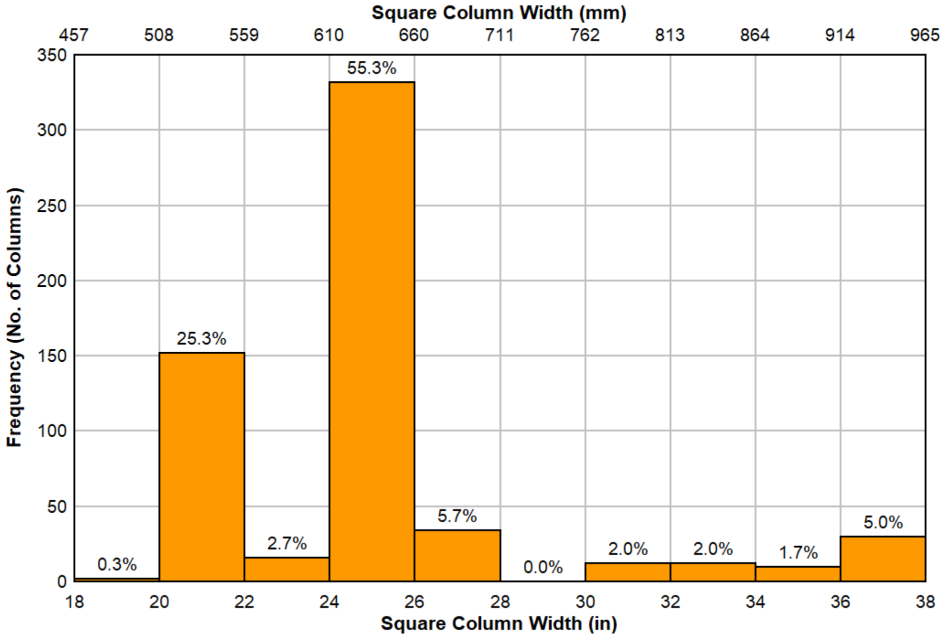

Figure 3.1: ODOT inventory square column width distribution

The column clear heights were measured from the bottom of the cap beam to the ground level or the top of footing in each column. The column heights were found to vary even in the same bridge depending on the gradient of the soil profile. The columns were thus treated individually to summarize the distribution of their clear height. Using a 3 ft (0.91 m) bin size, the mean clear height of the columns measured from the foundation top to the bottom of bent caps was 16 ft (5029 mm) with the mode being in the range of 15 ft (4.57 m) to 18 ft (5.49 m), as seen in Figure 3.2

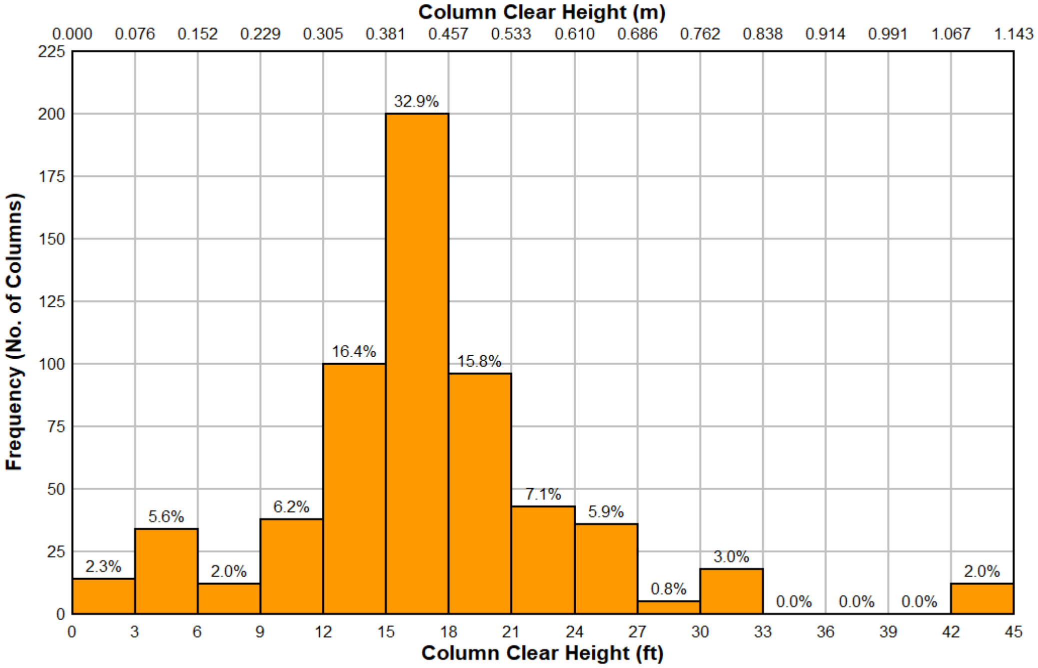

Figure 3.2: ODOT inventory square column clear height distribution

3.1.2 Reinforcement Details

The majority of square columns were reinforced with only four longitudinal bars laid out in each corner and tied with square ties having 90-degree hook details. The most common longitudinal reinforcement was 1% of the gross area of column with the most common rebar size used being intermediate grade (Grade 40 equivalent) #11 (#36M) deformed bars. Some columns had square longitudinal rebar. The most common transverse reinforcement arrangement was intermediate grade (Grade 40 equivalent) #3 (#10M) square ties provided at 12 in (305 mm) on-center starting 6 in (152 mm) from the top of footing. The average transverse reinforcement ratio was found to be 0.09% of the column shear area. Distributions of the observed reinforcing details are shown in Figure 3.3, Figure 3.4, Figure 3.5, and Figure 3.6. It is noted the transverse reinforcement data are skewed and the median value is approximately 0.07%.

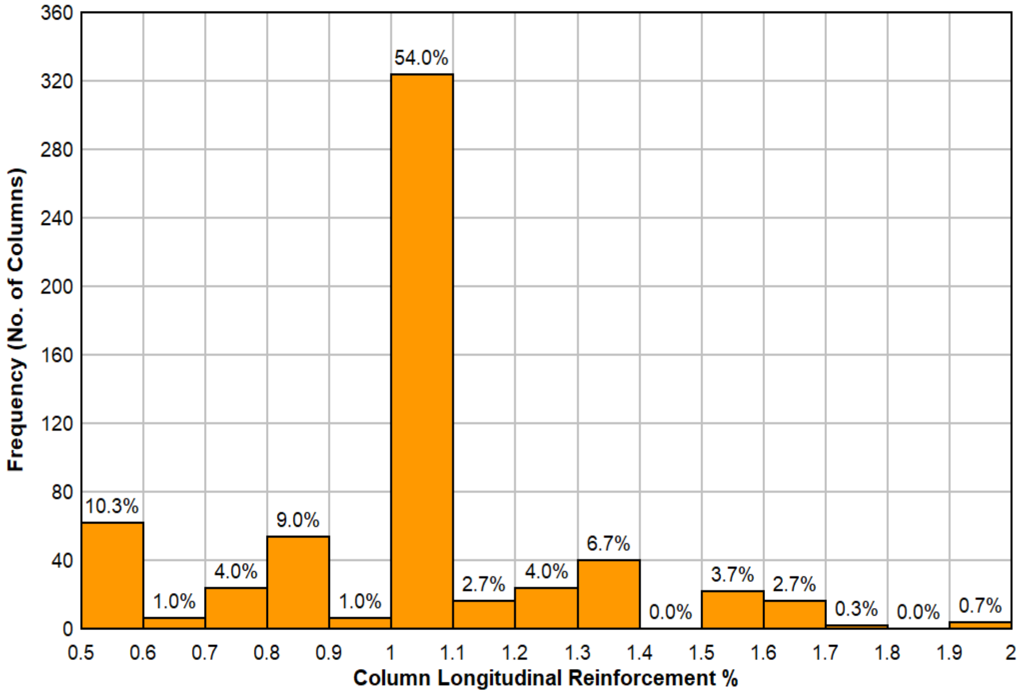

Figure 3.3: ODOT inventory column longitudinal reinforcement distribution

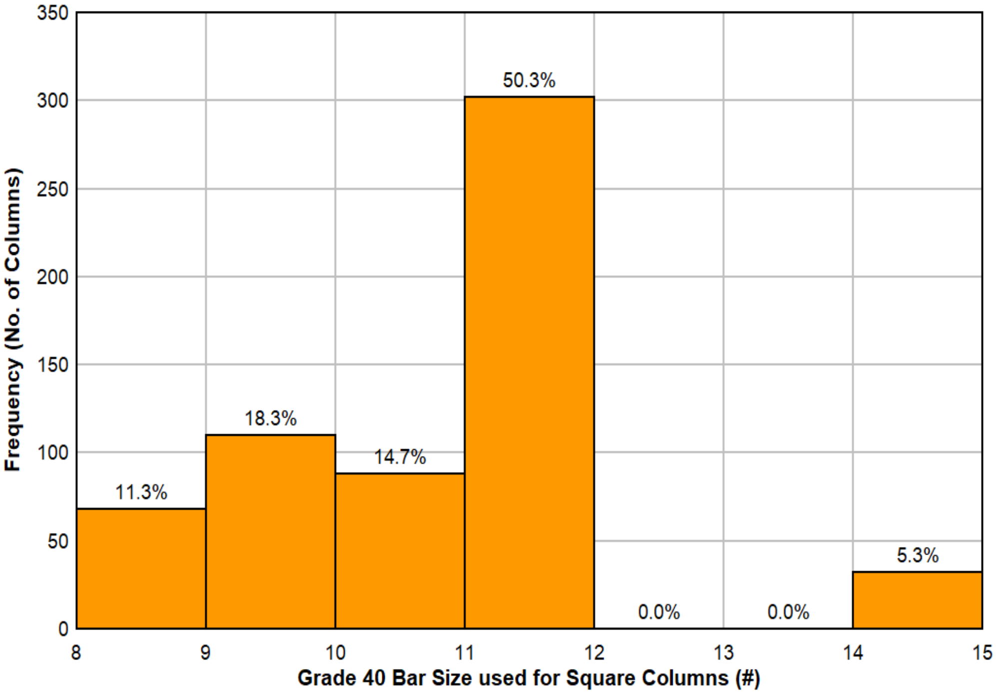

Figure 3.4: ODOT inventory column longitudinal reinforcement bar size distribution

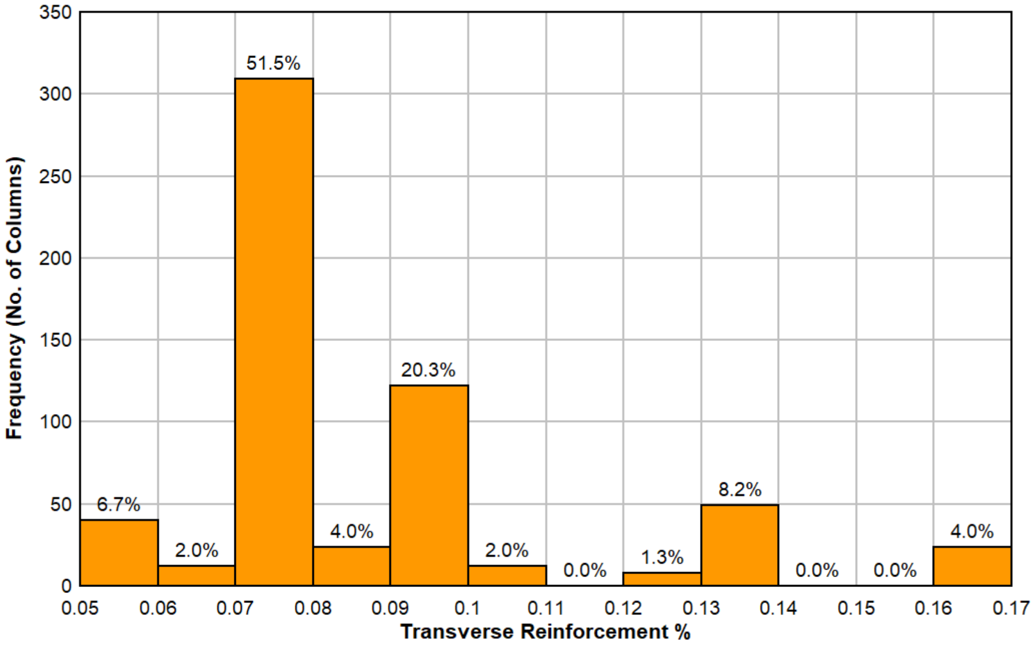

Figure 3.5: ODOT inventory column transverse reinforcement distribution

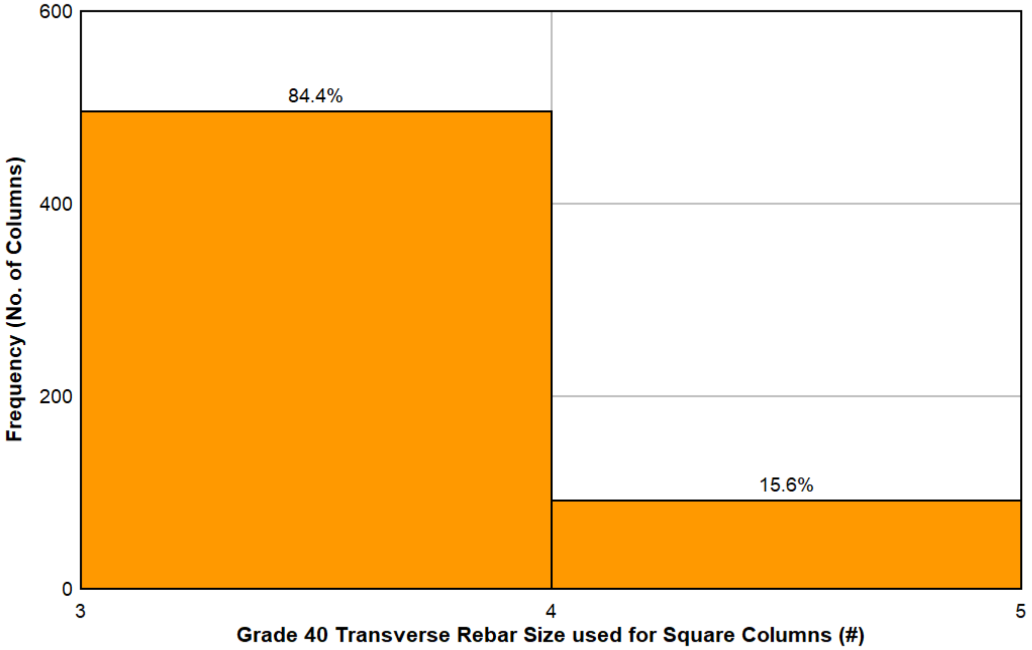

Figure 3.6: ODOT inventory column transverse reinforcement bar size distribution

3.1.3 Longitudinal splice detail

The column longitudinal bars were lap-spliced to the starter bars from the footing right above the footing (i.e., the base of the columns). The length of the starter bars measured from the top of the foundation (i.e. splice length) ranged from 24 in (609 mm) to 60 in (1524 mm) with no clear distribution pattern. The average lap-splice length was found to be 38.2 in (970 mm). To observe the distribution of splice length in terms of the diameter of starter bars (d_b) (which is the same as that of vertical reinforcement in columns), histograms were generated for splice length in terms of d_b. Average value was found to be 28.9 times d_b with the modal value ranging from $24d_b$ to $27d_b$. Since the most common reinforcement bar type was Grade 40 #11 bars, the distribution of splice length in terms of #11 bar diameter was presented. The average splice length for #11 bars was found to be $29d_b$ with the modal value ranging from $33d_b$ to $36d_b$. Histograms of the longitudinal splice details observed from the database are shown in Figure 3.7 and Figure 3.8.

Due to the unavailability of Grade 40 #11 bars, it was decided to use equivalent Grade 60 #10 bars as the longitudinal and starter bars. For equivalent Grade 60 #10 bars, average splice length using $29d_b$ is calculated to be 36 in (914 mm). As a result, the full-scale specimens were constructed with 36 in (914 mm) starter bars spliced with column longitudinal bars. It is noted that the current AASHTO-LRFD specifications would require a splice length of 52.4 in for the Grade 60 #10 bars.

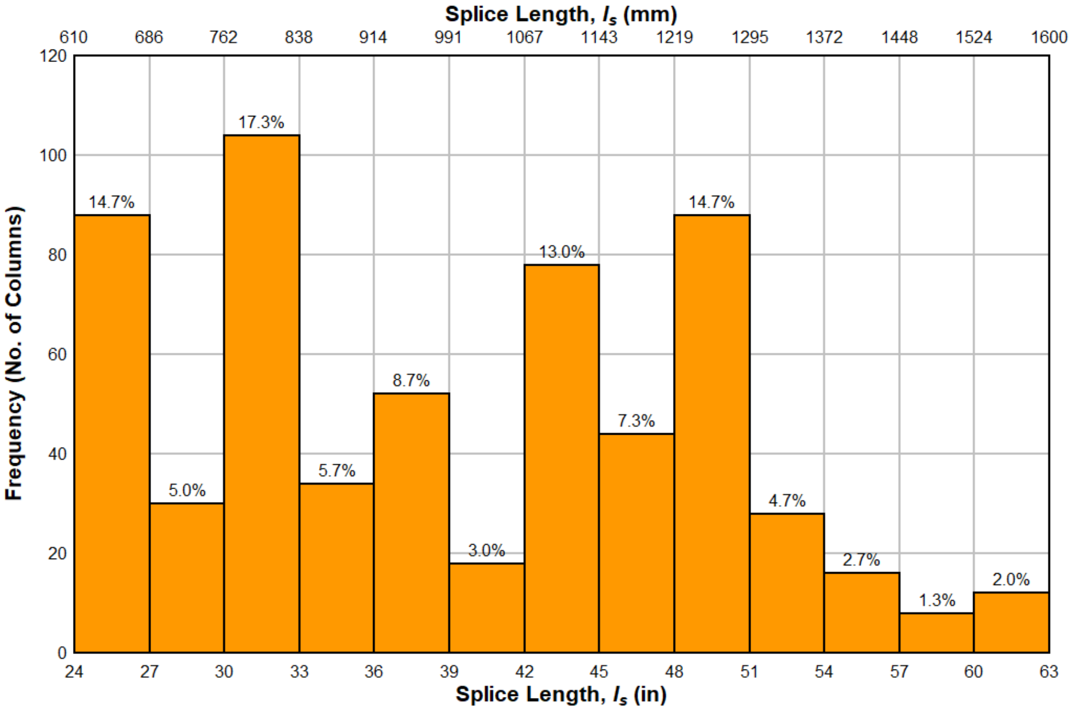

Figure 3.7: ODOT inventory splice length distribution

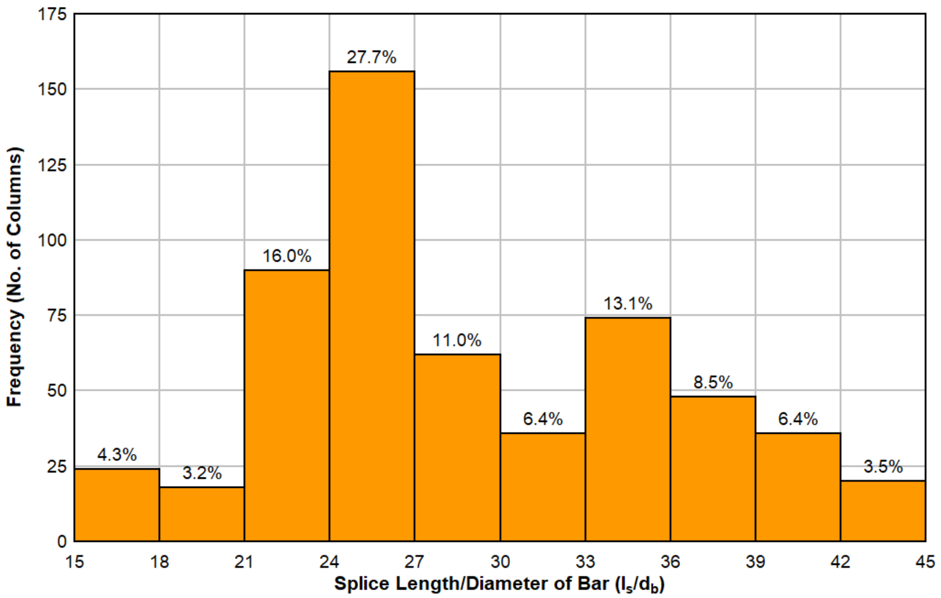

Figure 3.8: ODOT inventory splice length distribution in terms of diameter of bar

3.1.4 Axial Load

The number of square columns observed in a single bent across the bridge inventory is shown in Figure 3.9 and shows that most have either 2 or 4 columns per bent. Service-level axial loads in the columns produced by the weight of components (DC) and the weight of the wearing surface (DW) was calculated by distributing tributary weight of the superstructure to the bent columns and taking the load from the column with the largest load. A sample calculation of axial load based on structural drawings of a 1950's era reinforced concrete deck girder bridge located in Springfield, Oregon is shown below. Structural details of Springfield Bridge are provided in Appendix D.

Bridge Parameters
Grade of Concrete = 3300 psi
Grade of Steel = 40 ksi
Unit Weight of Concrete = 150 pcf
Unit Weight of Asphalt = 145 pcf
Thickness of deck = 6 in
Number of girders = 5
ft in
Deck width = 30 0
Span (L1) = 55 0
Span (L2) = 55 0
Average Span (L) = 55 0

Deck Load Calculation
Thickness of deck = 0.5 ft

Width of deck = 30 ft
Length of deck = 55 ft
Total weight of deck = 123,750 lb
= **124 kip**

Curb Load Calculation
Height of curb = 0.75 ft
Width of curb = 1.5 ft
Length of curb = 55 ft
Weight of one curb = 9,281 lb
Total weight of two (2) curbs = **19 kip**

Rail Load Calculation
Height of rail = 2 ft
Width of rail = 0.67 ft
Length of rail = 55 ft
Weight of one rail = 11,000 lb
Total weight of rail = **22 kip**

Girder Load Calculation
Total depth of girder = 5.39 ft
Depth excluding deck = 4.89 ft
Width of girder = 1.42 ft
Length of girder = 55 ft
Weight of one girder = 57,271 lb
Total weight of 5 girders = **286 kip**

Asphalt Load Calculation
Thickness of wearing = 0.17 ft
Width of wearing = 30 ft
Length of wearing = 55 ft
Total weight of wearing = 39875 lb
= **40 kip**

Total dead load per bent = 458 kip
Number of columns per bent = 2
Axial load per column = 229 kip

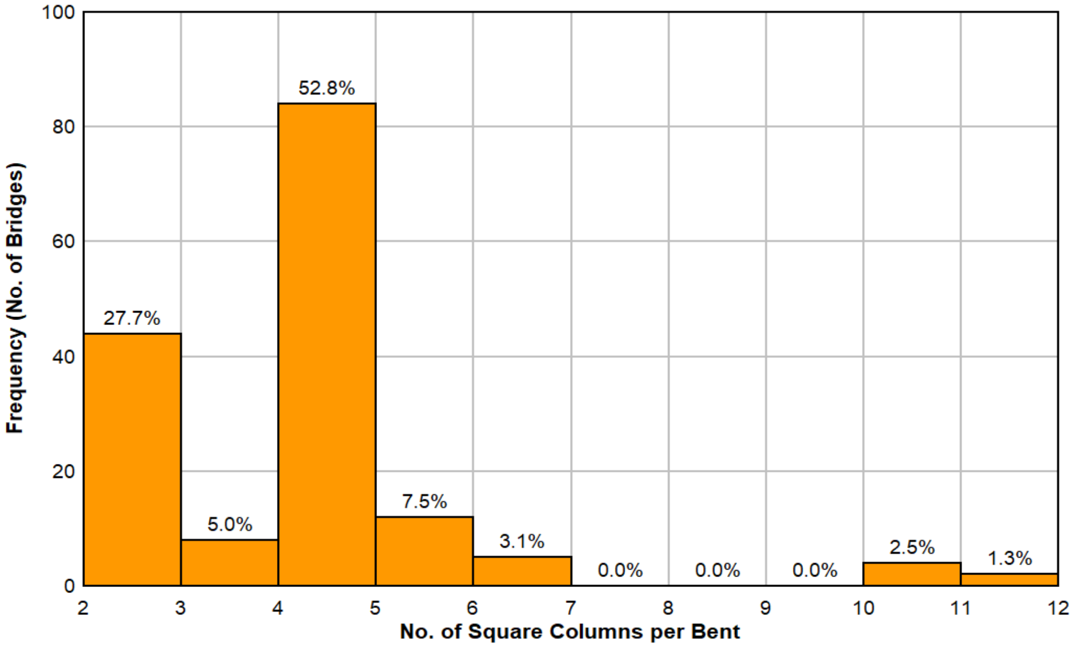

Figure 3.9: ODOT inventory square columns distribution per bent

Average service-level axial load per column was calculated to be approximately 120 kips with the modal value ranging from 50 to 100 kips (222 to 444 kN). This was equivalent to an average axial stress of 0.055*f'c* with the modal range 0.04*f'c* to 0.05*f'c*. The distribution is as shown in Figure 3.10.

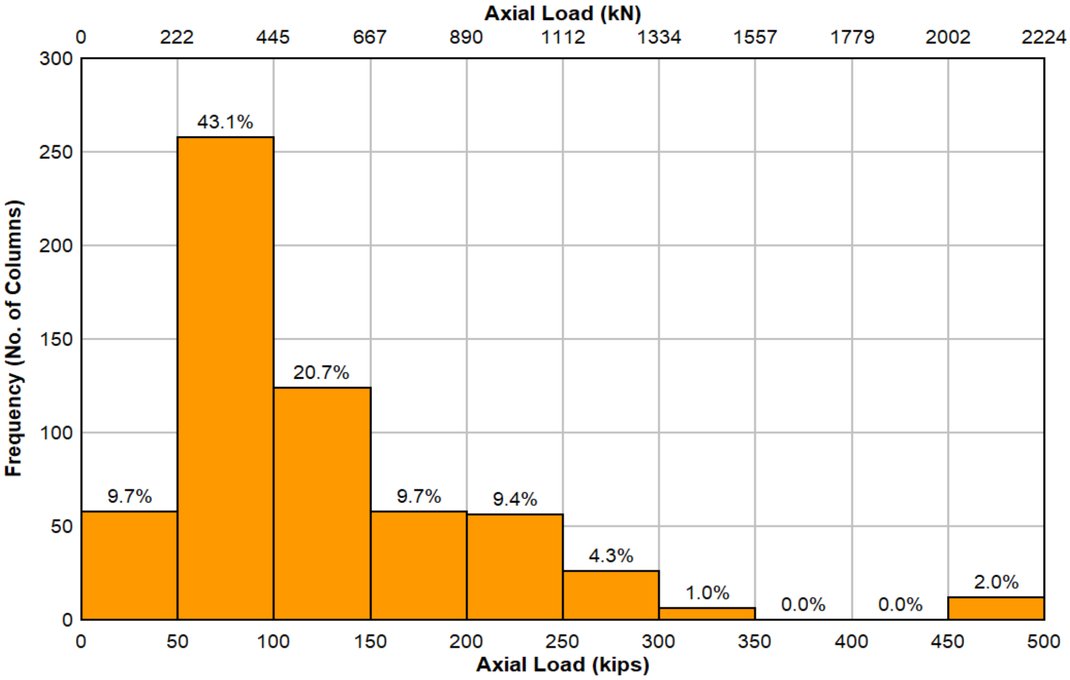

Figure 3.10: ODOT inventory square columns axial load distribution

3.1.5 Foundation Details

Histograms of the relevant spread footing details are shown in Figure 3.11, Figure 3.12, Figure 3.13, and Figure 3.14. Histograms of the relevant pile supported foundation details are shown in Figure 3.15, Figure 3.16, Figure 3.17, and Figure 3.18. The majority of square columns (79%) were found to be resting on RC spread footing and the rest (21%) on pile foundations. Of the pile foundations, 78% were built with timber piles (96% of the timber piles were found to be treated and the rest were untreated). Only 22% of the pile foundations were built with 10BP42 Steel Piles. The piles were capped with a RC pile cap with 6 in (152 mm) embedment on the timber pile into the pile cap without any supplemental connection. Both spread footings and pile caps are reinforced with a single mesh of reinforcement at the bottom with 3 in (76 mm) of clear cover.

The most common size for both spread footing and the timber pile caps was 60 in x 60 in (1524 mm x 1524 mm) and the most common depth for 60 in x 60 in (1524 mm x 1524 mm) spread footings and timber pile caps was 24 in (609 mm). Both spread footings and pile caps are reinforced with a single mesh of reinforcement at the bottom with 3 in (76 mm) of clear cover. The most common reinforcement used was Gr. 40 #5 (#16M) with average reinforcement of 0.21% in spread footings and 0.13% in timber pile caps.

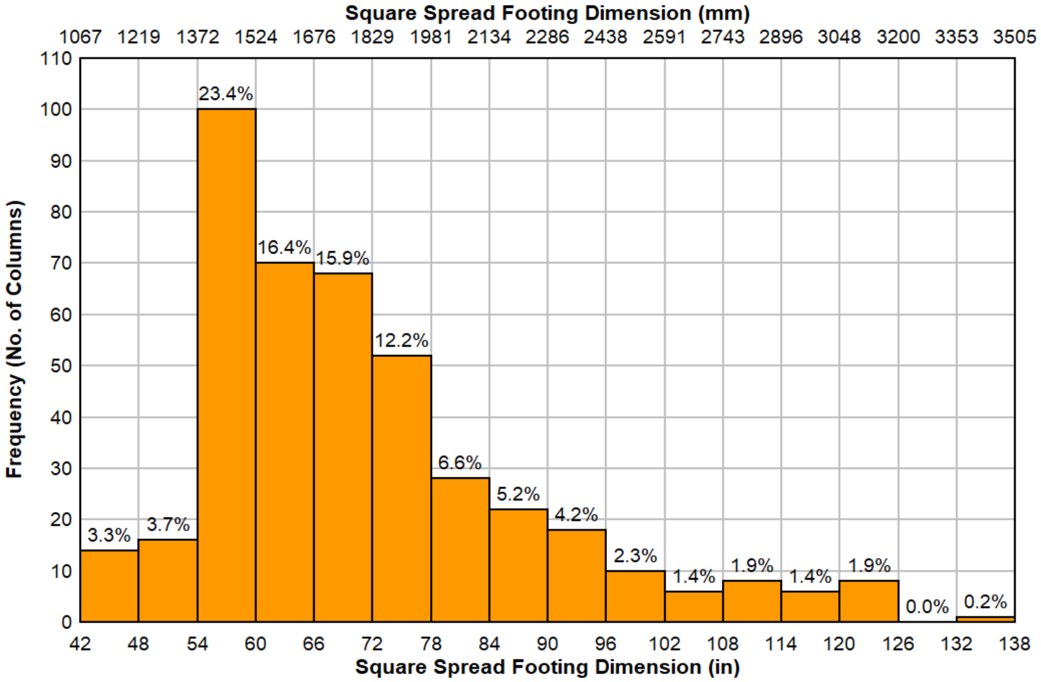

Figure 3.11: ODOT inventory square spread footing width distribution

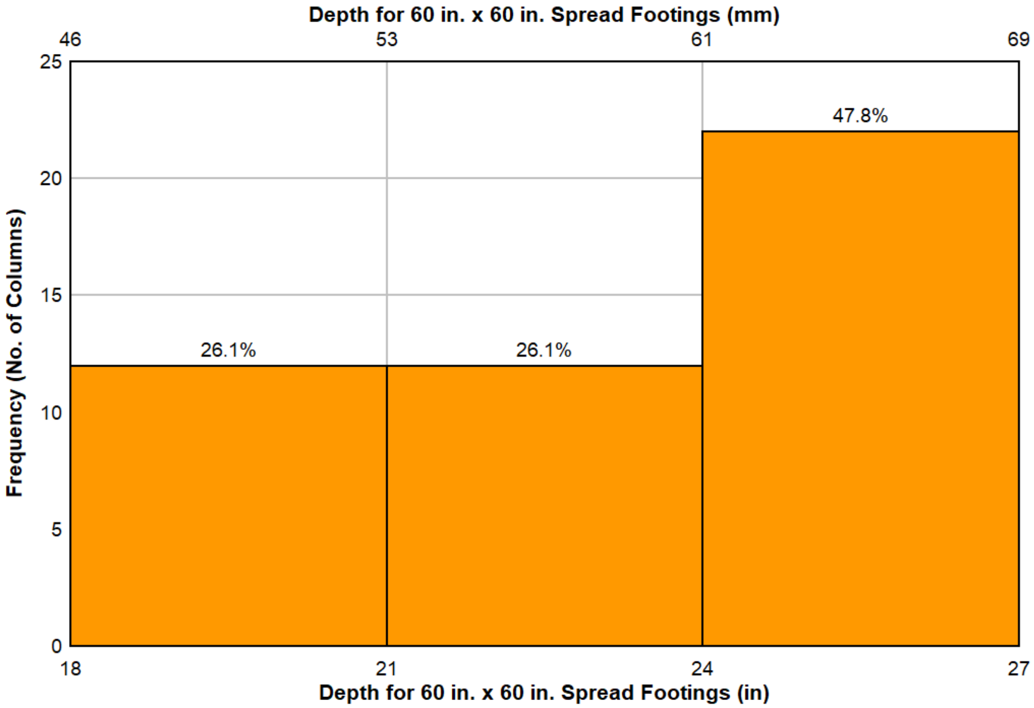

Figure 3.12: ODOT inventory depth distribution for 60 in x 60 in spread footings

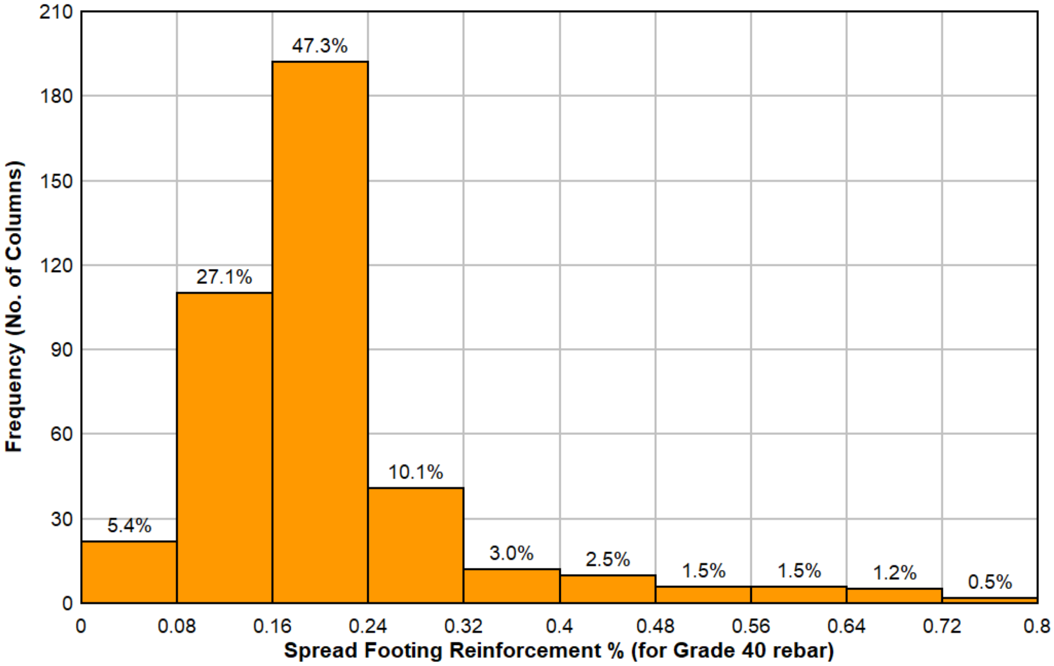

Figure 3.13: ODOT inventory spread footing reinforcement distribution

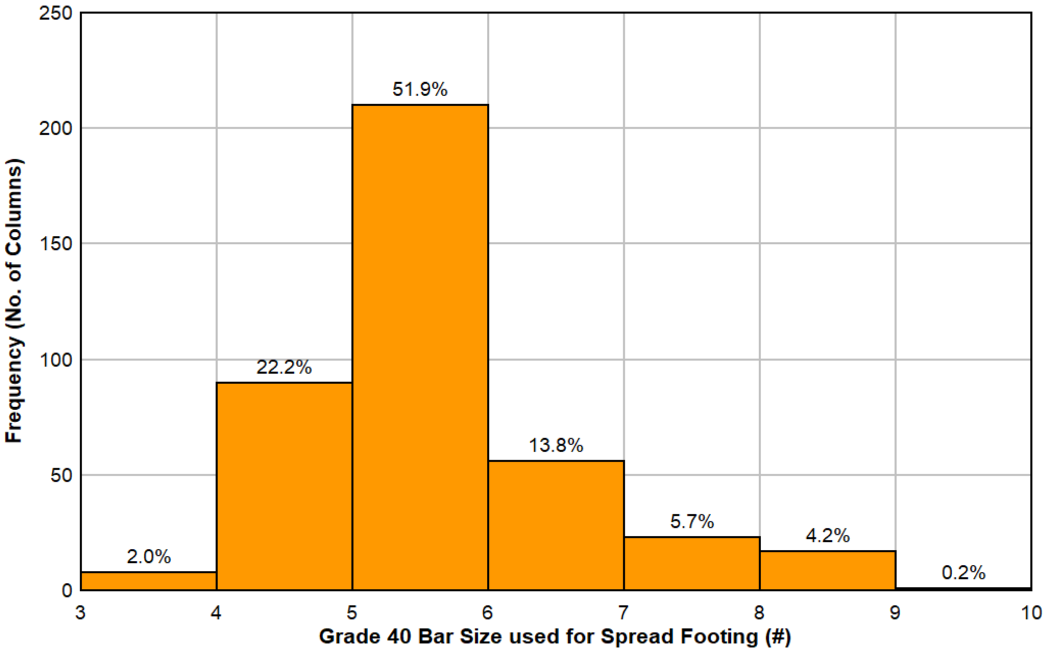

Figure 3.14: ODOT inventory spread footing reinforcement bar size distribution

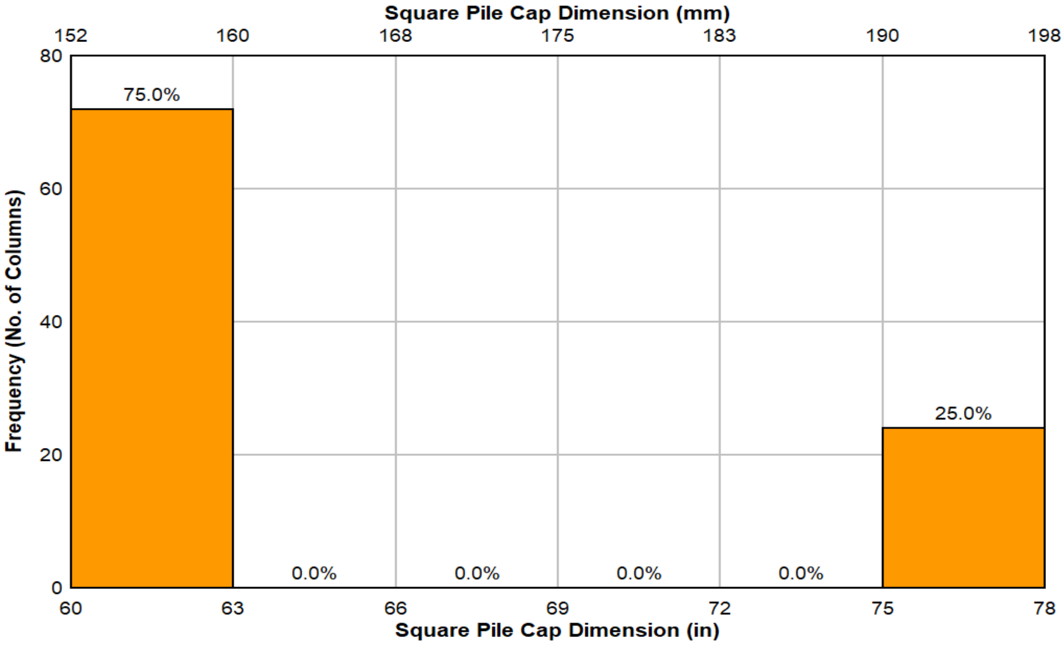

Figure 3.15: ODOT inventory square pile cap width distribution

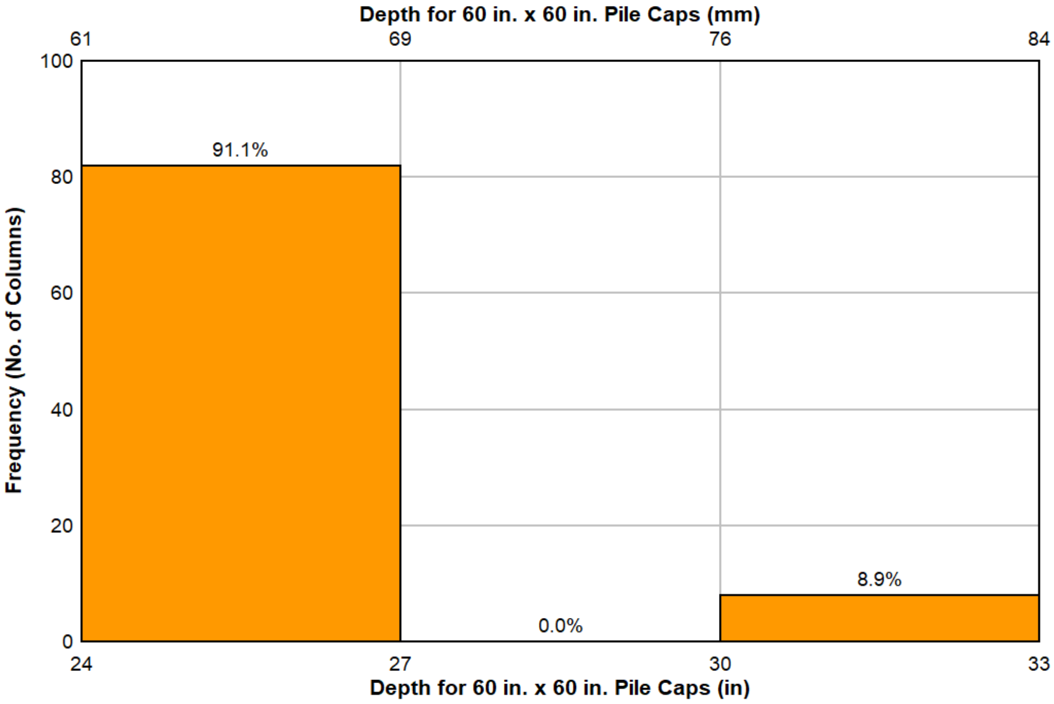

Figure 3.16: ODOT inventory depth distribution for 60 in x 60 in pile caps

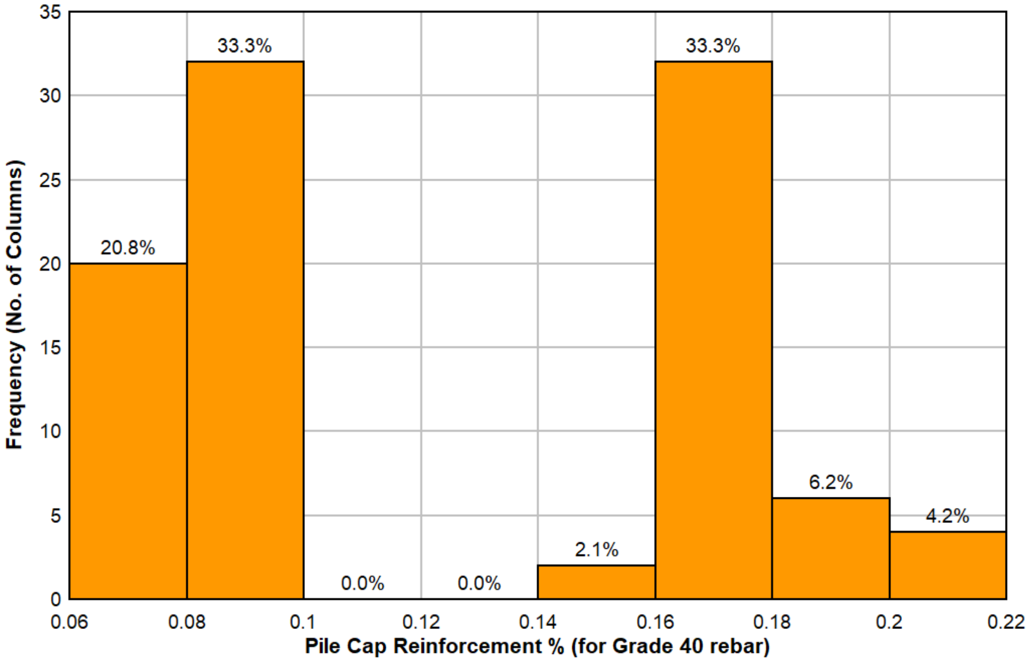

Figure 3.17: ODOT inventory pile cap reinforcement distribution

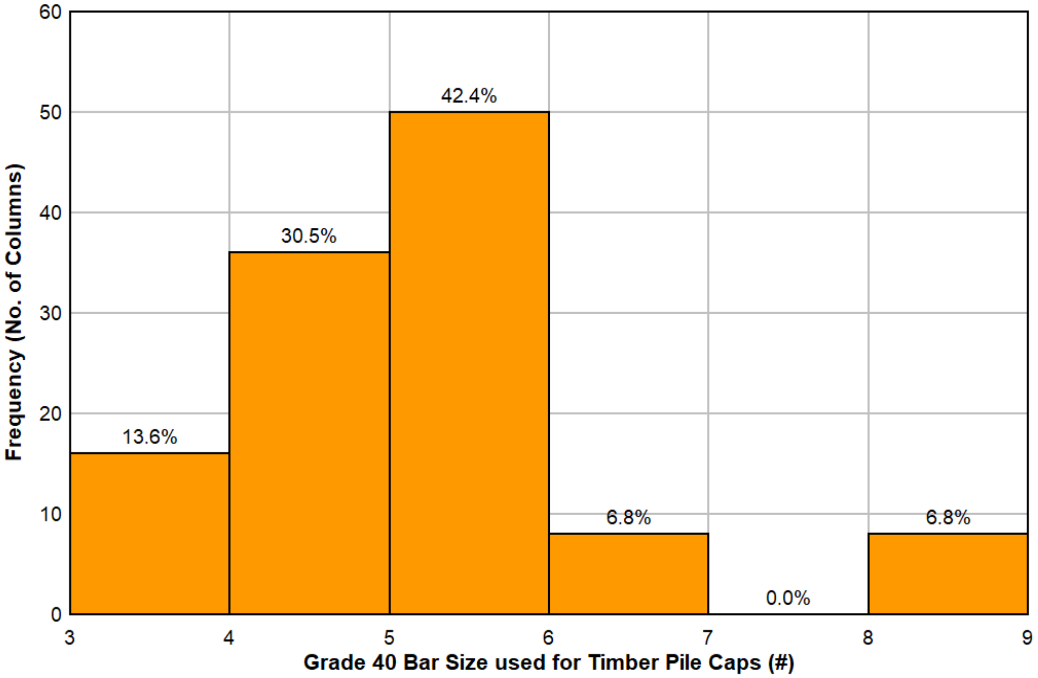

Figure 3.18: ODOT inventory pile cap reinforcement bar size distribution

3.1.6 Summary of Oregon Department of Transportation (ODOT) Bridge Inventory Review

The RC square columns in the inventory were mostly 24 in x 24 in square and their clear height mostly ranged from 15 ft. to 18 ft. The concrete used in these columns had characteristic compressive strength of 3300 psi with 1.5 in cover concrete. The most common longitudinal reinforcement details were 4-#11 round or square intermediate grade (equivalent to Gr. 40) bars provided in each corner. Average shear reinforcement was 0.09% with intermediate grade #3 ties at 12 in on-center. The vertical (longitudinal) column bars were spliced with the footing starter bars without extra confining hoops along the splice length. The average length of the spliced bars measured from the top of the foundation (i.e. lap splice length) was found to be 29.2 times the diameter of the bar (d_b). In the columns with Gr. 40 #11 bars, the average splice length was found to be 30 times the diameter of the bar. Thus, for the equivalent #10 Gr. 60 bars used for the specimens in this study, a 36 in lap splice length was used which is approximately 28.3 times d_b. About 71% of square columns were found to be resting on RC spread footing and the remainder on pile foundations. The majority of piles were timber piles. Both spread footings and pile caps have single mesh of reinforcement at the bottom with 3 in cover concrete. Average service-level axial load per column was calculated to be approximately 120 kips which is around 0.055 $f'_c A_g$. For our tests, axial load was kept constant throughout the test at 200 kips (0.1 $f'_c A_g$) for 12 ft. tall columns and 150 kips (0.08 $f'_c A_g$) for 8 ft. short columns.

These common parameters in the database were used as the basis for design of the specimens used in this testing program.

3.2 SPECIMEN DESIGN AND CONSTRUCTION

3.2.1 Conventional Column Details

The common parameters observed in the ODOT bridge database were used as the basis for design of the specimens used in the testing program.

All column specimens were 24 in x 24 in (609 mm x 609 mm) square columns with 4 – #10 (#32M) Gr. 60 longitudinal reinforcing steel bars (i.e. $\rho_l = 0.88\%$) which is equivalent to the most common vintage detail of 4 – #11 (#36M) Gr. 40 longitudinal reinforcement bars (i.e. $\rho_l = 1.0\%$) and #3 (#10M) Gr. 40 square hoops with 90-degree hooks at 12 in (305 mm) on-center (i.e. $\rho_v = 0.09\%$) with 1.5 in (38 mm) concrete cover. The #10 (#32M) Gr. 60 reinforcing bars were used in place of #11 (#36M) intermediate grade reinforcing bars for longitudinal bars since #11 (#36M) intermediate grade reinforcing bars are no longer produced. The specimen cross section is shown in Figure 3.19. The longitudinal reinforcement bars were spliced at the base of the column to the starter bars from the footing with the lap-splice length of 36 in (914 mm: approximately $28d_b$). The first group of specimens comprised of five "tall columns" with 13 ft (3962 mm) overall column height and the second group of specimens had nine "short columns" with 9 ft (2743 mm) overall column height. An extra foot height was provided for attachment of the lateral load assembly. The typical reinforcing steel details are shown along the elevation in Figure 3.20 and Figure 3.21. The column formwork and reinforcing cages and are illustrated in Figure 3.22 and Figure 3.23.

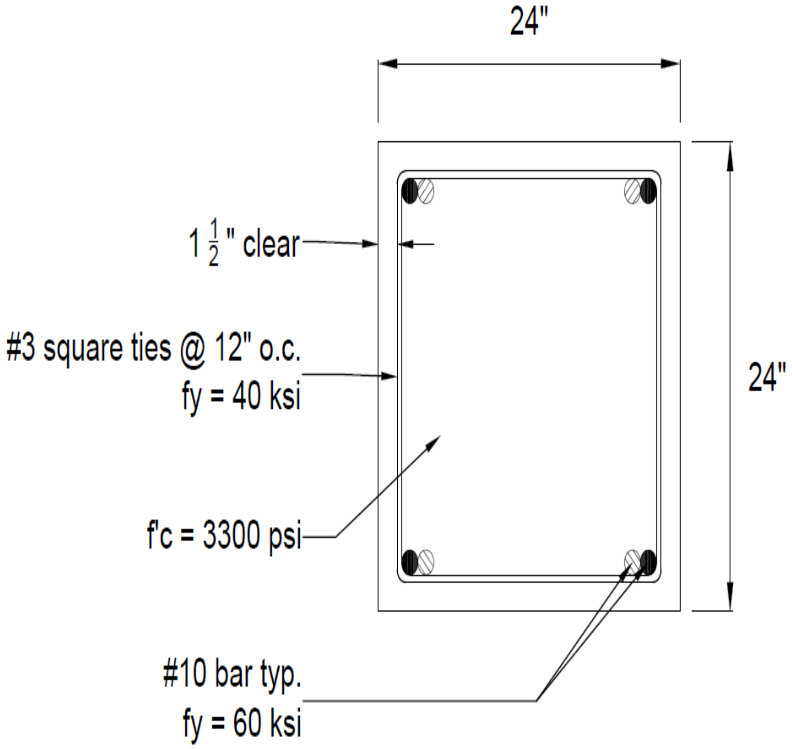

Figure 3.19: Cross section of column specimen in splice region used to match vintage dimensions and details

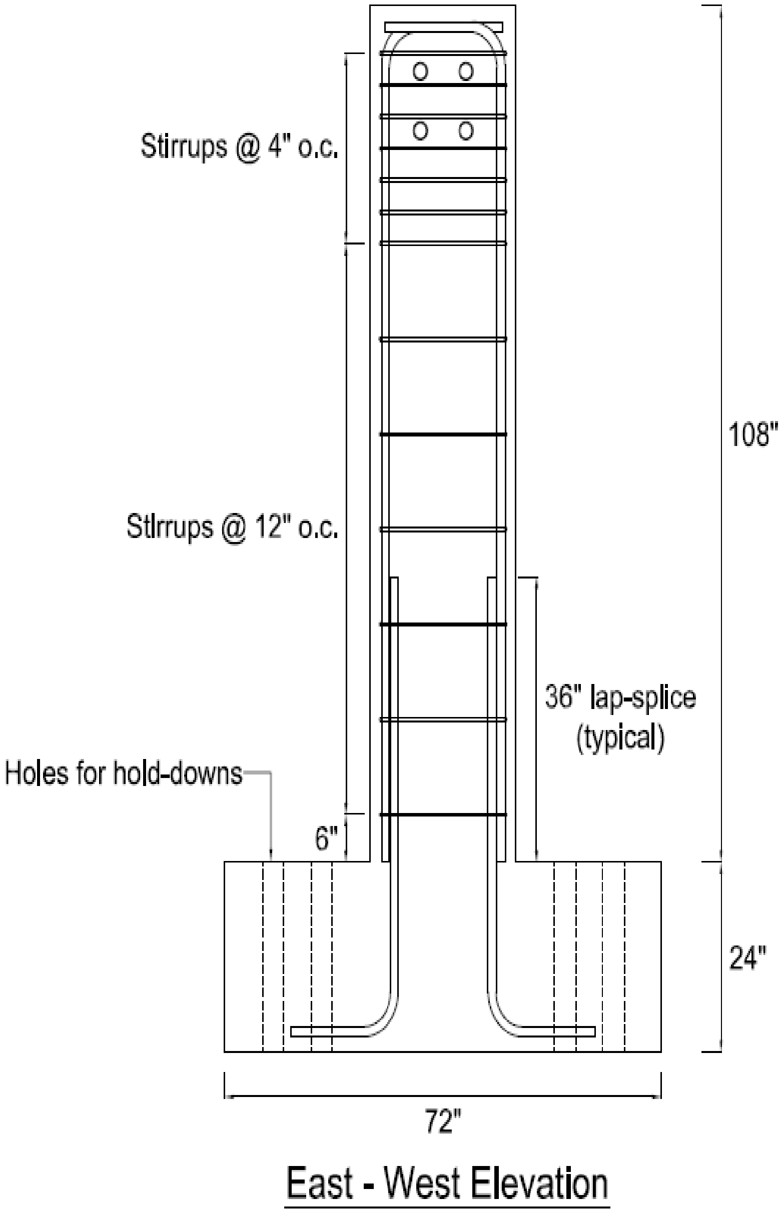

Figure 3.20: Elevation view of "short" column details and reinforcing steel (all dimensions in inches)

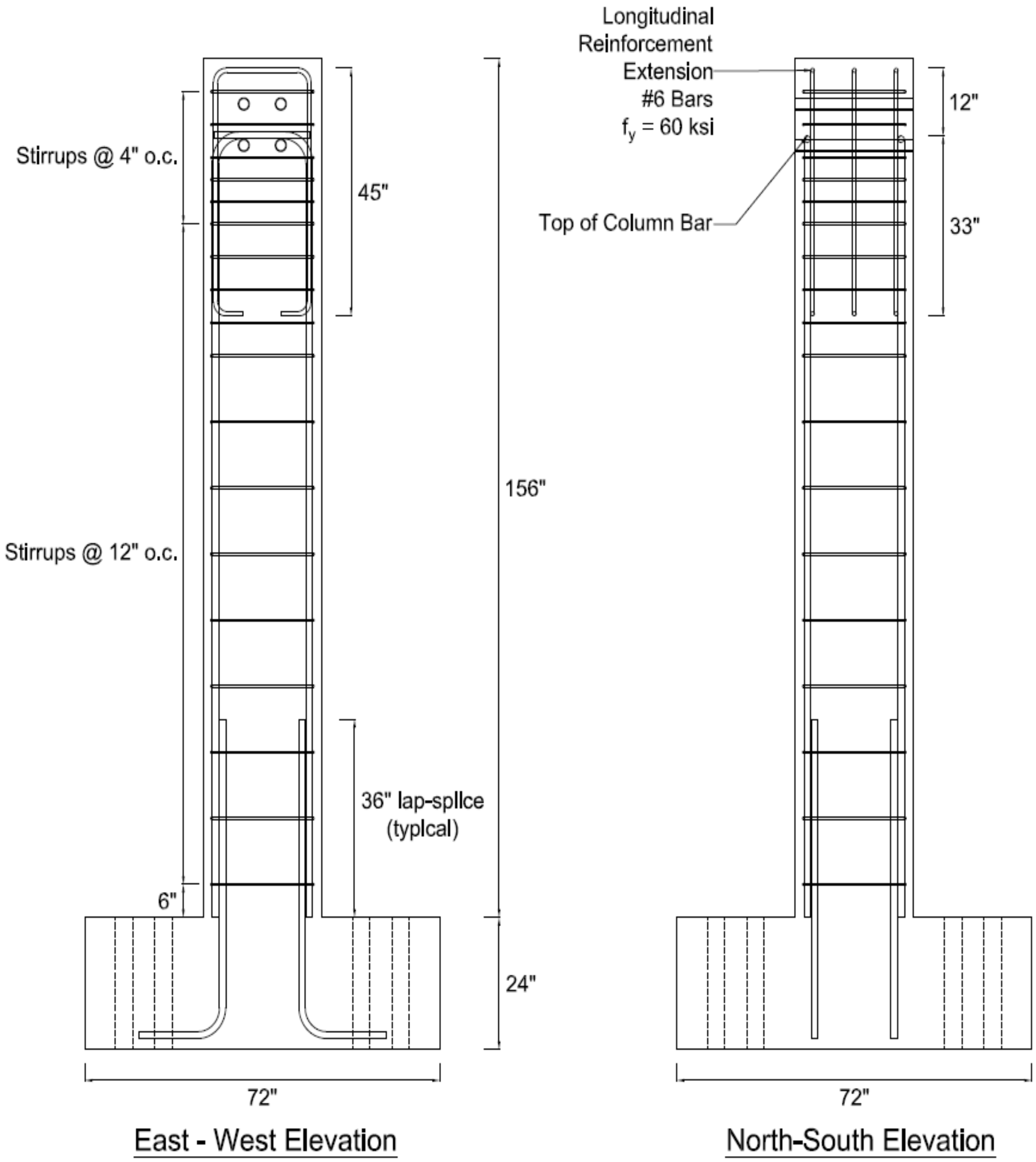

Figure 3.21: Elevation view of "tall" column details and reinforcing steel (all dimensions in inches)

Figure 3.22: Additional reinforcing steel near column loading point for tall columns

Figure 3.23: Typical reinforcing steel cage for tall column specimens

Of the fourteen (14) specimens in the test program, twelve (12) were constructed with heavily reinforced 6 ft. x 6 ft. (1828 mm x 1828 mm) and 2 ft. (609 mm) deep footing blocks having details shown in Figure 3.24 and Figure 3.25. The footing details for the diamond column orientation are shown in Figure 3.26. The footings of these specimens were over-designed to isolate the behavior and force the failure to occur in the column stub and not the foundation. These heavily reinforced footings are not representative of the actual details used in vintage bridge construction practice. The remaining two (2) specimens were constructed with footing details that were intended to reflect the actual vintage construction practices. One of the specimens was built with a spread footing containing a single layer of rebar mesh and the other was built with timber pile cap. The timber pile cap specimen contained four (4) Douglas fir timber piles having 10 in (254 mm) butt diameters that extended 6 in into and below the concrete pile cap block. The spread footing details are shown in Figure 3.27 and Figure 3.28. The timber pile cap details are shown in Figure 3.29 and Figure 3.30.

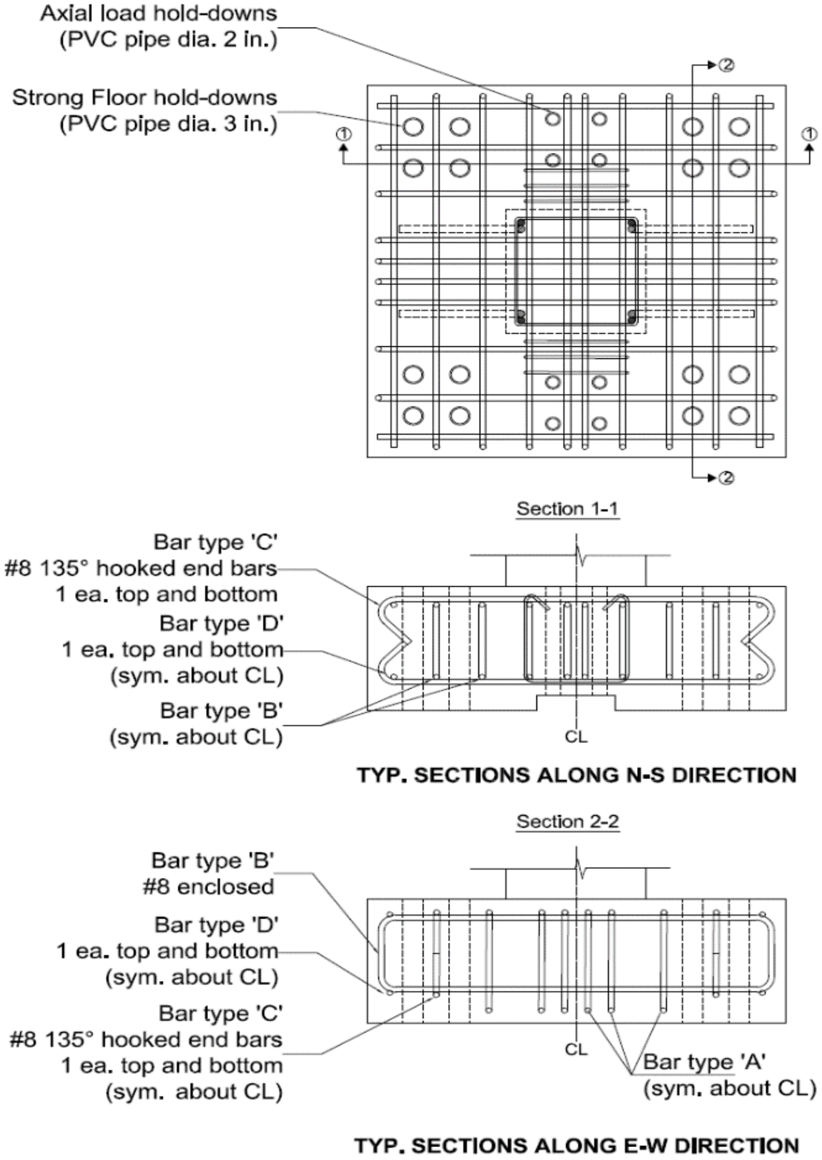

Figure 3.24: Typical footing reinforcing details for direct attachment to strong floor

Figure 3.25: Photograph of typical footing reinforcing details (not typical of footing designs for vintage columns

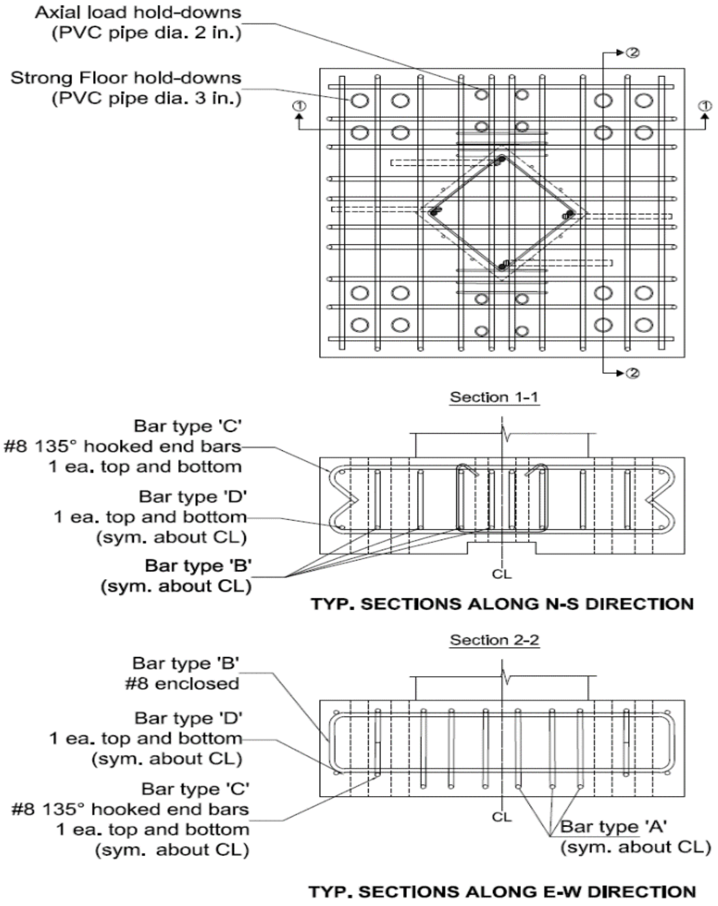

Figure 3.26: Footing reinforcing steel details for direct attachment to strong floor of diamond oriented column

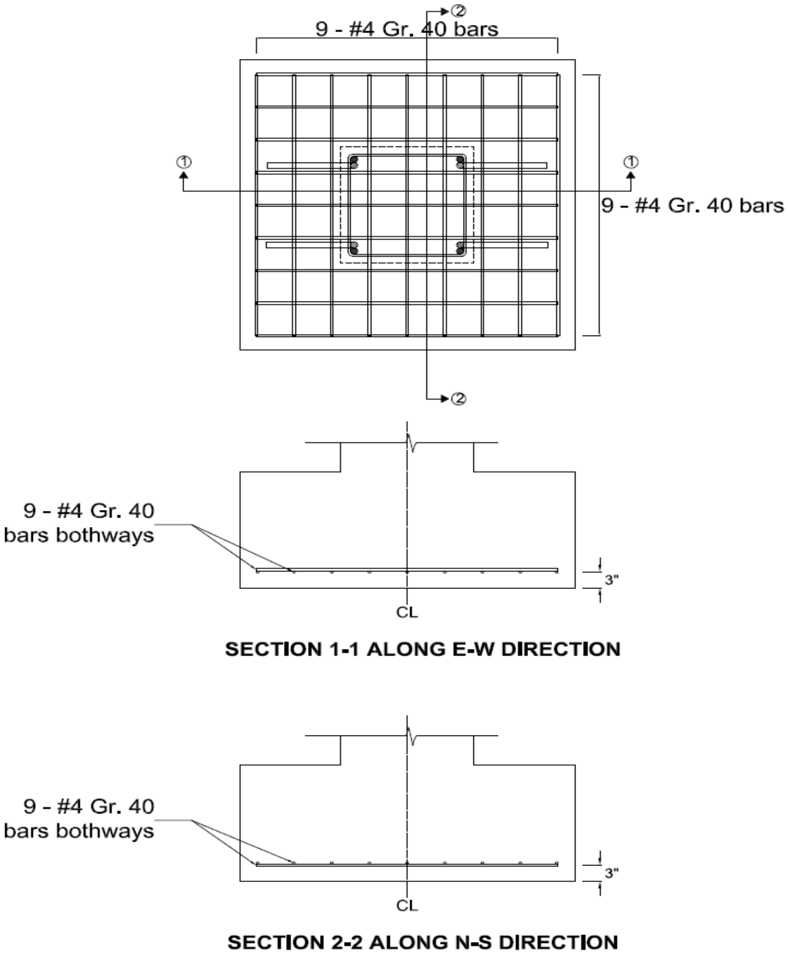

Figure 3.27: Footing reinforcing steel detail for spread footing column specimen

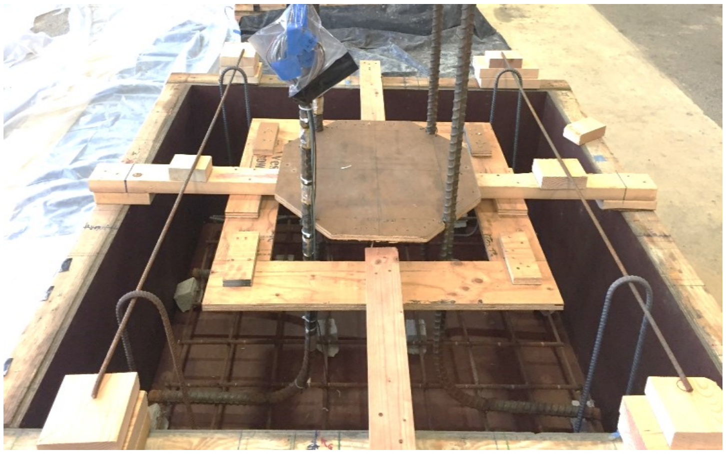

Figure 3.28: Image of spread footing prior to casting concrete

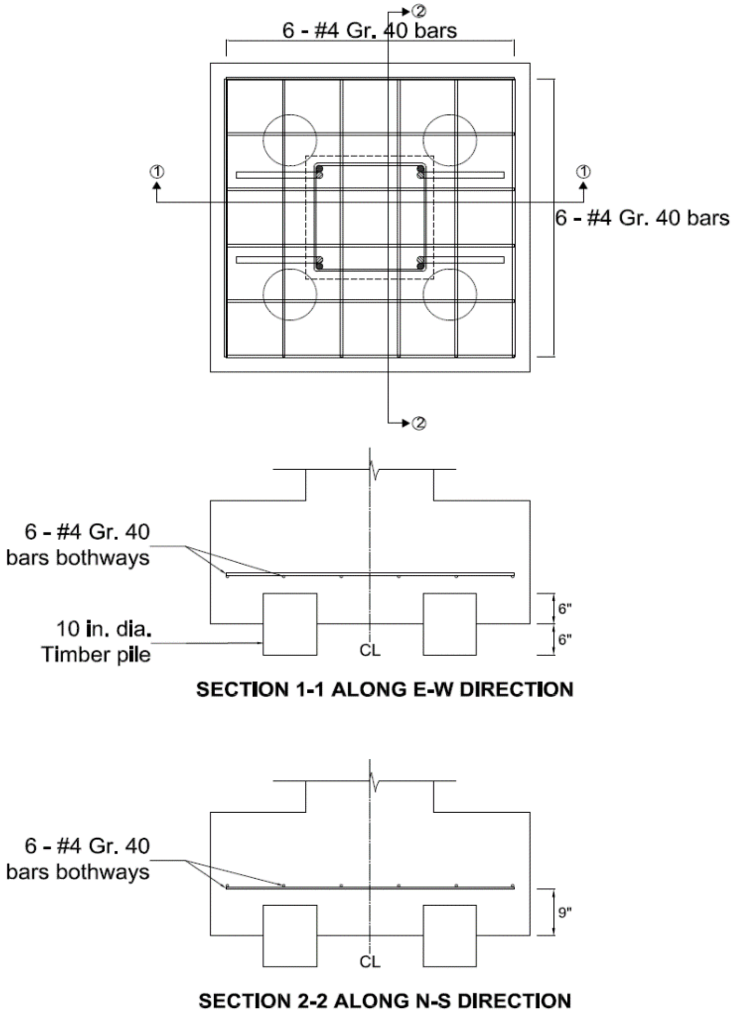

Figure 3.29: Footing reinforcing steel detail for timber pile cap foundation specimen

Figure 3.30: Image of timber pile cap prior to placement of column starter bars and casting concrete

3.2.2 Retrofit Details

The retrofit design consisted of external TiAB ligaments uniformly distributed on all column faces with a hooked end anchored into the column face on one end and straight end anchored to the footing on the other with an epoxy-based adhesive. The other portions of the ligament lengths were unbonded from the column. Confinement was provided through a continuous tightly wrapped TiAB spiral with concrete infill between the spiral and debonded column faces. No cover concrete is used over the TiAB spiral.

3.2.2.1 TiAB spiral

The pitch of the TiAB spirals were calculated using the guidelines from Priestley et al. (1996) based on the confinement model for circular RC column sections by Mander et al. (1988). The effective lateral pressure (f_l) of 320 psi (2.2 MPa) (approximately 10% of f'_c) was used in the design.

Sensitivity analysis was performed as shown in Figure 3.31 and Figure 3.32, for combinations of different diameter of spiral and pitch using nominal properties of TiAB (f_y = 130 ksi (896 MPa) and f_u = 140 ksi (965 MPa)) and concrete (f'_c = 3.3 ksi (22.8 MPa)). Although the retrofit shell is debonded from the bare column specimen, when determining the confinement effect, the retrofitted section was assumed circular with TiAB spiral where the circular sectors of solid grout inside the TiAB spiral applies confinement pressure to the square column faces. Uniform concrete was assumed for the entire circular section with properties matching the column concrete. The confinement is seen to increase the compressive strength of confined concrete and ultimate concrete crushing strain.

AASHTO LRFD Bridge Design Specifications (2017) has following recommendations for spirals to be used as transverse reinforcement:

Minimum spiral diameter = 0.375 in (3/8 in)

Maximum center to center spacing of the spirals = smaller of "6.0d_b" or "6.0 in"

Minimum clear spacing between the spirals = greater of "1.33 times the maximum size of aggregate" or "1.0 in"

A 3/8 in (9.5 mm) diameter TiAB spiral was chosen at 2.5 in (63.5 mm) pitch, which is designed to ensure elastic design and performance of the spirals during the testing. For given column longitudinal reinforcement and 3/8 in aggregate size used for retrofit shell, the TiAB spiral chosen meets the AASHTO LRFD Bridge Design Specifications (2017) requirements.

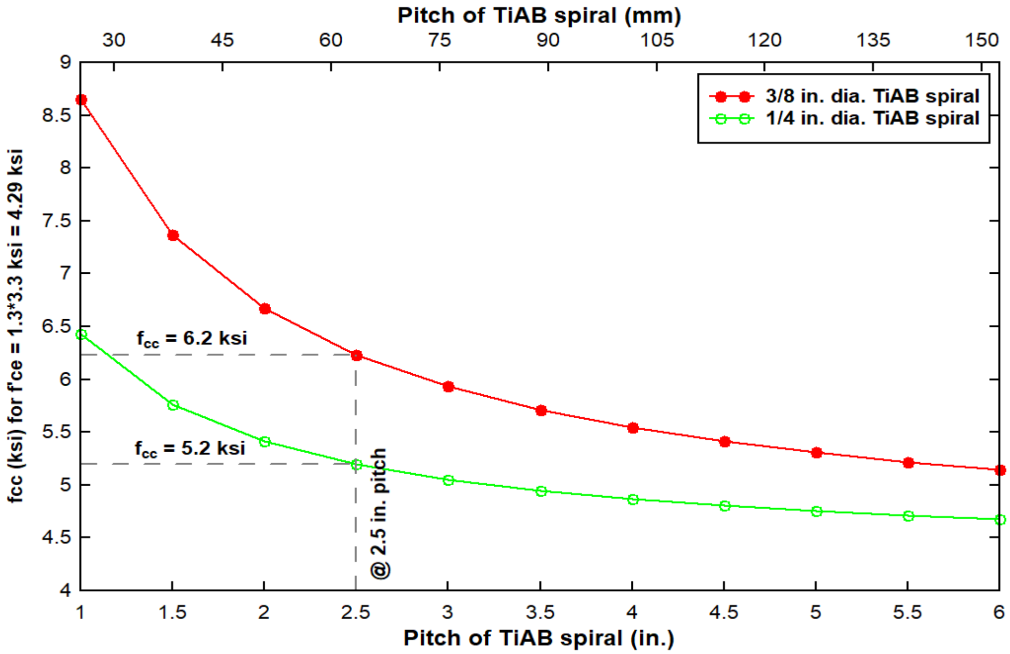

Figure 3.31: Variation of confined concrete compressive strength for different TiAB spiral pitch

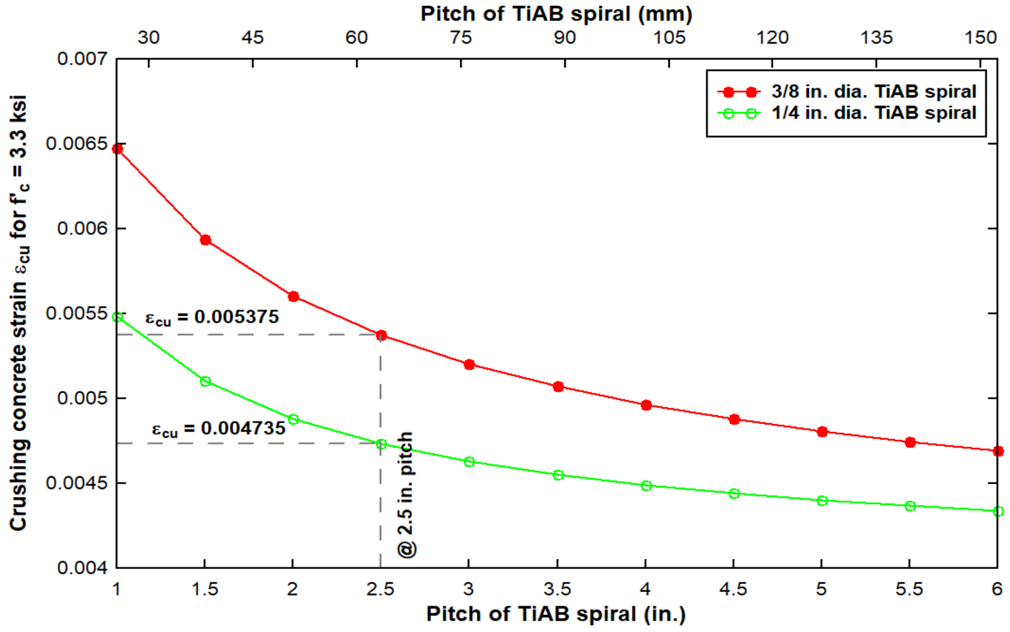

Figure 3.32: Variation of crushing concrete strain for different TiAB spiral pitch

The TiAB spirals were smooth along their length. The top of the spiral was anchored into the column and the bottom of the spiral was anchored into the footing for most specimens. The tops and bottoms of the spirals were anchored into the column sides for

Specimens 12 and 13. Anchorage depth of the TiAB spiral ends was 8 in (203 mm). The ends of the TiAB spirals were heated with an oxyacetylene torch and field bent to produce a 90° hook, as shown in Figure 3.33.

Figure 3.33: Straightened end of spiral TiAB and 90° anchorage hook

The material properties and production method (dead lay) of the TiAB spirals allowed the spiral to easily open and be wound around the column without permanent deformation and the coil naturally contacted the corners of the column. The spiral could be wrapped around the column by a single person without exertion. No other concrete preparation was required other than drilling eight (8) holes in the column face and eight (8) holes in the footing to anchor the ends of the vertical TiABs and two (2) holes to anchor the TiAB spiral.

The spiral pitch was reduced at the base to ensure anchorage at the top of the footing. In addition, the pitch was reduced to 1.5 in (37 mm) over the upper portion of the retrofit in the region where the hooked ends of the longitudinal TiABs were anchored in the column. This was done to provide resistance to TiAB hook pullout from the column. The specific spiral pitch details and the overall height of the retrofit for the specimens are described subsequently.

3.2.2.2 TiAB ligaments

The average length of the ligaments was calculated as the tension lap-splice length for column longitudinal bars recommended by AASHTO LRFD Bridge Design Specifications (2017). TiAB ligaments consisted of bars with one end hooked as illustrated in Figure 3.34 and Figure 3.35. Three different lengths of vertical TiABs were used in each column to stagger the terminations thereby reducing stress concentrations at a single section. The ligament lengths were thus staggered by 6 in (152 mm). Each vertical TiAB was fabricated with a 7.5 in (191 mm) long 90° hook with proprietary deformations machined into the extension on the hook. The lower ends of the bars were fabricated with 20 in (508 mm) long surface deformations in tall specimens and the entire deformed length was bonded. Concrete cracks in cone formation were observed around the TiAB ligaments at the footing surface which caused buckling of some TiAB ligaments in tall specimens. In order to prevent these cracks, only 15 in (381 mm) length of the straight end was deformed in short specimens to debond the top 5 in (127 mm) of undeformed length just below the footing surface. These deformed straight ends were placed into holes that were hammer-drilled into the footing to a depth of 22 in (559 mm). The deformation patterns in these TiAB ligaments are proprietary. Actual embedment length of the ligaments into the footing was 20 in (508 mm), 2 in (51 mm) extra depth provided to allow necessary bending of the ligaments to insert the hooks into the column. The remaining length of the vertical TiABs were smooth where they extended above the footing and below the 90° hooks. The nominal diameter of the vertical TiABs was 5/8 in (15.9 mm). The overall hook length was 10 in (254 mm) and the pin diameter for the 90° hook was 3 ¾ in (95 mm). The nominal yield stress of the vertical TiABs was 130 ksi (896 MPa), which was used in the design of the specimens.

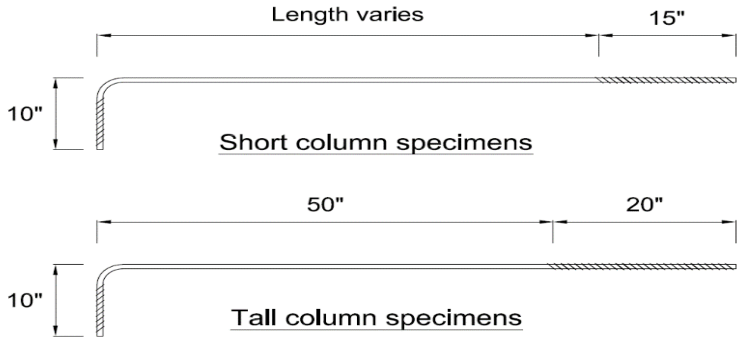

Figure 3.34: TiAB ligament dimensions with 90 degree hooked end

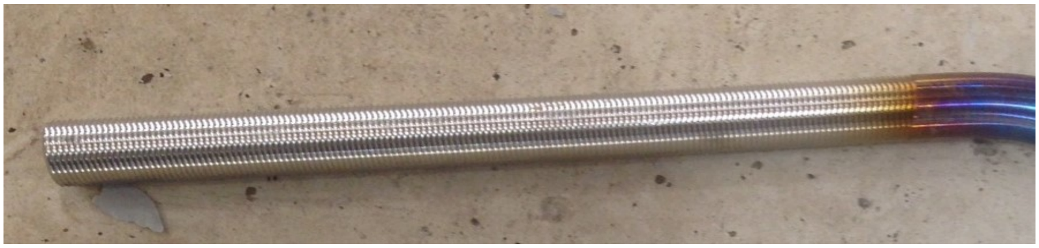

Figure 3.35: Surface deformations on extension of 90° hook on TiAB ligaments

For one specimen, the TiAB ligament hook bend angle was changed to 135 degrees, with all other characteristics being the same. This enabled comparison of the hook anchorage on the behavior and performance of specimen. To make the holes in the column at the proper angle required diamond core drilling the holes. The flexibility of the TiABs allows the bars to be inserted into the angled hole in the column at the same time the long straight portion of the TiAB is inserted into the hole in the footing.

The objective of introducing the ligaments was to provide a supplemental load path while the reinforcing steel lap-splices are intact and then to serve as an alternative flexural load path after the lap-splice between the starter reinforcing steel bars and column reinforcing steel bars decay during larger amplitude cyclic loading.

In one specimen, the footing starter reinforcing steel bars were cut at the top of the footing before installation of the TiAB retrofit. This removed the reinforcing steel from participating in resisting flexure at the foundation level. It was intended to reduce internal concrete damage in the splice region due to splitting when the steel lap splice eventually fails. It was also intended to prevent the column from reaching a higher strength when both the longitudinal reinforcing bars and TiAB ligaments work together before the reinforcing steel splice failure.

3.2.3 Construction Sequence

All column specimens were constructed in two sequences where the footings with starter reinforcing bars were constructed first, and then the column was constructed after the footing concrete had cured. The concrete mixture for the footings and columns were designed to provide properties that are consistent with concrete proportions and mechanical properties from the age of construction and considering long-term strength gains over time in service. The concrete mix contained ¾ inch (9.5 mm) maximum aggregate size and had a 28-day design compressive strength of 3 ksi (21 MPa). The control specimens were tested after the 28th day of column construction, while the remaining specimens were prepared for retrofit.

Holes were hammer drilled at the pre-determined locations for TiAB ligaments and spirals. To get the bend of the vertical TiABs to rest against the column, rounding out of the bottom side of the drilled holes was required prior to anchorage, as shown in Figure 3.36.

Figure 3.36: Drilled holes for vertical TiAB hook anchorages with rounding at bottom

The holes were carefully cleaned by brushing and vacuuming. The column was then wrapped in plastic sheathing to debond the concrete infill from the column faces as seen in Figure 3.37a. After placing and bonding the ligaments with epoxy (Figure 3.37b), one end of the TiAB spiral was bonded to the column face at the top of the retrofit height, the spirals were then wrapped around the columns (Figure 3.38a) and drawn tight around the corners at designated pitch (Figure 3.38b) and the other end was bonded to the hole drilled into the footing. Polycarbonate formwork was then placed directly around the spirals with no cover. The polycarbonate sheet was held together using ratchet straps as seen in Figure 3.39a. Concrete was then filled into the formwork to the height of the shell. The polycarbonate form allows visual inspection of the fill to ensure the shell is properly placed and consolidated. The final retrofitted specimen is shown in Figure 3.39b.

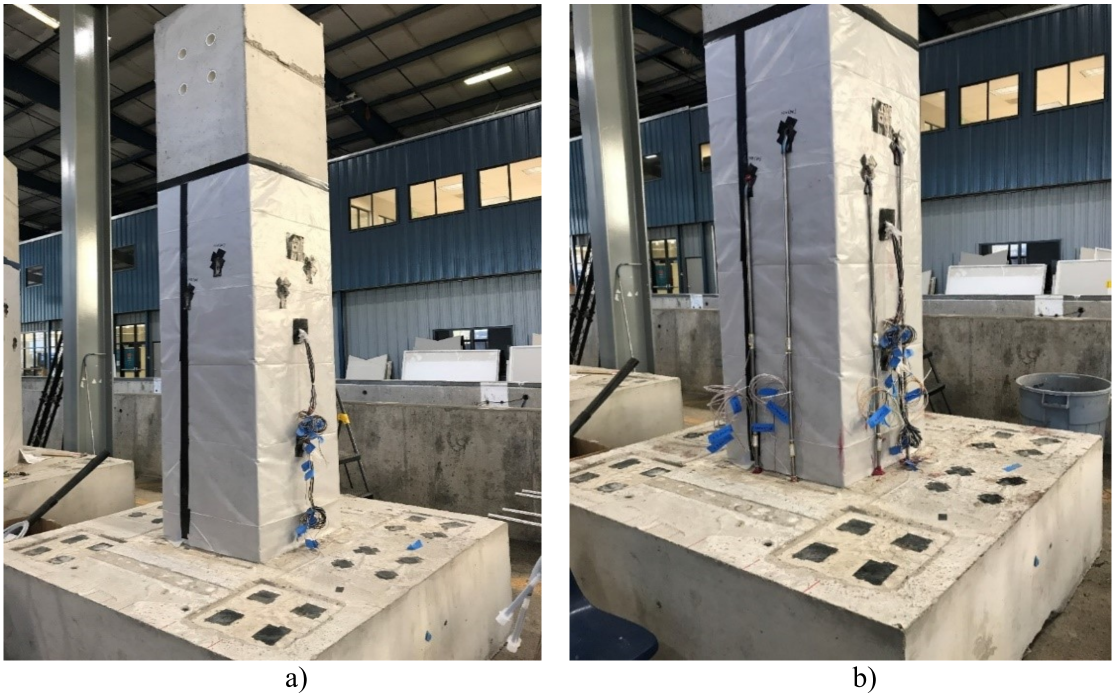
a) b)

Figure 3.37: a) Column wrapped in plastic sheathing, b) TiAB ligaments installed

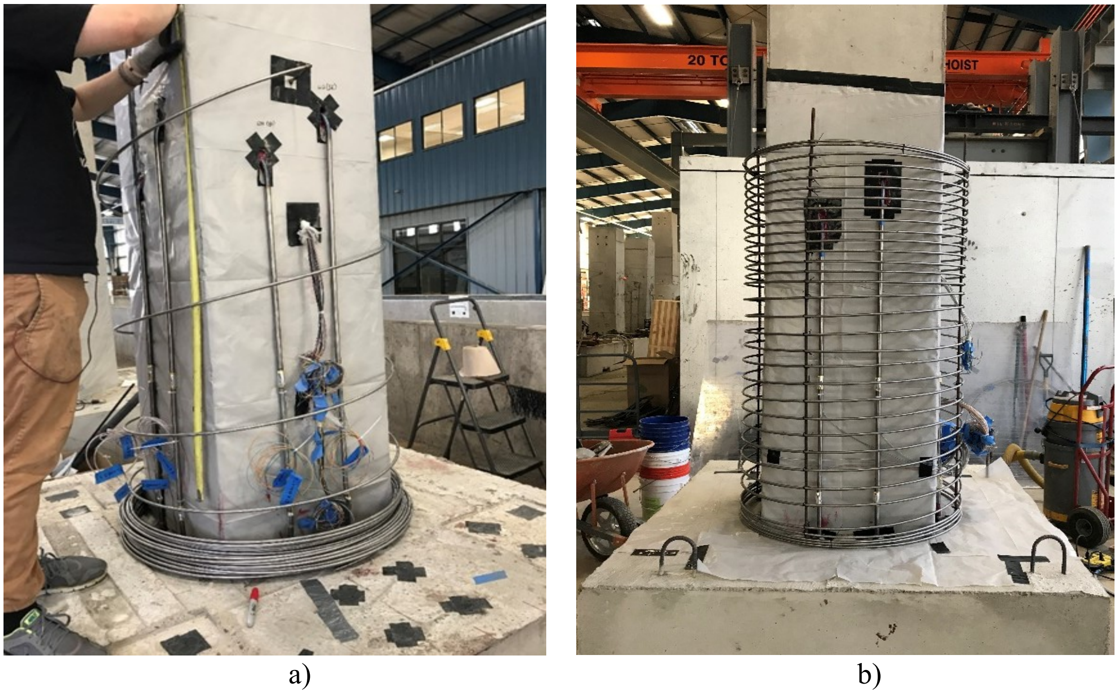
a) b)

Figure 3.38: a) TiAB spiral wrapped around column, b) TiAB spiral pitch tied in place

a) b)

Figure 3.39: a) Polycarbonate sheet forms held with ratchet straps, b) Completed TiAB seismic retrofit details for short columns

3.2.4 Column specimen naming convention

The specimens are identified by the notations given in Table 3.1. The specific characteristics of the individual specimens are also provided in the table. Drawings detailing the specimens are shown in Figure 3.40 through Figure 3.53.

Table 3.1: Column Specimens Naming Notation and Descriptions

S.N.	Specimen Name	Description of Specimens
1	C-S-R	Square short (8 ft.) control specimen
2	C-S-D	Diamond short (8 ft.) control specimen
3	R-S-R-LTi-90	Square short (8 ft.) standard TiAB retrofitted specimen
4	R-S-D-LTi-90	Diamond short (8 ft.) standard TiAB retrofitted specimen
5	R-S-R-LTi-135	Square short (8 ft.) 45° hooks TiAB retrofitted specimen
6	R-S-R-0	Square short (8 ft.) retrofitted specimen, TiAB spirals only
7	R-S-R-LSS-90	Square short (8 ft.) Stainless Steel Retrofitted Specimen
8	R-S-R-LTi-90-Spread	Square short (8 ft.) Standard TiAB Retrofitted Specimen with 5'x5' Spread Footing
9	R-S-R-LTi-90-Pile	Square short (8 ft.) Standard TiAB Retrofitted Specimen with 5'x5' 4-10"dia Timber Pile Footing
10	C-T-R	Square tall (12 ft.) control specimen
11	R-T-R-LTi-90	Square tall (12 ft.) standard TiAB retrofitted specimen
12	RS-T-R-LTi-90	Square tall (12 ft.) standard TiAB retrofitted specimen with short retrofit height
13	RN-T-R-LTi-90	Square tall (12 ft.) standard TiAB retrofitted specimen with no starter bars (i.e. starter bars cutoff at footing top level
14	R-T-R-0	Square tall (12 ft.) retrofitted specimen, TiAB spirals only

* S.N. – Specimen Number

In naming convention listed in the second column of Table 3.1 is interpreted according to the following schedule:

- The first letter represents whether the specimen is retrofitted or not (C for Control specimen and R for Retrofitted specimen with TiAB spiral and concrete shell for confinement). Note that for two of the tall specimens (specimens 12 and 13), an additional letter follows R in which S represents Short retrofit height and N represents No starter bars (i.e. flexural bars cut off).

- The second letter represents the height of the specimen (S for the Short specimen with 8 ft. height from the top of the footing to the lateral loading point and T for the Tall specimen with 12 feet height).

- The third letter represents the shape of the compression block based on the direction of lateral loading (R for Rectangular compression block, i.e. column loaded parallel to its principal axis, and D for Diamond compression block, i.e. column loaded at 45 degree angle to its principal axis).

- The fourth symbol is for the ligament material used (LTi for TiAB ligaments, LSS for Stainless Steel ligaments, and 0 for no ligaments).

- The fifth symbol for the ligament series is for the angle of the ligament hooks (90 for 90 degree hooks and 135 for 135 degree hooks).

- The last symbol is for the footing type (Spread for 5 ft. x5 ft. Spread Footing, Pile for Timber Pile cap with 5 ft. x5 ft. Pile Cap with 4-10in diameter timber piles, and nothing for standard 6 ft. x6 ft. footing anchored directly to the strong floor).

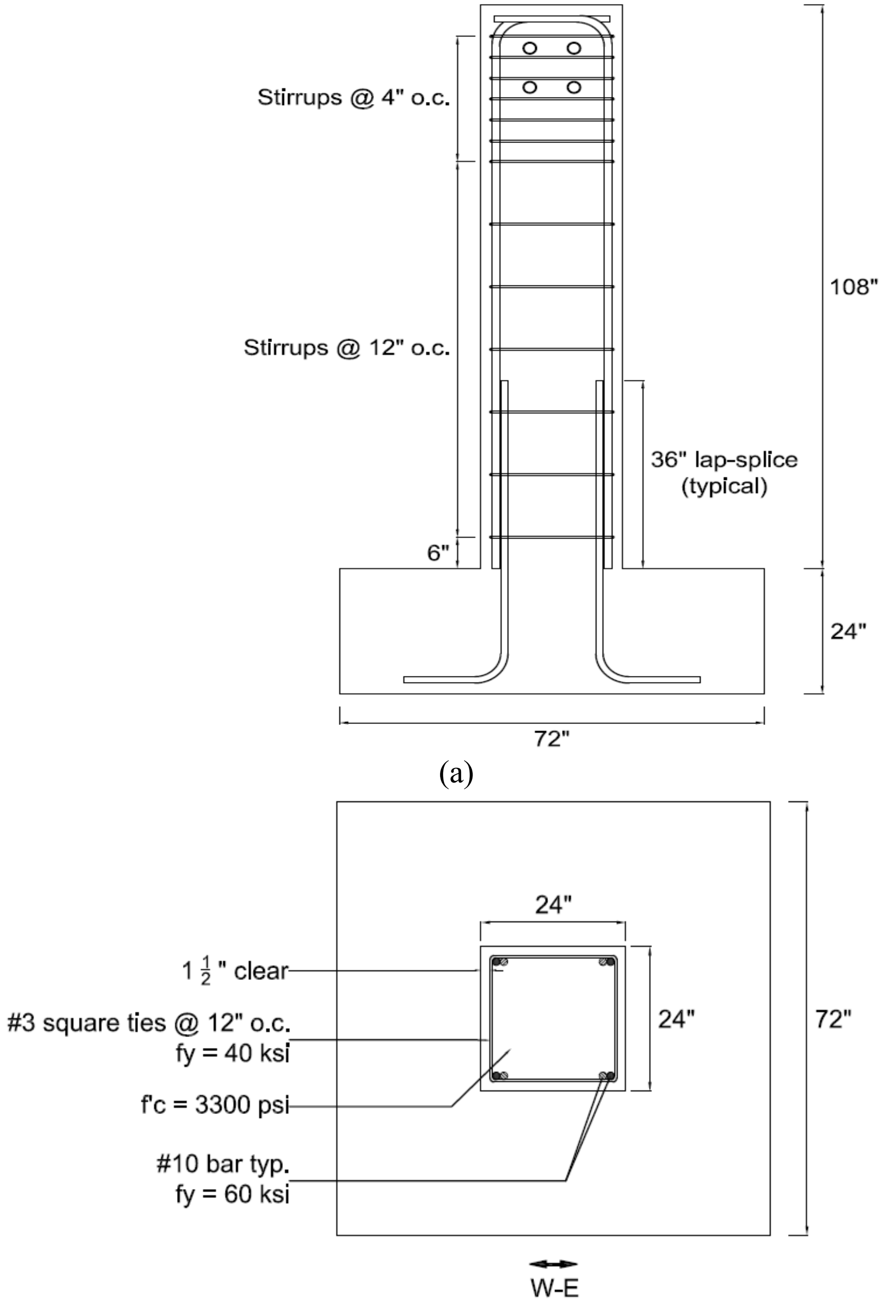

(b)

Figure 3.40: Specimen C-S-R: Dimensions and reinforcing steel details (a) E–W elevation view, (b) plan view (dimensions in inches)

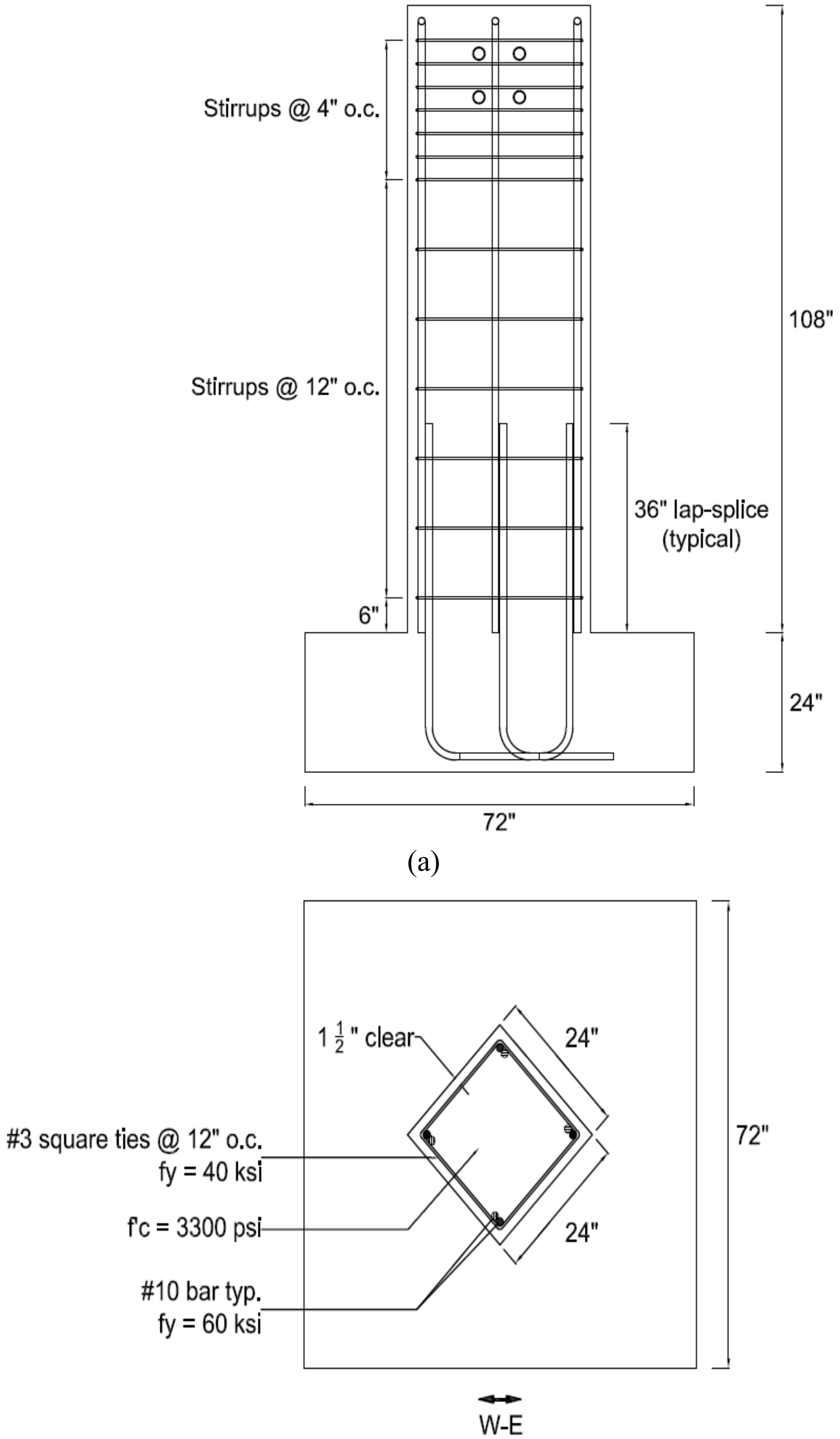

(b)

Figure 3.41: Specimen C-S-D: Dimensions and reinforcing steel details (a) E–W elevation view, (b) plan view (dimensions in inches)

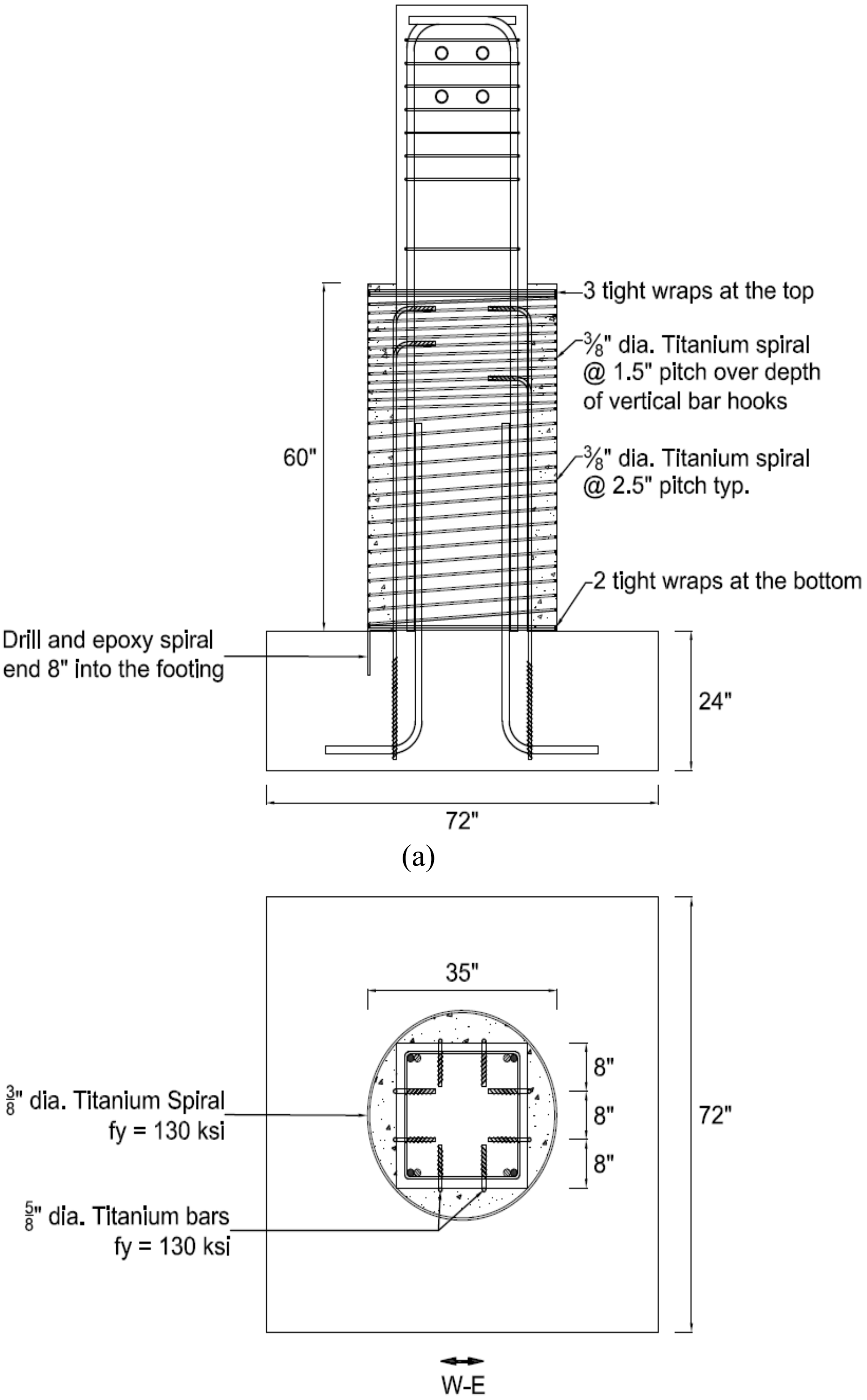

(a)

(b)

Figure 3.42: Specimen R-S-R-LTi-90: Dimensions and reinforcing steel details (a) E–W elevation view, (b) plan view (dimensions in inches)

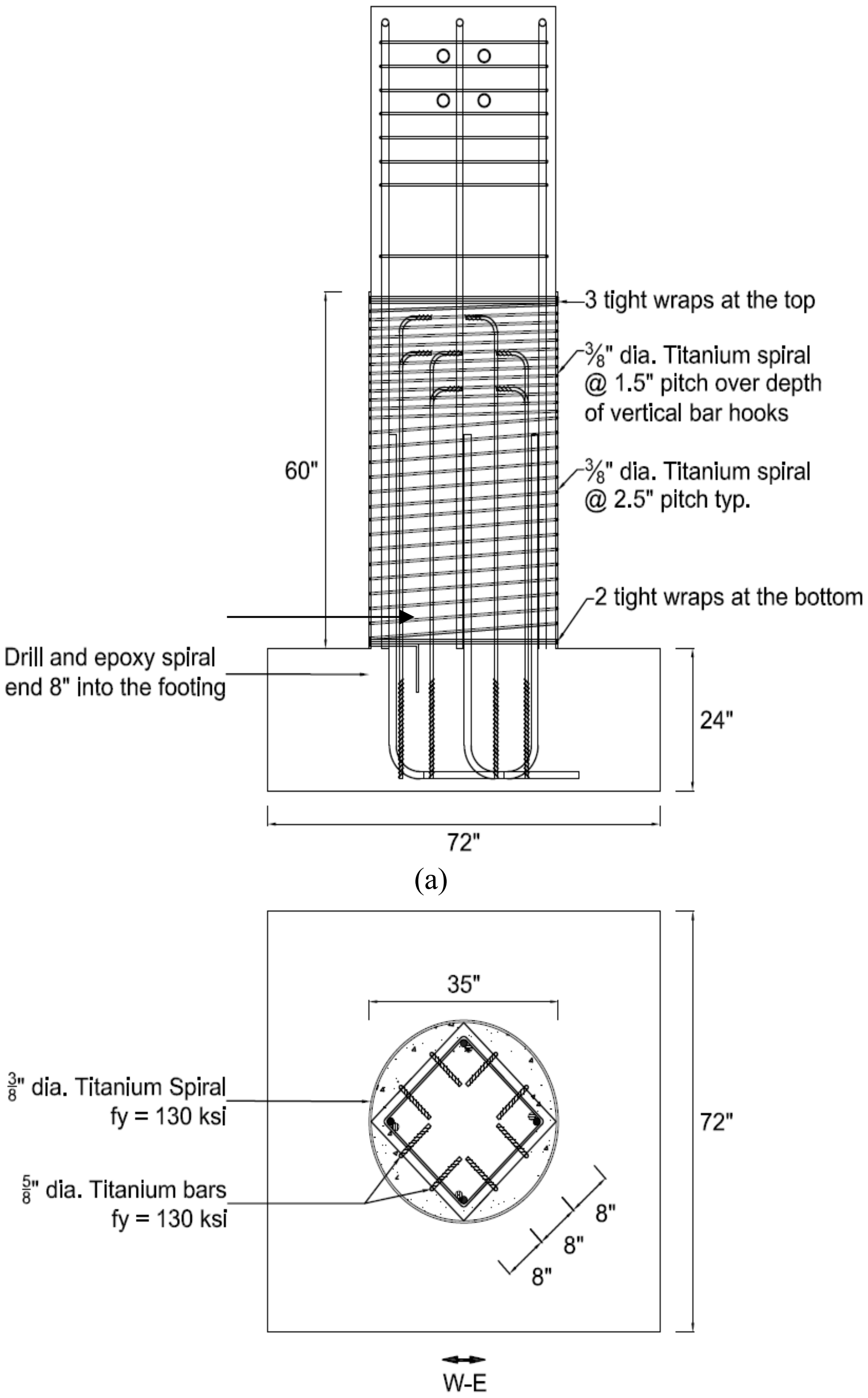

(a)

(b)

Figure 3.43: Specimen R-S-D-LTi-90: Dimensions and reinforcing steel details

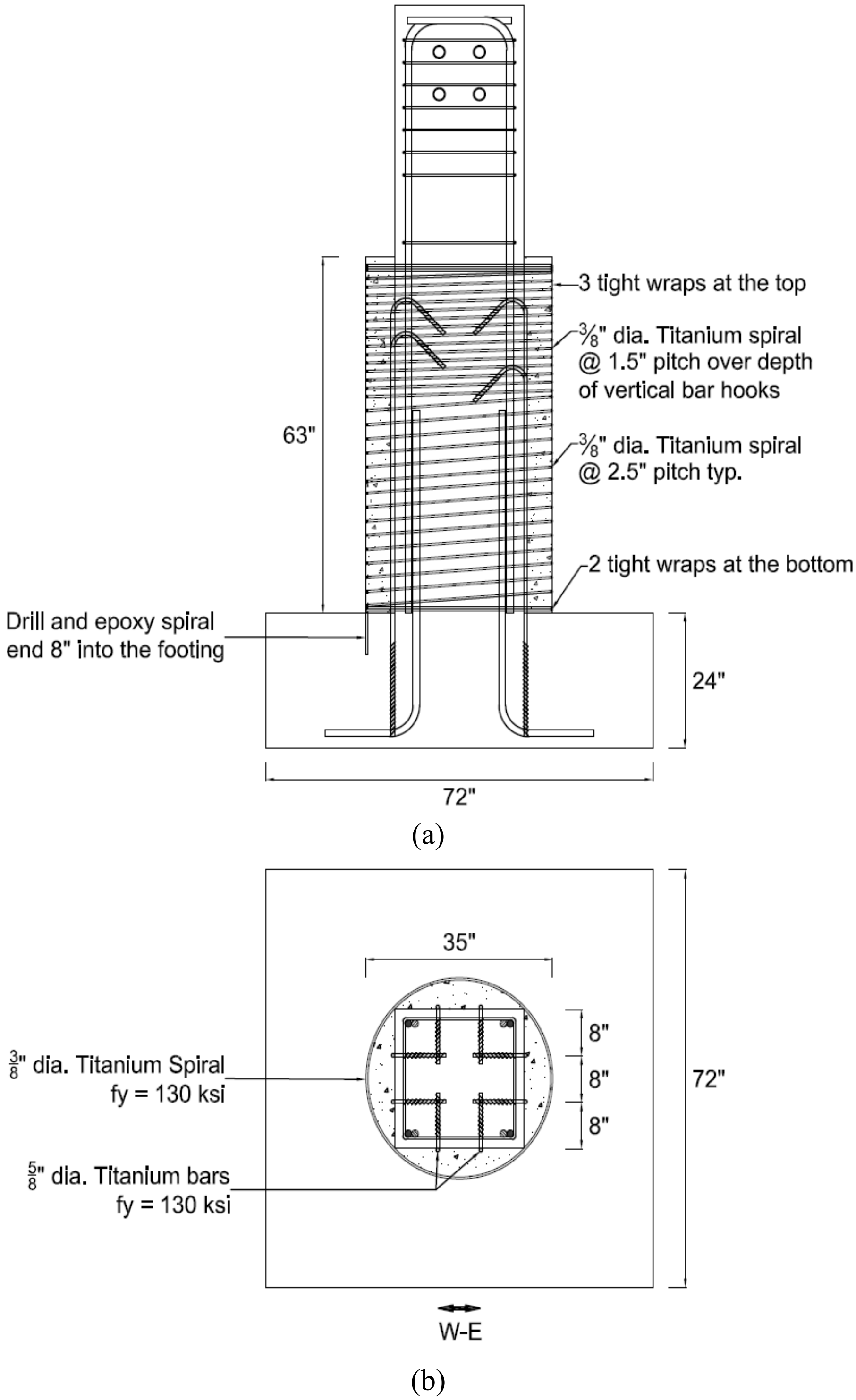

Figure 3.44: Specimen R-S-R-LTi-135: Dimensions and reinforcing steel details (a) E–W elevation view, (b) plan view (dimensions in inches)

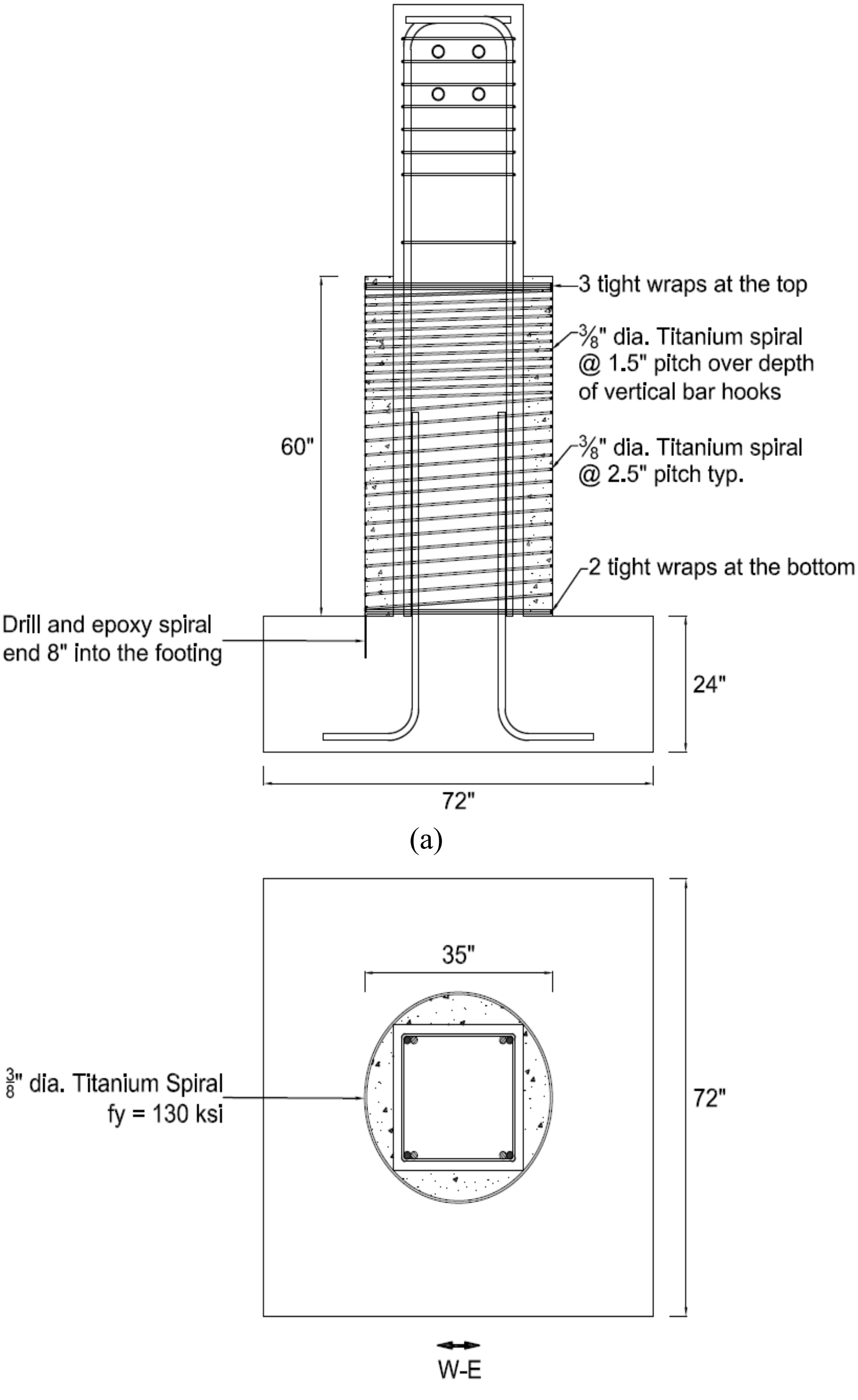

(a)

(b)

Figure 3.45: Specimen R-S-R-0: Dimensions and reinforcing steel details (a) E–W elevation view, (b) plan view (dimensions in inches)

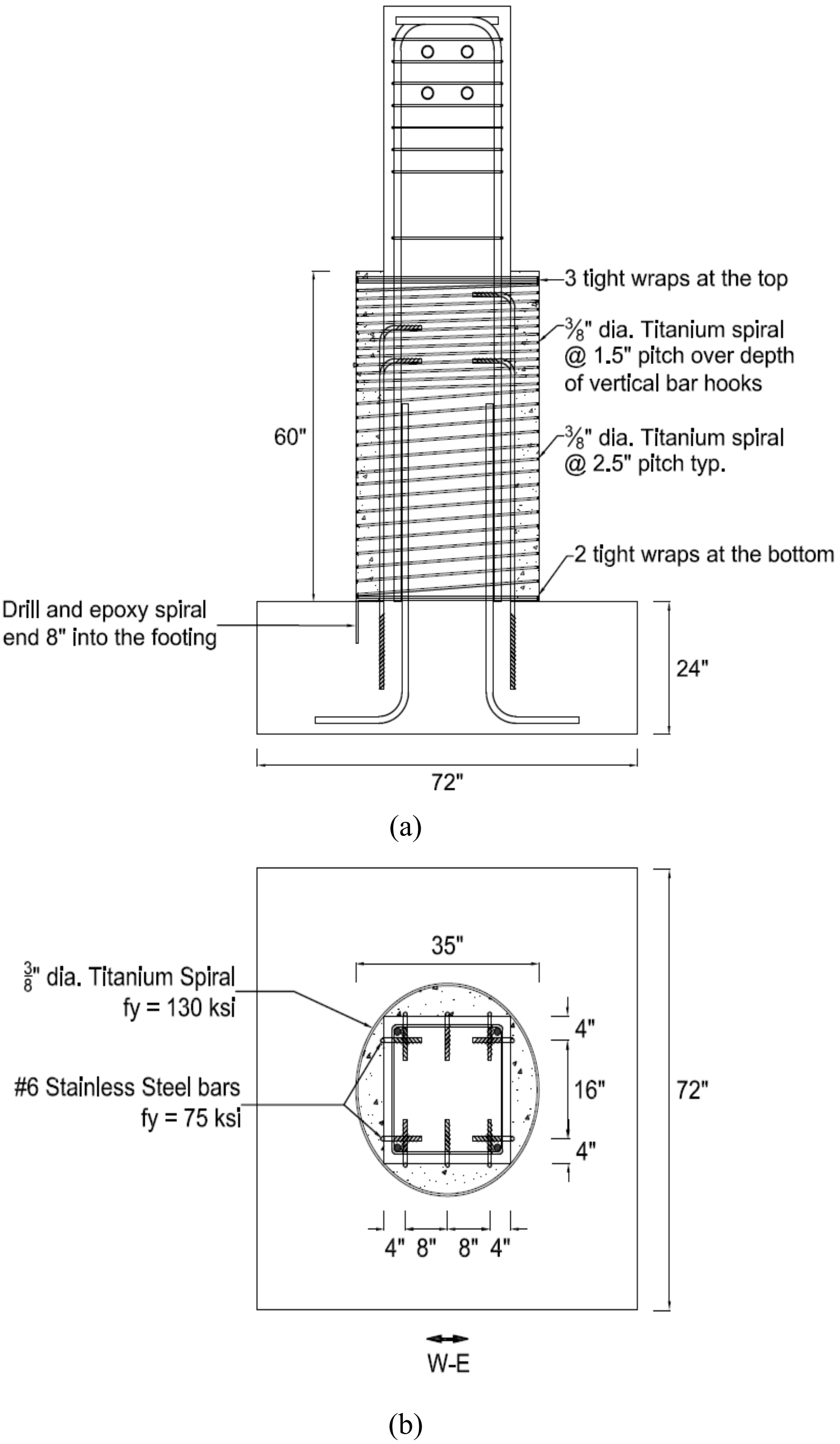

Figure 3.46: Specimen R-S-R-LSS-90: Dimensions and reinforcing steel details (a) E–W elevation view, (b) plan view (dimensions in inches)

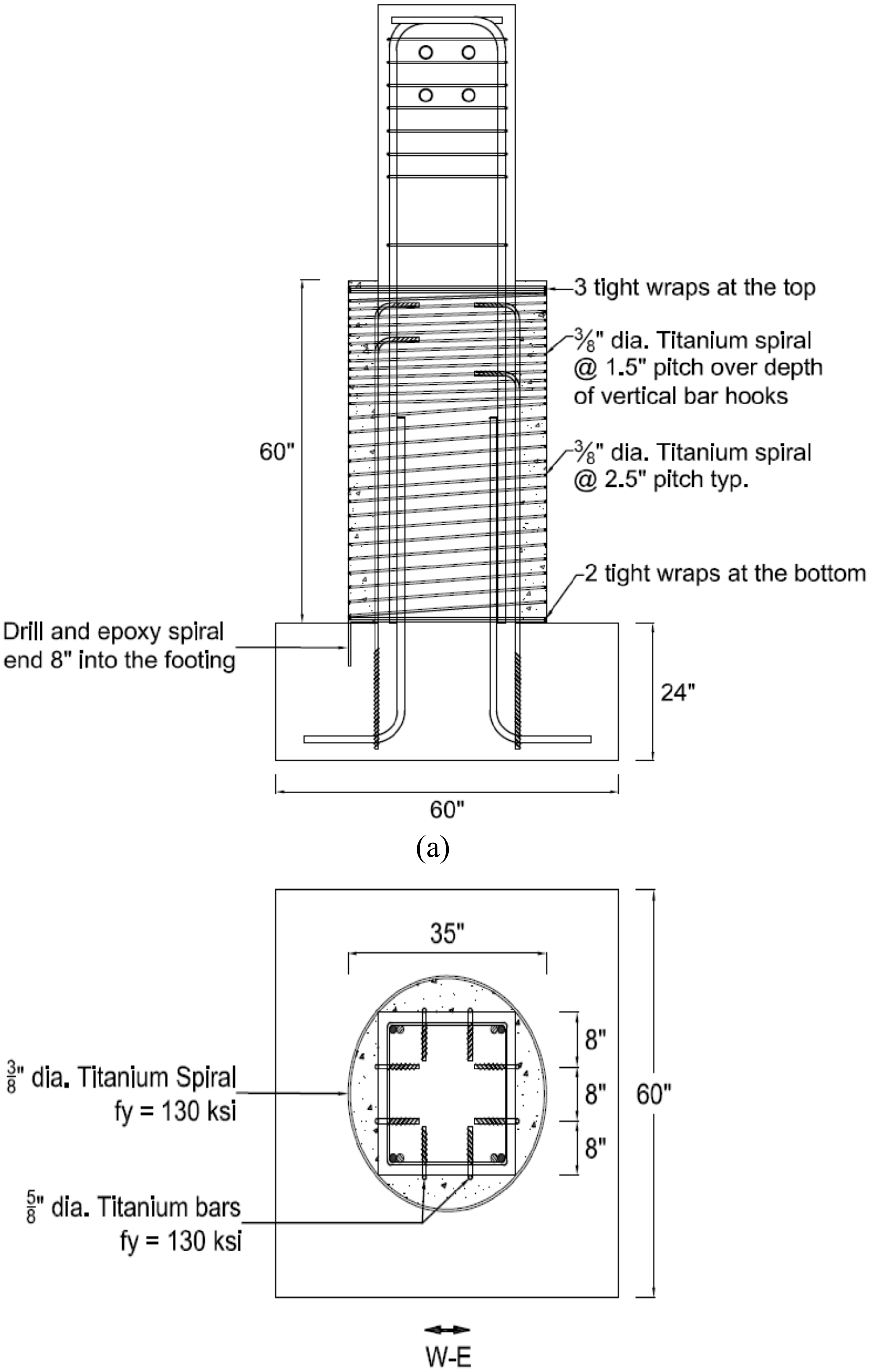

(a)

(b)

Figure 3.47: Specimen R-S-R-LTi-90-Spread: Dimensions and reinforcing steel details (a) E–W elevation view, (b) plan view (dimensions in inches)

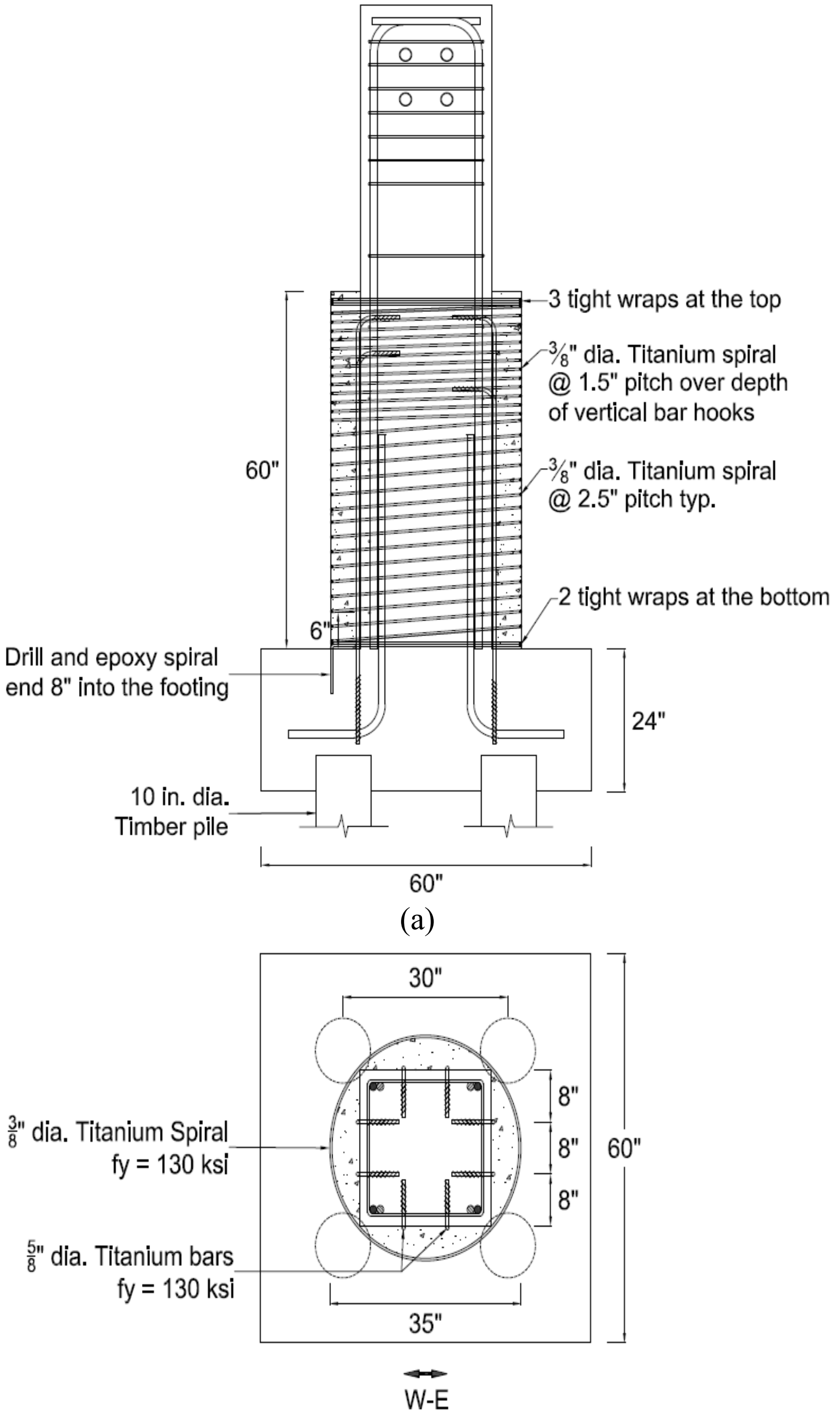

(a)

(b)

Figure 3.48: Specimen R-S-R-LTi-90-Pile: Dimensions and reinforcing steel details (a) E–W elevation view, (b) plan view (dimensions in inches)

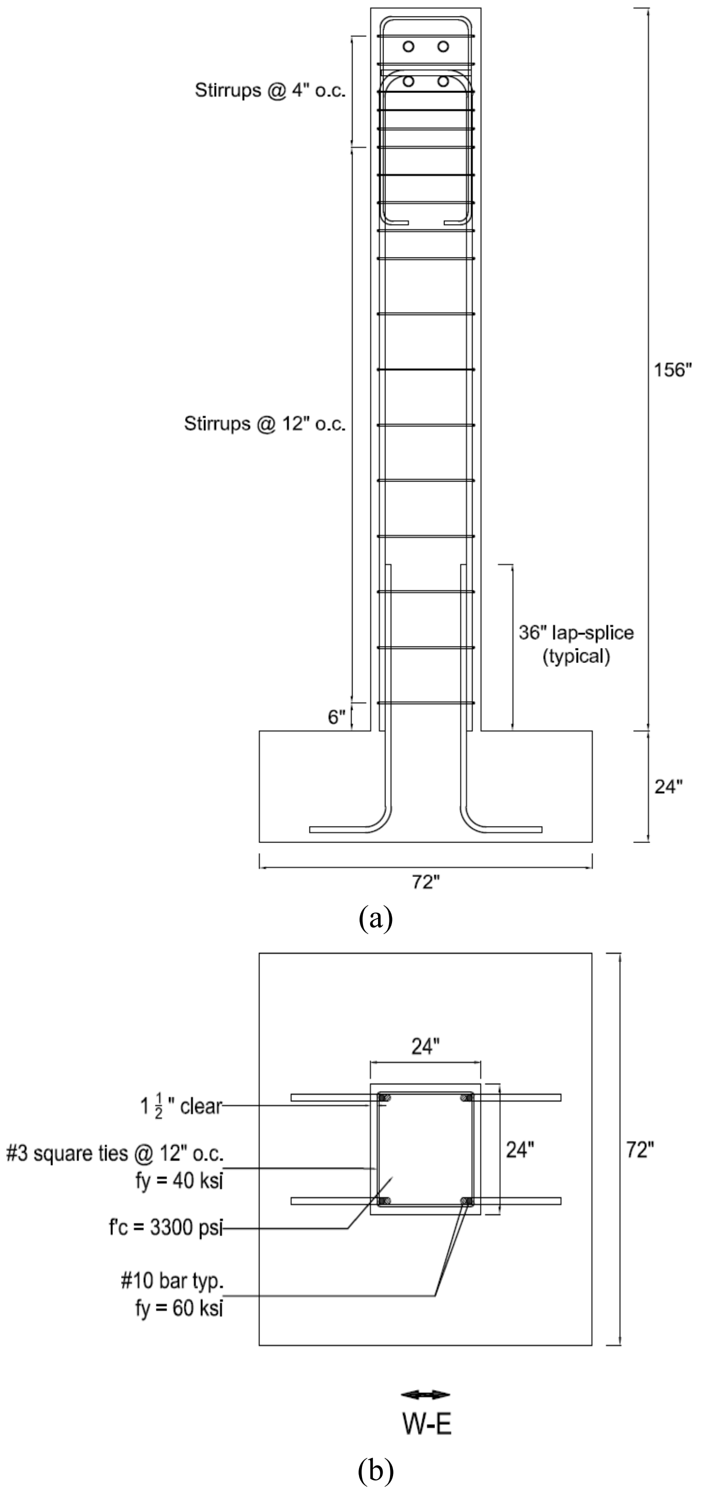

Figure 3.49: Specimen C-T-R: Dimensions and reinforcing steel details (a) E–W elevation view, (b) plan view (dimensions in inches)

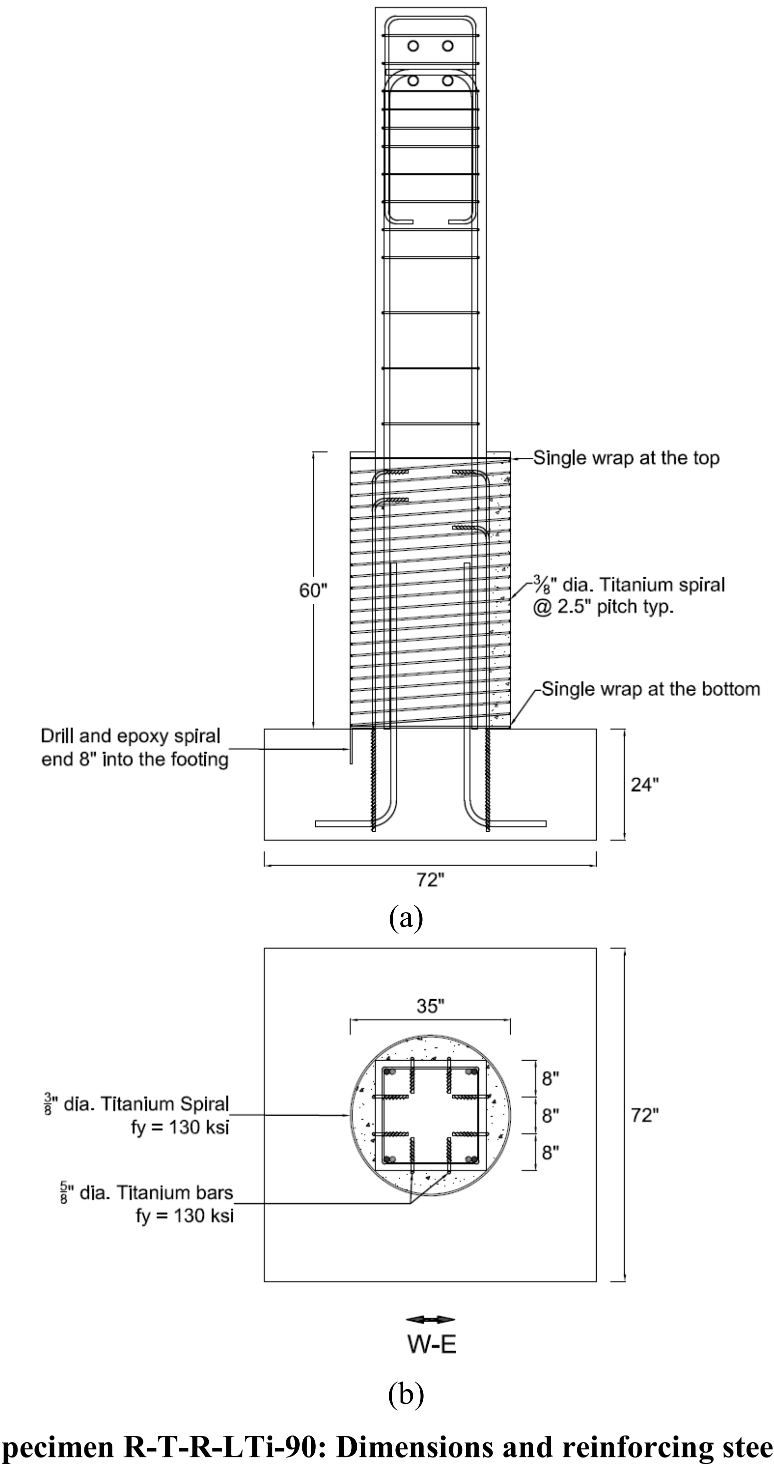

(a)

(b)

Figure 3.50: Specimen R-T-R-LTi-90: Dimensions and reinforcing steel details (a) E–W elevation view, (b) plan view (dimensions in inches)

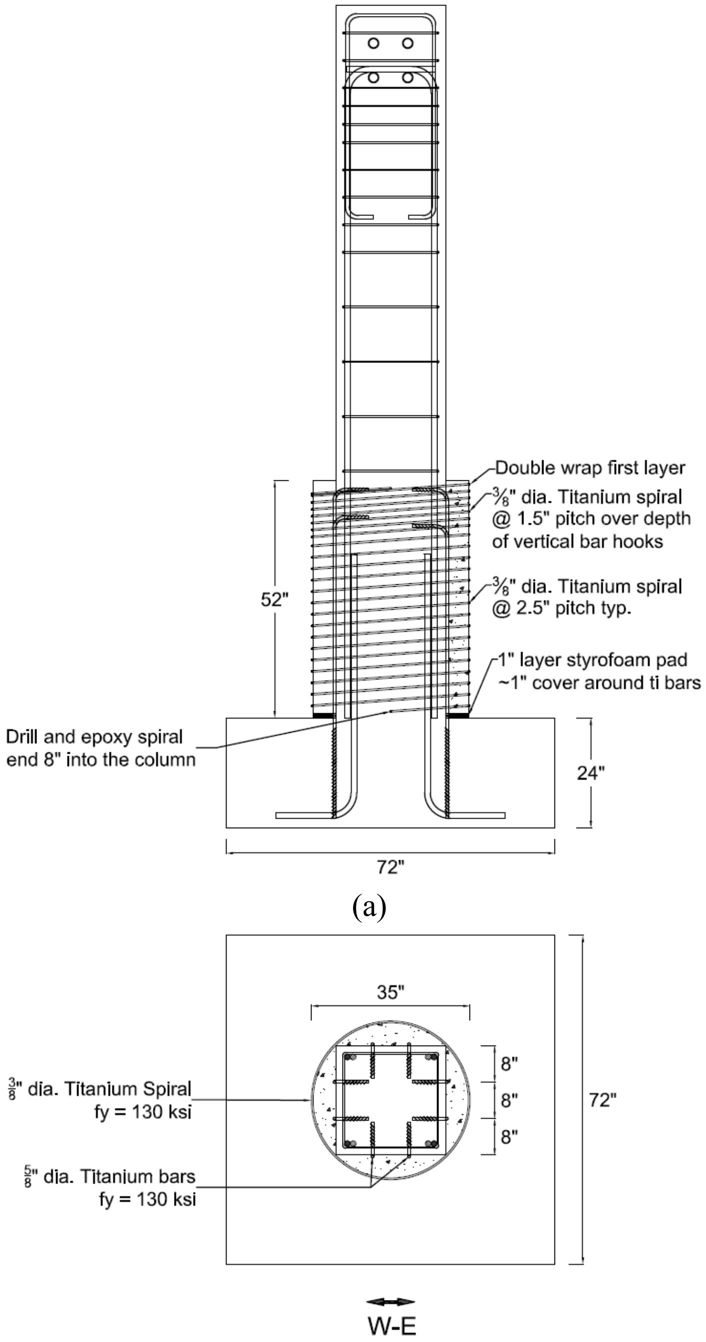

(a)

(b)

Figure 3.51: Specimen RS-T-R-LTi-90: Dimensions and reinforcing steel details (a) E–W elevation view, (b) plan view (dimensions in inches)

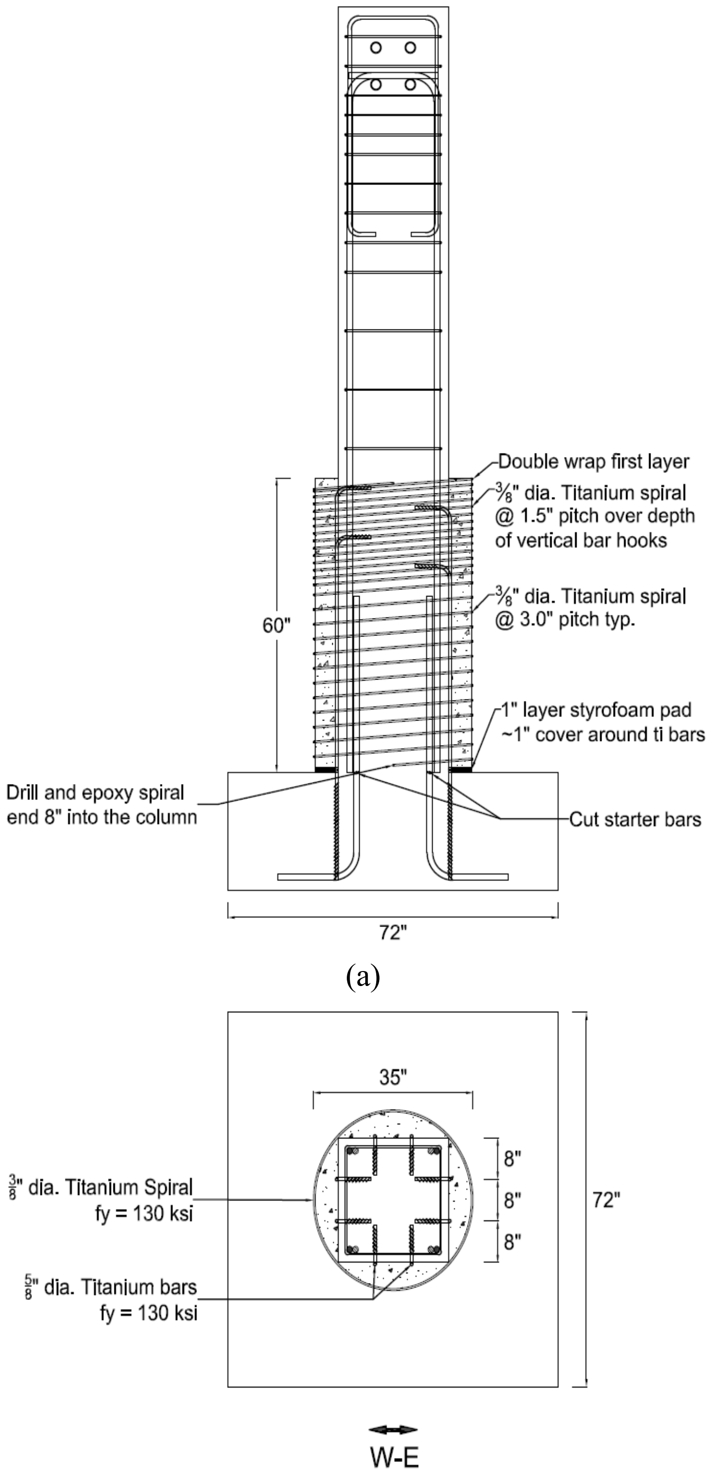

(a)

(b)

Figure 3.52: Specimen RN-T-R-LTi-90: Dimensions and reinforcing steel details (a) E–W elevation view, (b) plan view (dimensions in inches)

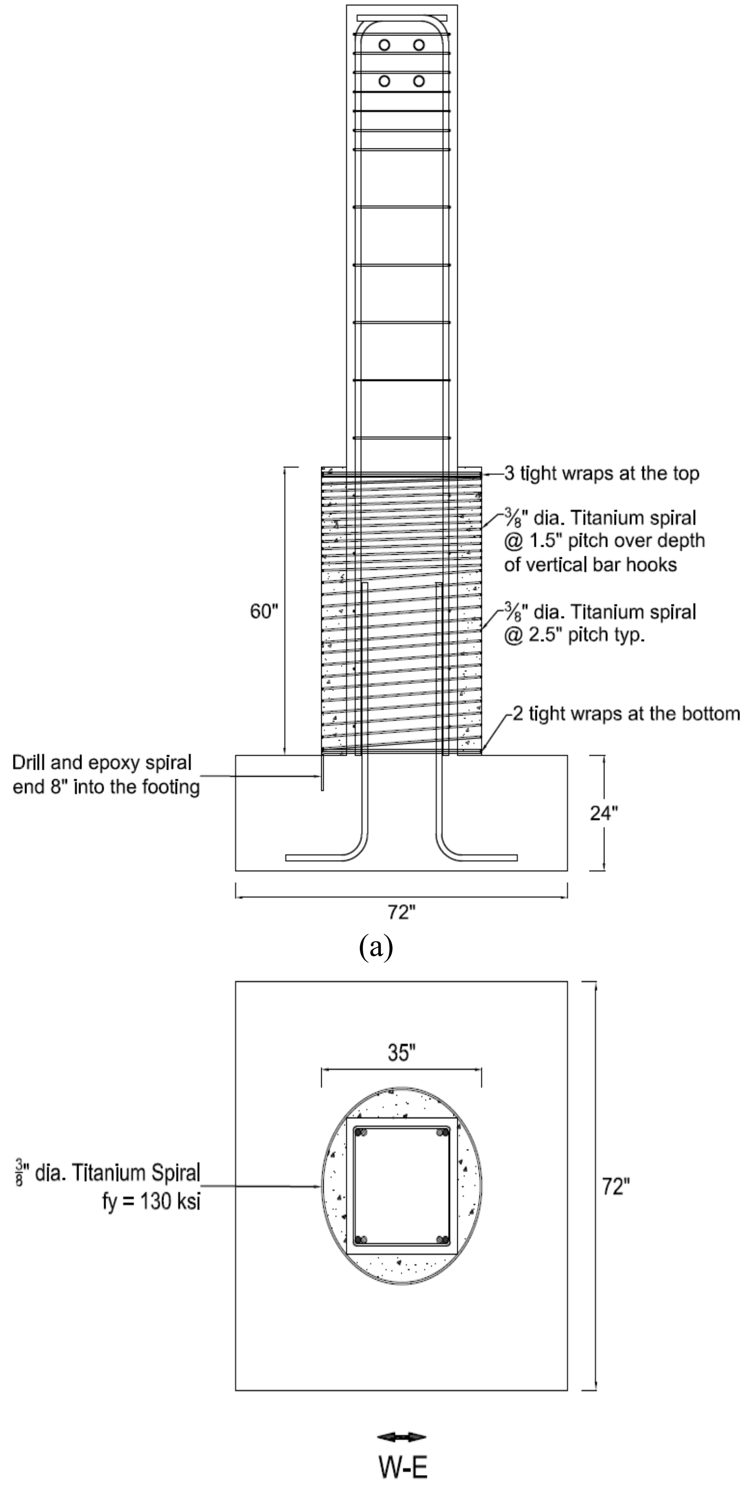

(a)

(b)

Figure 3.53: Specimen R-T-R-0: Dimensions and reinforcing steel details (a) E–W elevation view, (b) plan view (dimensions in inches)

3.3 MATERIAL PROPERTIES

3.3.1 Concrete

The concrete mix design was the same for all footing and column specimens. The concrete mix was provided by a local ready-mix supplier. The concrete mix contained ¾ in (9.5 mm) maximum aggregate size and had a 28-day design compressive strength of 3 ksi (21 MPa). The concrete mix used for the retrofit shell was comprised of 3/8 in (4.75 mm) maximum aggregate size and had a 28-day design compressive strength of 4 ksi (28 MPa).

In close inspection of the concrete used in the retrofit shell of specimen R-S-R-LSS-90, synthetic fibers were observed in the wet concrete. These fibers were confirmed to be Grace Microfiber ™ by the concrete supplier. The addition of these fibers was not intentional, however, they were not believed to alter the concrete strength or performance. Additional cylinders were tested to confirm the strength of this concrete was consistent with the other specimens.

The specified concrete compressive strength for the bare specimens was 3000 psi (21 MPa), which is comparable to the design strength of concrete used in pre-1970's bridges. Actual concrete compressive strengths were determined from 4 x 8 in (102 x 203 mm) cylinders which were tested on the 28th day of placing concrete, and on the day-of-test in accordance with ASTM C39M/ C39M-05 and ASTM C617-98. Tensile splitting tests were performed on 6 x12 in (152 x 305 mm) cylinders on the day-of-test to estimate the tensile splitting strength of concrete in accordance with ASTM C496/C496M-04. Test day compressive and tensile strength of concrete are presented in Table 3.2, Table 3.3, and Table 3.4. The footing concrete strengths for the specimens reported by Lostra (2016) (specimens 10 to 13) were not reported because all concrete damage was concentrated in the column.

Table 3.2: Test Day Concrete Properties of Columns and Retrofit Shell

No.	Specimen Name	Column concrete compressive strength, psi (MPa)		Column concrete tensile strength, psi (MPa)		Shell concrete compressive strength, psi (MPa)		Shell concrete tensile strength, psi (MPa)	
1	C-S-R	3012	(20.8)	151	(1.0)	-	(-)	-	(-)
2	C-S-D	2919	(20.1)	240	(1.7)	-	(-)	-	(-)
3	R-S-R-LTi-90	3220	(22.2)	251	(1.7)	4851	(33.4)	374	(2.6)
4	R-S-D-LTi-90	3656	(25.2)	263	(1.8)	5812	(40.1)	473	(3.3)
5	R-S-R-LTi-135	2915	(20.1)	262	(1.8)	4399	(30.3)	344	(2.4)
6	R-S-R-0	3430	(23.6)	350	(2.4)	2916	(20.1)	316	(2.2)
7	R-S-R-LSS-90	3402	(23.5)	259	(1.8)	3869	(26.7)	342	(2.4)
8	R-S-R-LTi-90-Spread	3674	(25.3)	323	(2.2)	5982	(41.2)	374	(2.6)
9	R-S-R-LTi-90-Pile	3850	(26.5)	277	(1.9)	7282	(50.2)	510	(3.5)
10	C-T-R	4440*	(30.3)*	520	(3.6)	-	-	-	-
11	R-T-R-LTi-90	4210	(29.0)	490	(3.4)	3420	(29.0)	490	(3.4)
12	RS-T-R-LTi-90	3710	(25.6)	310**	(2.0)**	5050	(25.6)	540	(3.7)
13	RN-T-R-LTi-90	3360	(25.2)	278**	(1.9)**	3250	(25.2)	430	(3.0)
14	R-T-R-0	2900	(20.0)	227	(1.6)	4537	(31.3)	426	(2.9)

* Estimated concrete strength based on split cylinder test relationships

** Estimated concrete strength based on tensile to compressive strength relationships

Table 3.3: Test Day Concrete Properties of Footings

No.	Specimen Name	Footing concrete compressive strength, psi (MPa)	Footing concrete tensile strength, psi (MPa)
1	C-S-R	4118 (28.4)	-
2	C-S-D	4345 (30.0)	-
3	R-S-R-LTi-90	3265 (22.5)	-
4	R-S-D-LTi-90	3448 (23.8)	-
5	R-S-R-LTi-135	3273 (22.6)	-
6	R-S-R-0	3059 (21.1)	-
7	R-S-R-LSS-90	3898 (26.9)	-
8	R-S-R-LTi-90-Spread	3674 (25.3)	235 (1.6)
9	R-S-R-LTi-90-Pile	3850 (26.5)	235 (1.6)
10	C-T-R	-	-
11	R-T-R-LTi-90	-	-
12	RS-T-R-LTi-90	-	-
13	RN-T-R-LTi-90	-	-
14	R-T-R-0	3251 (22.4)	-

Table 3.4: Test Day Ages of Concrete Elements

No.	Specimen Name	Footing concrete age (day of testing)	Column concrete age (day of testing)	Shell concrete age (day of testing)
1	C-S-R	184 days	153 days	-
2	C-S-D	229 days	198 days	-
3	R-S-R-LTi-90	238 days	217 days	29 days
4	R-S-D-LTi-90	286 days	265 days	50 days
5	R-S-R-LTi-135	371 days	352 days	31 days
6	R-S-R-0	152 days	132 days	34 days
7	R-S-R-LSS-90	282 days	262 days	36 days
8	R-S-R-LTi-90-Spread	295 days	282 days	141 days
9	R-S-R-LTi-90-Pile	324 days	311 days	153 days
10	C-T-R	-	97 days	-
11	R-T-R-LTi-90	-	169 days	35 days
12	RS-T-R-LTi-90	-	126 days	70 days
13	RN-T-R-LTi-90	-	140 days	21 days
14	R-T-R-0	111 days	92 days	29 days

3.3.2 Reinforcing Steel

The reinforcing steel was fabricated by a local rebar fabricator per OSU approved shop drawings. Three 18 in (457 mm) long steel samples were cut from randomly selected fabricated steel for each reinforcing bar type. These steel specimens were tested in a 110 kip (490 kN) capacity universal testing machine using a 2 in (51 mm) gage length extensometer to measure strain. The average yielding stress (f_y), the ultimate stress (f_u) and the ultimate elongation were obtained and are summarized in Table 3.5 and Table 3.6.

Table 3.5: Tensile Test Results of ASTM-A615 #10 (#32M) Grade 60 Reinforcing Steel Bars

S.N.	Specimen	Yield Stress, ksi (MPa)	Yield Strain (με)	Ultimate Stress, ksi (MPa)	Ultimate Elongation (%)
1	C-S-R	65 (448)	2,257	95 (655)	32.40
2	C-S-D	65 (448)	2,257	95 (655)	32.40
3	R-S-R-LTi-90	65 (448)	2,257	95 (655)	32.40
4	R-S-D-LTi-90	65 (448)	2,257	95 (655)	32.40
5	R-S-R-LTi-135	65 (448)	2,257	95 (655)	32.40
6	R-S-R-0	65 (448)	2,257	95 (655)	32.40
7	R-S-R-LSS-90	65 (448)	2,257	95 (655)	32.40
8	R-S-R-LTi-90-Spread	65 (448)	2,257	95 (655)	32.40
9	R-S-R-LTi-90-Pile	65 (448)	2,257	95 (655)	32.40
10	C-T-R	70 (483)	2,414	110 (758)	-
11	R-T-D-LTi-90	70 (483)	2,414	110 (758)	-
12	RS-T-D-LTi-90	70 (483)	2,414	110 (758)	-
13	RN-T-D-LTi-90	70 (483)	2,414	110 (758)	-
14	R-T-R-0	65 (448)	2,257	95 (655)	32.40

Table 3.6: Tensile Test Results of ASTM A615 #3 (#10M) Grade 40 Reinforcing Steel Bars

S.N.	Specimen	Yield Stress, ksi (MPa)	Yield Strain, με	Ultimate Stress, ksi (MPa)	Ultimate Elongation (%)
1	C-S-R	56 (386)	1,923	86 (583)	27.78
2	C-S-D	56 (386)	1,923	86 (583)	27.78
3	R-S-R-LTi-90	56 (386)	1,923	86 (583)	27.78
4	R-S-D-LTi-90	56 (386)	1,923	86 (583)	27.78
5	R-S-R-LTi-135	56 (386)	1,923	86 (583)	27.78
6	R-S-R-0	56 (386)	1,923	86 (583)	27.78
7	R-S-R-LSS-90	56 (386)	1,923	86 (583)	27.78
8	R-S-R-LTi-90-Spread	56 (386)	1,923	86 (583)	27.78
9	R-S-R-LTi-90-Pile	56 (386)	1,923	86 (583)	27.78
10	C-T-R	51 (352)	1,747	79 (545)	-
11	R-T-D-LTi-90	51 (352)	1,747	79 (545)	-
12	RS-T-D-LTi-90	51 (352)	1,747	79 (545)	-
13	RN-T-D-LTi-90	51 (352)	1,747	79 (545)	-
14	R-T-R-0	56 (386)	1,923	86 (583)	27.78

3.3.3 Retrofit Materials

TiABs and stainless steel bars were explored for the retrofit ligaments and TiAB spirals were used for all confinement shells. No extra TiABs were available for tensile testing so only one sample from the stock of TiABs that was not used was tested to verify the mill certificate properties. The test results were in good agreement with the mill certificate data so that the mill certificate properties were taken as the material properties for both #5 and #3 TiABs. The material properties are summarized in Table 3.7 and Table 3.8. Three (3) samples were tested for Grade 75 #6 (#19M) stainless steel bars (Enduramet Gr. 75) and the results are summarized in Table 3.9.

.

Table 3.7: Tensile Test Results of #5 (#16M) TiABs

S.N.	Specimen	Yield Stress, ksi (MPa)	Yield Strain (με)
1	C-S-R	-	-
2	C-S-D	-	-
3	R-S-R-LTi-90	152 (1048)	9,806
4	R-S-D-LTi-90	152 (1048)	9,806
5	R-S-R-LTi-135	152 (1048)	9,806
6	R-S-R-0	-	-
7	R-S-R-LSS-90	-	-
8	R-S-R-LTi-90-Spread	146 (1007)	9,419
9	R-S-R-LTi-90-Pile	146 (1007)	9,419
10	C-T-R	-	-
11	R-T-D-LTi-90	131 (903)	8,452
12	RS-T-D-LTi-90	131 (903)	8,452
13	RN-T-D-LTi-90	131 (903)	8,452
14	R-T-R-0	-	-

Table 3.8: Tensile Test Results of #3 (#10M) TiABs

No.	Specimen Name	Yield Stress, ksi (MPa)	Yield Strain (με)
1	C-S-R	-	-
2	C-S-D	-	-
3	R-S-R-LTi-90	136 (1048)	8,774
4	R-S-D-LTi-90	129 (1048)	8,323
5	R-S-R-LTi-135	133 (1048)	8,581
6	R-S-R-0	136 (1048)	8,774
7	R-S-R-LSS-90	129 (1048)	8,323
8	R-S-R-LTi-90-Spread	136 (1007)	8,774
9	R-S-R-LTi-90-Pile	136 (1007)	8,774
10	C-T-R	-	-
11	R-T-D-LTi-90	131 (903)	8,452
12	RS-T-D-LTi-90	131 (903)	8,452
13	RN-T-D-LTi-90	131 (903)	8,452
14	R-T-R-0	136 (1048)	8,774

Table 3.9: Tensile Test Results of #6 (#19M) Grade 75 Stainless Steel Reinforcing Bars

No.	Specimen Name	Yield Stress, ksi (MPa)	Yield Strain (με)	Ultimate Stress, ksi (MPa)	Ultimate Elongation (%)
1	R-S-R-LSS-90	95 (655)	3,287	136 (938)	32.40

3.3.4 Foam used as pseudo-soil

FOAMULAR$^{®}$ 1000 Extruded Polystyrene (XPS) Rigid Foam Insulation was used as pseudo-soil to test the specimen with realistic spread footing details (Specimen R-S-R-LTi-90-Spread).

Two layers of 3 in thick foam were overlaid to produce 6 in thick pseudo-soil on the strong floor. The specimen was squeezed onto the foam with the specified axial load and was allowed to rock on the foam.

Relevant physical material properties from manufacturer's product data sheet are given below. Other material specifications can be found in the manufacturer's website[1].

- Minimum Compressive Strength = 100 psi (689 kPa)

- Minimum Flexural Strength = 140 psi (965 kPa)

Summary of the compression test results of this foam and main findings can be found in Appendix A.

3.3.5 Bonding material

Hilti HIT-RE 500 V3 Epoxy Adhesive was used for anchoring the TiABs to the concrete substrate. Listed below are the relevant material specifications provided by the manufacturer. Other material specifications can be found in the manufacturer's website (www.hilti.com).

- *Bond Strength ASTM C882-13A*: 1,560 psi (10.8 MPa) for 2 day cure and 1,690 psi (11.7 MPa) for 14 day cure period.

- Tensile Strength 7 day ASTM D638-14: 7,150 psi (49.3 MPa)

The manufacturer also specifies the following specifications for rebar installed with Hilti HIT-RE 50 V3 epoxy.

- *Nominal bit diameter:* ½ in for #3 bar, ¾ in for #5 bar and 7/8 in for #6 bar.

- *Effective minimum embedment:* 2-3/8 in (60 mm) for #3 bar and 3 in (76 mm) for #5 and #6 bars.

Pull-out tests were performed #5 TiAB and #6 stainless steel bars to verify that the bond-stress could be developed in the retrofit ligaments with the epoxy adhesive that was used over their prescribed embedment length. When performing these pull-out tests, the ligament specimens were debonded near the surface of the concrete substrate to prevent small cone pull-out at maximum stress levels. The #5 TiAB was able to develop an average bond strength of approximately 1.4 ksi (9.6 MPa) over the embedded length of 15 in (381 mm) and #6 stainless steel bars developed approximately 1.6 ksi (11.0 MPa) over the embedded length of 12 in (305 mm). Results of pull-out tests performed are presented in the Appendix A.

3.4 INSTRUMENTATION

The specimens were instrumented to capture global and local structural responses. Applied loads including lateral and gravity forces were measured directly with load cells mounted to hydraulic

---

[1] www.commercial.owenscorning.com

cylinders. The column deflection at the point of lateral load application, flexural and shear deformation of the column and rigid body motion of the footing were measured with displacement sensors. In addition, strains in vertical and transverse reinforcing steel, TiAB and stainless steel ligaments, and TiAB spirals were measured using an array of electrical resistance strain gages. Data were acquired and stored for subsequent data reduction using PC-based data acquisition hardware and software.

String potentiometers of range 4.7 in and 10 in were used to measure the shear and flexural deformations in sections along the column specimens. The position and orientation of each string potentiometer are shown in Figure 3.54, Figure 3.55, and Figure 3.56. Individual ¼ in thick aluminum plates were used to position the string potentiometers at the required angle and orientation at each control node. String potentiometers were attached to drilled and tapped holes on the aluminum plates. Holes were hammer drilled into the columns and threaded rods anchored in the holes using epoxy. Threaded rods were 5/16 in diameter for specimen C-S-R and 3/8 in diameter rods were used for the other specimens. To anchor the threaded rods into the column core, the outer 1.5 in (clear cover) for the control specimens and the clear cover plus retrofit shell thickness for retrofitted specimens, of the hole used to anchor the instrument rods was enlarged. The standard hole was drilled through the oversized hole 3.0 in into the column core. The purpose of debonding the threaded rods from the cover concrete and shell was to capture the behavior of the core concrete alone and try to prevent contamination due to cover concrete spalling off at higher displacement demands.

In all square column specimens loaded orthogonal to the surface, string potentiometers were placed on three faces (North, South, and West) of the column. The actuator displaced the column in the North and South directions, so string potentiometers were positioned in a square pattern 4 in off the corner of the columns on the West face to capture the shear deformation through vertical, horizontal and diagonal deformations of the column during cyclic loading. String potentiometers on the North and South face were placed centered to the column face to capture the curvature. The first level of string potentiometers was placed directly on the surface of the footing/the base of the column, the second level was 4 in off the base and the third and the subsequent ones were placed 20 in apart. This provided some redundancy on the measurement of curvature as the deformation of the vertical string potentiometers on the West face of the column could also be used to compute the curvature in addition to the vertical string potentiometers stationed at the North and South face of the column. All the threaded rods on the square oriented columns extended past and were perpendicular to the column surface. For the diamond columns the rods were bent so that they extended past the surface and perpendicular to the North-South plane.

Four string potentiometers were attached to the footing top surface close to the column face to measure the strain penetration.

Total column drift at the point of application of lateral load was measured by 30 in stroke range string potentiometer that was clamped onto an angle connected to a rigid steel column affixed to the strong floor and connected with the brass wire to a high-force magnet attached to the center of the steel plate on the column at the load point. Sensors with a range of 1 in were used for footing slip measurements and 0.5 in ranges sensors were used for footing rocking measurements. The transducers to measure rocking of the footing were positioned along the centerline of the footing top surface 2 in from the side of the footing, as shown in the picture on the North and South; the one measuring the slip was positioned 2 in off the base of the footing along the centerline on the North face.

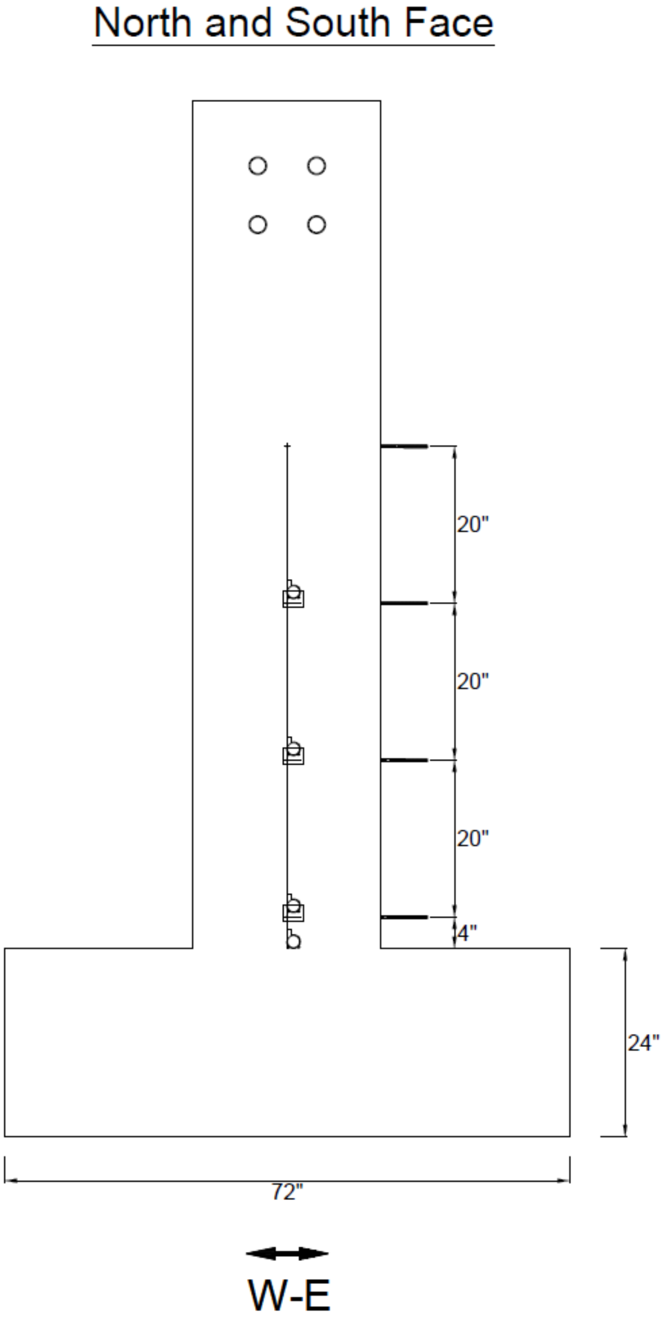

Figure 3.54: Displacement sensors distributed along column specimens on N and S faces

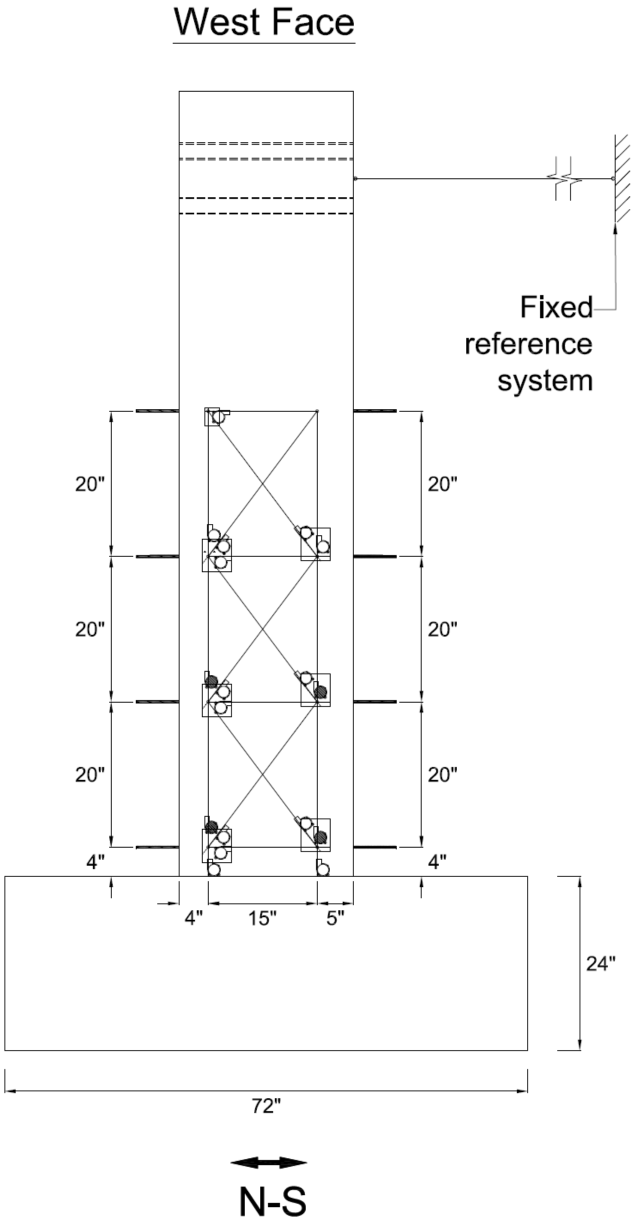

Figure 3.55: Displacement sensors distributed along column specimens on west face

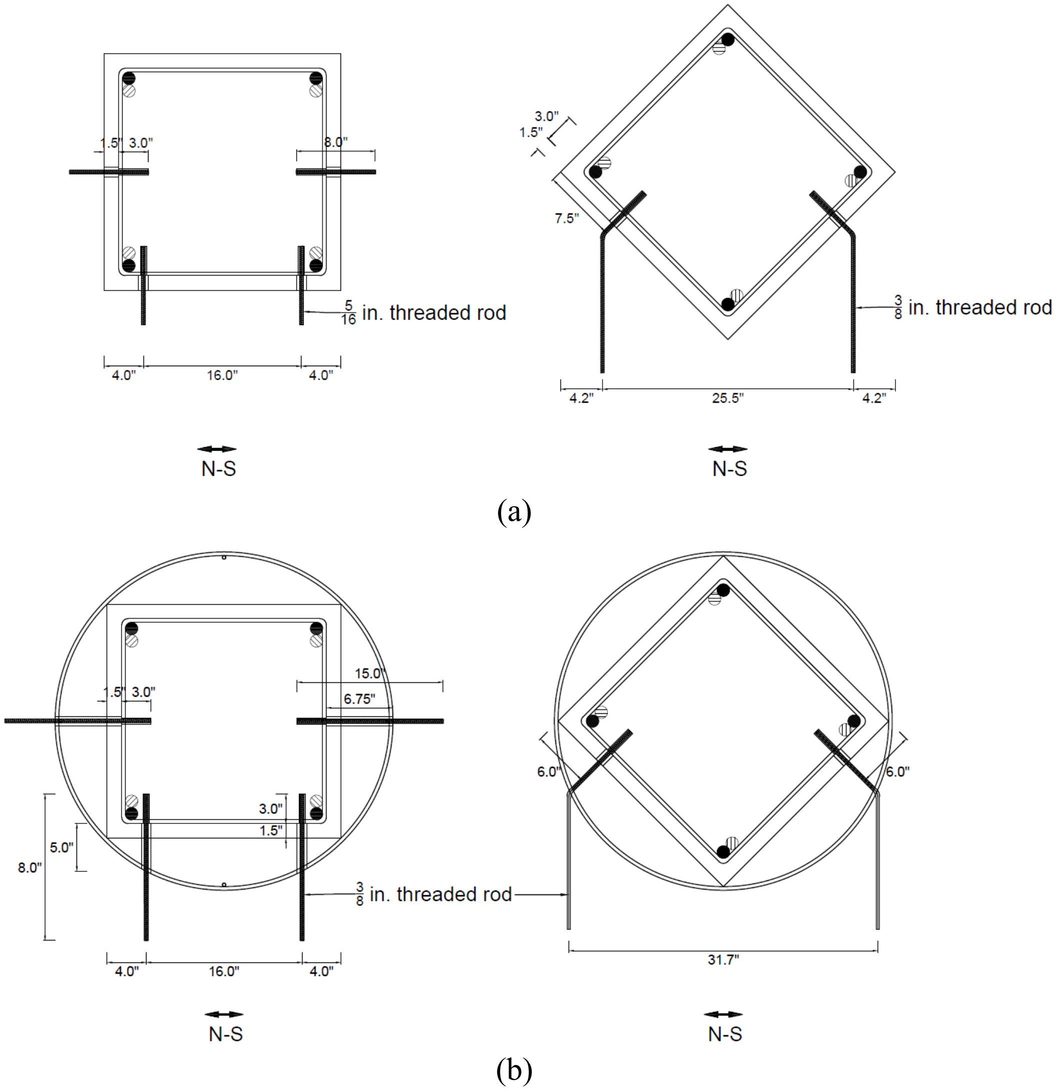

Figure 3.56: Section view showing the threaded rods used to attach displacement sensors to columns: (a) control specimens, (b) retrofitted specimens

Strain gages were mounted on the embedded reinforcing steel and to the TiABs prior to concrete placement. The strain gage naming convention is illustrated in Figure 3.57. Strain gages were installed on the longitudinal reinforcing steel footing starter bars, column bars, and ties prior to concrete placement. The locations of the strain gages are illustrated in Figure 3.58 through Figure 3.65.

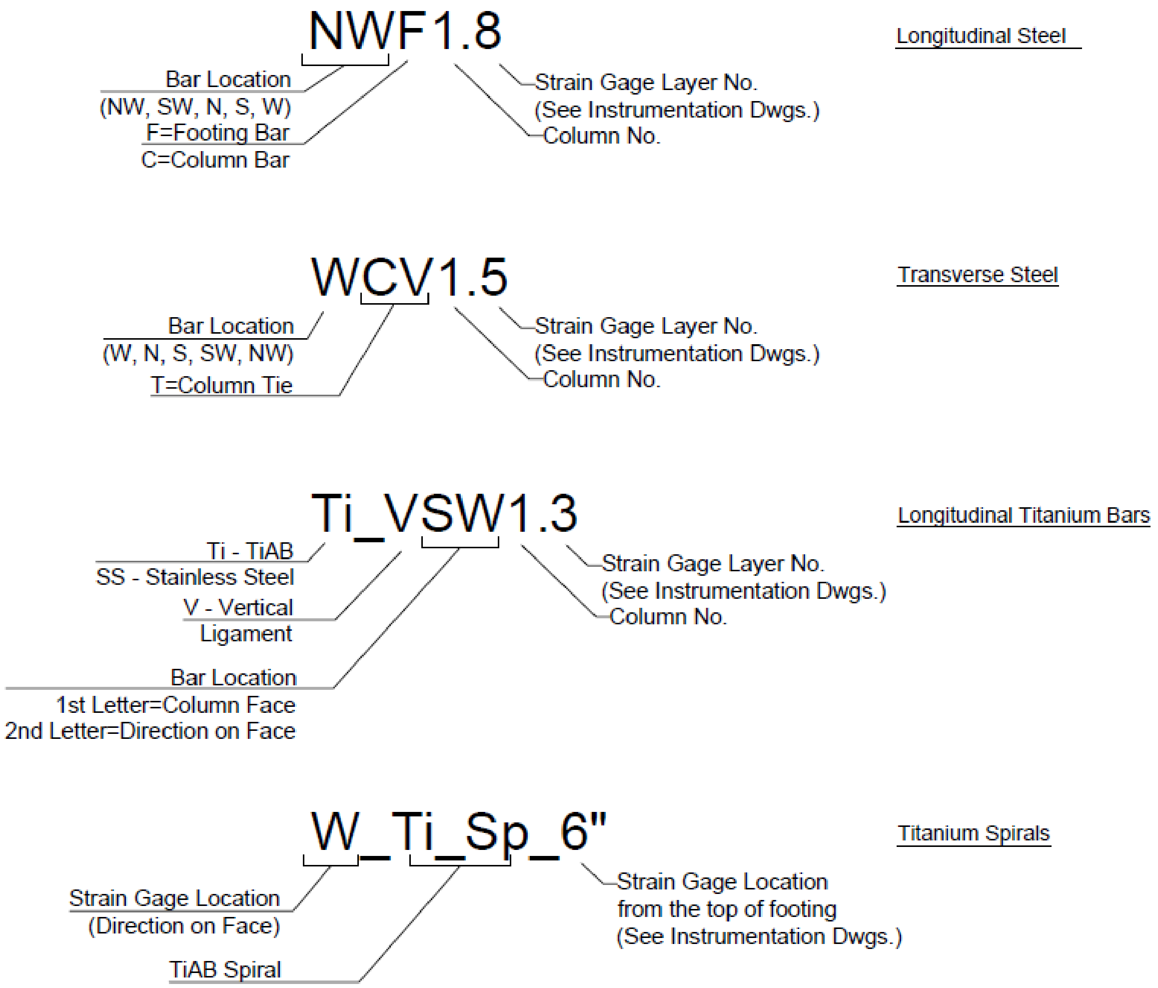

Figure 3.57: Naming convention for strain gages

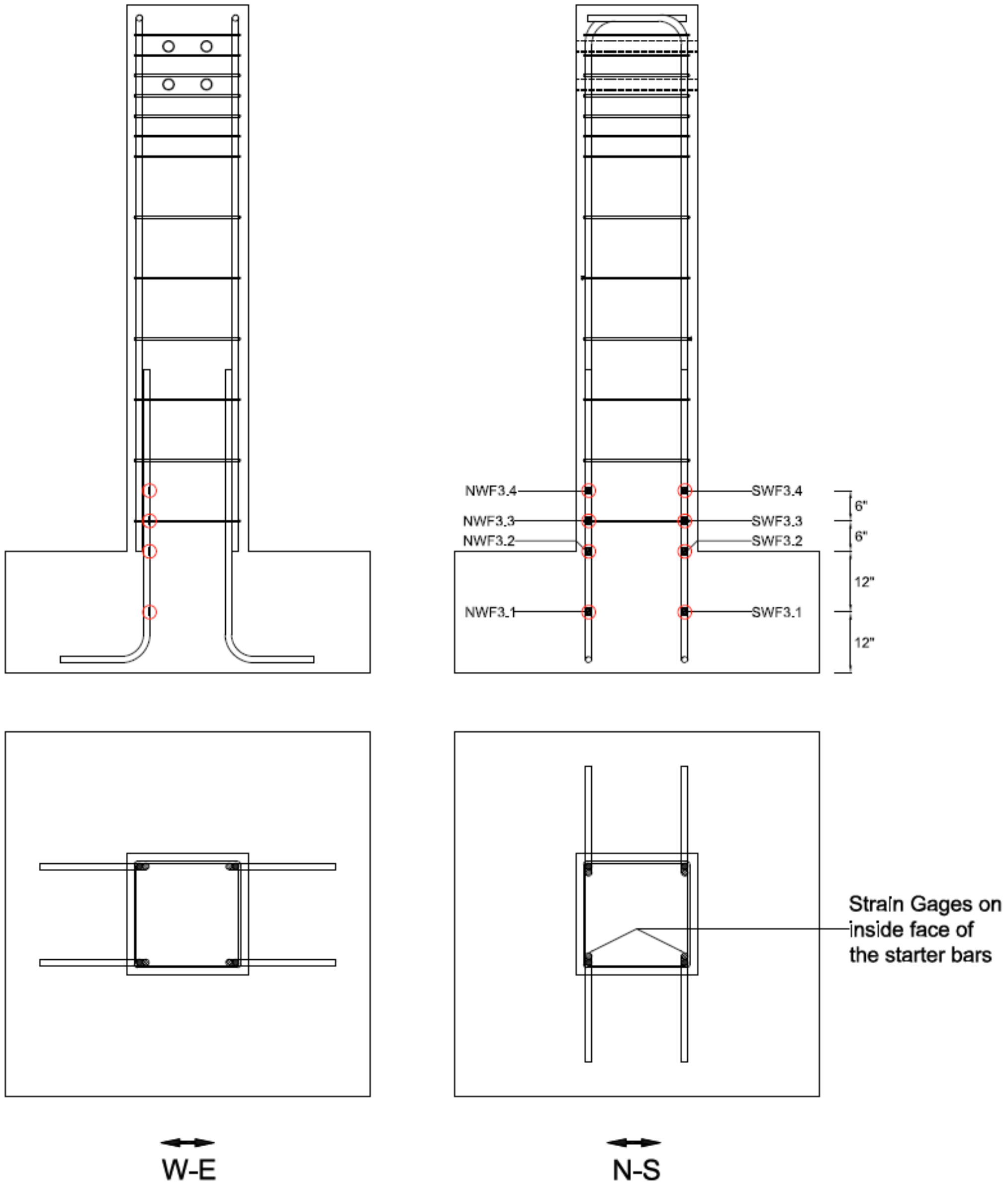

Figure 3.58: General strain gage locations on starter bars

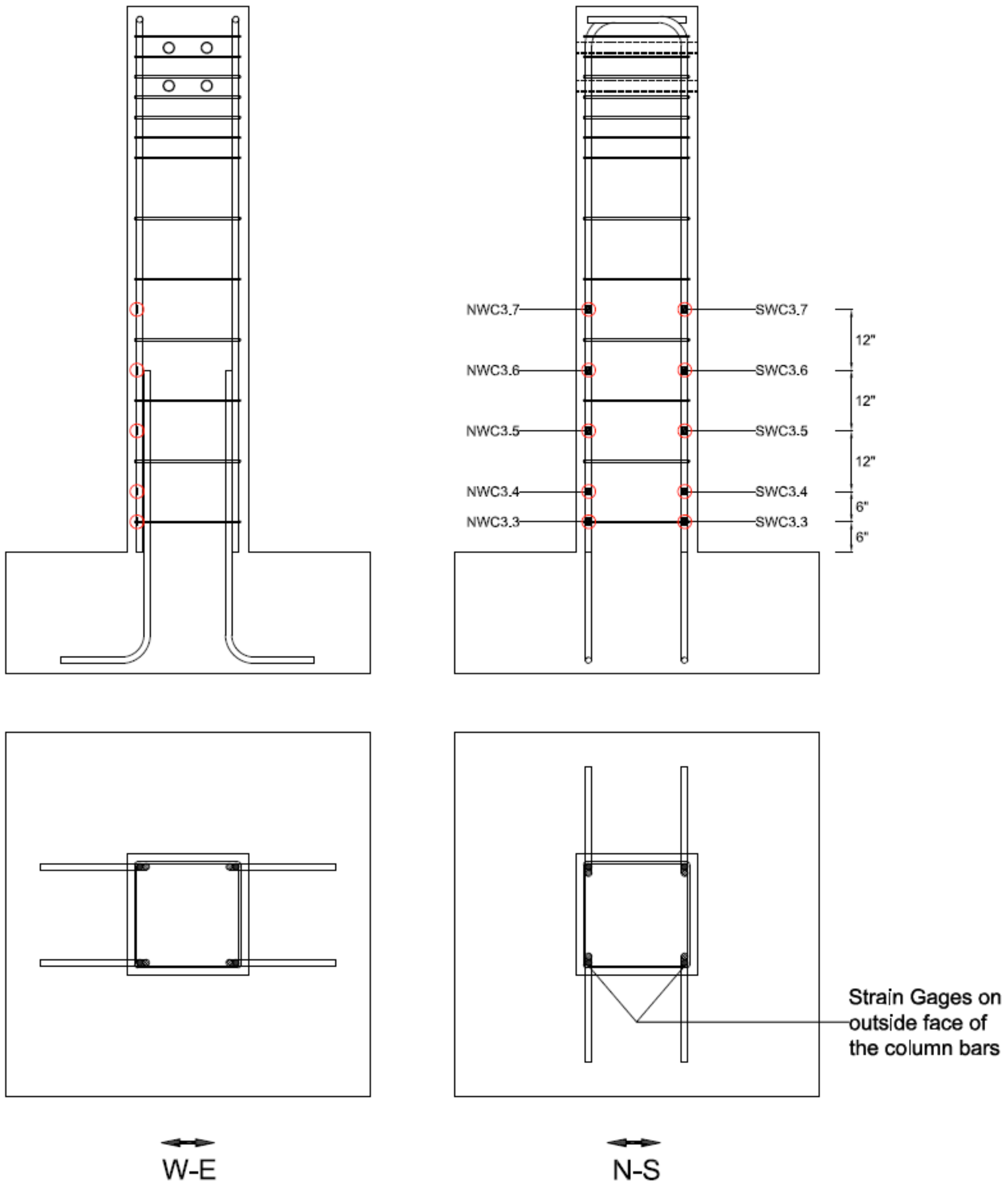

Figure 3.59: General strain gage locations on column bars

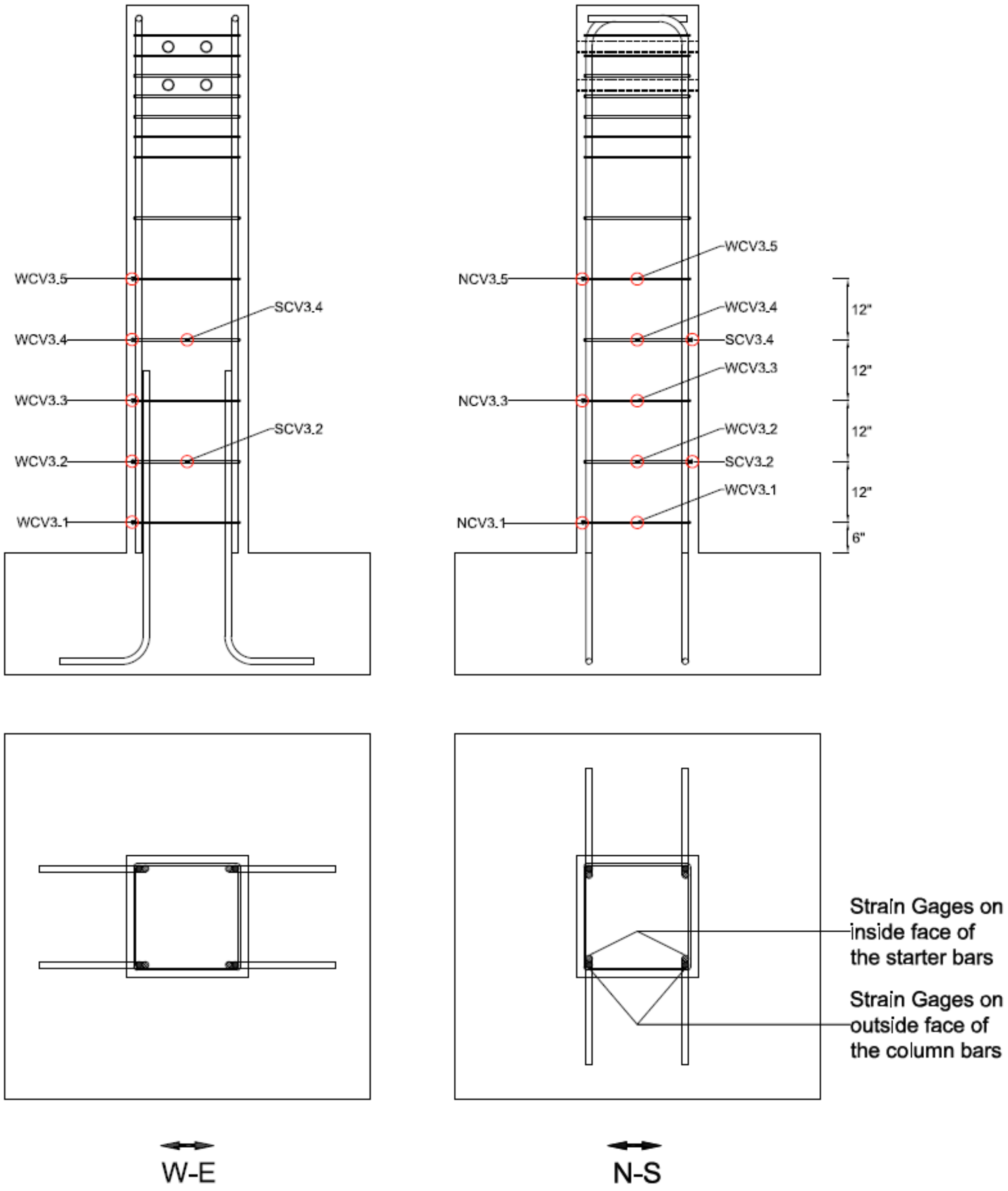

Figure 3.60: General strain gage locations on column ties

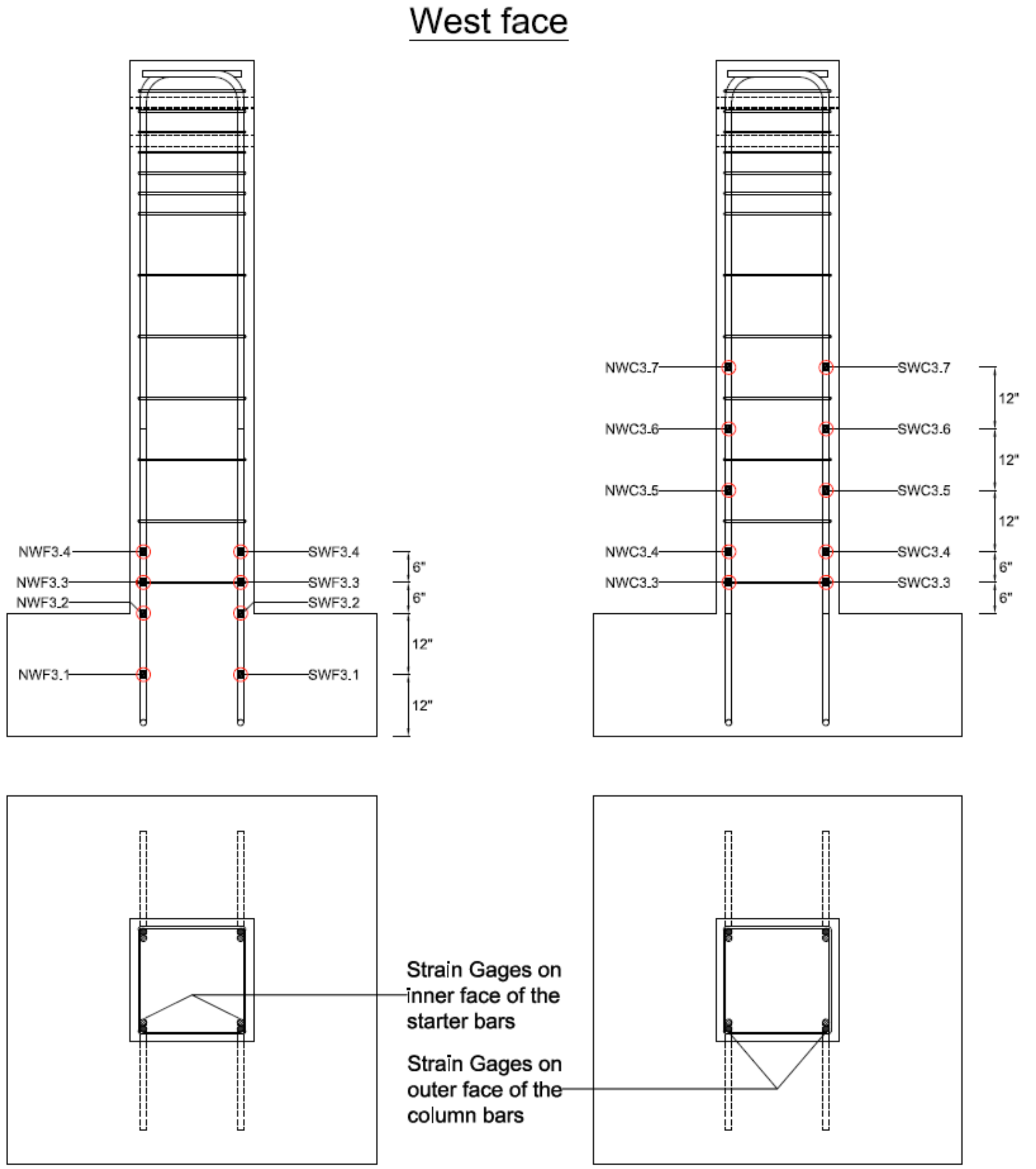

Figure 3.61: Specimen R-S-R-LTi-90: Strain gage layout (a) Starter bars (left) (b) Column bars (right)

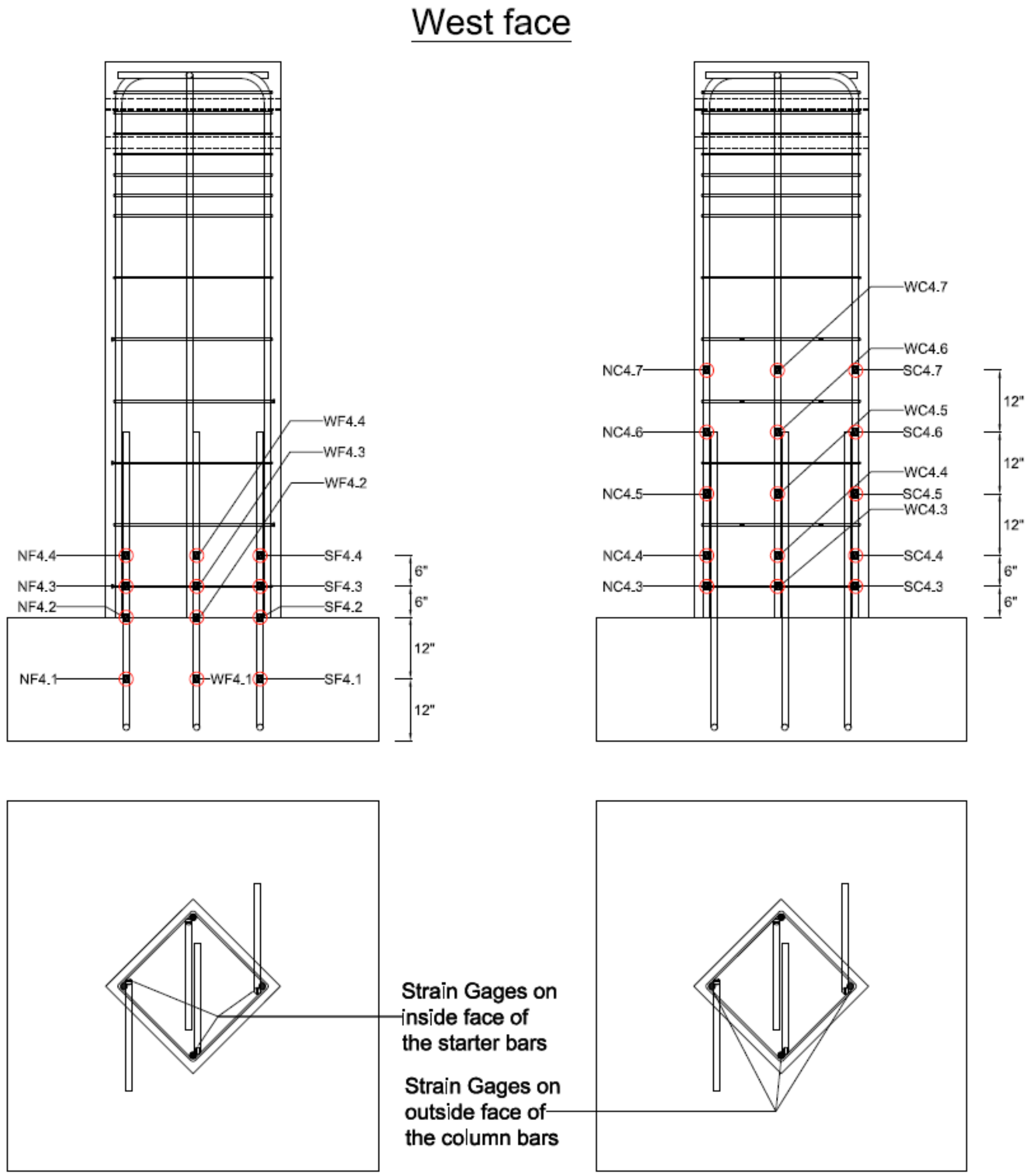

Figure 3.62: Specimen R-S-D-LTi-90: Strain gage layout (a) Starter bars (left) (b) Column bars (right)

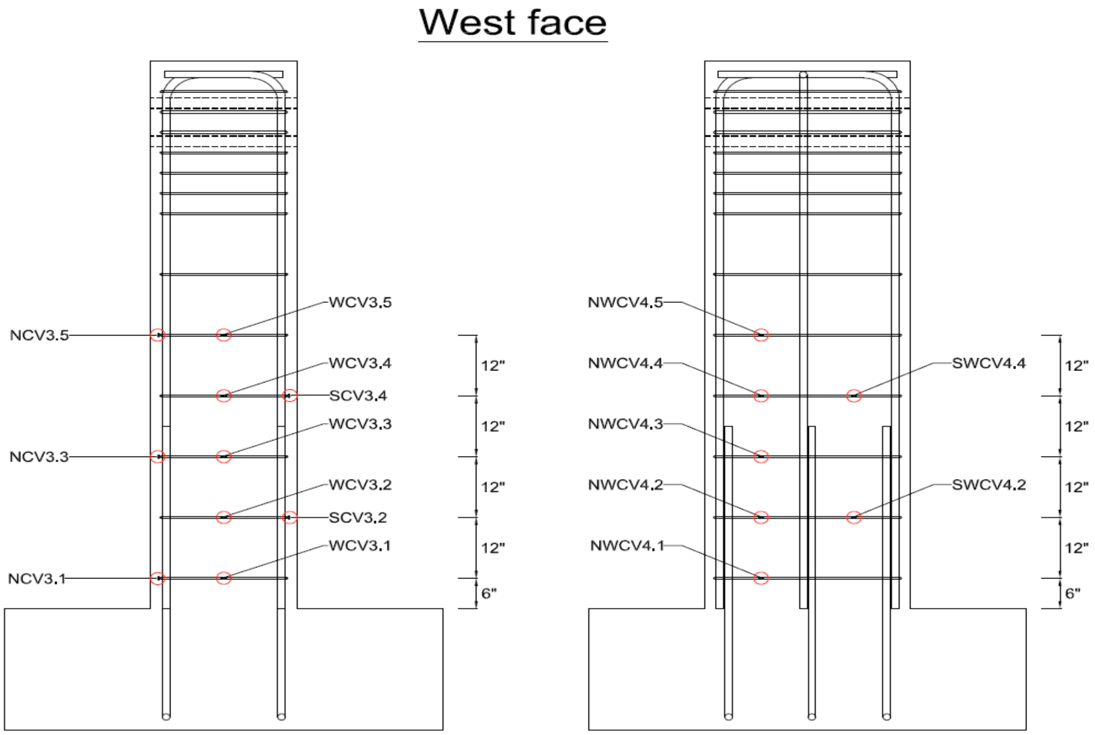

Figure 3.63: Strain gages layout in column ties: (a) Specimen R-S-R-LTi-90 (left) (b) Specimen R-S-D-LTi-90 (right)

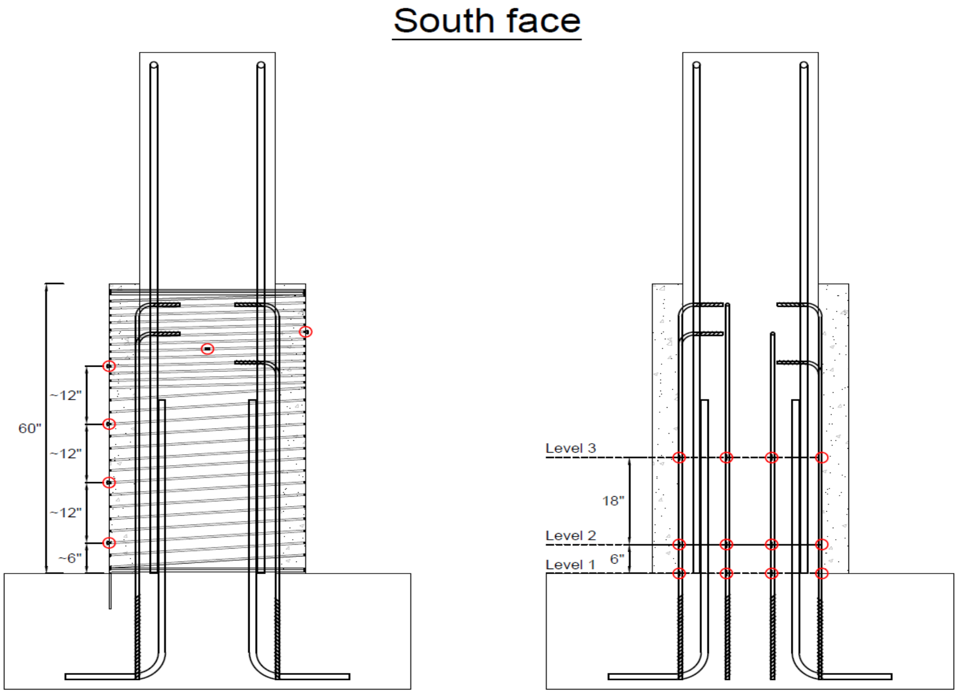

Figure 3.64: Strain gages layout in TiAB spirals and TiAB ligaments on south face

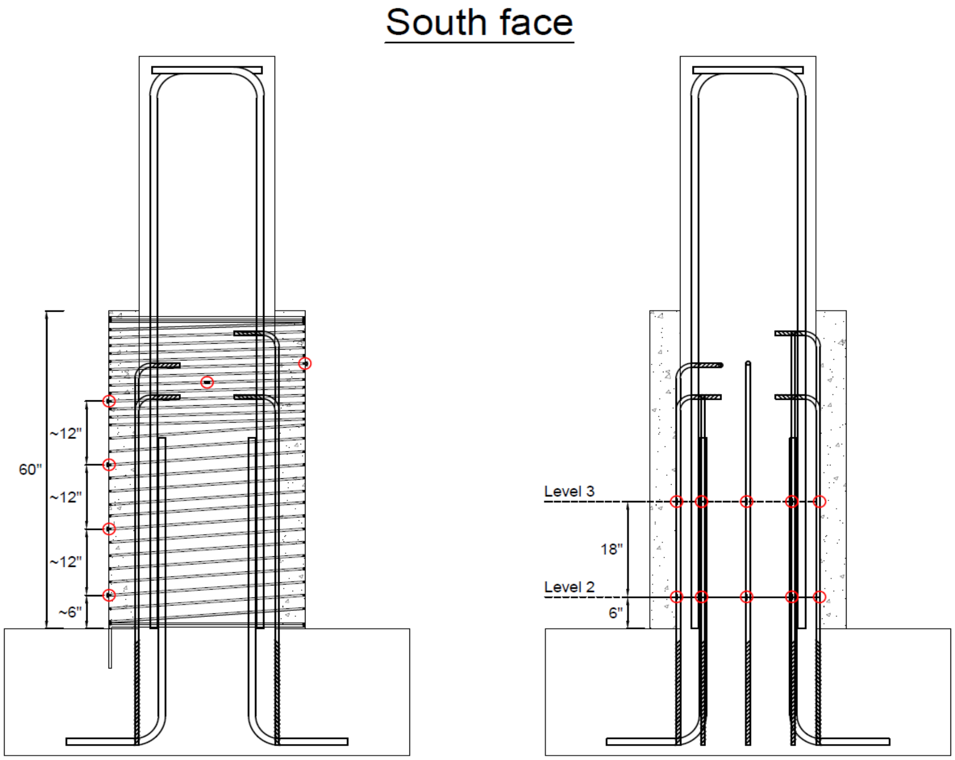

Figure 3.65: Strain gages layout in TiAB spirals and stainless steel ligaments on south face

3.5 EXPERIMENTAL SETUP AND METHODOLOGY

3.5.1 Test setup

The test setup consisted of a servo-hydraulic controlled horizontal actuator with the capacity of 110 kips (489 kN) mounted on the strong wall to apply lateral load. The lateral load point was located 12 in (305 mm) below the finished top surface of the column. Lateral load was applied normal to the South face for specimens loaded parallel to the principal axis. For the two (2) diagonally loaded specimens, a steel loading assembly was constructed of mild carbon steel plates and angles to load the specimen on the corners. The typical setup with lateral and axial loading is shown in Figure 3.66 and Figure 3.67.

The vertical axial loading setup consisted of a hydraulic jack mounted on the steel spreader beam as seen in Figure 3.68. The applied axial force was measured by a 500 kip (2225 kN) capacity load cell. The hydraulic jack was positioned on a 1/8 in (3.2 mm) thick copper plate placed on top of the column surface finished with Hydrostone. The copper plate was intended to allow uniform pressure distribution to the column by accommodating surface imperfections. The column was compressed by tensioning Dywidag bars on the East and West side of the column. The Dywidag bars were anchored to the steel spreader beam at the top and connected to steel plates attached to the specimen footing. The Dywidag bars were anchored with special spherical nuts (and spherical bearings in the case of specimens R-T-R-LTi-90-Spread and R-T-R-LTi-90-

Pile) to allow the rotation of the bars during cyclic lateral deformation. In the specimens with the over-reinforced footing details, the footings were post-tensioned by using four threaded rods at each corner bolted to the laboratory strong floor to achieve fixity at the base.

The specimens with the realistic foundation details (i.e. specimens R-T-R-LTi-90-Spread and R-T-R-LTi-90-Pile) were squeezed into the strong floor by the applied column axial load alone. Horizontal sliding of the pile and spread footings was prevented by placing a steel framework around the footings as seen in Figure 3.69 through Figure 3.72 for the spread footing and Figure 3.73 through Figure 3.75Figure 3.76 for the pile foundation. The contact points on the concrete footing had roller bearing to allow the footing to move up or down, but that restricted horizontal translation. A hydraulic jack with load cell ensured contact between the restraining system and the foundation so that no gaps occurred. The timber piles were connected to the strong floor to prevent uplift using steel brackets that were through bolted through the piles and threaded anchor rods epoxied into the piles and into the strong floor as seen in Figure 3.76 and Figure 3.77 .

At the beginning of the test, the axial load was slowly applied to the top of the specimen until the desired level was achieved. The axial load was then maintained at a constant value of 150 kips (667 kN) in "short columns" and 200 kips (900 kN) in "tall columns" corresponding to 8% and 10% of the nominal axial compressive capacity of the column respectively. The fluctuations in axial load when the column was pushed and pulled through higher drifts were monitored and actively controlled by releasing and adding jack pressure as needed.

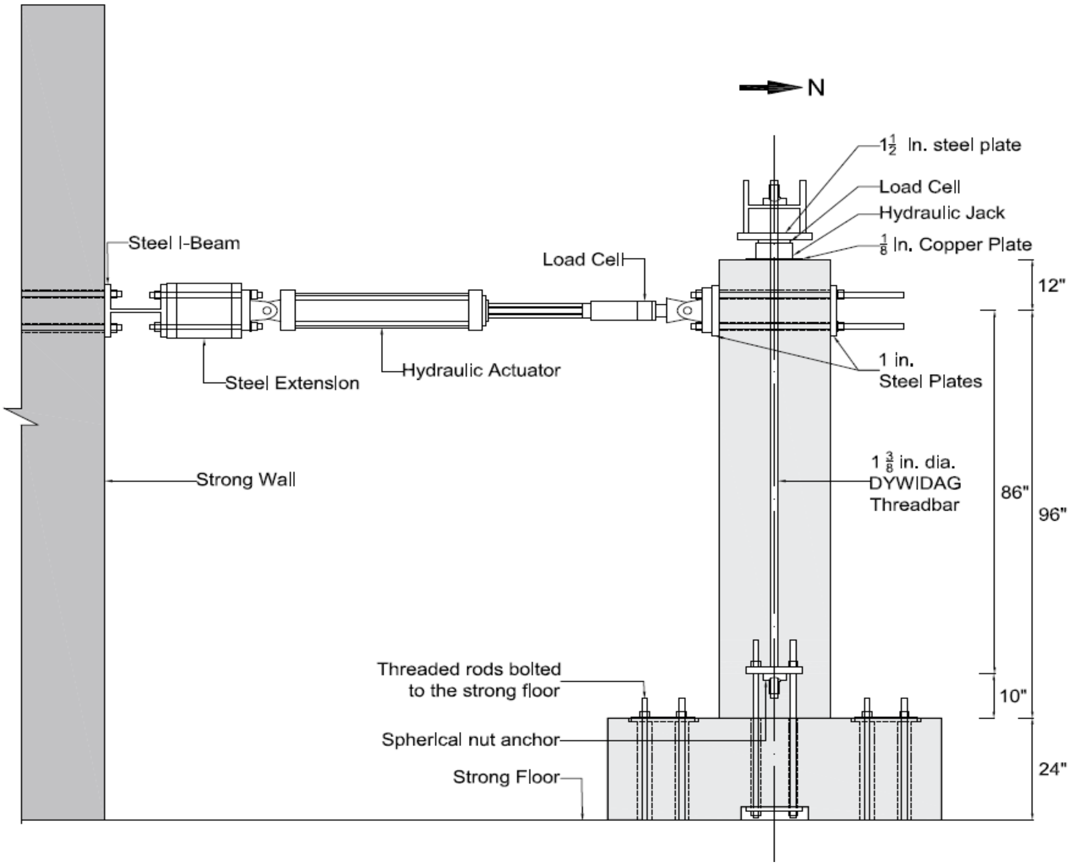

Figure 3.66: Typical lateral loading setup (East elevation, short specimen shown)

Figure 3.67: Photograph of experimental setup (diagonal control specimen shown with top loading fixture)

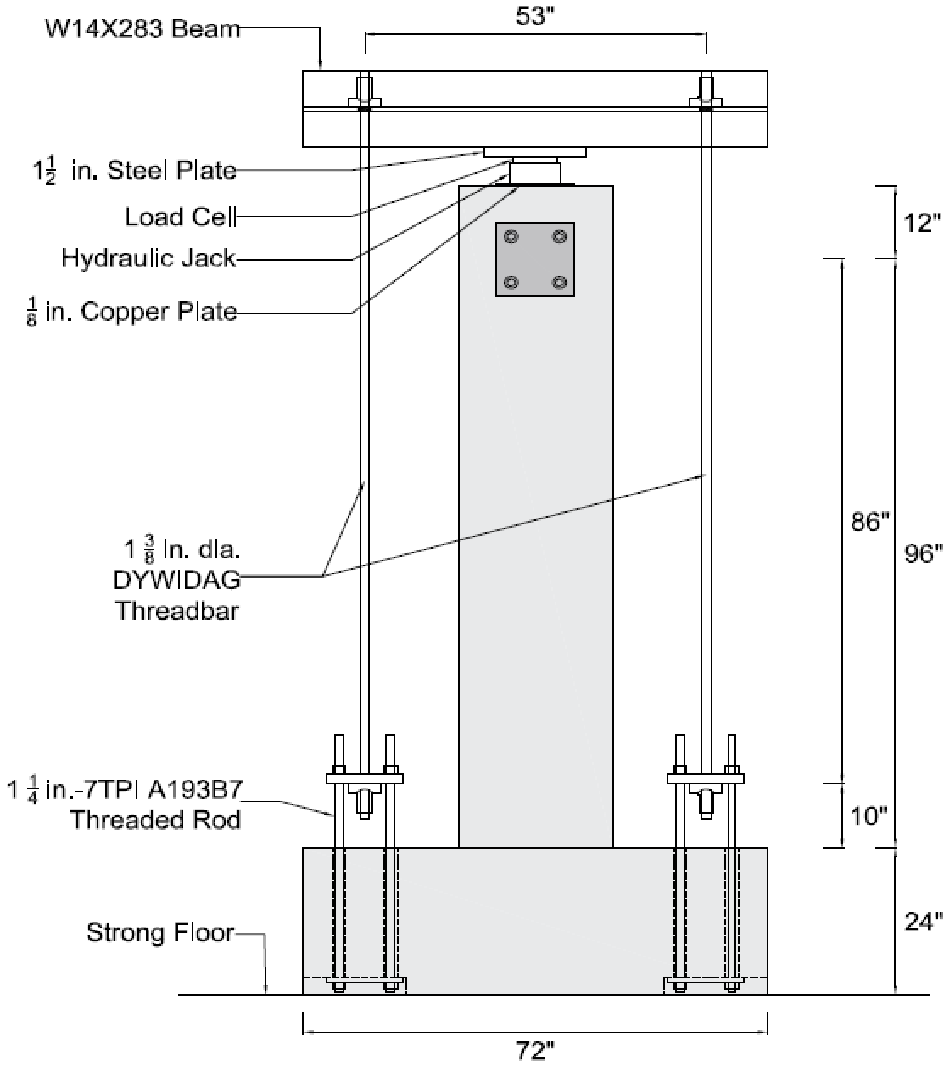

Figure 3.68: Typical vertical loading setup (North elevation) for typical over reinforced footing foundation

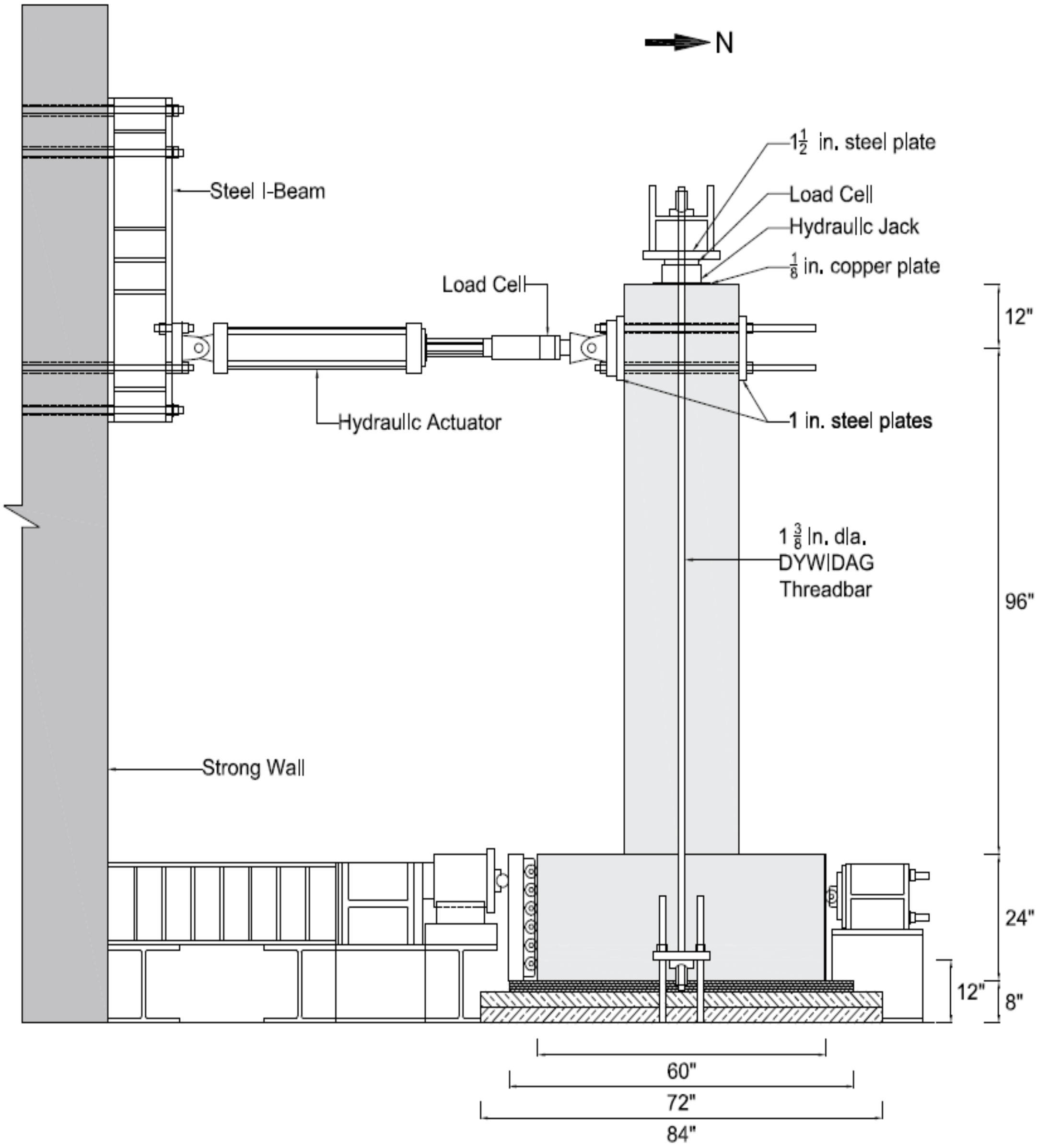

Figure 3.69: Specimen R-S-R-LTi-90-Spread: Lateral loading setup (East elevation, lateral restraints for footing not shown completely)

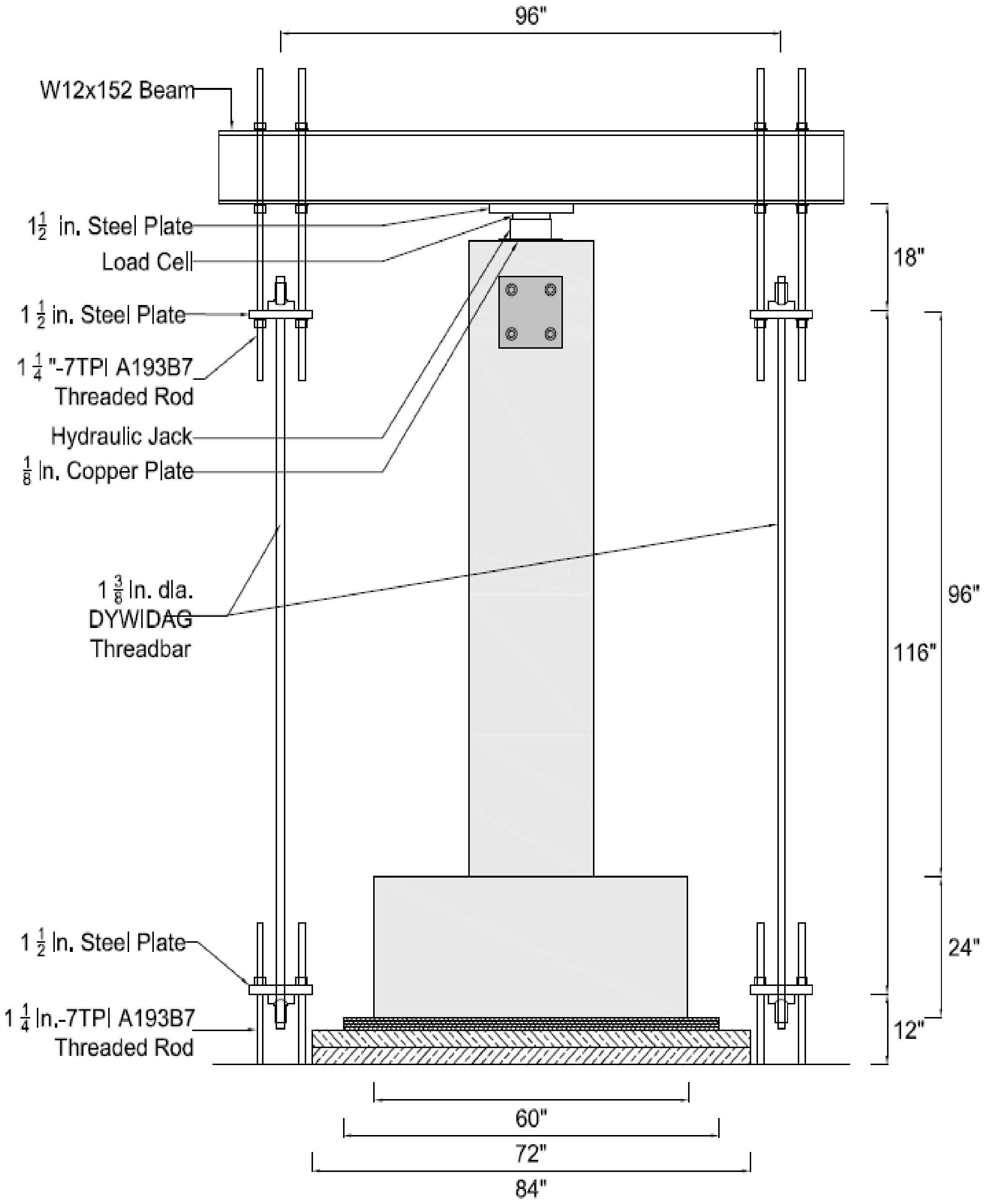

Figure 3.70: Specimen R-S-R-LTi-90-Spread: Vertical loading setup (North elevation, lateral restraints for footing not shown)

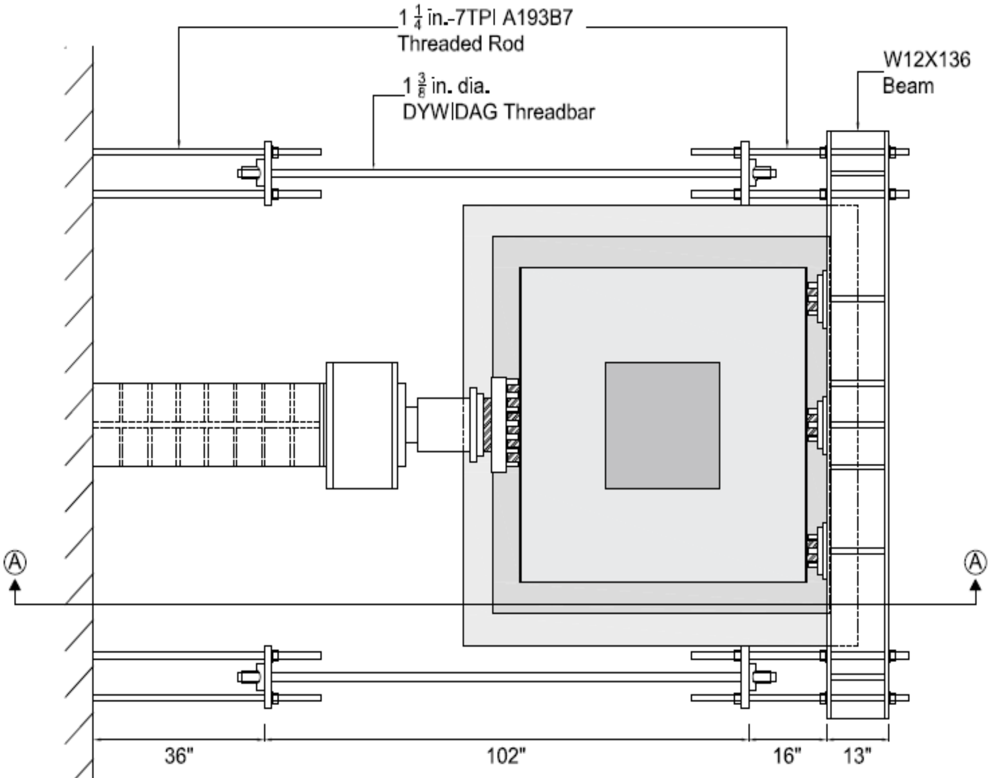

Plan Layout

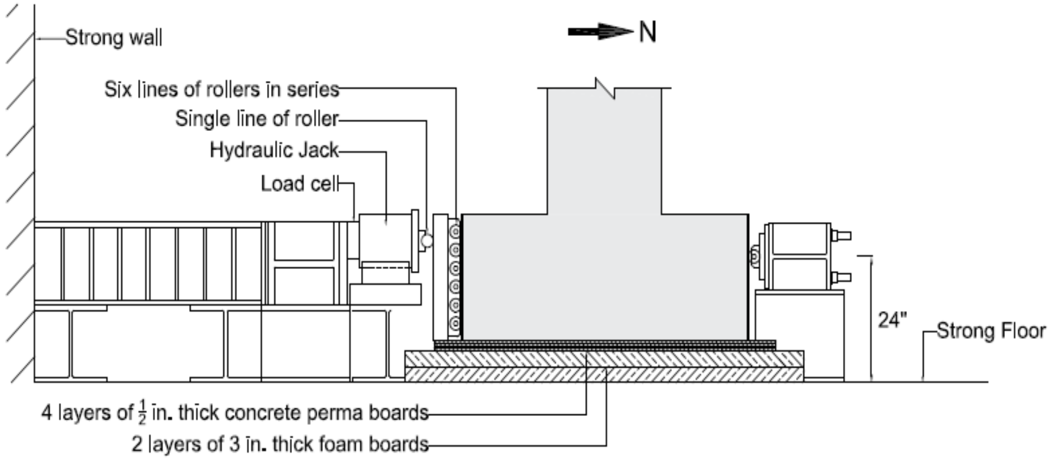

Section A-A

Figure 3.71: Specimen R-S-R-LTi-90-Spread: Lateral restraints for footing

Figure 3.72: Photograph of setup details for spread footing

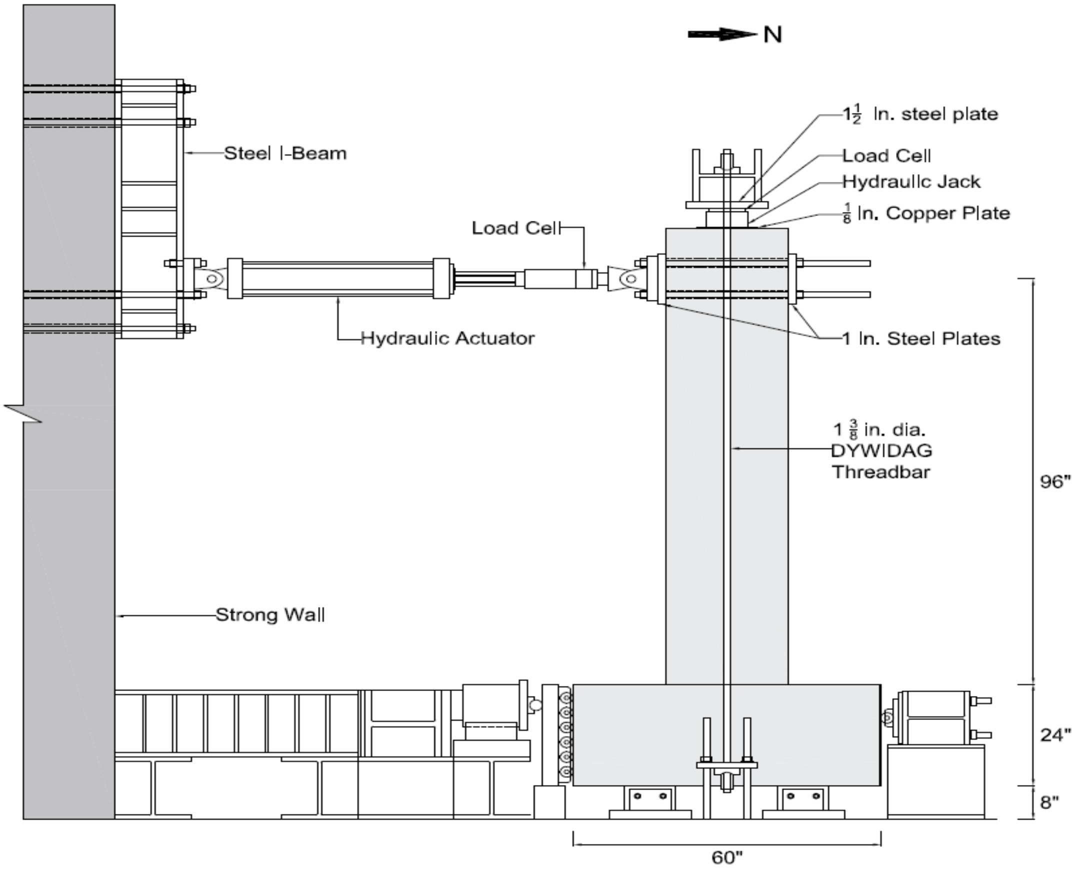

Figure 3.73: Specimen R-S-R-LTi-90-Pile: Lateral loading setup (East elevation, lateral restraints for footing not shown completely)

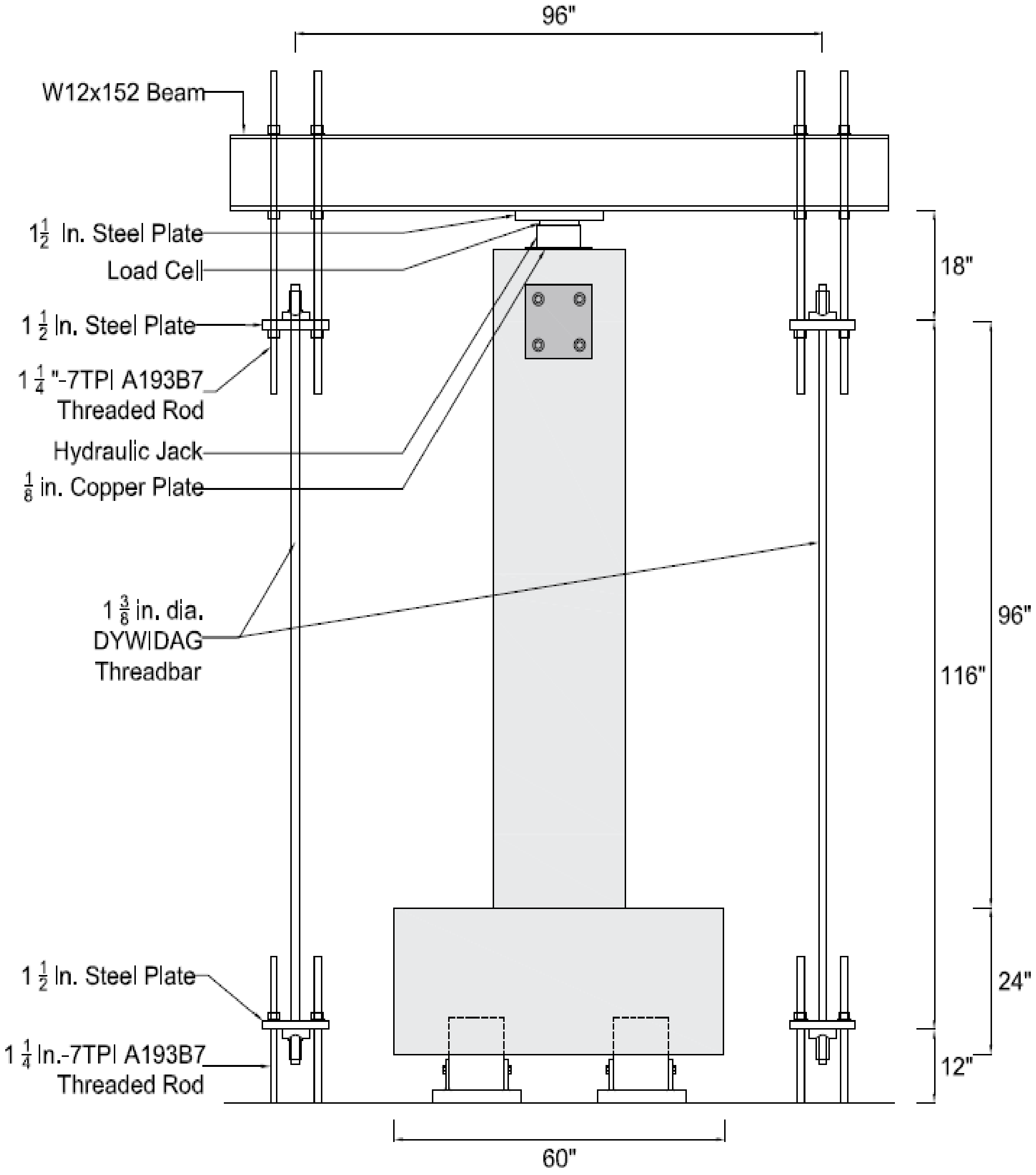

Figure 3.74: Specimen R-S-R-LTi-90-Pile: Vertical loading setup (North elevation, lateral restraints for footing not shown)

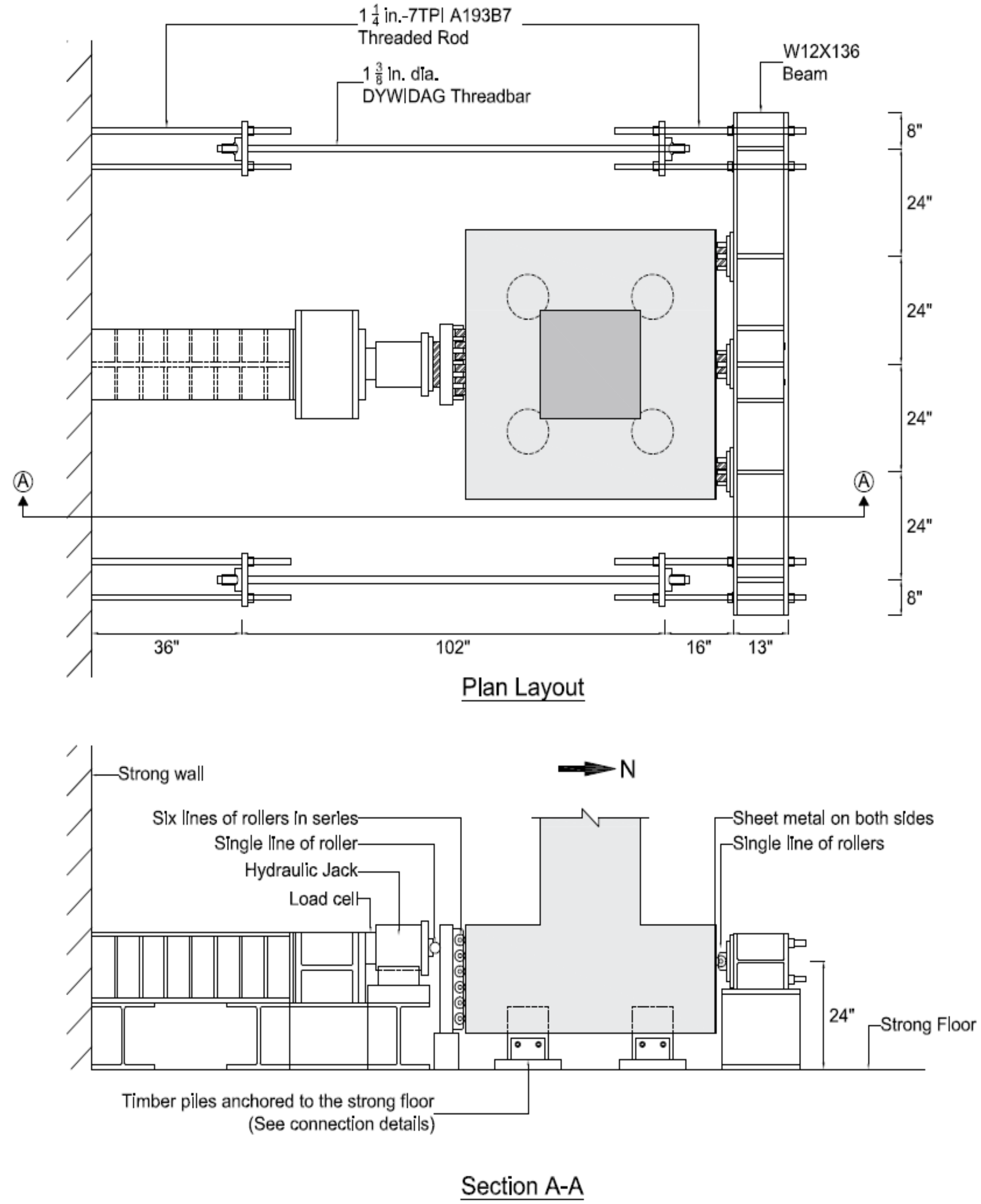

Plan Layout

Section A-A

Figure 3.75: Specimen R-S-R-LTi-90-Pile: Lateral restraints for the pile cap

(a)

(b)

(c)

Figure 3.76: Photographs of specimen R-S-R-LTi-90-Pile: (a) Pile cap restraints; (b) Restraints for timber piles; (c) Timber piles restraint setup

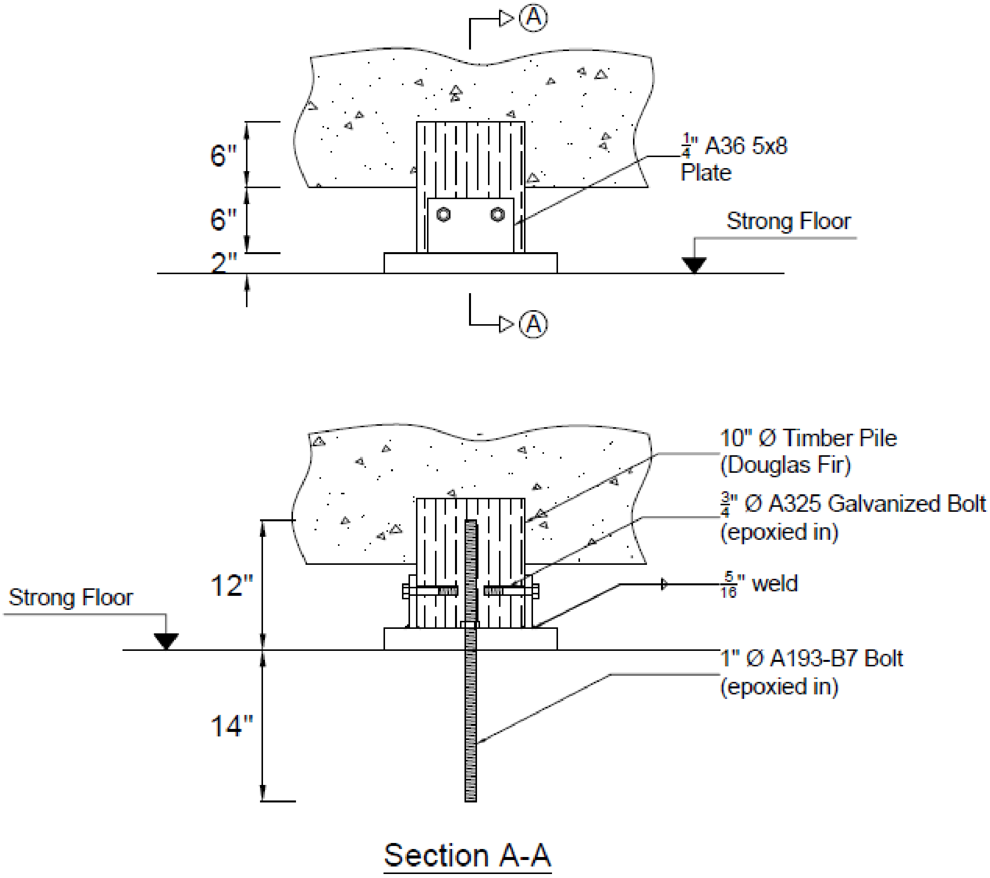

Figure 3.77: Specimen R-S-R-LTi-90-Pile: Timber pile connection details

3.5.2 Loading Protocol

The column specimens were subjected to displacement-controlled reversed cyclic loading. Two different loading orientations were considered for the test program. Two (2) specimens, (C-S-D and R-S-D-LTi-90), were loaded on the section diagonal, and all others were loaded parallel to the principal axes.

The loading history was derived according to the ACI 374.2R-13 (2013) (ACI Committee 374, 2013) protocol. Moment-curvature analysis was used to determine the reference yield displacement based on the nominal properties of concrete and reinforcing bars of the control specimens. There were two different loading profiles: (1) short column specimens, and (2) tall column specimens. Loading profile for each column height group was expressed as a factor and increment of the reference yield displacement. The reference yield displacement was calculated for control specimens from each column height group using moment-curvature analysis with characteristic compressive strength for concrete i.e. $f'_c = 3300$ psi (22.7 MPa) and nominal yield strength of the longitudinal steel i.e. $f_y = 60$ ksi (414 MPa) at a constant axial load of 150 kips (667 kN) for 8 ft. columns and 200 kips (900 kN) for 12 ft. columns, respectively. The loading profiles are shown in Figure 3.78 and Figure 3.79 for the short and tall column specimens, respectively.

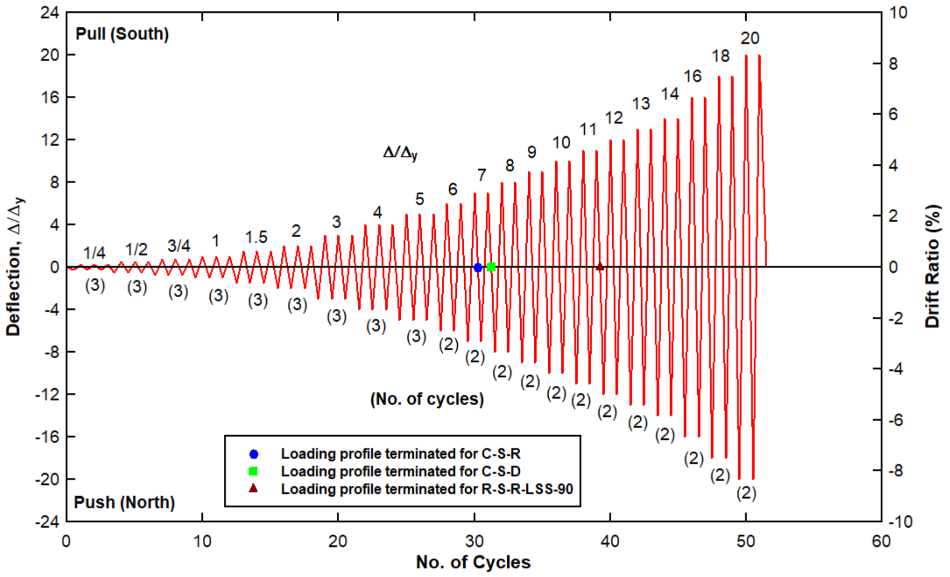

Figure 3.78: Standard loading profile for short columns

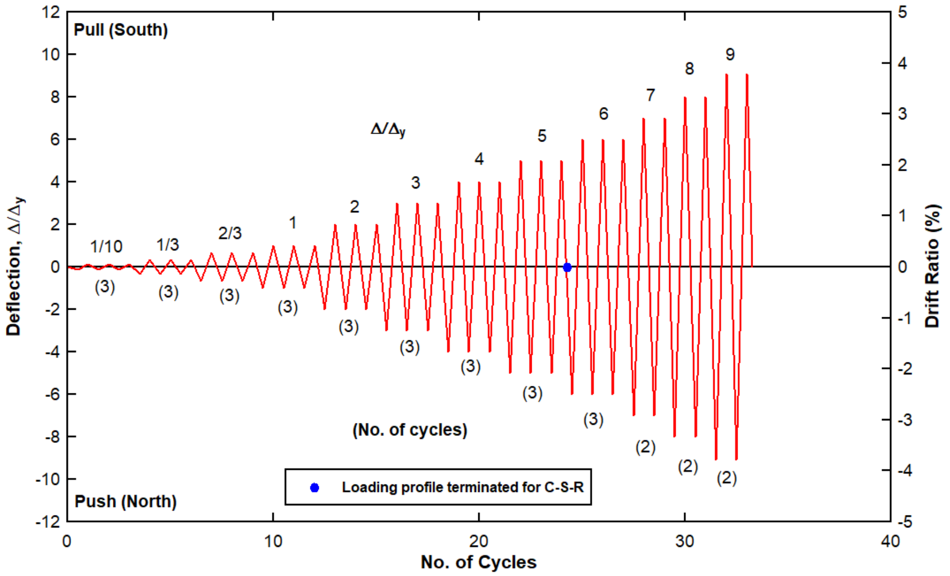

Figure 3.79: Standard loading profile for tall columns

To calculate the yield displacement from moment-curvature analysis, the curvature distribution when the reinforcing steel achieves yield at the top of the footing was distributed along the height of the column based on the linear moment gradient to the load point. The curvature distribution was integrated twice to get the yield drift at the top of the column assuming zero rotation at the top of the footing. The computed displacement at the top of the column was then used as the initial assumption for yield drift of column. The computed reference yield drift for short columns was 0.4 in (10.2 mm) and for tall columns was 1.3 in (33 mm).

It should be noted, however, that upon further moment-curvature analysis for each individual specimen using the actual material properties of concrete and steel, the yield drift value was calculated to be higher than the initially assumed values. Therefore, to calculate the displacement ductility of columns, the actual yield drift for each specimen was calculated based on their actual material properties was used (which was different for each specimen) as described in the results section.

The loading of the specimens continued until sufficient loss of capacity or the displacement capacity of the test setup was achieved. The data were collected, and are reported in Chapter 4.

4.0 EXPERIMENTAL RESULTS AND ANALYSIS

4.1 INTRODUCTION

In this chapter, experimental results from the reverse cyclic testing of 14 full-scale reinforced concrete square columns are presented. The experimental test results have been grouped based on the height of the column specimens. There were five (5) tall column specimens and nine (9) short column specimens. All columns with 12 ft. (3658 mm) height from the top of the footing to the point of application of lateral load will be termed "tall" columns and those with 8 ft. (2438 mm) height will be termed "short" columns in the remainder of the report.

The response of each specimen is presented and compared in terms of overall structural behavior, force-deformation response, strength degradation, displacement ductility, energy dissipation, viscous damping, and stiffness degradation. In addition, strain response of transverse and longitudinal reinforcement, and that of elements used in the retrofit system are also discussed.

4.2 GLOBAL STRUCTURAL BEHAVIOR

All column specimens were tested according to the pre-designated reverse cyclic loading protocol. Their performance was observed throughout the test and any significant changes in terms of crack progression and other visible damage were noted at each displacement step. The control specimens C-S-R, C-S-D and C-T-R were tested to failure and the rest of the specimens were tested until reaching the limits of the experimental setup while the specimens still exhibited some degree of lateral resistance. The performance and failure mode of all tested specimens were controlled by flexure in both column height groups although small shear deformations would tend to be more prominent in case of short columns. This can be attributed to relatively low ratio of longitudinal reinforcement (less than 1%) in both specimens and smaller M/V ratio in the case of the short columns.

Considering the observed strain profile of the starter and column longitudinal bars of all the specimens, first yielding was observed in the starter bars of all short columns with tied footing at 0.6 in (15 mm) (0.6%) drift level. The columns with the actual footing details performed elastically throughout the test; the overall non-linear behavior coming from the inelastic pseudo-soil (foam) in case of column with spread footing detail, and pile cap cracking and withdrawal of timber piles from the pile cap in case of column with timber pile details.

Overall structural response of the tested specimens based on the observation during the tests are discussed in detail in the following sections.

4.2.1 Observed Performance: Specimen C-S-R, Short square control column

Specimen C-S-R exhibited brittle behavior with no notable displacement ductility. The failure mechanism was characterized by a bond failure between the longitudinal bars of the column and the starter bars of the foundation. This failure mode was indicated by vertical cracking and progressive splitting at column corners over the lap-splice region and spalling of the concrete at the base of the column.

Horizontal flexural cracks started appearing at 0.2 in (5.08 mm) (0.2%) drift level in the North and South face close to the stirrups level. At 0.3 in (7.62 mm) (0.3%) drift level, 45° diagonal cracks started appearing on the East face that extended to the North and South faces. Flexural cracks appeared at this drift level that extended throughout the column width. Additional shear and flexural cracks appeared at 0.4 in (10.2 mm) (0.4%) drift level which was estimated to be the yield displacement. Some splitting cracks began to appear around the splice length at this drift level indicating the beginning of splice failure. Progressive splitting cracks appeared at 0.6 in (15.2 mm) (0.6%) drift level initiating concrete cover spalling that was an indication of the lap-splice bond failure and slippage of the bars as seen in Figure 4.1a. At 0.8 in (20.3 mm) (0.8%) drift level, additional flexural cracks on the North and South sides and additional splitting cracks appeared along the splice length at four corners. For drift levels greater than 0.8 in (20.3 mm) (0.8%), no new cracks appeared; only the existing cracks widened further causing spalling of the cover concrete at 1.2 in (30.5 mm) (1.2%) drift level exposing the column longitudinal and shear reinforcement and footing starter bars (Figure 4.1b). Concrete spalling allowed observation of the slip occurring between column bars relative to the starter bars (Figure 4.1c).

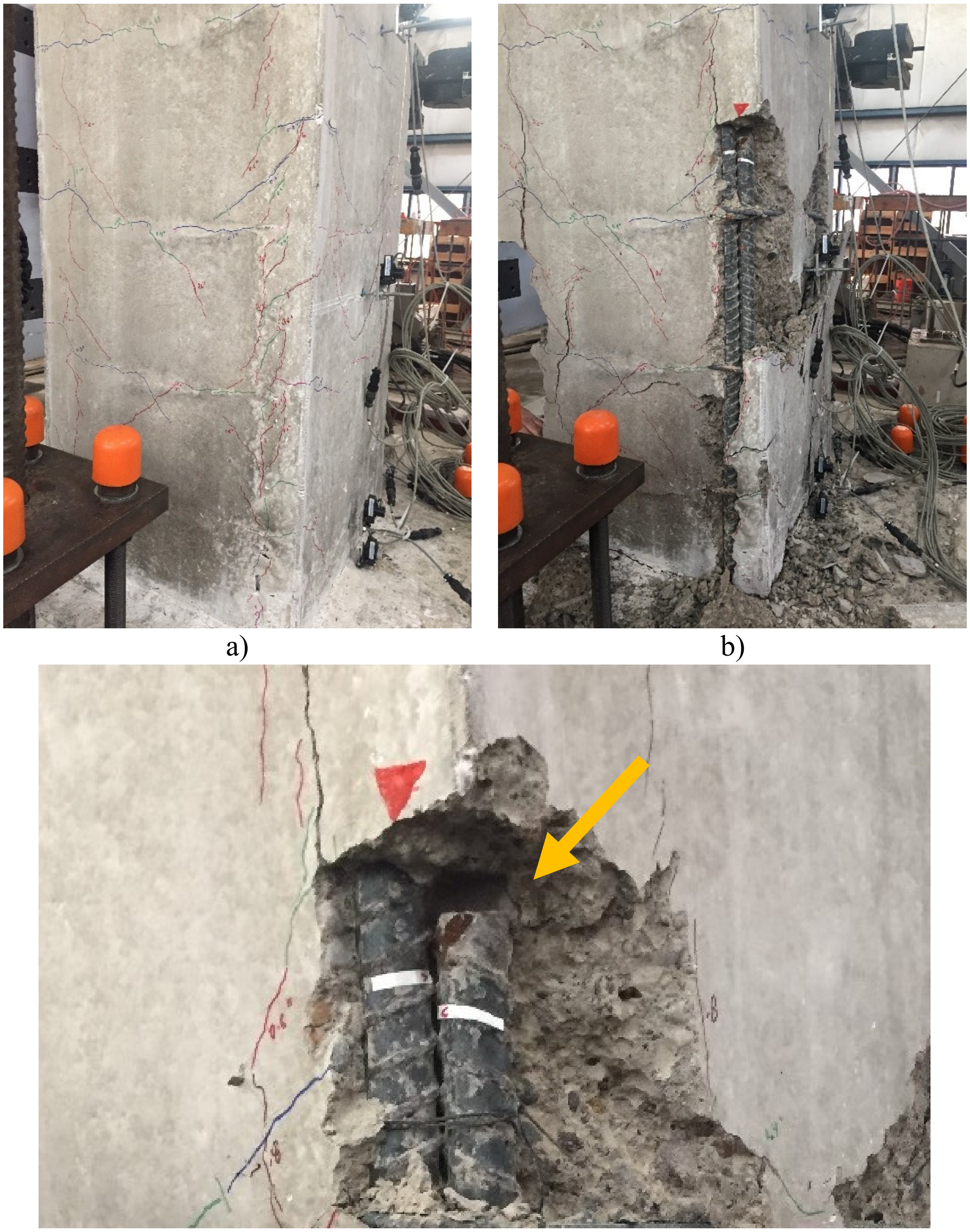

a)

b)

c)

Figure 4.1: Specimen C-S-R: Progression of visual distress: a) at 0.6 in (approx. 0.6%) drift level, b) at the end of testing (approx. 2.8% drift level), c) Slip between spliced bars (NE corner)

4.2.2 Observed Performance: Specimen C-S-D, Short diagonal control column

The behavior and failure pattern of specimen C-S-D was similar to specimen C-S-R despite the loading direction on the diagonal. The failure mechanism in this specimen was also characterized by the bond-slip failure of the spliced column longitudinal and footing starter bars. Because of the orientation of the lateral load application, crossing diagonal shear cracks were not clearly formed in any faces, although some 45° cracks extended from one face to the other face of the column on the East and West faces.

Apart from the shrinkage cracks on the column surfaces, cracks did not appear until 0.3 in (7.62 mm) (0.3%) drift level at which horizontal flexural cracks were seen along the transverse steel location. At 0.4 in (10.2 mm) (0.4%) drift level, additional flexural cracks developed on the North and South corner. It was not until 0.6 in (15.2 mm) (0.6%) drift level that vertical and diagonal splitting cracks began to appear along the splice region on the North and South corner indicating the initiation of splice failure. At this drift level, new horizontal flexural cracks and diagonal cracks were seen on the column faces. This was followed by more splitting cracks along the splice regions in the North and South corners and extended horizontal flexural cracks at 0.8 in (20.3 mm) (0.8%) drift level. At 1.2 in (30.5 mm) (1.2%) drift level, concrete cover started to spall off on the North corner and extensive vertical splitting crack appeared on the South corner as seen in Figure 4.2a. Some flexural cracks were also seen on the footing at this drift level. No new cracks appeared beyond this drift level; only the existing cracks widened causing the concrete cover to spall off as seen in Figure 4.2b. As in the case of the first control specimen, visible slip could be seen during the cyclic loading in higher drift loading cycles as seen in Figure 4.2c.

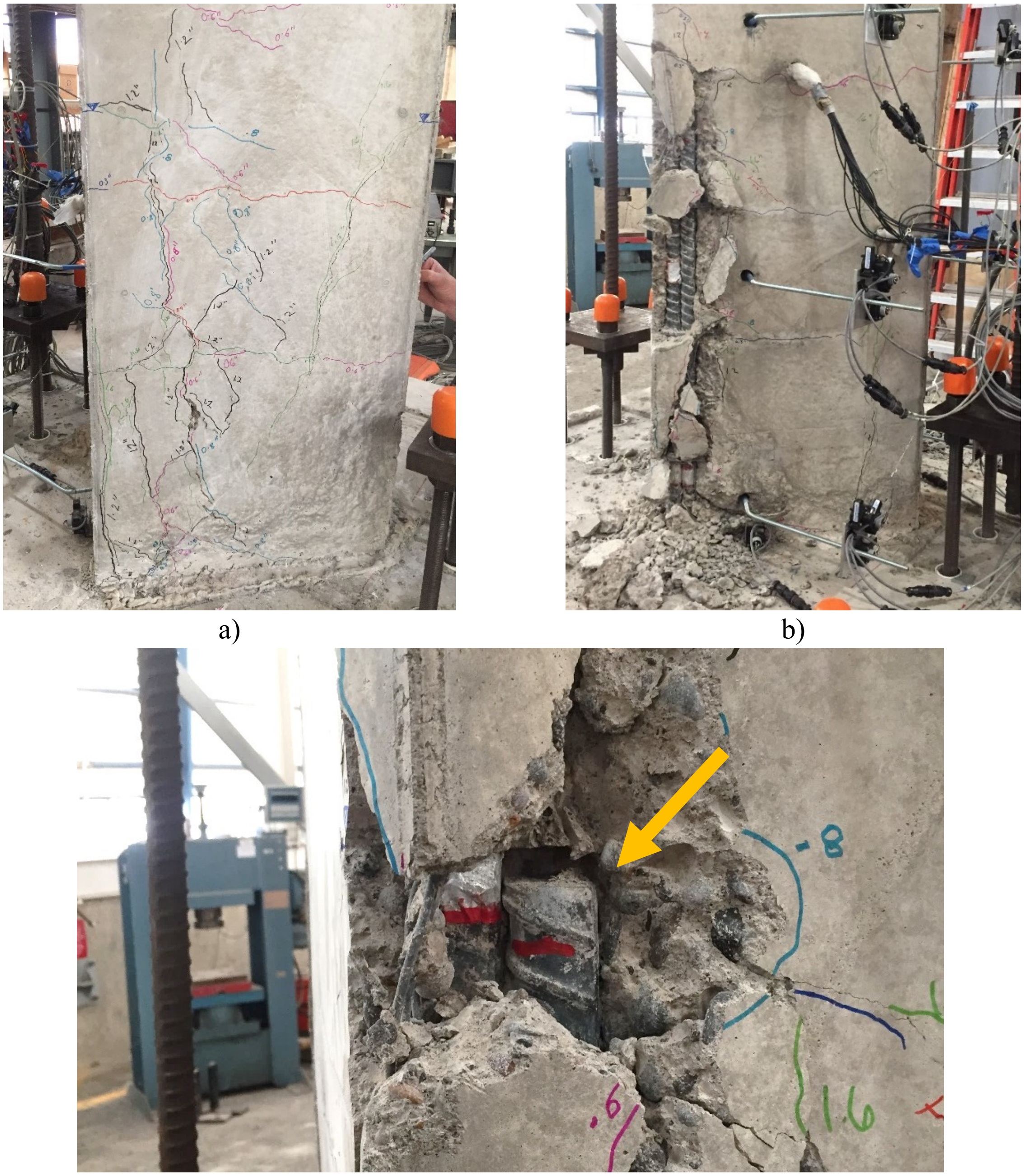

a)

b)

c)

Figure 4.2: Specimen C-S-D: Progression of visual distress: a) at 1.2 in (approx. 1.2%) drift level, b) at the end of testing (approx. 2.8% drift level), c) Slip between spliced bars (N corner)

4.2.3 Observed Performance: Specimen R-S-R-LTi-90, Short square column with typical TiAB retrofit

The behavior of this specimen is typical of the progression of cracking and visual distress for other retrofitted specimens with TiABs. Photographs are provided to detail the progression of visual distress, which was typical of the retrofitted specimens. For other specimens, only the visual condition at around the yield displacement and when the test was terminated are shown.

Shrinkage cracks were marked both on column and retrofit shell surface before applying any loads to the column specimen. The shrinkage cracks on the retrofit shell start opening up at 0.4 in (10.2 mm) (0.4%) drift level. Splitting diagonal cracks started appearing on the retrofit shell along the corners of the column at 0.8 in (20.3 mm) (0.8%) drift level. These cracks were concentrated near the top of the retrofit shell and were sparse in the region below. At 1.2 in (30.5 mm) (1.2%) drift level, diagonal cracks appeared on the East and West face of the column and horizontal flexural cracks were seen on the North and South faces above the retrofit shell. Shrinkage cracks started opening up and separation of retrofit shell from the footing surface was visible. At 1.6 in drift (40.6 mm) (1.6%) drift level, crossing diagonal cracks on the east and west faces of the column were observed and a 45° crack appeared on the retrofit shell on the east face. At 2.4 in drift (61 mm) (2.4%) drift level, additional splitting cracks appeared on the shell in the column corners and spalling of cover concrete started in the top region of the retrofit shell exposing TiAB spirals. Additional cracks were observed beyond this drift level and toe crushing of the retrofit shell was observed in the compression side. At 3.2 in (81.3 mm) (3.2%) drift level, there was significant spalling of concrete from the retrofit shell at the column corners in the region above the end of splice which further extended along the full height of the retrofit shell in the following cycles.

The load capacity dropped in the push cycle at 4.4 in (112 mm) (4.4%) drift level while on the pull cycle maintained its capacity. New diagonal cracks were observed forming on the column and spalling of the retrofit shell concrete followed beyond this drift level. Dilation near W TiAB hook with some concentrated cracks could be observed in the region at 4.8 in drift. Popping sound was heard at 5.6 in (142 mm) (5.6%) and 6.4 in (163 mm) (6.4%) drift levels followed by bulging of concrete around the hook region on the South side indicating hook pull-out from the column. The progression of observed distress is shown in Figure 4.3, and was typical of most retrofitted specimens. Visual distress to the concrete shell near the ligament hooks is shown in Figure 4.4 and indicated hook extraction from the concrete column.

While inspecting the specimen after removing the confinement shell, the base of the column was crushed exposing the column and starter bars on North and South faces as seen in Figure 4.5. Vertical splitting cracks along the lap-splice length were visible on SE, SW and NW corners. Angled cracks connecting the hooks were seen on all faces. A diagonal crack was also seen on the east face initiating from EN ligament.

The TiAB ligament hooks in the loading faces (North and South) were seen to have pulled out from the column holes with a separation from the epoxy. Hook pull-out in east and west faces were negligible. However, the straight ends of all the ligaments except EN ligament were still intact with no signs of extraction or cone pull-out from the footing. EN ligament end had pull-out out about ¼ in from the footing surface. Slight buckling was observed in the South face ligaments with concentrated buckling at the bottom of the SW ligament.

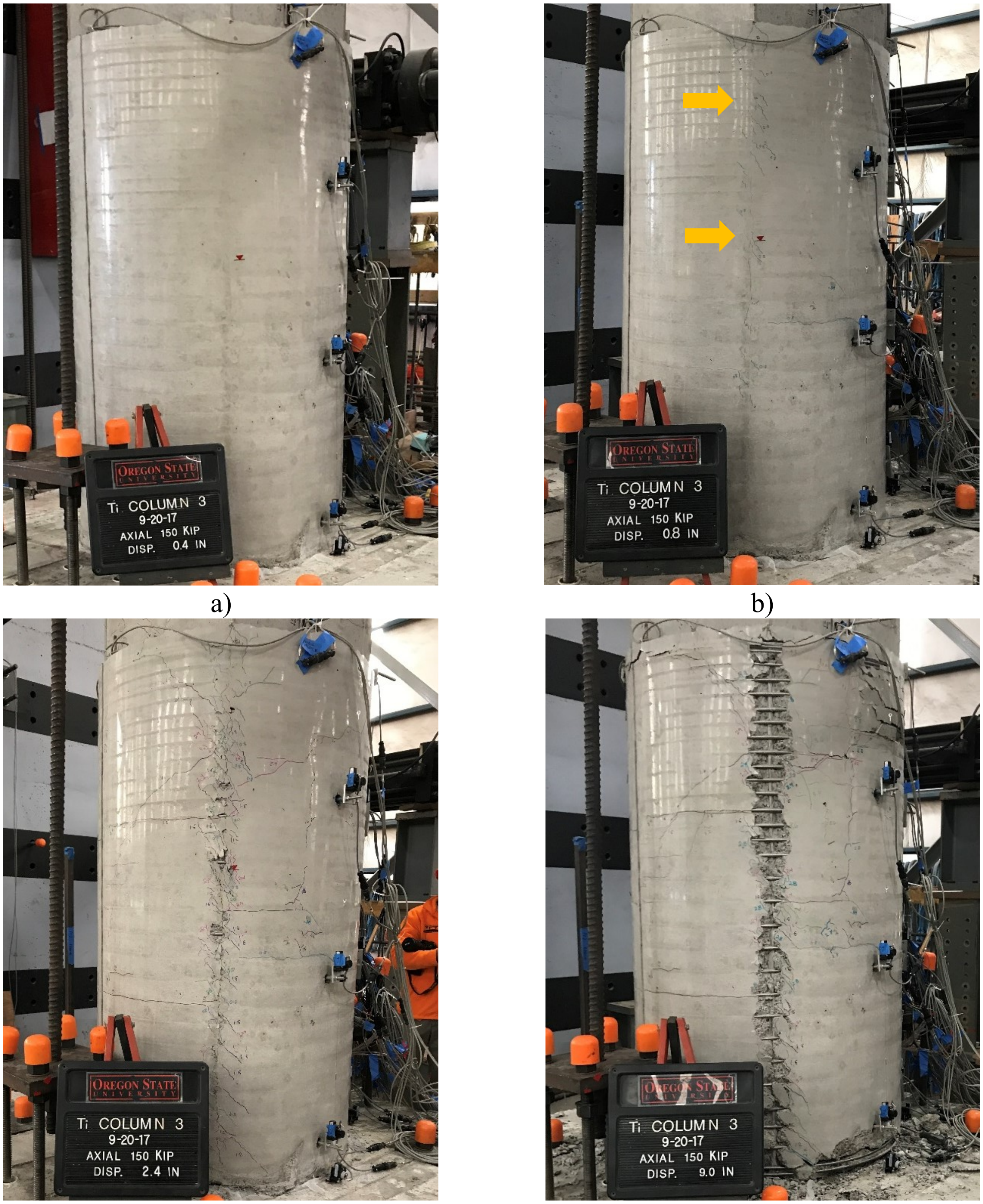

a) b)

c) d)

Figure 4.3: Specimen R-S-R-LTi-90: Progression of visual distress: a) at 0.4 in (approx. 0.4%) drift level, b) at 0.8 in (approx. 0.8%) drift level, c) at 2.4 in (approx. 2.4%) drift level, d) at the end of testing (approx. 9% drift level)

Figure 4.4: Specimen R-S-R-LTi-90: Distress in shell near the TiAB hooks (South face) at the end of testing

a) b)

Figure 4.5: Specimen R-S-R-LTi-90: Column after removal of shell: a) Overall, b) Close-up view

4.2.4 Observed Performance: Specimen R-S-D-LTi-90, Short diagonal column with typical TiAB retrofit

Shrinkage cracks began opening up over the TiAB spirals and at the corners of the column at 0.4 in (10.2 mm) (0.4%) drift level which further extended and widened up at 0.6 in (15.2 mm) (0.6%) drift level. Some new vertical cracks on the retrofit shell along the column corners starter appearing at 0.8 in (20.3 mm) (0.8%) drift level. First, 45° diagonal cracks appeared on North and South corners of the column above the retrofit shell. At 1.2 in (30.5 mm) (1.2%) drift level, splitting cracks started appearing on the shell near the vicinity of the end of spliced starter bar on east face and the existing cracks widened and extended further. At 1.6 in (40.6 mm) (1.6%) drift level, new diagonal cracks formed on North and South faces of column above the retrofit shell and additional splitting cracks appeared on top of the retrofit shell along column corners. Diagonal cracks formed on the retrofit shell on the west and east face at 2.0 in (50.8 mm) (2.0%) drift level and 2.4 in (61 mm) (2.4%) drift level respectively. Further splitting and spalling of concrete was observed and shear cracks on the column above the shell extended through the column width. Shell uplift was visible and toe crushing of shell started at 2.8 in (71.1 mm) (2.8%) drift level. Further spalling of concrete due to splitting exposed the spirals along east and west corners beyond these drift levels. Additional shear cracks formed on the column which extended up to 2 feet above the shell. The progression of specimen condition during the test are shown in Figure 4.6.

At 4.4 in (112 mm) (4.4%) drift level, concentrated damage with some dilation was seen around SE and NE TiAB hook regions indicating the initiation of hook extraction. Damage in terms of diagonal cracks, concrete spalling, toe crushing and dilation around the TiAB hooks was more pronounced beyond this drift level. At 6.4 in (163 mm) (6.4%) drift level, a loud popping sound was heard which could be due to one of the TiAB hooks pulling out.

Upon removal of retrofit shell, vertical splitting cracks were seen on the North and South corners along the lap-splice length as seen in Figure 4.7. Cracks connecting the ligament hooks could also be seen in all faces. The concrete was powdered in North and South corners due to crushing. The TiAB ligaments were straight with no buckling. However, all the ligament hooks had withdrawn from the concrete column with more significant pullout in the ligament hooks near North and South corner and less near the neutral axis.

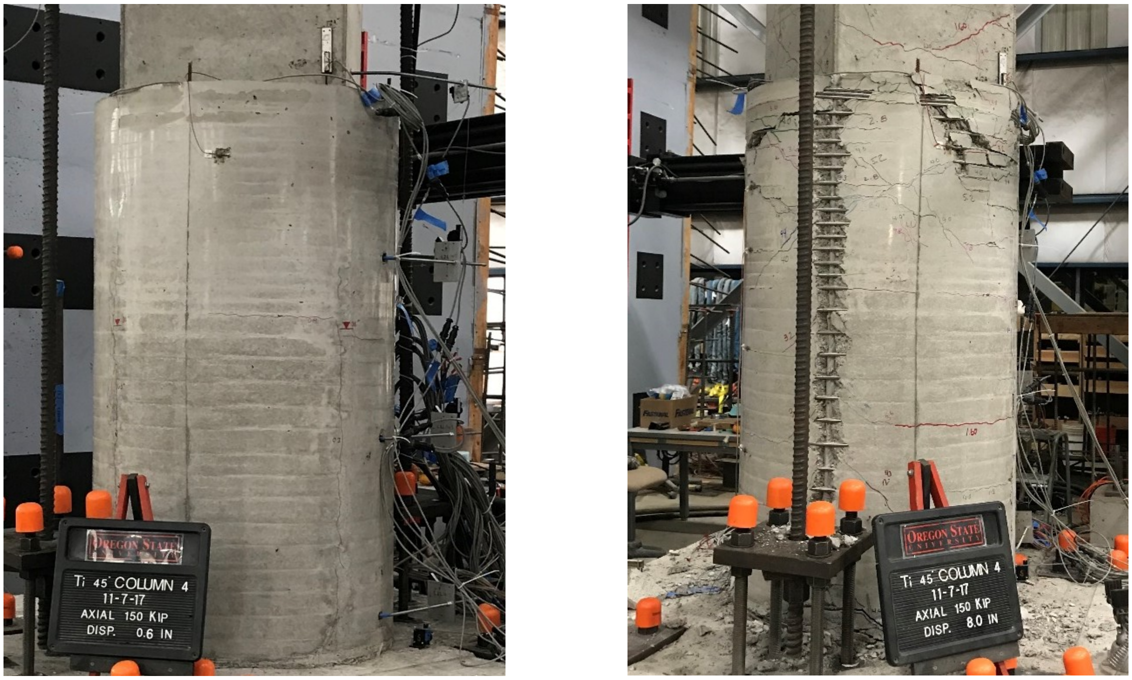

a) b)

Figure 4.6: Specimen R-S-D-LTi-90: Progression of visual distress: a) at 0.6 in (approx. 0.6%) drift level, b) at the end of testing (approx. 8% drift level)

a) b)

Figure 4.7: Specimen R-S-D-LTi-90: Column after removal of shell: a) Overall, b) Close-up view

4.2.5 Observed Performance: Specimen R-S-R-LTi-135, Short square column with standard retrofit having 135-degree TiAB hook

The main objective of introducing the TiAB hook angle to the test matrix was to study the influence of hook angle in hook extraction from the column as was observed in some specimens with 90° hooks. The rationale behind it was the anchored hook when placed in 90° angle would align with a potential plane weakened by horizontal flexural cracks which could otherwise be prevented if the hook is oriented in a different angle. The 135° hook was successful in somewhat suppressing the hook extraction as indicated by reduced cracking and dilation around the hook regions. Because of the way the holes were cored for 135° hooks, about 3 in (76.2 mm) of concrete had to be chipped off from just above the region of holes drilled. This resulted in the increase in the retrofit shell height by about 3 in (76.2 mm). This increased the stiffness of the specimen by about 45% compared to the specimens with 90° TiAB ligaments hooks and tied footing. The stiffness was computed directly from the force-deformation response as tangent and secant stiffness as shown in section 4.12.

One of the characteristic observations in this test was the formation of diagonal cracks crossing several spirals on the East and West face of the retrofit shell starting at 1.6 in (40.6 mm) (1.6%) drift level. The progression of visual distress is shown in Figure 4.8.

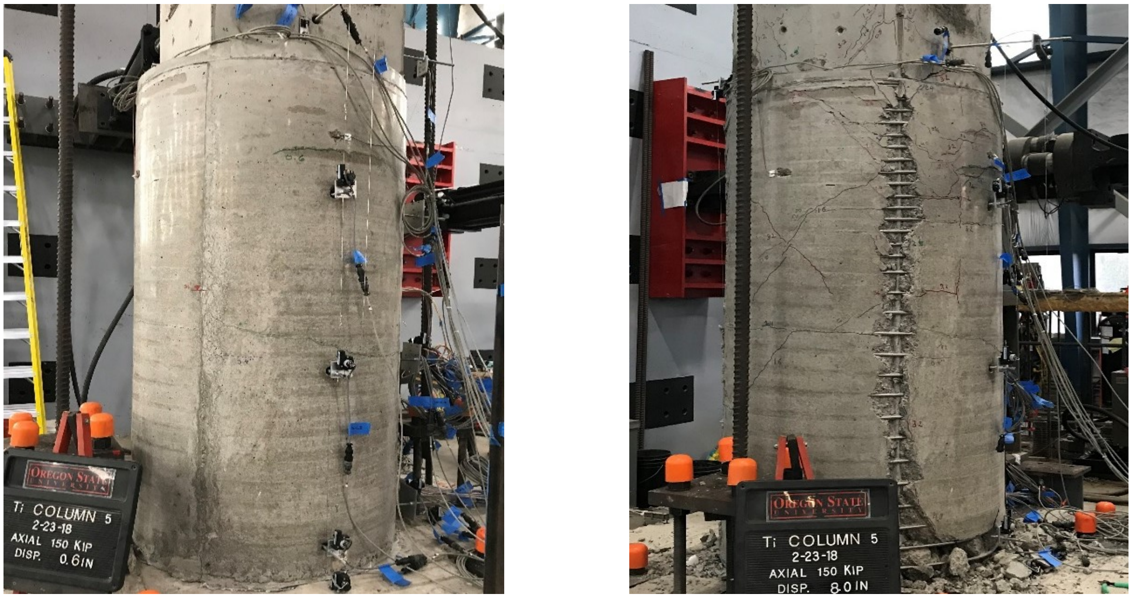

a) b)

Figure 4.8: Specimen R-S-R-LTi-135: Progression of visual distress: a) at 0.6 in (approx. 0.6%) drift level, b) at the end of testing (approx. 8% drift level)

Sliding of the column was observed along the bottom plane of the column interface with the top of footing after the second cycle of 4.0 in (102 mm) (4.0%) drift level. The column started translating South across the column-footing plane and did not center in the consecutive cycles. This caused the bottom spirals to open up exposing the ligaments at the base. The bottom of the retrofit shell started to break up and failed to provide proper confinement at the base of the column as seen in Figure 4.9. This initiated buckling of TiAB ligaments that eventually led to fracture at the two of the ligaments. The fracture of the TiAB ligaments produced incrementally observed sudden drops in load capacity. Only moderate damage to the shell was observed at hook anchorage locations as seen in Figure 4.10.

Figure 4.9: Specimen R-S-R-LTi-135: Buckled and fractured NE TiAB ligament at the bottom of the retrofit shell due to column sliding

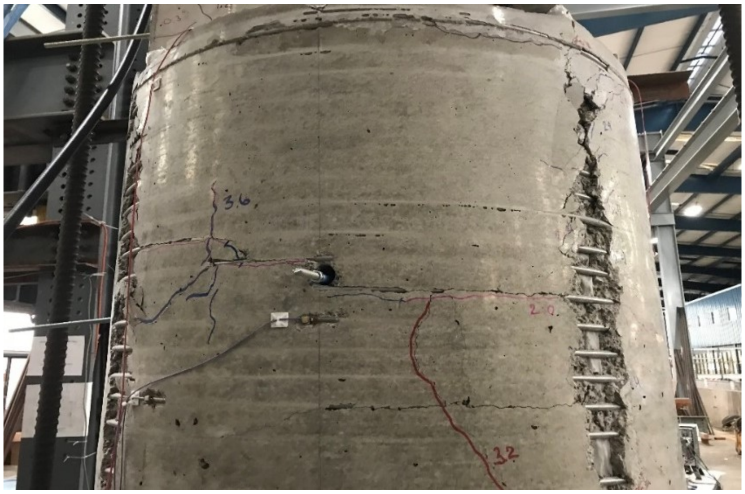

Figure 4.10: Specimen R-S-R-LTi-135: Reduced visual distress near the TiAB hooks (South face) at the end of testing

After removal of the shell, the column exhibited vertical cracks along the splice length could be seen on all column faces along with some diagonal cracks on East and West faces originating at hook regions and some hairline flexural cracks on North and South faces. Angled cracks connecting the hooks could also be seen on all column faces. Concrete crushed at the base exposing permanently bent starter bars due to sliding of the column at the footing interface were also observed.

Due to the sliding behavior, the North and South ligaments exhibited severe local bending, as seen in Figure 4.11 and caused the NE and SE ligaments to fracture at the base of the column. Slight bending was seen along the length of WN and ES ligaments as well. The ligament hooks were intact with negligible pullout. A comparison of the hook extraction from the column for 90 and 135 degree hooks is shown in Figure 4.12. The 90 degree hooks exhibited more distortion at the column face than the 135 degree hooks.

North face South face

Figure 4.11: Specimen R-S-R-LTi-135: TiAB ligaments after removal of shell

a) b)

Figure 4.12: TiAB hooks at the end of testing: a) Specimen R-S-R-LTi-90, b) Specimen R-S-R-LTi-135

4.2.6 Observed Performance: Specimen R-S-R-0, Short square column retrofitted with TiAB spiral alone

Shrinkage cracks started opening up at 0.2 in (5.1 mm) (0.2%) drift level. Cracking was heard at 0.6 in (15.2 mm) (0.6%) drift level but no new cracks were visible until 0.8 in (20.3 mm) (0.8%) drift level. First splitting cracks on the retrofit shell along the column corners started appearing at 0.8 in (20.3 mm) (0.8%) drift level. Some horizontal flexural cracks also appeared on the column above the retrofit shell. At 1.2 in (30.5 mm) (1.2%) drift level, horizontal cracks along the TiAB spirals started appearing on the North and South sides at different levels. Some splitting cracks were also seen along the column corners mostly on the top half of the retrofit shell. At 1.6 in (40.6 mm) (1.6%) drift level, new splitting cracks started appearing along the lap-splice starting at the end of the spliced starter bar end. Visible gaps were seen on the North and South toe of the shell during cyclic motion indicating the shell uplift relative to the column. The progression of visual distress is shown in Figure 4.13.

a) b)

Figure 4.13: Specimen R-S-R-0: Progression of visual distress: a) at 1.2 in (approx. 1.2%) drift level, b) at the end of testing (approx. 8% drift level)

At 2.0 in (50.8 mm) (2.0%) drift level, diagonal cracks appeared on the column above the retrofit shell that further extended at 2.4 in (61 mm) (2.4%) drift level. Splitting and spalling of shell concrete along the corners of the column became more progressive beyond this drift level. Toe crushing was also observed on the North and South side that became more pronounced in bigger drift levels. At 3.6 in (91.4 mm) (3.6%) drift level, splitting and slipping sounds were heard which was followed by the drop in the load capacity in South cycles. Progressive damage was seen at the bottom of the column with concrete crushing that exposed the spirals. At 6.4 in (163 mm) (6.4%) drift level, it was observed that the shell had shifted about 1.5 in (38.1 mm). South from its original position that kept further increasing indicating permanent sliding movement of the column relative to the footing at the base, as seen in Figure 4.14a.

Upon further inspection after taking off the confinement shell, it was clear that the concrete at the bottom of the column was pulverized and the starter bars were all been bent along the same plane as the column permanently shifted about 2 in (50.8 mm) to the South as seen in Figure 4.14b. Some hairline flexural cracks could also be seen on the North and South faces. Splice failure was evident from the cracks along the splice length of the columns in all four corners. The condition of the specimen after removal of the shell is seen in Figure 4.15.

a) b)

Figure 4.14: Specimen R-S-R-0: a) String Pot showing the sliding of the column at column-footing interface (string highlighted in yellow), b) NW starter bar bent towards South after testing

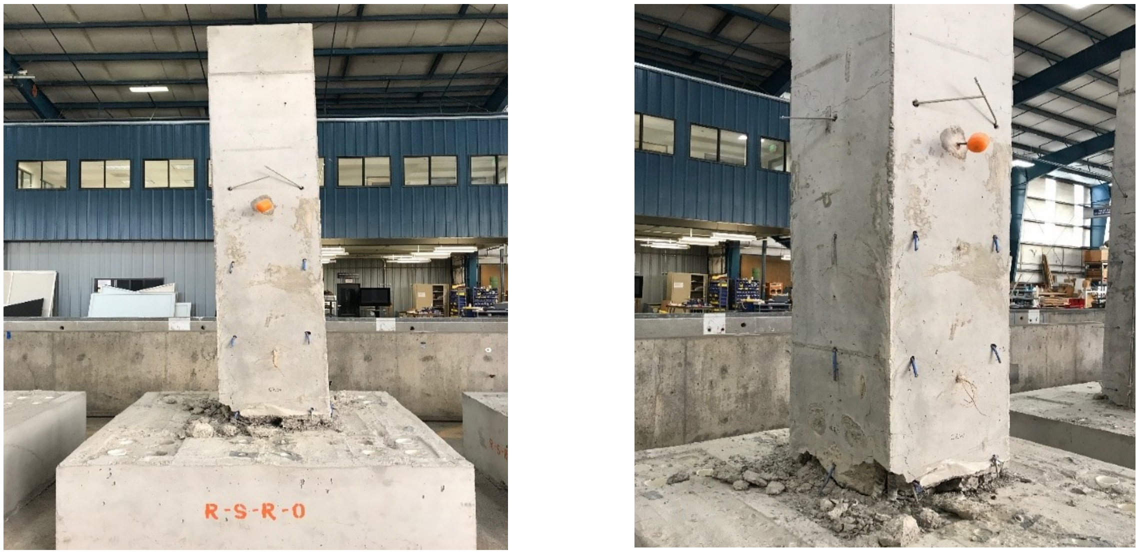

a) b)

Figure 4.15: Specimen R-S-R-0: Column after removal of shell: a) Overall, b) Close-up view

It is worth noting that the column behavior can range from the degrading pull cycle behavior to very stable push cycle behavior. This when compared to the column retrofitted with both TiAB ligaments and spiral clearly shows the importance of the ligaments to obtain stable and symmetrical hysteretic response with self-centering behavior.

4.2.7 Observed Performance: Specimen R-S-R-LSS-90, Short square column retrofitted with stainless steel (SS) ligaments and TiAB spiral

The progression of visual distress is shown in Figure 4.16. The first cracking sound was heard at 0.4 in (10.2 mm) (0.4%) drift level but the first cracks appeared in the form of splitting cracks around the corner at 0.6 in (15.2 mm) (0.6%) drift level. Some diagonal and horizontal cracks were also seen on the column corners right above the shell that initiated from locations where the SS ligaments were anchored to the column. A diagonal crack on the SE corner of the column above the retrofit shell opened up at 1.6 in (40.6 mm) (1.6%) drift level. Additional splitting cracks on the shell in the region of column corners and 45° cracks on the shell started appearing in the subsequent cycles. The shrinkage cracks were also seen to have opened up noticeably. Some flexural cracks started appearing along the centerline of the footing that seemed to start from the column and ran along the footing faces. At 3.2 in (81.3 mm) (3.2%) drift level, a loud pop sound was heard when the column was being pushed to the North. Damage was observed on the South face of the column above the retrofit shell and grew more prominent with formation of new cracks and old cracks opening up at subsequent cycles as seen in Figure 4.17a. At 3.6 in (91.4 mm) (3.6%) drift level, the vertical crack on the SW corner of the column went all the way up to the actuator plate. A large piece of cover concrete from the South face fell off at the end of 4.4 in (112 mm) (4.4%) drift level and for safety reasons, the column was then pulled to South in single half cycles in the rest of the drift levels from the loading profile. This document only includes the behavior of specimen R-S-R-LSS-90 up until 4.4 in (112 mm) (4.4%) drift level where the column followed the standard loading profile.

a) b)

Figure 4.16: Specimen R-S-R-LSS-90: Progression of visual distress*:* a) at 0.6 in (approx. 0.6%) drift level, b) at 4.4 in drift (approx. 4.4%) drift level

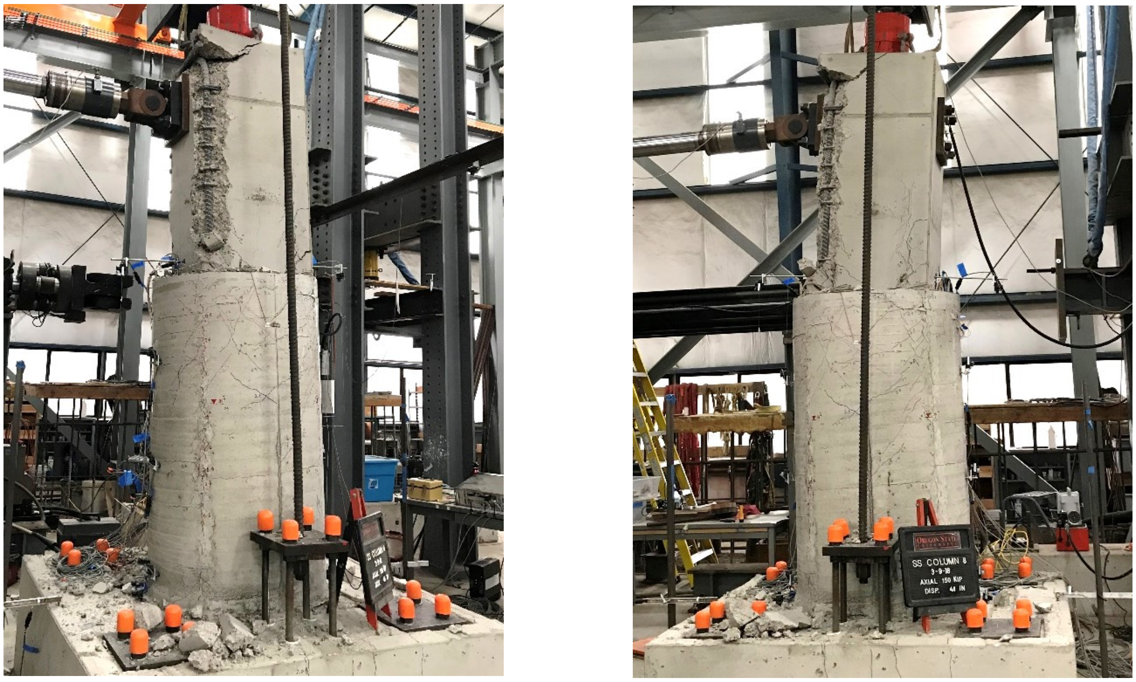

a) b)

Figure 4.17: Specimen R-S-R-LSS-90: Critical observations at 4.4 in (approx. 4.4%) drift level: a) Spalling of cover concrete on South side above the retrofit shell, b) Column cranking about the top of the retrofit shell

The plastic hinge formed just above the top of the retrofit shell and the column started rotating about the top of the retrofit shell with negligible motions below as seen in Figure 4.17b. After removing the retrofit shell after testing, negligible damage was seen in the column below the region where the SS ligaments hooks were anchored to the column faces as seen in Figure 4.18a. Fine vertical cracking along the splice region were seen along with some diagonal shear cracks in east and west faces. The ligaments were still intact with slight extraction in the hook region. Cone-pull-out was visible on the footing at the base of North ligaments. The damage above the shell was more dramatic with wide cracks connecting the hooked region of all ligaments creating a weak failure plane at the level of the hooks of tallest ligaments about which the column was rotating as seen in Figure 4.18b. Severe spalling of concrete above the retrofit shell exposed the longitudinal and transverse reinforcing bars of the column. The observed failure mode and hinge shifting were not intended or desirable.

Figure 4.18: Specimen R-S-R-LSS-90: Column after removal of shell: a) Overall, b) Close-up view

4.2.8 Observed Performance: Specimen R-S-R-LTi-90-Spread, short square standard TiAB retrofit with spread footing

The column and footing both remained elastic throughout the test. The almost elasto-plastic load-deformation behavior can be attributed to the rocking motion of the footing and the damage in the foam that simulated the soil underneath. The foam had permanent deformation with a convex curve profile on top as seen in Figure 4.19. The rocking motion of the footing damaged the thin concrete panels placed between the foam to prevent localized tearing of the foam and provide a transition of the axial load into the foam. Minor hairline cracks were seen in the footing after the test. The cracks were all connected and ran through the middle of each face of the footing dividing the footing into four quadrants as seen in Figure 4.20 and Figure 4.21. A photograph of the specimen at the completion of the test is shown in Figure 4.22. The strain gages on the footing rebar were damaged during placement of the concrete so it was not possible to tell if they yielded or not. Although a little separation of the retrofit shell from the footing top was noticed during testing, no new cracks were seen either on the retrofit shell or the column above the shell.

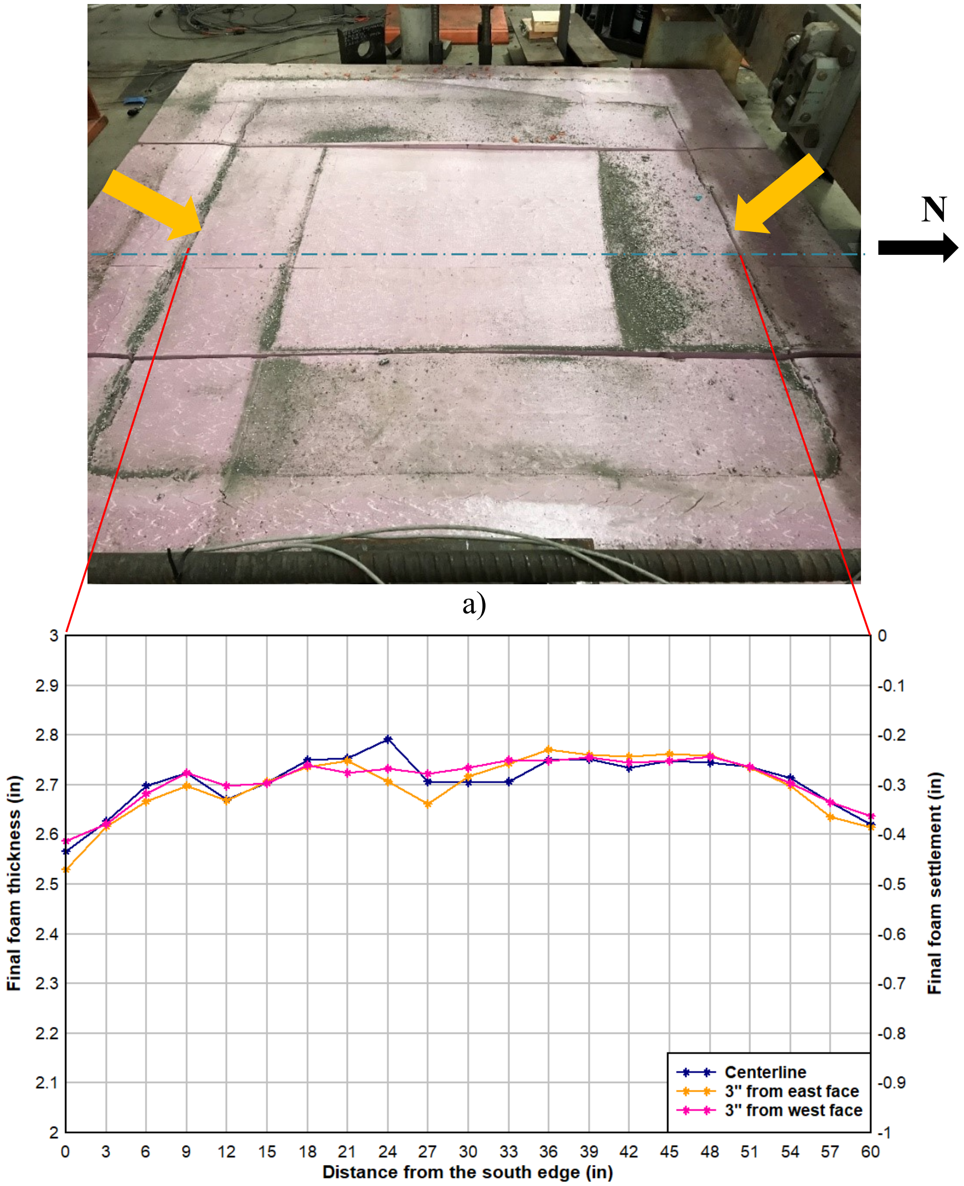

a)

b)

Figure 4.19: Specimen R-S-R-LTi-90-Spread: a) visual damage to top layer of 3 in (76.2 mm) foam "soil" after removal of specimen b) foam profile at the end of testing

Figure 4.20: Specimen R-S-R-LTi-90-Spread: Cracking on spread footing

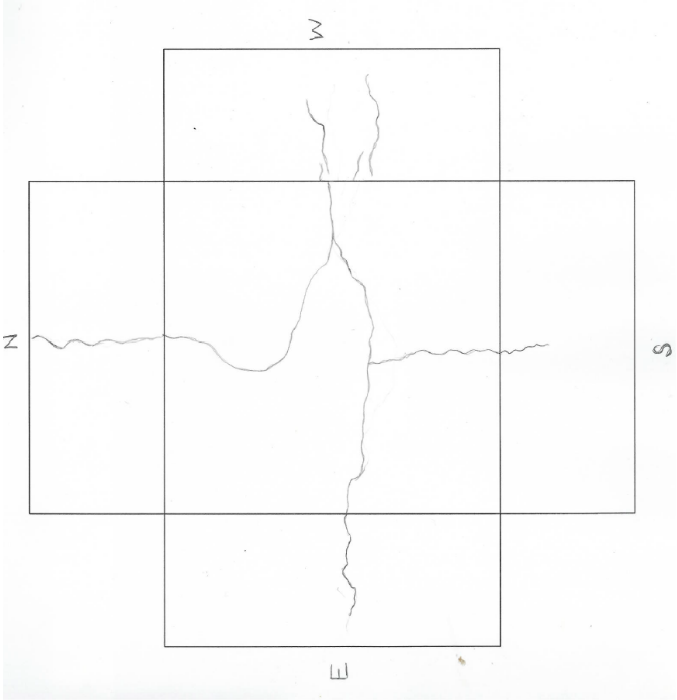

Figure 4.21: Specimen R-S-R-LTi-90-Spread: Cracking layout on spread footing (oriented to match Figure 4.20)


a) b)

Figure 4.22: Specimen R-S-R-LTi-90-Spread: a) Column at the end of testing (at approx. 2.1% total drift) cracks observed in footing, b) limited cracking in column and retrofit

After isolating the contribution of footing rigid body motion, the deformation response of the column was observed to be elastic. The major contribution to the overall deformation was deformation of the simulated soil and highlights the importance of considering soil-structure interactions for seismic retrofits. Again, it is important to note that without the retrofit, the column would likely have failed considering the strength provided by the simulated soil was above that of the unretrofitted column.

4.2.9 Observed Performance: Specimen R-S-R-LTi-90-Pile, Short square standard retrofit with timber pile foundation

The column remained elastic throughout the test with no significant cracks observed in the column. The elastic behavior is supported by the measured strains in the starter bars and column longitudinal bars (Appendix C). Damage was observed in the concrete pile cap as seen in Figure 4.23. Some of the cracks in the pile cap opened up substantially to about ¾ in (19 mm) width. Spalling of the cover concrete around the timber piles was observed which was followed by cracks initiating through the pile cap. Damage around the timber piles due to extraction of the pile from the cap are shown in Figure 4.24and Figure 4.25. The inelastic behavior seen after isolating the footing rigid body motion was sourced to the damage in the pile cap rather than the retrofitted column. Wood splintering noise was heard at the 0.6 in (15.2 mm) (0.6%) drift level. Vertical cracks were seen on East and West faces of the pile cap. Cone pull-out was noticed in the region of NE and SE timber piles with cover concrete spalling off from around these piles. Vertical and diagonal cracks started in the pile cap from the pile locations and these cracks connected on top of the pile cap. These cracks opened up in the subsequent cycles reaching about 3/16 in (4.8 mm) wide at 2.8 in (71.1 mm) (2.8%) drift level. The cracks observed on the footing of the specimen are shown in Figure 4.25 and Figure 4.26. Here also, it is important to note that without the retrofit, the column would likely have failed considering the strength provided by the pile foundation was above that of the unretrofitted column.

Figure 4.23: Specimen R-S-R-LTi-90-Pile: Column at the end of testing (at approx. 4% total drift level), limited cracking in column, large cracks in footing

Figure 4.24: Specimen R-S-R-LTi-90-Pile: Damage around piles on pile footing

Figure 4.25: Specimen R-S-R-LTi-90-Pile: Cracking on pile cap

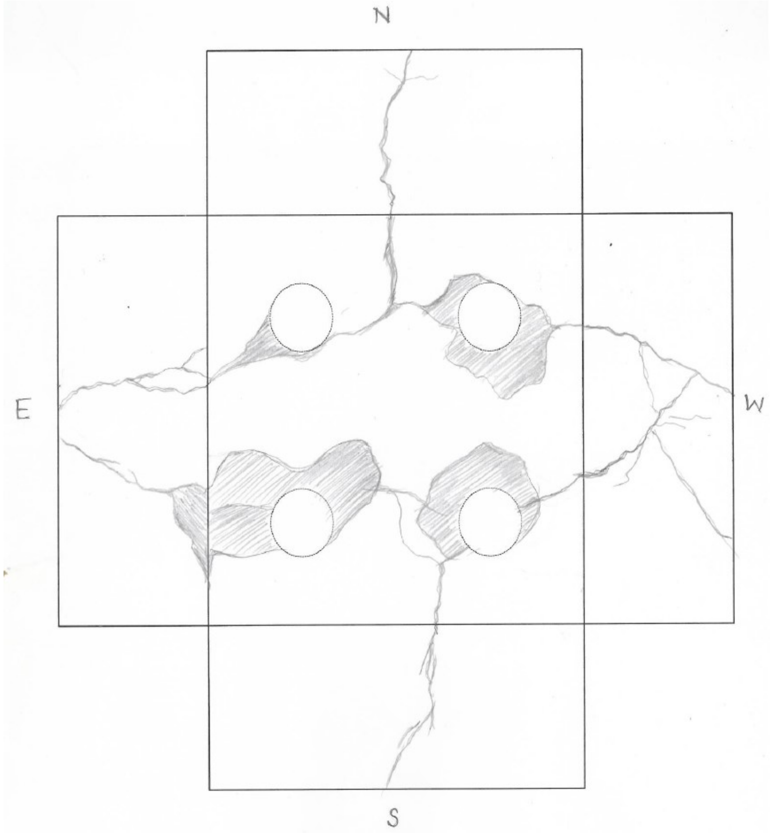

Figure 4.26: Specimen R-S-R-LTi-90-Pile: Cracking and spalling observed on pile cap

4.2.10 Observed Performance: Specimen C-T-R, Tall square control column

The performance of specimen C-T-R was poor. Failure was observed at a low drift displacement of 1.30 in (33 mm), corresponding to a drift limit of 0.9%. Axial-carrying capacity was maintained throughout the drift displacement cycles. Flexural strength decreased by over 50% by the displacement cycle at 2.5% drift. Failure of the lap splice and inability to resist flexural tension was the mode of failure. Strength degradation occurred quickly after lap splice failure. Flexural cracking was initially observed at the base of the column and extended to a height of approximately one-half of the overall column height. This initiated at a drift displacement of 1.30 in (33 mm) (0.9%). Splitting cracks along the lap splice lengths appeared followed by diagonal cracking within the lap zone. Once splitting cracks extended along the entire lap splice length, spalling of the cover concrete was observed, exposing the lapped bars, as shown in Figure 4.27.

Figure 4.27: Condition of specimen C-T-R at end of test (maximum 5.4% drift)

4.2.11 Observed Performance: Specimen R-T-R-LTi-90, Tall square standard retrofitted column

Specimen R-T-R-LTi-90 exhibited similar behavior to other retrofitted specimens with flexural cracking, diagonal cracking of the column above the retrofit, and corner cracking of the shell. The peak lateral strength was approximately 54 kips (240 kN) and the specimen maintained strength up to 6.5 in (165 mm) (4.5%) drift level. Failure of the lap splice reduced the strength to a lateral strength level of approximately 28 kips (125 kN). During testing, audible noise was heard from the vertical TiABs caused by localized damage to the anchorage locations in the column and footing. These tended to occur when the specimens were moving through their neutral point (zero displacement) where the vertical TiABs experienced stress-reversals. Localized damage of the TiAB spiral reinforced concrete shell included stable withdrawal of the hooked ends of the TiAB ligaments from the column face. The condition of the specimen at the end of the test is shown in Figure 4.28.

Figure 4.28: Condition of specimen R-T-R-LTi-90: corner spalling of concrete shell and cracking at TiAB ligament hook locations at end of test (maximum 8.2% drift)

The specimen sustained a lateral displacement of 11.8 in (300 mm), corresponding to a drift ratio of 8.2%. The test was terminated because the stroke capacity of the actuator was achieved and additional drift could not be imposed.

4.2.12 Observed Performance: Specimen RS-T-R-LTi-90, Tall square short retrofit with foam column

Foam insulation, 1 in thick, was added in between the shell and top of footing to prevent the segment of concrete shell from bearing against the footing. The purpose of the foam was to reduce cracking of the shell at the column corners. Based on the observed response, corner cracking of the shell was delayed but was not prevented and the cracked condition at the end of the test was similar to other specimens without the foam.

Specimen RS-T-R-LTi-90 exhibited similar performance to specimen R-T-R-LTi-90 as seen in Figure 4.29. This indicated that the TiAB spiral reinforced shell length of $1.67l_s$ and $1.5l_s$ did not seem to greatly affect their performance. The peak lateral strengths were similar. Failure of the lap splice was observed at approximately 3.89 in (98.8 mm) (2.7%) drift level. Afterwards the specimen slowly lost strength. Specimen RS-T-R-LTi-90 showed strength reduction earlier than R-T-R-LTi-90. Localized damage included stable withdrawal of the hooked end from the column face, as shown by cracking of the concrete shell in Figure 4.30. Concrete pullout cones were observed forming at the TiAB anchorage to the footing, as shown in Figure 4.31. The TiABs for this specimen were bonded along the entire length in the footing which resulted in the formation of the pullout cones. To prevent this, subsequent specimens were constructed with a debonded length at the footing surface. The specimens achieved a displacement of 11.8 in (300 mm), corresponding to a drift ratio of 8.2%. The condition of the specimen at the end of the test is shown in Figure 4.32. Ultimate lateral strength was approximately 56% of the peak strength. The test was terminated because the stroke capacity of the actuator was achieved and additional drift could not be imposed.

Figure 4.29: Specimen RS-T-R-LTi-90: Flexural and diagonal cracking above shell

Figure 4.30: Specimen RS-T-R-LTi-90: Foam insulation and opening of shell at top of footing

Figure 4.31: Specimen RS-T-R-LTi-90: Concrete cone pulled at top of the footing (shell removed after testing)

Figure 4.32: Condition of specimen RS-T-R-LTi-90 at peak drift (8.2% drift)

4.2.13 Observed Performance: Specimen RN-T-R-LTi-90, Tall square standard retrofit with cut starter steel rebar and foam

The progression of cracking and overall behavior of specimen RN-T-R-LTi-90 was similar to the other tall retrofitted specimen tests. However, this specimen did not exhibit the same rate of strength reduction after yield. This is because no failure of the steel lap splice occurs, having been removed before testing. Removal of the lap splice bypasses the strength degradation that occurred as the lap splice degraded in the comparable tests. Fracture of the first TiAB occurred at the second cycle at a drift ratio of 5.8%. The column performed in a ductile manner, yielding until the TiABs on the South face of the column fractured during the 7.8% drift cycle. Fracture of the second TiAB occurred at a drift ratio of 7.0%, just past the prior maximum reached drift level of 6.9%. The ultimate failure mode was fracture of the TiABs. It occurred within the threaded section of the TiABs and in the region of the foam board. Out-of-plane, local buckling of the SE vertical TiAB occurred during the previous 6.9% displacement cycle was observed within the threaded section of the TiAB ligament above the footing.

The combined effects of the foam insulation, which does not brace the TiAB ligament, and fairly wide pitch spacing of the TiAB spiral reinforcement may have contributed to local buckling of the TiAB and subsequent fracture. The bottom end of the spiral was terminated 2-3/4 in (70 mm) above the footing whereas the bottom of the spiral was drilled into the column within 1 in (25.4 mm) or less from the top of the footing for the other tall column specimens. There was also increased flexural demand on the vertical TiABs in this specimen because the steel reinforcement was removed, eliminating the alternative load paths.

After testing, the TiAB reinforced concrete shell was removed for inspection of the internal damage that was not visible during testing. Local, in-plane buckling occurred to the SW TiAB and global, in-plane buckling occurred to the WS vertical TiAB, as shown in Figure 4.33. Concrete pullout cones were also observed and resulted in pieces of the footing concrete to be able to be removed after formation as illustrated in Figure 4.34. The condition of the specimen at the end of the test is shown in Figure 4.35.

Figure 4.33: RN-T-R-LTi-90: Buckled deformation to WS TiAB ligament (shell removed after testing)

Figure 4.34: Specimen RN-T-R-LTi-90: Fractured SE and SW TiABs ligaments and damage to top of footing (shell removed after testing)

Figure 4.35: Condition of specimen RN-T-R-LTi-90 at end of test (maximum 7.8% drift)

4.2.14 Observed Performance: Specimen R-T-R-0, Tall square retrofitted with TiAB spiral alone

The evolution of the visual condition of the specimen is shown in Figure 4.36. The first cracks were observed at 1.3 in (33.0 mm) (0.9%) drift level. Vertical hairline cracks were seen on the top of retrofit shell along the corner of the column and horizontal flexural cracks were seen on North and South faces above the retrofit shell. At 2.59 in (65.8 mm) (1.8%) drift level, horizontal cracks appeared on the retrofit shell along the spirals. There was visible uplift of retrofit shell and formation of splitting cracks along the splice at 3.89 in (98.8 mm) (2.7%) drift level. Progressive diagonal splitting cracks on the column corners appeared on the following drift cycles. Pieces of concrete started spalling from the end of splices at the end of last cycle of 5.18 in (132 mm) (3.6%) drift level. Toe crushing was seen at the bottom of the retrofit shell in the following drift cycles.

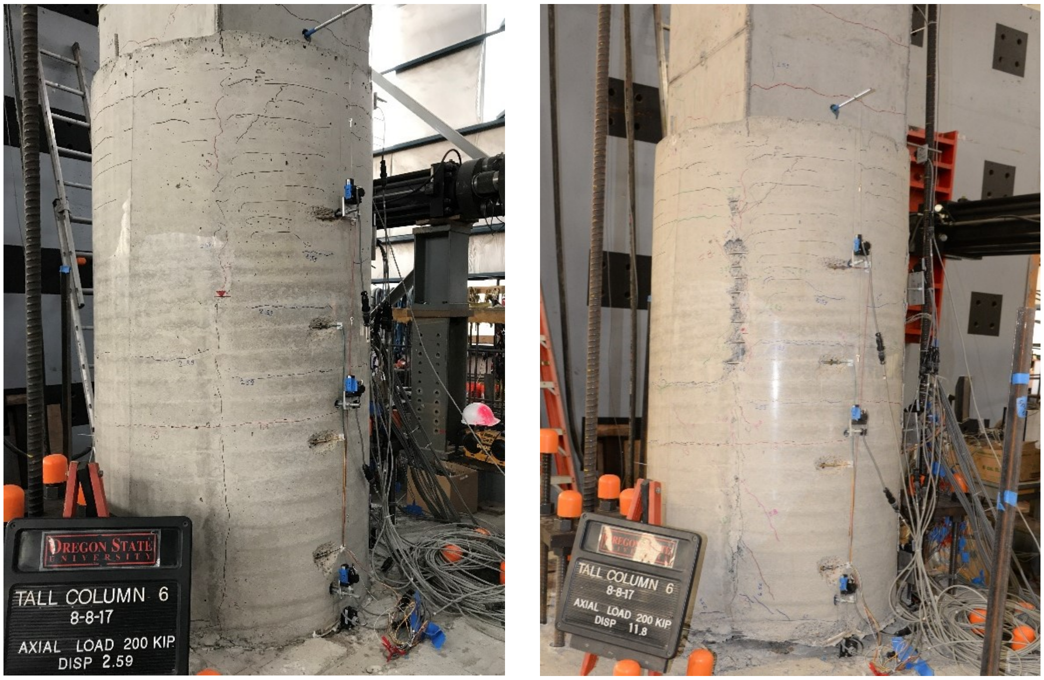

Figure 4.36: Specimen R-T-R-0: Damage progression: (a) at 2.59 in (approx. 1.8%) drift level, (b) at the end of testing (approx. 7% drift level)

4.2.15 Summary of Observed Performance

A common phenomenon observed in the retrofitted column specimens was the formation of chevron type (V-shaped) cracks which started on the retrofit shell along the column corners at the top of the shell which gradually progressed down below. At higher drift levels, these cracks were mostly seen to be clustered near the end of the splice i.e. 36 in (914 mm) above the footing level. In the specimens with vertical ligaments, diagonal cracks were observed near the hooked ends of the ligaments indicating that the hooks tend to pull-out, which causes bulging and cracking in the shell near that region. The extent of these cracks was larger in specimens with 90° hooks than that with 135° hooks. Diagonal cracks above the retrofit shell were also common with some flexural cracks around the column corners. The sliding of the retrofit shell up on the column was evident with a gap forming at the bottom of the retrofit shell when the column was pushed back and forth with some minimal crushing at the toe region of the shell. The sliding of the retrofit shell relative to the column surface is evident from the displacement measurements of LVDT sensors mounted on the North and South faces of the column right above the retrofit shell as seen in Figure 4.37. The negative values of uplift suggest that there was some toe crushing taking place. This relative sliding motion of the retrofit shell also supports the hypothesis that there was non-composite action of shell with respect to the square column. This sliding motion, however, interfered with the threaded rods attached to the instruments and therefore contaminated displacement measurements at higher drift levels when the shell came into contact with the instrument anchorage rods.

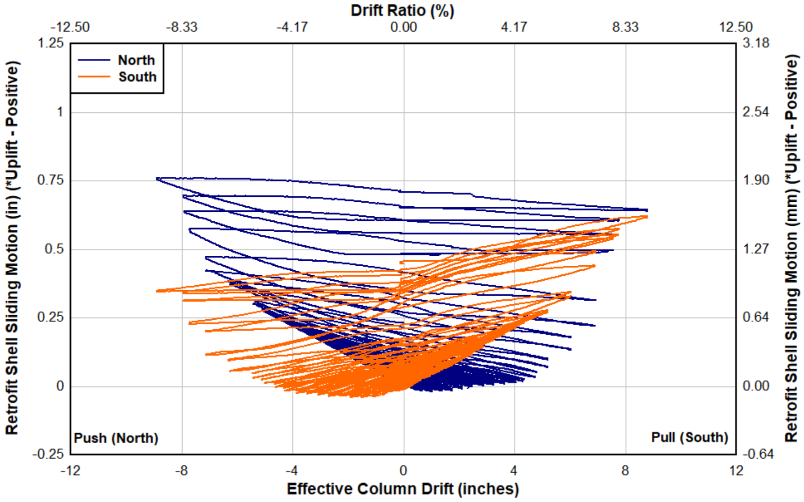

Figure 4.37: Specimen R-S-R-LTi-90: Example of retrofit shell sliding up column face

Horizontal slip occurred in all tested specimens at the column-footing interface, some were quite visible as was observed in the specimens R-S-R-LTi-135 and R-S-R-0 (as illustrated previously in Figure 4.11 and Figure 4.14, but in others sliding was not as pronounced. Specimens always exhibited more stable behavior in one particular direction compared to the other. This is explained by the fact that when the column slips relative to the footing at the interface, it starts to lose its strength on that side but in the slipping process, it locks the other side increasing the confinement, which ends up increasing the performance on the other side. The columns constructed were representative of the column construction in the field where there is a cold joint between column and footing interface. This surface is usually raked (as were the specimens), but the small amount of dowel steel and weak cold joint between the column and footing, as well as less well consolidated concrete in this region, may make sliding more likely for vintage columns. This is one of the important observations made which is an important aspect to consider when designing retrofit strategies. The TiAB spirals were only anchored on one side (which prevented sliding in that direction). If two (2) spirals were used in the lowest section of the column, it could potentially be possible to anchor the spirals on opposite faces of the column and thus prevent sliding. This detail should be considered for future study as its efficiency has not been verified experimentally.

Another characteristic observation in the retrofitted columns with ligaments was some concentration of cracks at the hooked ends of ligaments on the same face of the column. This was expected and motivated the staggering of ligament lengths to prevent a weak horizontal plane due interactions of these cracks.

Although hook extraction is not preferred, the hook extractions that occurred were stable and ductile. Tighter spiral pitch over the hook locations reduced hook extraction and use of 135° hooks also reduced potential hook extraction.

Despite all the distress observed during the testing, the retrofitted column specimens retained self-centering capacity even at very large drifts and all specimens maintained their axial load carrying capacity.

4.3 OVERALL FORCE-DEFORMATION RESPONSE

Overall force-deformation response was developed for each specimen. The response was described by the applied lateral load (column shear) vs. drift ratio (calculated by dividing the column displacement at the location of lateral load application by the height of the column from the footing top surface to that point). The top drift sensor measurement consisted of column deformation components and rigid body motions from the footing. Effective column drift was calculated by removing the rigid body motions from the total column drift measured. Column shear was calculated by removing the horizontal component of axial load from the lateral actuator force. The details of calculation of effective column drift and column shear are given in subsequent sections.

4.3.1 Calculation of Effective Column Drift

The column drift measured by the sensor included additional column drift due to footing slip and rotation and had to be adjusted for these rigid body motions. The rigid body motions are detailed in Figure 4.38.

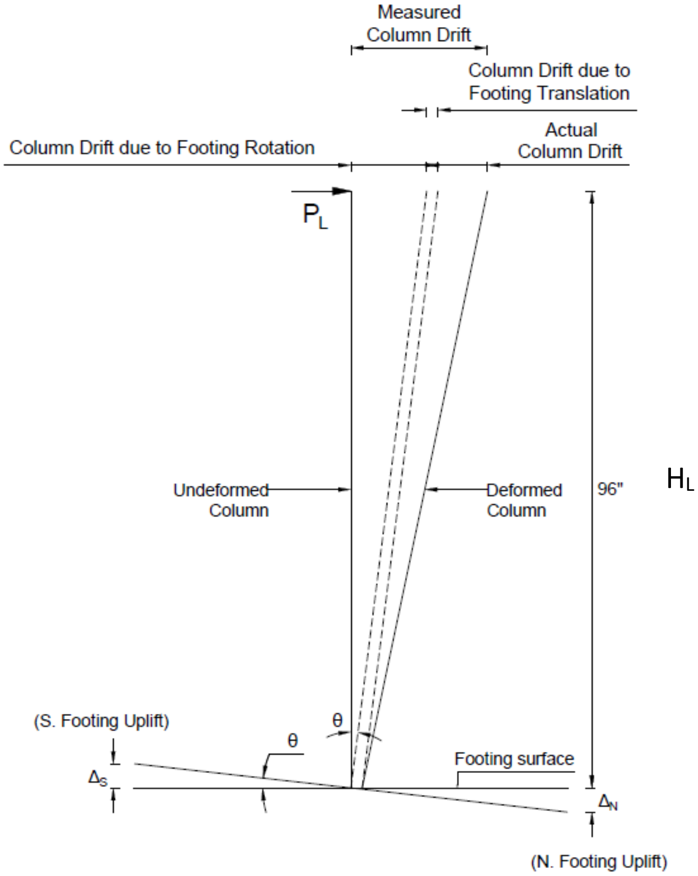

Figure 4.38: Variables used in estimating the effective column drift calculation

For the columns tested with tied footings, rocking of the footing was measured by the displacement sensors measuring uplift at the top of the footing on North and South side. The rocking sensors were placed along the line of loading (center-line of the column) and 2 in off from North and South faces of the footing, respectively. The sliding of the column is measured by a displacement sensor on the North side 2 in from the bottom of the footing. The rocking angle and the additional drift due to rocking were calculated at each loading step as follows:

$$\tan\theta = \frac{(\Delta_N - \Delta_S)}{68\ in.} \tag{4-1}$$

$$\Delta_1 = H_L \tan\theta \tag{4-2}$$

$$\Delta_{eff} = \Delta_{string} - \Delta_1 - \Delta_2 \tag{4-3}$$

Where:

Δ_N = uplift at North side,

Δ_S = uplift at South side,

Θ = footing rocking angle,

H_L = distance from the top of the footing to the lateral load point,

Δ_1 = additional drift due to footing rocking,

Δ_2 = drift due to footing sliding,

Δ_{string} = measured column drift at load point, and

Δ_{eff} = effective column drift at the lateral load point without rigid body motions associated with foundation effects.

For the columns tested with realistic foundations (spread and pile), the specimen was held into position by two lines of rollers on North and South face of the footing. These rollers allowed the rocking of the footing (vertical motions) but restrained translation of the footing to simulate the earth pressure that would be provided by the soil around the footing. Vertical motions of the footing were still permissible and measured by four string potentiometers at the mid-height of the footing on NW, NE, SW, and SE corners. The vertical motions on the North side were calculated by averaging the NE and NW sensors and this was similarly done for the South side. The foundation sliding at the strong floor was measured by two string potentiometers on the SE and SW sides. These sensors could also measure any torsion in the footing. The foundation rocking angle and the additional column drift due to rocking were calculated at each time step similar to the method described above with the following modifications:

$$\boldsymbol{\Delta_N = \frac{\Delta_{NE} + \Delta_{NW}}{2}} \tag{4-4}$$

$$\boldsymbol{\Delta_S = \frac{\Delta_{SE} + \Delta_{SW}}{2}} \tag{4-5}$$

$$\boldsymbol{\tan\theta = \frac{(\Delta_N - \Delta_S)}{56\ in.}} \tag{4-6}$$

4.3.2 Calculation of Column Shear (Effective Lateral Load)

The measured applied lateral load was adjusted to account for the horizontal component of the axial load in the column that is produced in the test setup due to the lateral drift of the column. The horizontal component of axial force applied at the column top was calculated as the axial load times the sine of the angle of total rotation of the column. To calculate the angle of total rotation of the column, the center of rotation through which the axial load passes was located and the total drift of the column was calculated. The deformed shape and geometrical properties for this procedure are shown in Figure 4.39.

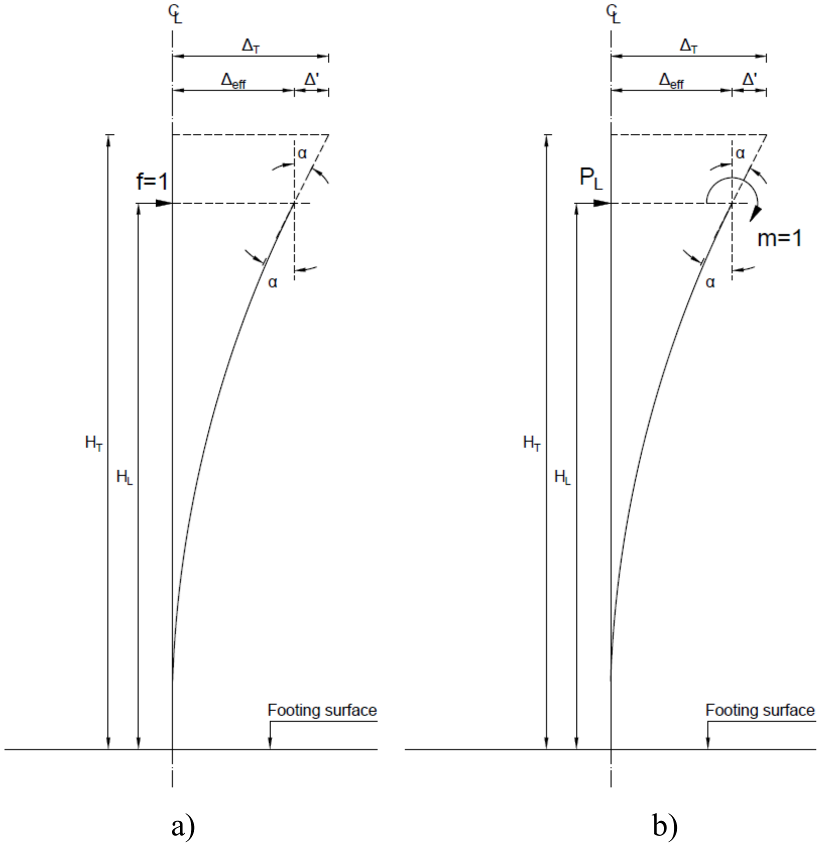

a) b)

Figure 4.39: Axial load axis rotation: a) VWM for displacement at load point, b) VWM for rotation at load point

4.3.2.1 Calculation of angle of rotation for axial load axis, β

The experimental setup had axial load applied at the top of the column (which was built 1 foot taller than the nominal height) and the lateral load was applied 1 ft. below the top of the column surface i.e. the intended moment arm from the top of the footing. Hence the computation of effective lateral load i.e. the column shear had to be adjusted for all these geometric factors.

4.3.2.2 Calculation of angle of rotation at the lateral load point, α

The angle of rotation at the point of application of lateral load and hence the additional drift due to the extra foot of column above the lateral load were calculated using Virtual Work Method (VWM).

It is to be noted that only the portion of the column below the point of application of lateral load is subjected to bending and the portion above that is straight.

Using the VWM, Δ_{eff} (Figure 4.39) was computed as:

$$\boldsymbol{\Delta_{eff}} = \frac{\mathbf{1}}{\boldsymbol{EI}} \int_{\mathbf{0}}^{H_L} \boldsymbol{Mmdx} = \frac{\mathbf{1}}{\boldsymbol{EI}} \int_{\mathbf{0}}^{H_L} (\boldsymbol{F.x}).(\mathbf{1}.\boldsymbol{x})\boldsymbol{dx} = \frac{\boldsymbol{FH_L}^{\mathbf{3}}}{\mathbf{3}\boldsymbol{EI}}$$

(4-7)

Where:

The geometrical parameters are shown in Figure 4.39. Using the VWM, α, the column rotation at the load point was computed as:

$$\boldsymbol{\alpha} = \frac{\mathbf{1}}{\boldsymbol{EI}} \int_{\mathbf{0}}^{H_L} \boldsymbol{Mmdx} = \frac{\mathbf{1}}{\boldsymbol{EI}} \int_{\mathbf{0}}^{H_L} (\boldsymbol{F.x}).(\mathbf{1})\boldsymbol{dx} = \frac{\boldsymbol{FH_L}^{\mathbf{2}}}{\mathbf{2}\boldsymbol{EI}}$$

(4-8)

Substituting EI from Eqn. 4-7 into Eqn. 4-8, α was simplified as:

$$\boldsymbol{\alpha} = \frac{\mathbf{3}\ \Delta_{\boldsymbol{eff}}}{\mathbf{2}\ \boldsymbol{H_L}}$$

(4-9)

Therefore, the additional drift due to the column rotation at the load point, was computed as:

$$\Delta' = \boldsymbol{\alpha}(\boldsymbol{H_T} - \boldsymbol{H_L}) = \frac{\mathbf{3}\ \Delta_{\boldsymbol{eff}}}{\mathbf{2}\ \boldsymbol{H_L}}(\boldsymbol{H_T} - \boldsymbol{H_L})$$

(4-10)

Total drift of the column at the top was computed as:

$$\Delta_{\boldsymbol{T}} = \Delta_{\boldsymbol{eff}} + \Delta'$$

(4-11)

The angle of rotation of axial load axis, β, was calculated as:

$$\boldsymbol{tan(\beta) = \frac{\Delta_T}{H'}}$$

(4-12)

Where:

H′ is the distance of the center of rotation of axial load axis from the top of the column.

4.3.2.3 Location of the center of rotation of axial load axis, H′

The center of rotation of the axial load was assumed to be at the column and footing interface. However, due to the slightly larger holes provided to anchor the Dywidag bars for axial load, the Dywidag bars can shift in the holes. The center of rotation of axial load moves depending on where the axial load hold-down anchors are positioned. To determine the location of this center of rotation, calibration of the setup was conducted using one of the column specimens (R-S-R-0, short column with spiral only retrofit). This column was displaced laterally to 4.4 in (112 mm) (approximately 4.4% drift level) and held in the displaced position while the axial load was reduced from 150 kips (667 kN) to 25.6 kips (114 kN). As the axial load reduced, the lateral load required to hold the position reduced due to the geometric effects of the axial loading system. The process was repeated as the axial load was increased back to the prescribed level of 150 kips (667 kN). The relationship between the axial load and the corresponding lateral actuator load at the maximum and minimum axial loads in the loading and unloading cycles are shown in Table 4.1.

Table 4.1: Relationship between Lateral Load and Axial Load during Calibration of Setup

Loading	**Axial Load, kips (kN)**		**Lateral Load, kips (kN)**	
	Initial	**Final**	**Initial**	**Final**
Unloading	150	25.6	21.6	9.22
Loading	25.6	151	9.22	18.2

The interactions between the two loads were plotted and the response was observed to be fairly linear, one for the unloading and one for the reloading, as shown in Figure 4.40. An average linear curve fit for those two curves was selected as the approximate variation of lateral load with the axial load. The slope of the average curve fit was 12.2 kip axial (54 kN)/kip (kN) lateral. Considering the geometry of the deformed column, seen in Figure 4.33, and the relationships established in the prior section, the distance between the center of rotation of the axial load force vector and the column top was determined as H′=116.5 in (2960 mm) for the short columns. The dimension H′ for the tall columns is 48 in (1219 mm) longer =164.5 in (4178 mm). The resulting geometries are shown in Figure 4.41.

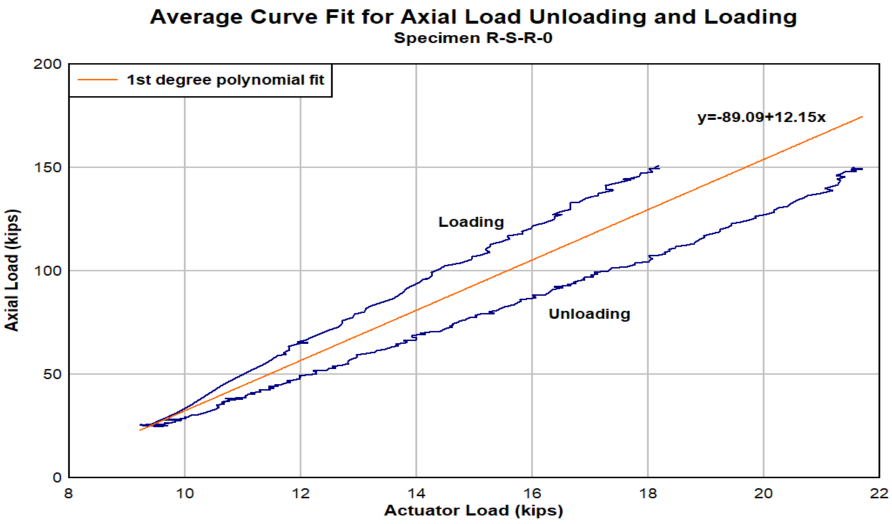

Figure 4.40: Relationship between axial load and lateral load as specimen was held in displaced position @ 4.4 in (112 mm) (approximately 4.4%) drift level

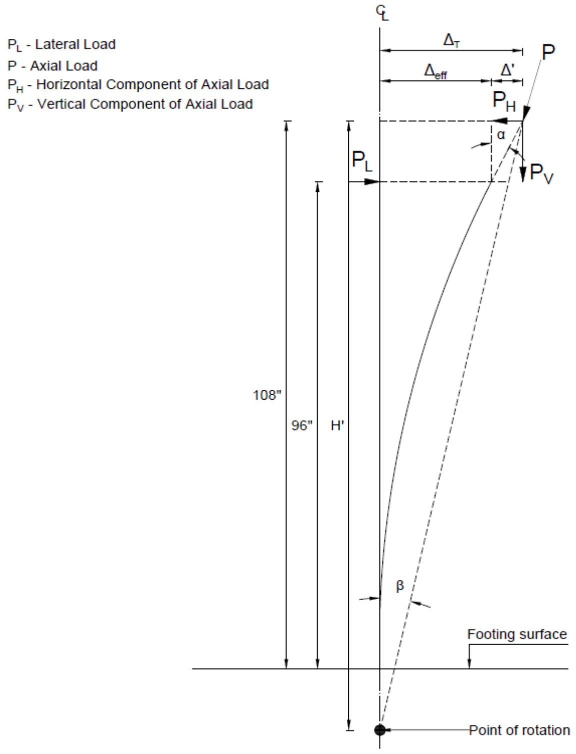

Figure 4.41: Geometry used in calibration of axial load system

4.3.3 Overall Load Deformation Responses

With the center of rotation established, the moment in the column at the top of the footing, including the P-Delta effect was computed as:

$$M_{base} = P_L H_L + P_V \Delta_T - P_H \Delta_T H$$

(4-13)

The moment in the column at the top of the footing can also be calculated by removing the P-Delta effects as:

$$M_{base} = P_L H_L - P_H \Delta_T H'$$

(4-14)

The equivalent lateral load was computed as the column shear from the moment (M_{base}) and the known height of the applied lateral load (H_L) as $V = M_{base}/H_L$.

4.3.3.1 Individual Specimens Force-deformation Responses

The equivalent lateral load, expressed as column shear, versus drift response for each specimen, including correction for the geometrical effects of the axial loading system with P-delta effects included are shown for all specimens in Figure 4.42 through Figure 4.55. Horizontal reference lines in each plot show the shear that would produce the nominal yield moment in the column at the top of the footing. The value corresponds to the actual concrete and steel properties, specimen height, and cross sectional geometry but does not include the influence of the addition of TiABs (represents the RC column alone). A fine dotted line shows the magnitude of shear representing 80% of the peak load measured during the test and is commonly taken to represent a threshold for determination of ductility capacity.

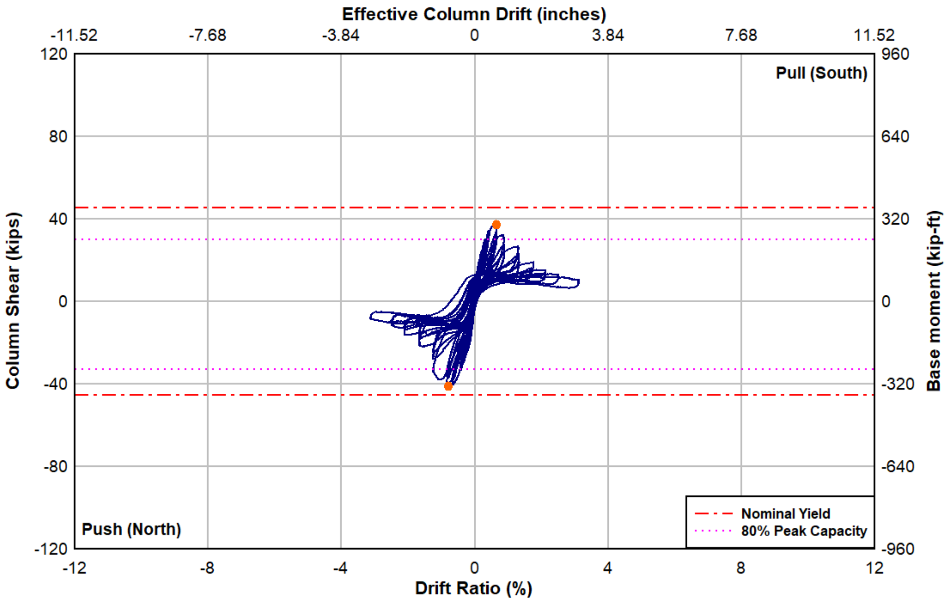

Figure 4.42: Specimen C-S-R: Overall load-drift response

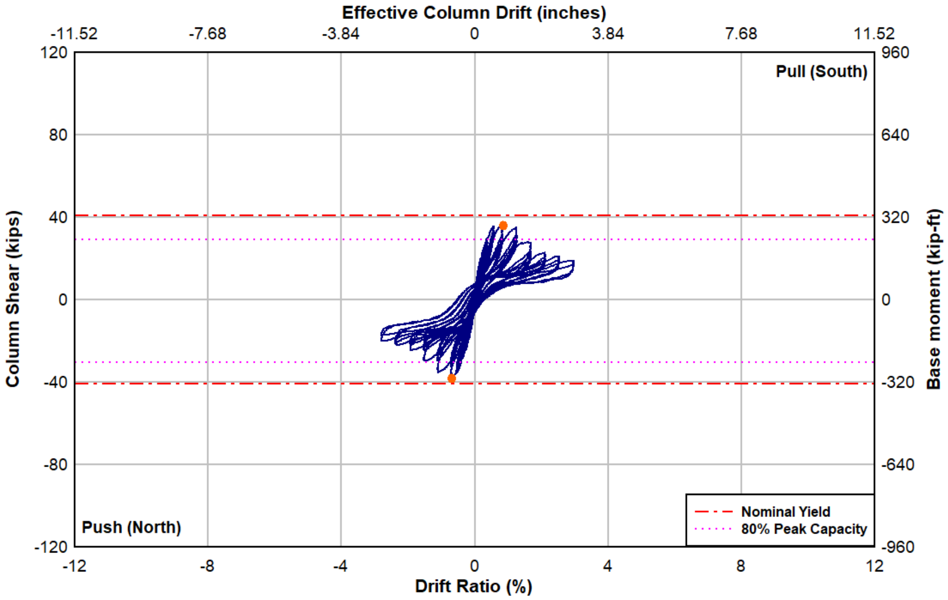

Figure 4.43: Specimen C-S-D: Overall load-drift response

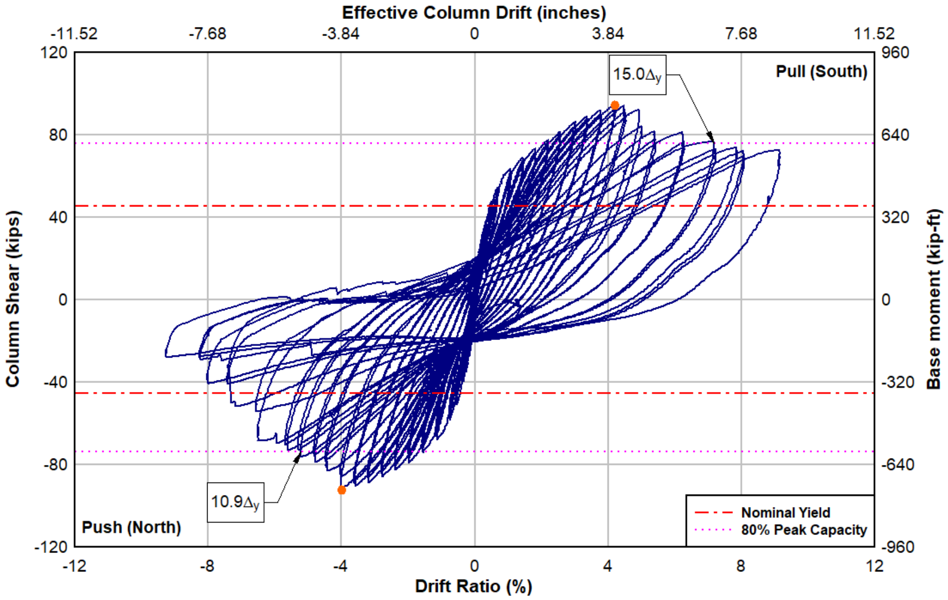

Figure 4.44: Specimen R-S-R-LTi-90: Overall load-drift response

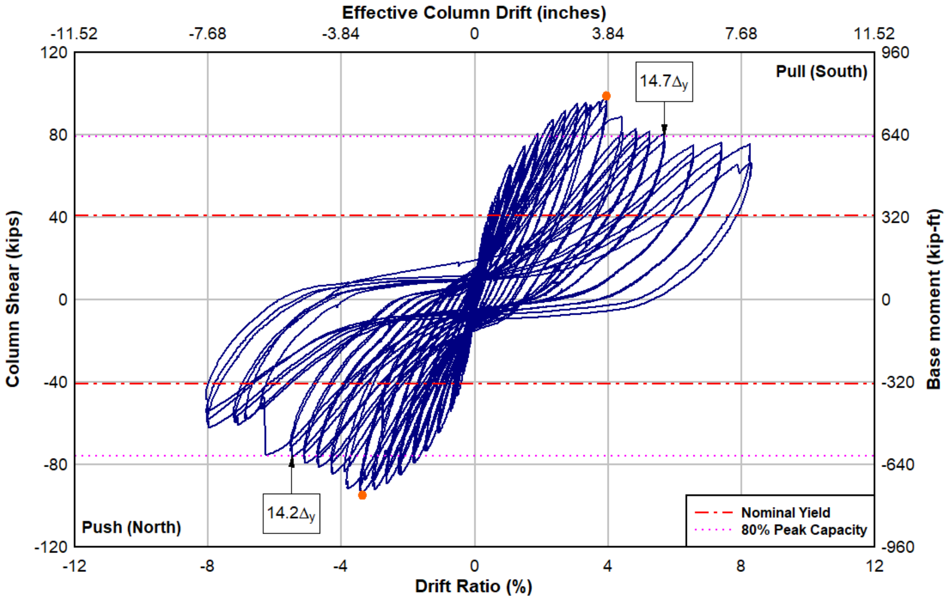

Figure 4.45: Specimen R-S-D-LTi-90: Overall load-drift response

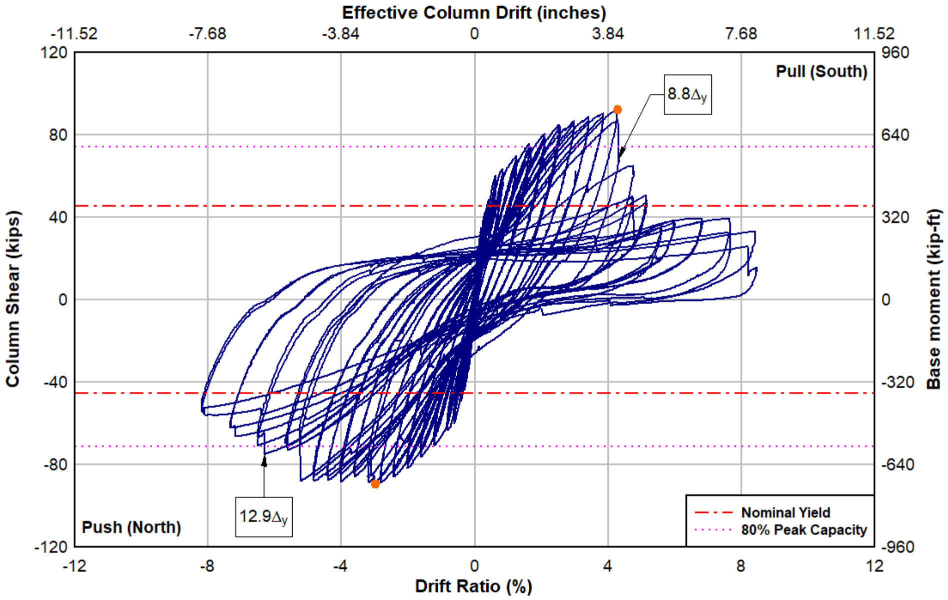

Figure 4.46: Specimen R-S-R-LTi-135: Overall load-drift response

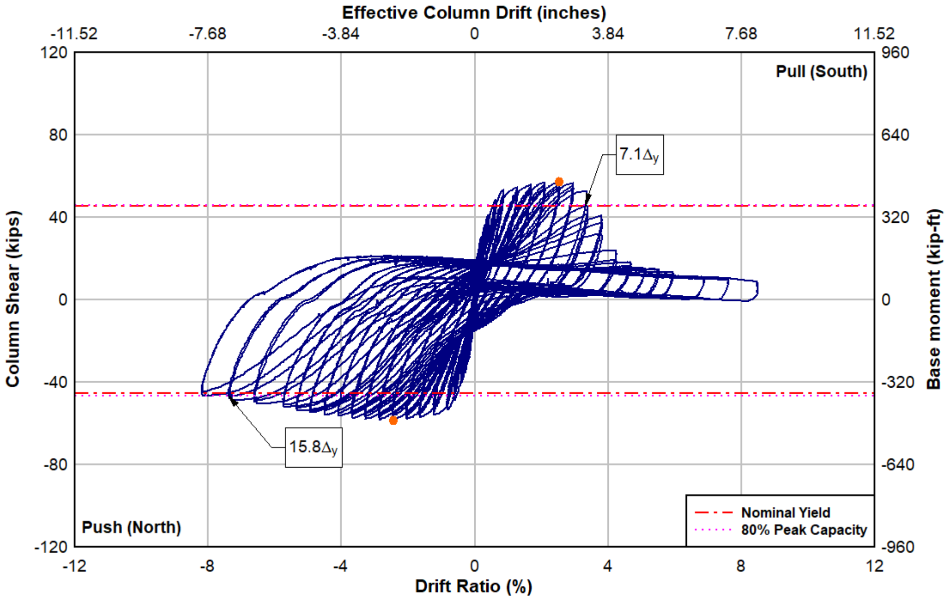

Figure 4.47: Specimen R-S-R-0: Overall load-drift response

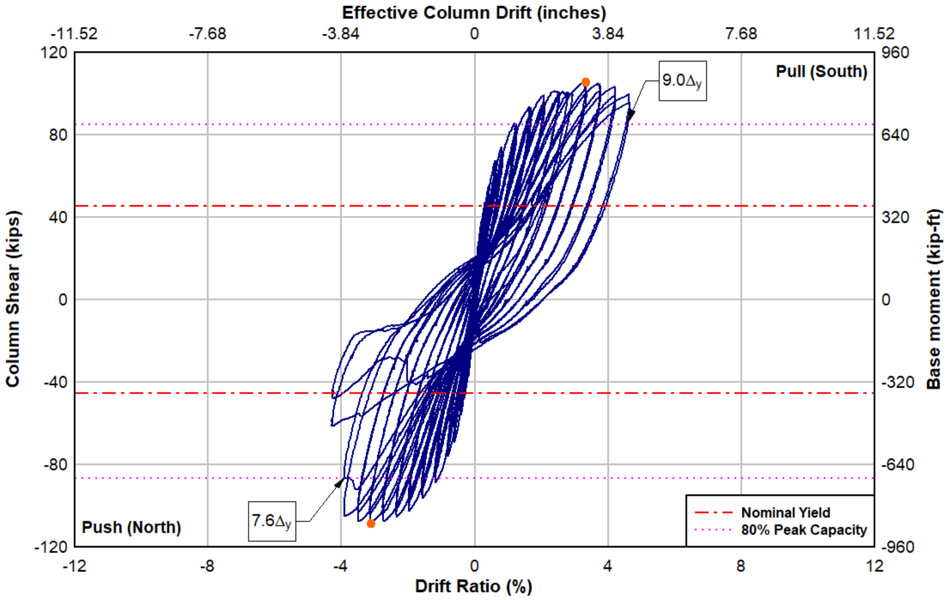

Figure 4.48: Specimen R-S-R-LSS-90: Overall load-drift response

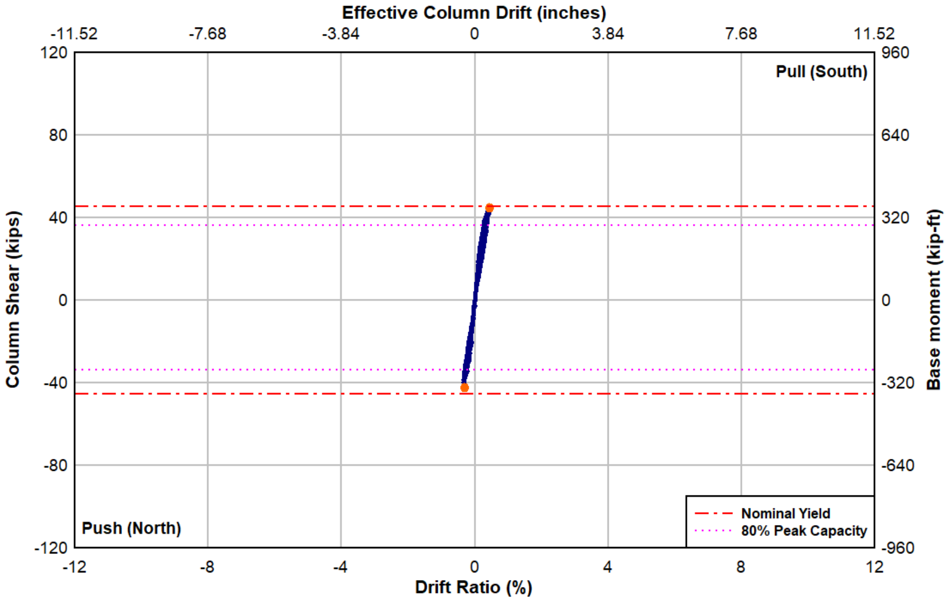

Figure 4.49: Specimen R-S-R-LTi-90-Spread: Overall load-drift response

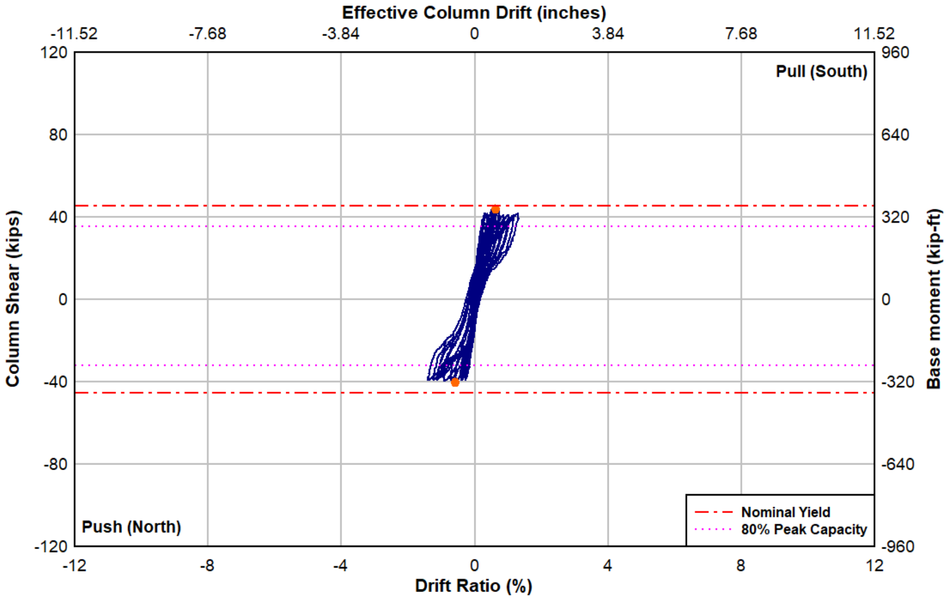

Figure 4.50: Specimen R-S-R-LTi-90-Pile: Overall load-drift response

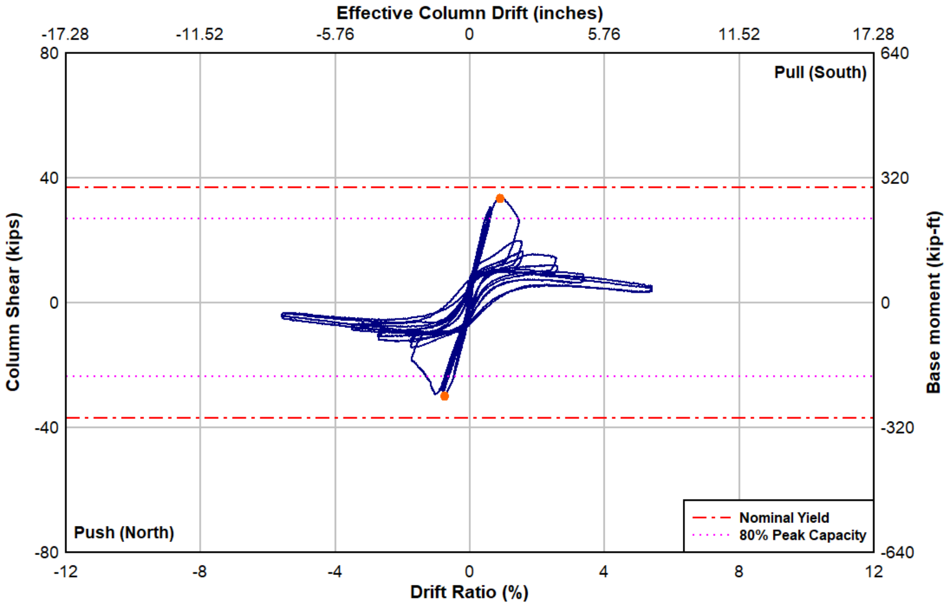

Figure 4.51: Specimen C-T-R: Overall load-drift response

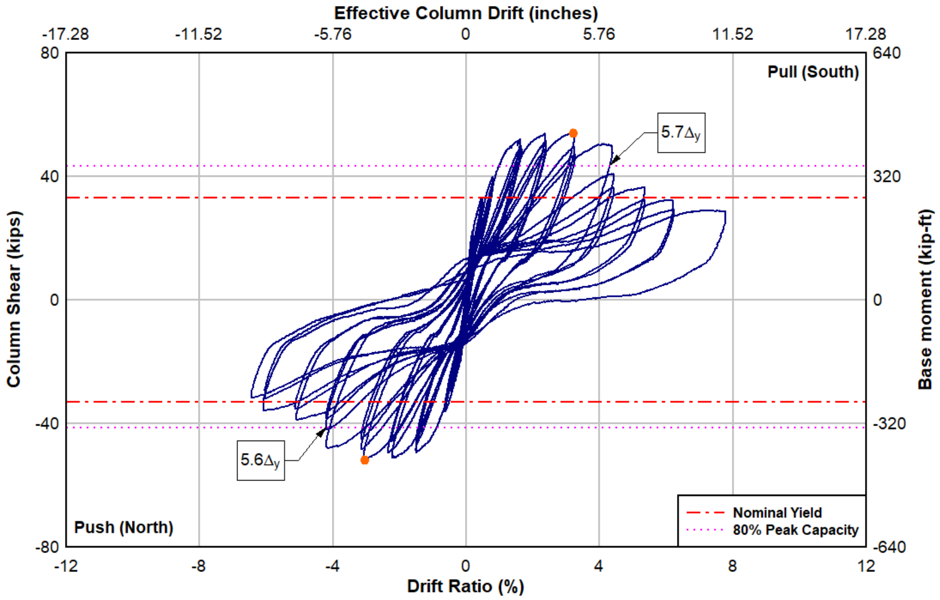

Figure 4.52: Specimen R-T-R-LTi-90: Overall load-drift response

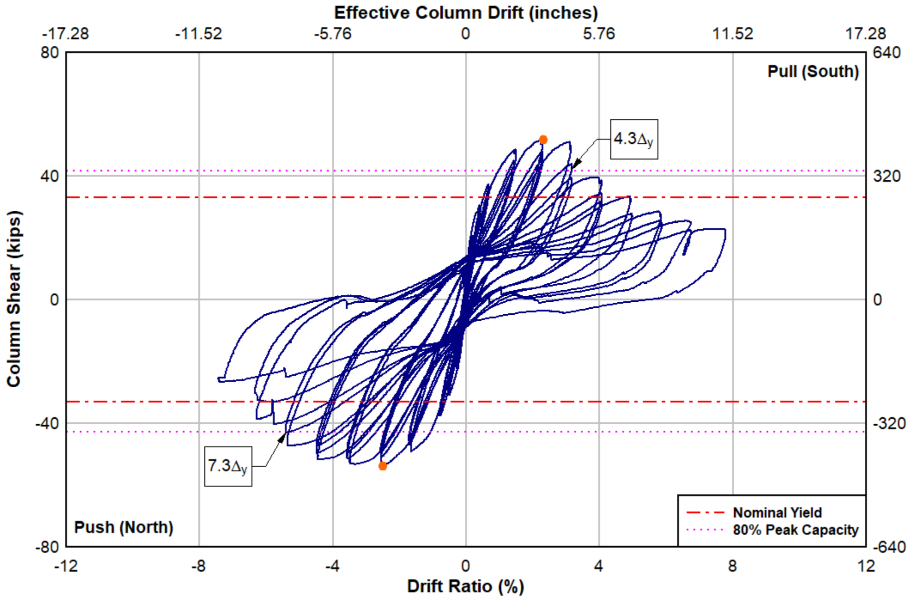

Figure 4.53: Specimen RS-T-R-LTi-90: Overall load-drift response

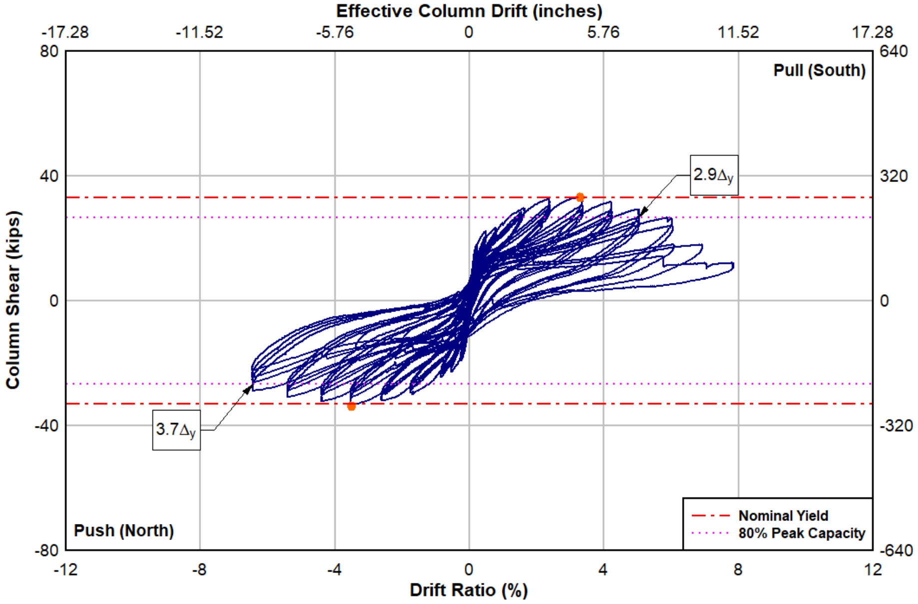

Figure 4.54: Specimen RN-T-R-LTi-90: Overall load-drift response

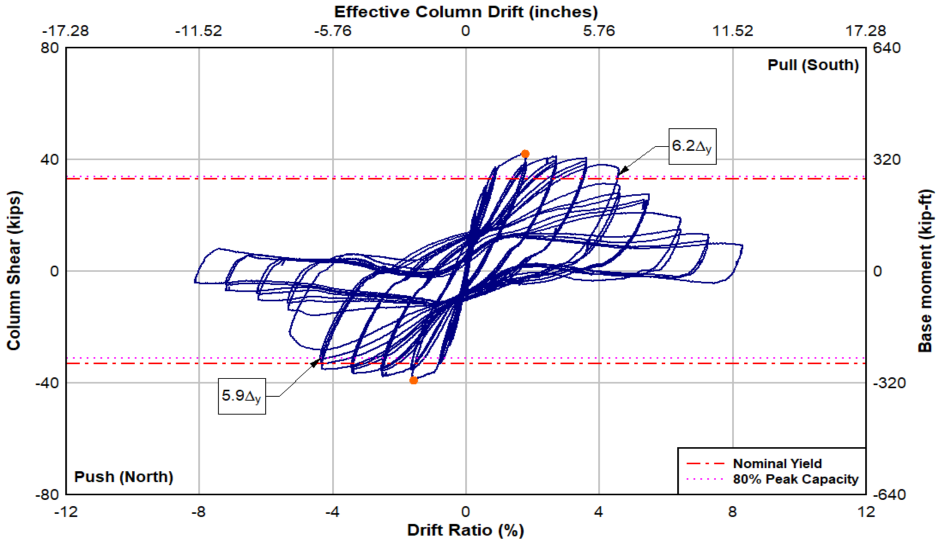

Figure 4.55: Specimen R-T-R-0: Overall load-drift response

Both short control specimens C-S-R (square control) and C-S-D (diamond control) behaved in a similar manner irrespective of the loading direction. The square and diamond control specimens attained a peak force of approximately 37 kips and 36 kips respectively and the drift ratio at failure was 0.87% for square and 1.25% for diamond column. Both columns failed prior to achieving the nominal moment capacity of the column and are non-ductile.

The peak load capacities for square (R-S-R-LTi-90) and diamond (R-S-D-LTi-90) retrofitted columns were approximately 92 and 94 kips respectively. This yields a degree of strengthening was a factor of about 2.5 that of the controls. The square specimen attained displacement ductility of about 11 for push- and 15 for pull-cycles while the diamond specimen’s displacement ductility was about 15 in both cycles. This was dramatic improvement over the control specimens.

Specimens R-S-R-LTi-90 and R-S-D-LTi-90 maintained their upper shelf strength up to drift level of 4.0% and 3.4% respectively when the lateral load dropped to a lower strength shelf due to internal lap-splice failure. This shows that the retrofit method was successful in delaying the lap-splice failure although it was not completely prevented. Both specimens maintained a lower strength shelf in the pull-cycles: square column at about 72 kips and diamond column at about 75 kips with a slight negative slope associated with the P-Delta effect. The strength drop in the push-cycles was more dramatic with lateral strength of square column dropping to approximately 27 kips and diamond column to about 64 kips at 8% drift.

The load-drift response for specimen R-S-R-LTi-135 was fairly symmetric until failure with the peak capacity of approximately 89 kips and 92 kips for push- and pull-cycles, respectively. The failure in the pull-cycle was earlier (at 4.3% drift ratio) than the push cycle (at 6.3% drift ratio). The displacement ductility also ranged from 9 for the pull-cycles to as high as 13 for the push-cycles.

Specimen R-S-R-0 demonstrated unsymmetrical load-drift response for the push and pull cycles. This can be attributed to the lateral translational movement along the shear plane at the bottom of the column towards the strong wall (South). This specimen had only the confining shell without TiAB ligaments. The relatively small amount of dowel action at the footing level may contribute to sliding. Despite the unsymmetrical behavior, the column attained approximately same peak load in both push- and pull-cycles at about same drift level. The column reached a peak capacity of 58.3 kips (259 kN) for push- and 57.3 kips (255 kN) for pull-cycles, respectively at approximately 2.5% drift level. The capacity dropped to 80% for pull-cycles at about 3.3% drift while the other side maintained its capacity up to 7.4% drift level with a very stable hysteretic response because the sliding of the column constantly engaged the flexural steel on that side. At the end of the test, the capacity in pull cycles dropped to 9 kips while the capacity on the other side was maintained at 46 kips. It was observed that the anchorage of the TiAB hoop allowed for the continued engagement of one side of the flexural steel, even as the opposite side opened up.

Specimen R-S-R-LSS-90 attained the highest peak load capacity of all the column specimens tested with a degree of strengthening of approximately 2.7 that of the control. The overall response was fairly symmetric up to the point of failure with the specimen reaching a peak load capacity of 108 kips (482 kN) at 3.12% drift for push-cycle and 106 kips (472 kN) at 3.31% drift for pull-cycle. The load capacity dropped more than 50% in the push cycle at 4.4 in drift level which marked the failure of the specimen. The specimen attained displacement ductility of about 8 for push- and 9 for pull-cycles which was slightly lower than the specimens retrofitted with TiAB ligaments. The over-strength of the stainless steel produced higher shear and moment in the column leading to failure of the column above the retrofit shell leading to reduced seismic performance and unintended damage.

Overall response of specimen R-S-R-LTi-90-Spread was fairly symmetric. The specimen was able to attain a peak load capacity of 42 kips at 0.33% drift level and 45 kips at 0.42% drift level for push- and pull-cycles respectively. The peak capacity was slightly higher than the control specimen and the lateral force was fused out by the deformations in the simulated soil. The retrofitted column remained very close to elastic. Considering the control specimen response, without the TiAB retrofit, the column would likely have failed by loss of the splice above the footing rather than in the simulated soil.

The overall load-deformation response of specimen R-S-R-LTi-90-Pile was a symmetric non-linear elastic flagging behavior. The peak load capacity was 40.2 kips (179 kN) for push-cycles and 44.1 kips (196 kN) for pull-cycles at 0.6% drift level. No significant degree of strengthening was observed as the specimen failed due to foundation failure.

4.3.3.2 Specimen Force-deformation Response Comparison

Backbone curves were established for all the specimens and are compared according to the column height with short columns shown in Figure 4.56 and tall columns shown in Figure 4.57. Table 4.2 summarizes the key response values from the corrected load-displacement response including the P-Delta effects for each specimen. As seen in these figures and table, the TiAB retrofit significantly enhanced the overall cyclic performance of the vintage square RC columns.

Table 4.2: Summary of Load-Deformation Response

No.	**Specimen Name**	**Peak Column Shear, kip (kN)**		**Drift Ratio at Peak Force, %**		**Drift Ratio at Failure, %**		**Degree of strengthening Pmax, Specimen/Pmax, Control**	
		North (Push) [-] Cycle	**South (Pull) [+] Cycle**	**North (Push) [-] Cycle**	**South (Pull) [+] Cycle**	**North (Push) [-] Cycle**	**South (Pull) [+] Cycle**	**North (Push) [-] Cycle**	**South (Pull) [+] Cycle**
1	C-S-R	40.9	37.4	0.81	0.62	1.25	0.87	1.00	1.00
		(182)	(166)						
2	C-S-D	38.1	36.4	0.70	0.83	1.09	1.25	1.00	1.00
		(170)	(162)						
3	R-S-R-LTi-90	92.1	94.6	4.00	4.18	5.22	7.17	2.25	2.53
		(410)	(421)						
4	R-S-D-LTi-90	94.6	99	3.40	3.94	5.47	5.68	2.48	2.72
		(421)	(440)						
5	R-S-R-LTi-135	89.1	92.6	3.00	4.27	6.30	4.30	2.18	2.47
		(396)	(412)						
6	R-S-R-0	58.3	57.3	2.46	2.52	7.40	3.34	1.43	1.53
		(259)	(255)						
7	R-S-R-LSS-90	108	106	3.12	3.31	3.90	4.60	2.65	2.84
		(482)	(472)						
8	R-S-R-LTi-90-Spread	42	45.1	0.33	0.42	-	-	1.03	1.21
		(187)	(201)						
9	R-S-R-LTi-90-Pile	40.2	44.1	0.61	0.61	-	-	0.98	1.18
		(179)	(196)						
10	C-T-R	29.7	33.7	0.78	0.86	1.30	1.45	1.00	1.00
		(132)	(150)						
11	R-T-R-LTi-90	51.6	54.2	3.06	3.20	4.19	4.31	1.74	1.61
		(230)	(241)						
12	RS-T-R-LTi-90	53.6	52	2.51	2.30	5.40	3.16	1.81	1.54
		(238)	(231)						
13	RN-T-R-LTi-90	33.5	33.3	3.53	3.26	6.45	5.05	1.13	0.99
		(149)	(148)						
14	R-T-R-0	38.8	42.3	1.59	1.76	4.36	4.54	1.31	1.26
		(173)	(188)						

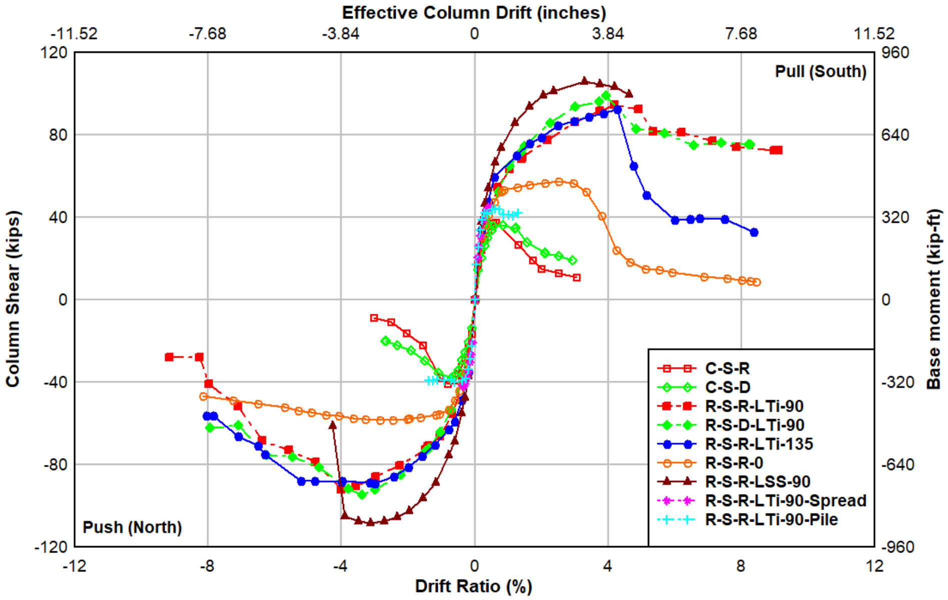

Figure 4.56: Short (8 ft.) specimen load-drift backbone curves

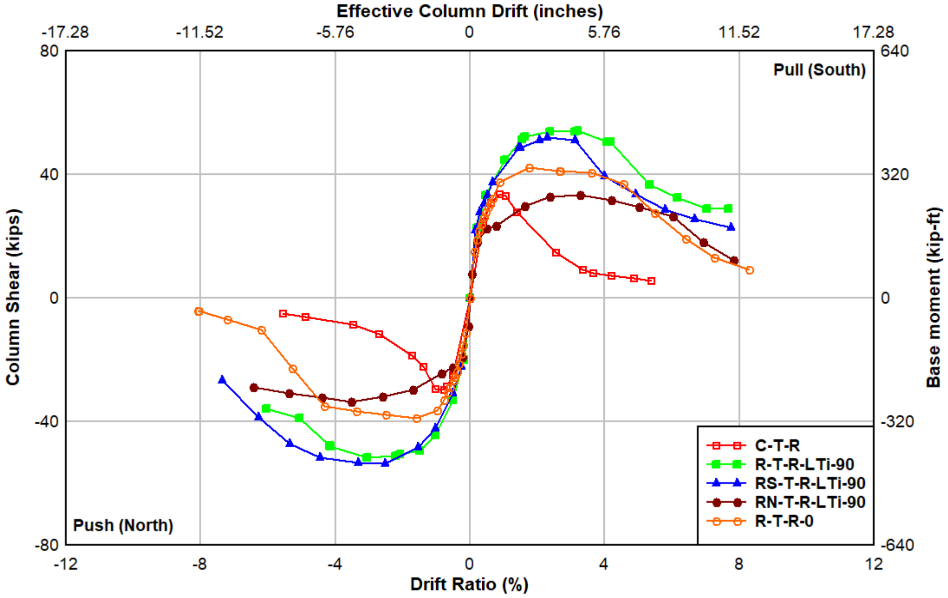

Figure 4.57: Tall (12 ft.) specimen load-drift backbone curves

A series of string potentiometers were used to measure the curvature and shear deformation along the length of the columns. Vertical string pots data were used to calculate the base rotation and curvature along the height of the column. A combination of vertical, horizontal and diagonal string pots on the west face were used to calculated the shear deformation of the column. The measured displacements were used to compute the curvatures and shear deformations as shown in Appendix B. The curvature and shear deformations for all specimens are shown in Appendix C. In general where the measurements were not contaminated by coming into contact with the spiral reinforced shell moving relative to the concrete surface curvatures were linear along the length of the column prior to large inelastic responses and the curvature distributions assumed in analysis are reasonable. Shear deformations were small for all the specimens as flexure is the dominant mode of behavior, even for the short columns.

Strain measurements were taken from the reinforcing steel and TiABs for all specimens and are reported in Appendix C. The strain gages positioned on the longitudinal reinforcing steel and TiAB ligaments showed that both these components on the retrofitted specimens reached yield. The steel ties reached yield in all specimens. The TiAB spirals were well below yield in all cases with strains only around ¼ of the yield strain at instrumented locations. For the control specimens, the longitudinal reinforcing bars were below or just at yield. While the global response showed the control specimens to be elastic, the strain measurements slightly higher than yield in the starter bars were likely due to the positioning of the strain gages on the bar surface which measure both bending and tension strains. Such bending is produced due to sliding at the footing-column interface as seen previously in Figure 4.14(b).

4.4 P-DELTA EFFECTS

Axial load creates an additional overturning moment under lateral loading due to the vertical component of the axial load acting at some distance from the center of the column. This effect is significant at higher drift levels and creates a softening response due to the negative slope effect that is linearly dependent on the lateral drift magnitude. In order to better understand the load-deformation behavior and to isolate the degrading effect of P-Delta behavior from the retrofit degradation, load-deformation responses were also calculated by removing the P-Delta effects mathematically, based on the geometrical relationships established in Section 4.3. Looking at the load-deformation response with the P-Delta effect removed, showed that much of the post-peak degradation for the retrofitted specimens was attributed to the P-Delta effect. It is only at the larger drift levels that the retrofitted column contributed greatly to the strength degradation.

This is demonstrated in the load-deformation responses of two standard retrofitted specimens R-S-R-LTi-90 and R-S-D-LTi-90. For these specimens, the response with and without the effect of P-Delta are shown in Figure 4.58 and Figure 4.59**Error! Reference source not found.**. In both of these specimens, the softening behavior of P-Delta effect is evident. In the pull-cycles (South) which is the better performing side for both of specimens, the strength degradation after peak capacity when the strength reduced due to loss of bond in the steel lap splice, the negative slope of the response envelope was primarily due to P-Delta effect. The response without the P-Delta effect for both of the specimens are uniform and stable on the pull-cycles. The effect of P-Delta in other specimens are shown in the Appendix C.

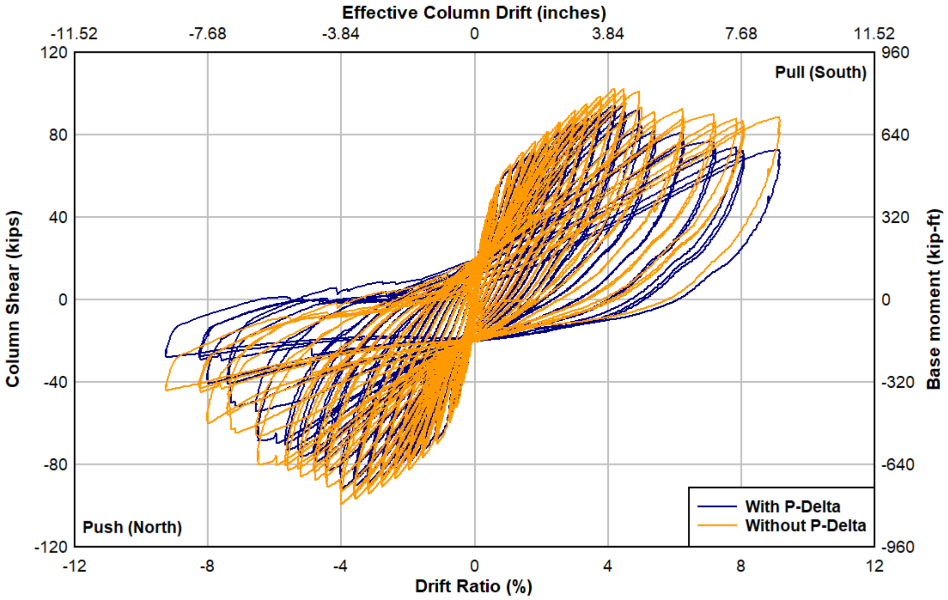

Figure 4.58: Specimen R-S-R-LTi-90: P-Delta effect on load-drift response

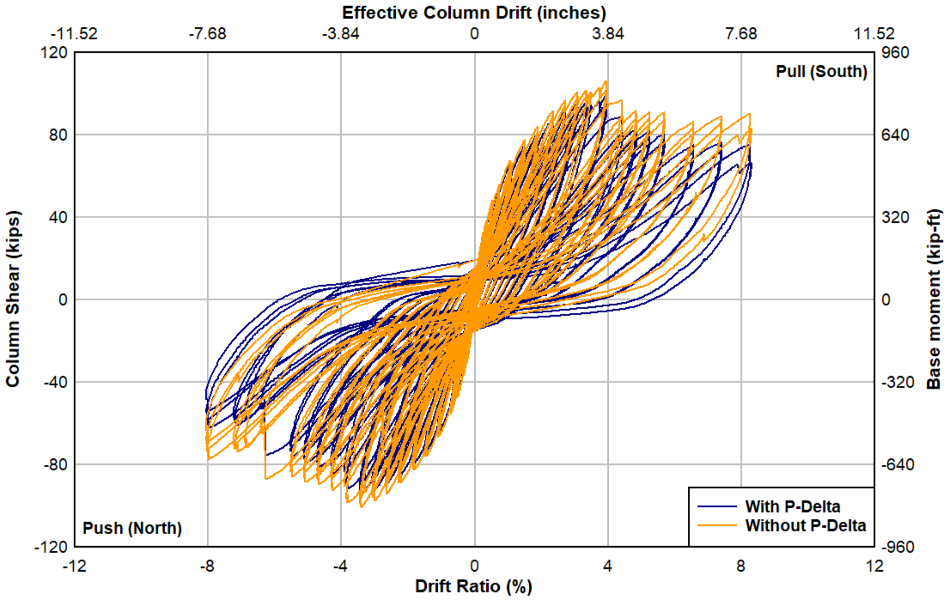

Figure 4.59: Specimen R-S-D-LTi-90: P-Delta effect on load-drift response

4.5 PREDICTION OF LOAD-DEFORMATION RESPONSE FROM MOMENT CURVATURE ANALYSIS

Actual material properties were used to generate moment-curvature plots for each specimen. These included concrete properties obtained from the standard cylinder tests from the day-of-test, longitudinal reinforcement yield stress, and retrofit ligaments yield stress (TiABs and SS bars) obtained from the standard tensile coupon tests. The Todeschini concrete model (Todeschini 1952) was used for the concrete and a modified steel model from the coupon test results was used as a steel model.

The ultimate concrete strain was taken as 0.003 for the control specimens that did not have any external confinement from the TiAB retrofit shell. The widely spaced transverse steel reinforcement in the control specimens was not enough to develop effective confinement so it is reasonable to assume the concrete crushing strain for control specimens as that of unconfined concrete. The ultimate concrete strain in retrofitted column specimens was calculated using the confinement model by Mander et al. (1988). Axial load was kept constant at 150 kips (667 kN) and 200 kips (890 kN) for short and tall column specimens, respectively. It should be noted that this moment-curvature analysis assumed continuous longitudinal bars extending from footing to column and thus does not capture bond-slip behavior which is possible in the columns where the starter bars are spliced with the column longitudinal bars.

When deriving the moment-curvature relationship of each column specimen, the contribution of steel reinforcing bars in compression was considered but that of the external ligaments (TiABs and stainless steel bars) was ignored for the ligaments in compression because they were debonded along the length. The crushing strain for the confined concrete was calculated using the confinement model (Mander et al., 1988) and was assumed to be at the surface of the cross-section used regardless of the shape. It is also assumed that the concrete crushes before the failure of steel reinforcing bars or the retrofit ligaments which was true for the present case. The strain-hardening behavior of longitudinal rebar (which tends to increase the tensile capacity of steel beyond its yield capacity) was considered based on a modified steel model idealized based on the coupon tests as illustrated in Figure 4.60.

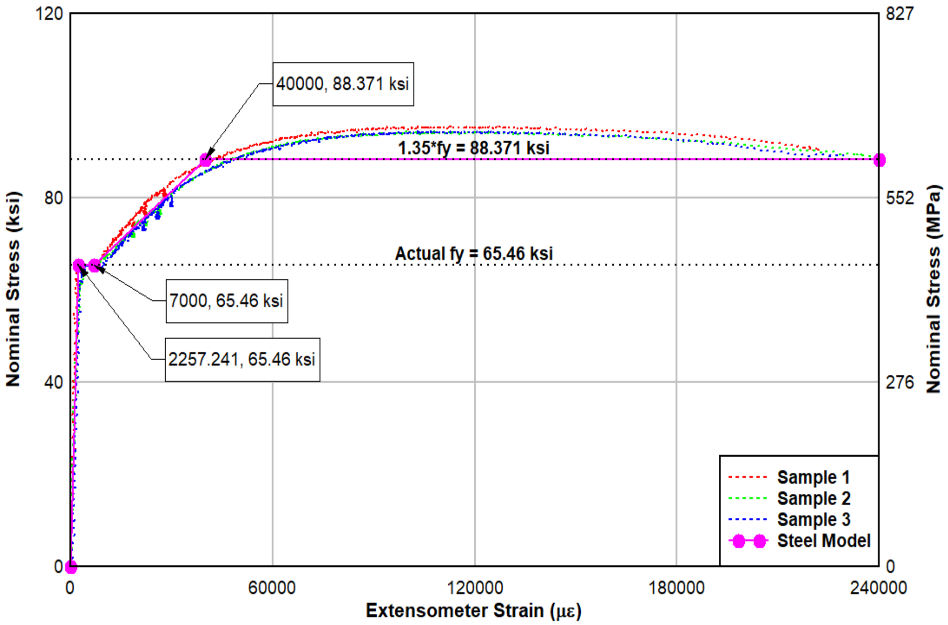

Figure 4.60: Rebar stress-strain model for #10 (#32M) ASTM Gr. 60 bar based on coupon test results

To understand the actual behavior of the retrofitted columns that would help predict the load-displacement response more accurately, eight different possible combinations were explored to generate moment-curvature response for standard retrofitted short column specimen: R-S-R-LTi-90. The parameters explored were: (1) composite action of the retrofit shell which defined the shape of the column section (square for non-composite action and circular for fully composite action), (2) the confining effect of the retrofit shell (unconfined or confined concrete), and (3) the strain-compatibility of the TiAB ligaments (100% strain compatibility assuming fully bonded TiABs, derived as shown in Figure 4.61 and no strain compatibility that results in reduced efficiency for fully unbonded ligaments derived as shown in Figure 4.62. Table 4.3 through

Table 4.8 show efficiency factors derived for fully-unbonded TiAB ligaments for different ligament length and column height combinations. Table 4.11 shows the eight (8) combinations used to generate moment-curvature responses for preliminary estimation of specimen R-S-R-LTi-90 force-deformation response.

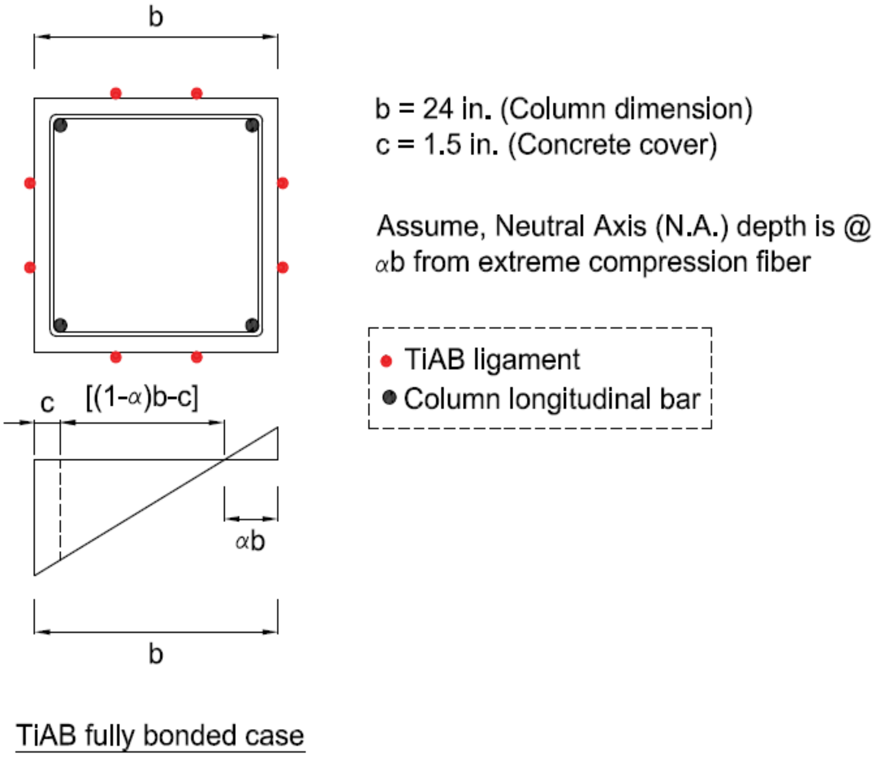

Figure 4.61: Geometry and strain conditions for estimating strain in TiAB ligaments if fully bonded along length

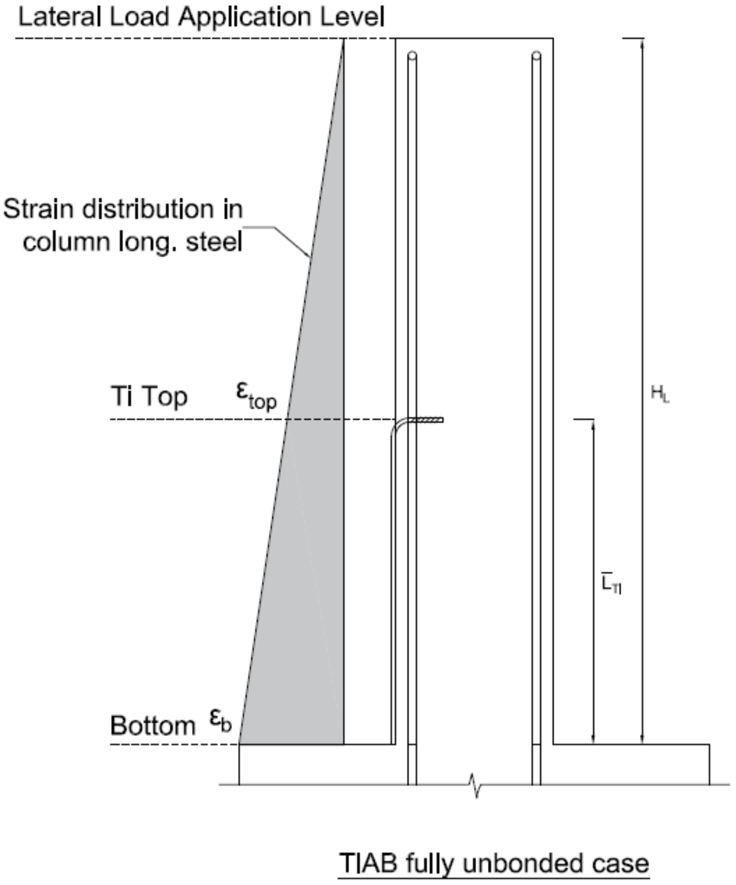

Figure 4.62: Geometry and strain conditions for estimating strain in TiAB ligaments if fully bonded along length

1. Fully bonded case

$$\varepsilon_{Ti,true} = \varepsilon_b \frac{[(1-\alpha)b]}{[(1-\alpha)b-c]}$$

(4-15)

2. Fully unbonded case

$$\varepsilon_{Ti,top} = \varepsilon_b \frac{(H_L - \overline{L_{Ti}})}{H_L} = \varepsilon_b \left(1 - \frac{\overline{L_{Ti}}}{H_L}\right)$$

(4-16)

$$\varepsilon_{Ti,bottom} = \varepsilon_b$$

(4-17)

$$\varepsilon_{Ti} = \bar{\varepsilon} = \varepsilon_b \, \frac{(\varepsilon_{Ti,top} + \varepsilon_{Ti,bottom})}{2} = \varepsilon_b - \varepsilon_b \left(\frac{\overline{L_{Ti}}}{2H_L}\right) = \varepsilon_b \left(1 - \frac{\overline{L_{Ti}}}{2H_L}\right)$$

(4-18)

Therefore, the efficiency of unbonded vs. fully bonded TiAB ligaments,

$$\eta = \frac{\varepsilon_{Ti,unbonded}}{\varepsilon_{Ti,bonded}}$$

(4-19)

$$\eta = \left(1 - \frac{\overline{L_{Ti}}}{2H_L}\right) * \left(\frac{[(1-\alpha)b - c]}{(1-\alpha)b}\right)$$

(4-20)

Eqn. 4-20 shows that the efficiency of unbonded TiAB ligaments depend on the relative length of ligaments compared to the column height. The column height, H_L is the height of the column from the maximum moment to the point of inflection. The efficiency calculation summary below shows the variation of efficiency of unbonded TiAB ligaments with the variation of neutral axis.

Table 4.3: Efficiency of Average Length Unbonded TiAB Ligament in Short Column

Column width, b		**Clear cover, c**		**Cantilever column height, HL**		**Average length of TiAB ligament, LTi**		**Neutral axis depth as a factor of column width, α**	**Efficiency of unbonded TiAB ligament**	**Average Efficiency of unbonded TiAB ligament**
in	**(mm)**	**in**	**(mm)**	**in**	**(mm)**	**in**	**(mm)**	**(%)**	**(%)**	**(%)**
24	(610)	1.5	(38)	96	(2438)	50	(1270)	0	69.3	60.4
24	(610)	1.5	(38)	96	(2438)	50	(1270)	10	68.8	
24	(610)	1.5	(38)	96	(2438)	50	(1270)	20	68.2	
24	(610)	1.5	(38)	96	(2438)	50	(1270)	30	67.4	
24	(610)	1.5	(38)	96	(2438)	50	(1270)	40	66.3	
24	(610)	1.5	(38)	96	(2438)	50	(1270)	50	64.7	
24	(610)	1.5	(38)	96	(2438)	50	(1270)	60	62.4	
24	(610)	1.5	(38)	96	(2438)	50	(1270)	70	58.6	
24	(610)	1.5	(38)	96	(2438)	50	(1270)	80	50.8	
24	(610)	1.5	(38)	96	(2438)	50	(1270)	90	27.7	

Table 4.4: Efficiency of Average Length Unbonded TiAB Ligament in Tall Column

Column width, b		Clear cover, c		Cantilever column height, HL		Average length of TiAB ligament, LTi		Neutral axis depth as a factor of column width	Efficiency of unbonded TiAB ligament	Average Efficiency of unbonded TiAB ligament
in	(mm)	in	(mm)	in	(mm)	in	(mm)	(%)	(%)	(%)
24	(610)	1.5	(38)	144	(3658)	50	(1270)	0	77.5	67.5
24	(610)	1.5	(38)	144	(3658)	50	(1270)	10	76.9	
24	(610)	1.5	(38)	144	(3658)	50	(1270)	20	76.2	
24	(610)	1.5	(38)	144	(3658)	50	(1270)	30	75.3	
24	(610)	1.5	(38)	144	(3658)	50	(1270)	40	74.0	
24	(610)	1.5	(38)	144	(3658)	50	(1270)	50	72.3	
24	(610)	1.5	(38)	144	(3658)	50	(1270)	60	69.7	
24	(610)	1.5	(38)	144	(3658)	50	(1270)	70	65.4	
24	(610)	1.5	(38)	144	(3658)	50	(1270)	80	56.8	
24	(610)	1.5	(38)	144	(3658)	50	(1270)	90	31.0	

For short columns, the efficiency of 50 in (1270 mm) long unbonded TiAB ligaments can range anywhere from 27.7% to 69.3% depending on the neutral axis depth and the average efficiency can be taken as 60.4%. For tall columns, the efficiency of 50 in (1270 mm) long unbonded TiAB ligaments can range anywhere from 31.0% to 77.5% depending on the neutral axis depth and the average efficiency can be taken as 67.5%.

Table 4.5: Efficiency of Full Length Unbonded TiAB Ligament in Short Column

Column width, b		Clear cover, c		Cantilever column height, H_L		Average length of TiAB ligament, LTi		Neutral axis depth as a factor of column width, α	Efficiency of unbonded TiAB ligament	Average Efficiency of unbonded TiAB ligament
in	(mm)	in	(mm)	in	(mm)	in	(mm)	(%)	(%)	(%)
24	(610)	1.5	(38)	96	(2438)	96	(2438)	0	46.9	40.8
24	(610)	1.5	(38)	96	(2438)	96	(2438)	10	46.5	
24	(610)	1.5	(38)	96	(2438)	96	(2438)	20	46.1	
24	(610)	1.5	(38)	96	(2438)	96	(2438)	30	45.5	
24	(610)	1.5	(38)	96	(2438)	96	(2438)	40	44.8	
24	(610)	1.5	(38)	96	(2438)	96	(2438)	50	43.8	
24	(610)	1.5	(38)	96	(2438)	96	(2438)	60	42.2	
24	(610)	1.5	(38)	96	(2438)	96	(2438)	70	39.6	
24	(610)	1.5	(38)	96	(2438)	96	(2438)	80	34.4	
24	(610)	1.5	(38)	96	(2438)	96	(2438)	90	18.8	

Table 4.6: Efficiency of Full Length Unbonded TiAB Ligament in Tall Column

Column width, b		Clear cover, c		Cantilever column height, H_L		Average length of TiAB ligament, LTi		Neutral axis depth as a factor of column width, α	Efficiency of unbonded TiAB ligament	Average Efficiency of unbonded TiAB ligament
in	(mm)	in	(mm)	in	(mm)	in	(mm)	(%)	(%)	(%)
24	(610)	1.5	(38)	144	(3658)	144	(3658)	0	46.9	40.8
24	(610)	1.5	(38)	144	(3658)	144	(3658)	10	46.5	
24	(610)	1.5	(38)	144	(3658)	144	(3658)	20	46.1	
24	(610)	1.5	(38)	144	(3658)	144	(3658)	30	45.5	
24	(610)	1.5	(38)	144	(3658)	144	(3658)	40	44.8	
24	(610)	1.5	(38)	144	(3658)	144	(3658)	50	43.8	
24	(610)	1.5	(38)	144	(3658)	144	(3658)	60	42.2	
24	(610)	1.5	(38)	144	(3658)	144	(3658)	70	39.6	
24	(610)	1.5	(38)	144	(3658)	144	(3658)	80	34.4	
24	(610)	1.5	(38)	144	(3658)	144	(3658)	90	18.8	

For both short and tall columns, the efficiency of full-length unbonded TiAB ligaments can range anywhere from 18.8% to 46.9% depending on the neutral axis depth and the average efficiency can be taken as 40.8%.

Table 4.7: Efficiency of Zero Length Unbonded TiAB Ligament in Short Column

Column width, b		Clear cover, c		Cantilever column height, H_L		Average length of TiAB ligament, LTi		Neutral axis depth as a factor of column width, α	Efficiency of unbonded TiAB ligament	Average Efficiency of unbonded TiAB ligament
in	(mm)	in	(mm)	in	(mm)	in	(mm)	(%)	(%)	(%)
24	(610)	1.5	(38)	96	(2438)	0	(0)	0	93.8	77.5
24	(610)	1.5	(38)	96	(2438)	0	(0)	10	93.1	
24	(610)	1.5	(38)	96	(2438)	0	(0)	20	92.2	
24	(610)	1.5	(38)	96	(2438)	0	(0)	30	91.1	
24	(610)	1.5	(38)	96	(2438)	0	(0)	40	89.6	
24	(610)	1.5	(38)	96	(2438)	0	(0)	50	87.5	
24	(610)	1.5	(38)	96	(2438)	0	(0)	60	84.4	
24	(610)	1.5	(38)	96	(2438)	0	(0)	70	37.5	
24	(610)	1.5	(38)	96	(2438)	0	(0)	80	68.8	
24	(610)	1.5	(38)	96	(2438)	0	(0)	90	37.5	

Table 4.8: Efficiency of Zero Length Unbonded TiAB Ligament in Short Column

Column width, b		Clear cover, c		Cantilever column height, H_L		Average length of TiAB ligament, LTi		Neutral axis depth as a factor of column width, α	Efficiency of unbonded TiAB ligament	Average Efficiency of unbonded TiAB ligament
in	(mm)	in	(mm)	in	(mm)	in	(mm)	(%)	(%)	(%)
24	(610)	1.5	(38)	144	(3658)	0	(0)	0	93.8	77.5
24	(610)	1.5	(38)	144	(3658)	0	(0)	10	93.1	
24	(610)	1.5	(38)	144	(3658)	0	(0)	20	92.2	
24	(610)	1.5	(38)	144	(3658)	0	(0)	30	91.1	
24	(610)	1.5	(38)	144	(3658)	0	(0)	40	89.6	
24	(610)	1.5	(38)	144	(3658)	0	(0)	50	87.5	
24	(610)	1.5	(38)	144	(3658)	0	(0)	60	84.4	
24	(610)	1.5	(38)	144	(3658)	0	(0)	70	37.5	
24	(610)	1.5	(38)	144	(3658)	0	(0)	80	68.8	
24	(610)	1.5	(38)	144	(3658)	0	(0)	90	37.5	

When the length of TiAB ligament approaches zero, the efficiency of unbonded TiAB ligaments can range from 37.5% to 93.8% with an average efficiency of 77.5%.

Table 4.9: Combinations Investigated for Response Prediction of Specimen R-S-R-LTi-90

No.	Combinations	Shape of column section	Confinement	Strain compatibility of TiABs
1	A-C-E	Square (non-composite)	Unconfined	Fully bonded (100%)
2	A-C-F	Square (non-composite)	Unconfined	Fully unbonded (68%)
3	A-D-E	Square (non-composite)	Confined	Fully bonded (100%)
4	A-D-F	Square (non-composite)	Confined	Fully unbonded (68%)
5	B-C-E	Circular (fully-composite)	Unconfined	Fully bonded (100%)
6	B-C-F	Circular (fully-composite)	Unconfined	Fully unbonded (68%)
7	B-D-E	Circular (fully-composite)	Confined	Fully bonded (100%)
8	B-D-F	Circular (fully-composite)	Confined	Fully unbonded (68%)

A reinforcing steel stress-strain model was defined for the reinforcing steel bars based on the coupon tests of #10 (#32M) Gr. 60 bars used in the specimens. The steel model consists of a linear elastic range and a yield plateau that extends from the yield strain up to 7,000 με and has a linear strain-hardening zone up to 40,000με, which corresponds to 1.35 times the yield stress of steel as the maximum stress due to strain-hardening. The peak stress is assumed to be constant until the fracture of the bar. The fracture itself was not defined, as at the ultimate state of all specimens crushing of the concrete occurs and no fracture of the reinforcing bars was observed.

Moment curvature responses for specimen R-S-R-LTi-90 considering the eight different combinations are shown in Figure 4.63.

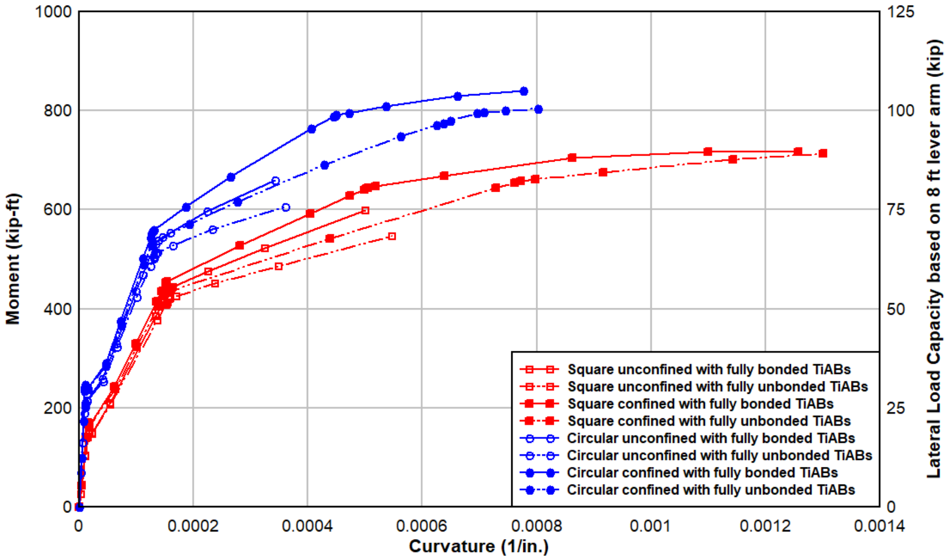

Figure 4.63: Range of moment-curvature responses for specimen R-S-R-LTi-90

The capacities predicted by these different combinations were compared with the actual capacity obtained from the experimental result and are shown in Table 4.10. The experimental shear capacity for specimen R-S-R-LTi-90 was 92.1 kips (410 kN) and 94.6 kips (421 kN) in push- and pull-cycles, respectively. Circular fully-composite model well over-predicted the column capacity when the concrete is assumed to be confined. Unconfined concrete model for both square and circular cross-section under-predicted the capacity. Square confined model with fully bonded and unbonded TiAB ligament options (combinations A-D-E and A-D-F, respectively) predicted the capacity very well. Therefore, flexural response predicted by these two sets of assumptions were used to predict the total deformation response.

Table 4.10: Capacity Predicted by Moment-Curvature Analysis for Specimen R-S-R-LTi-90

No.	Combinations	Moment capacity, kip-ft (kN-m)		Shear Capacity, kip (kN)		Predicted Capacity/Actual Capacity	
						North (Push)	South (Pull)
						[-] Cycle	[+] Cycle
1	A-C-E	599	(812)	74.9	(333)	0.81	0.79
2	A-C-F	547	(742)	68.4	(304)	0.74	0.72
3	A-D-E	718	(973)	89.7	(399)	0.97	0.95
4	A-D-F	713	(967)	89.1	(396)	0.97	0.94
5	B-C-E	660	(895)	82.5	(367)	0.90	0.87
6	B-C-F	606	(822)	75.8	(337)	0.82	0.80
7	B-D-E	840	(1139)	105.0	(467)	1.14	1.11
8	B-D-F	804	(1090)	100.5	(447)	1.09	1.06

To obtain the moment-curvature responses for the retrofitted specimens, two options were explored: one assumed that the confining shell only provided confinement to the square column with no composite action (i.e. square effective cross-section with confined concrete properties), the second one assumed the full composite action of the shell (i.e. circular effective cross-section with confined concrete properties). The contribution of TiAB and stainless steel ligaments were considered when present in both models.

These moment-curvature distributions along the height of the column were used to predict the load-flexural displacement response of each column. Examples of curvature distributions along the column height at three specific load levels are shown in Figure 4.64. These were integrated to obtain the deformation at the load point for each load level. The moment-curvature analysis predicted only the flexural response of the specimen. To include the contribution to drift at the load point from strain penetration and bar-slip in the splice region, the rotations at the footing interface were collected from the experimental measurements. The two string pots located on the west face at the lowest level on the column and connected to the footing were used to compute the base rotation. The predicted contribution of the base rotation to the displacement at the load point were computed based on small angle theory. Lumped contribution to lateral drift from strain penetration and bar-slip for the column used in this example are shown in Figure 4.65. The predicted combined response of column bending along the height with end rotation was compared with the experimental cyclic response for the different modeling assumptions as shown in Figure 4.66. As discussed above, the composite circular model predicted stiffer behavior and higher strength compared to the non-composite square model. Based on the experimental behavior slip was observed between the spiral shell and core concrete and the behavior of the retrofitted columns was considered to be semi-composite, but closer to non-composite. The predicted ultimate moment capacity from the moment-curvature analysis, however, was below the experimentally observed maximum moment capacity. This can be attributed to the semi-composite behavior as the retrofit shell takes some compression at the toe of the shell when it goes into bearing despite the ability to slide along the column surface. To account for the semi-composite behavior on strength, a calibrated over strength factor of 10% was applied to each loading increment. The predicted strength was better correlated with this modification for all retrofitted column specimens. Considering the over-strength factor, the contributions to drift for different load levels are shown in Figure 4.67 and the final predicted response is shown in Figure 4.68. As seen here, the predicted lateral force-drift response was well predicted. This was consistent for all specimens as seen in Appendix C. Final moment-curvature relationships developed for all specimens are shown in Figure 4.69 and Figure 4.70, for short and tall columns, respectively. The flexural stiffness, EI, of the specimens from the moment-curvature responses using nominal and expected material properties are shown in Table 4.11 and Table 4.12 respectively. As seen here the TiABs retrofitted specimens tended to increase the initial stiffness by about 25% compared to the controls. The stainless steel ligaments produced the largest change in cracked stiffness of almost 65% increase compared to that of the control.

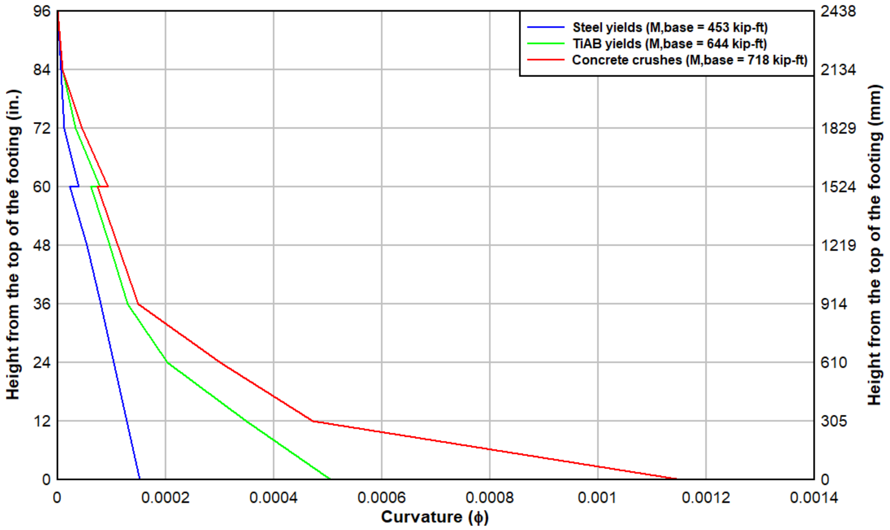

Figure 4.64: Specimen R-S-R-LTi-90: Curvature distribution along the height of the column

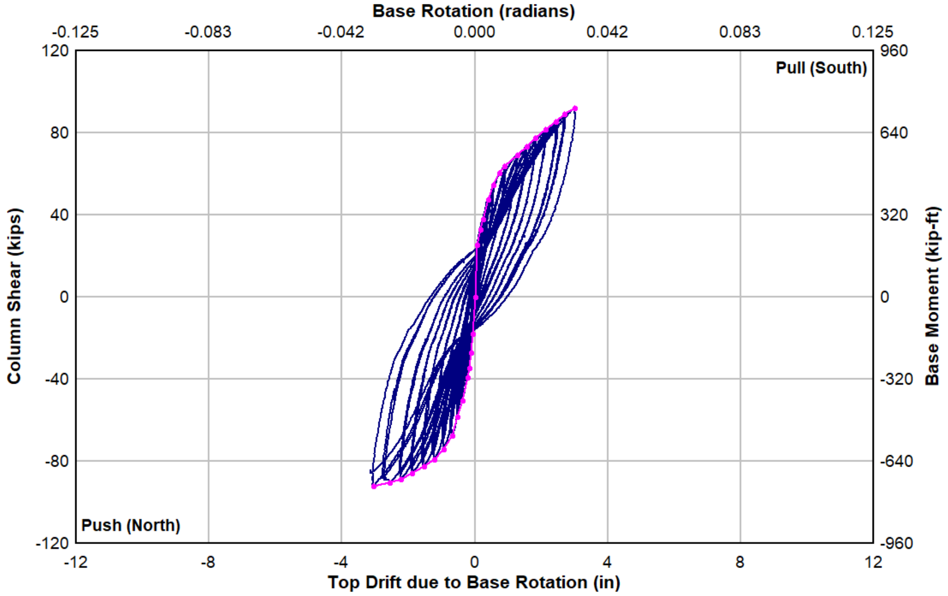

Figure 4.65: Specimen R-S-R-LTi-90: Top drift due to base rotation from strain penetration and bar-slip

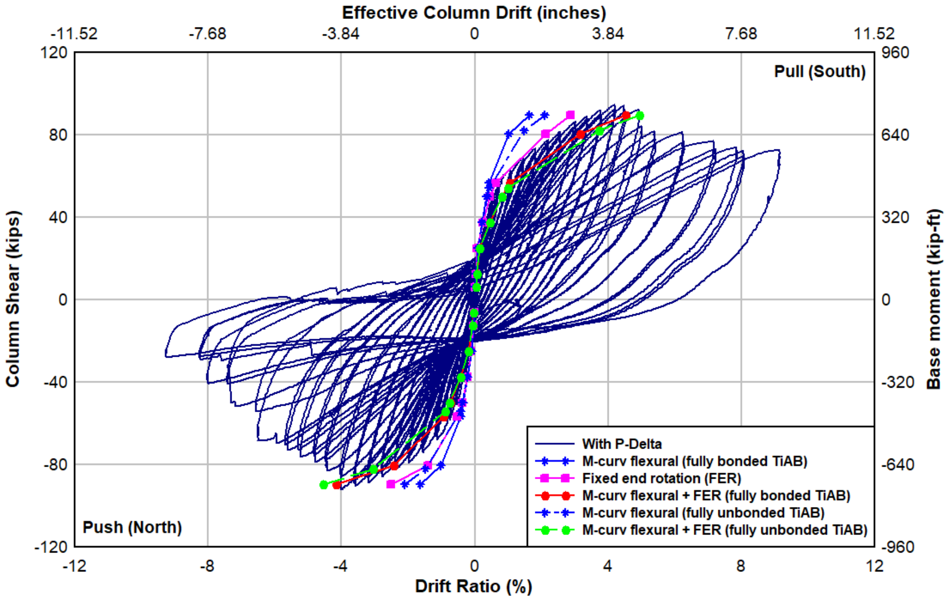

Figure 4.66: Specimen R-S-R-LTi-90: Predicted response for different assumed TiAB bonding conditions and footing interface rotations (all non-composite)

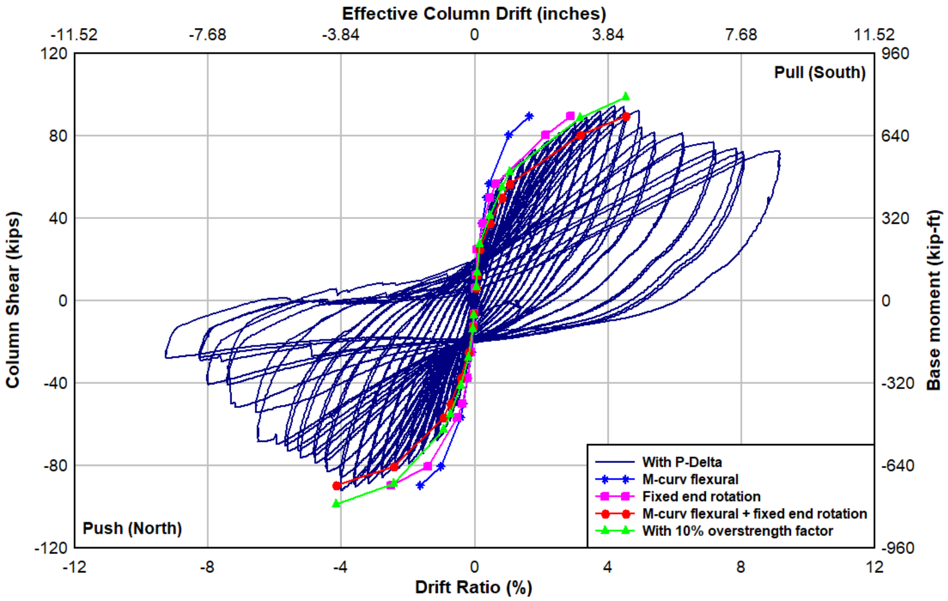

Figure 4.67: Specimen R-S-R-LTi-90: Predicted contributions to response for selected TiAB bonding conditions, footing interface rotations, and over-strength

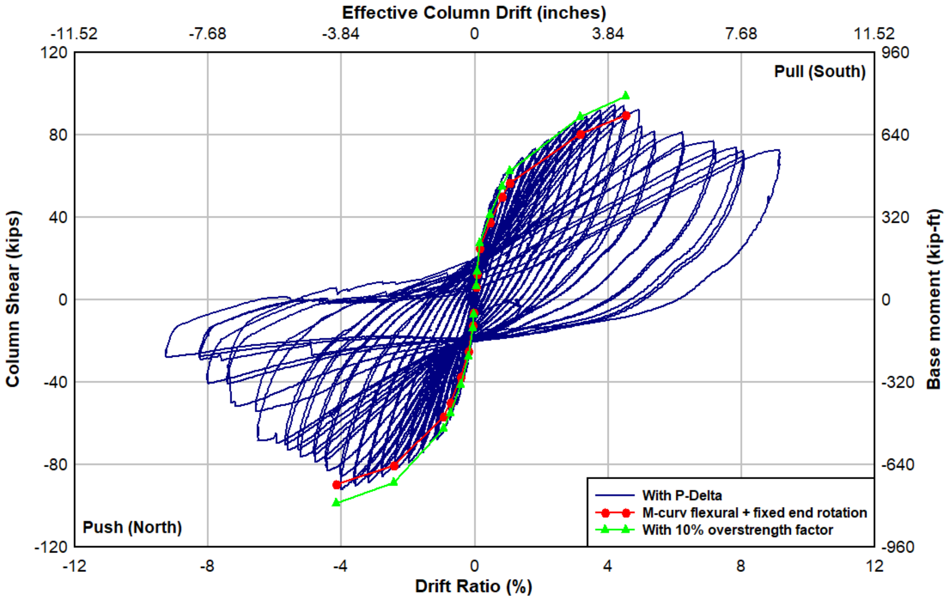

Figure 4.68: Specimen R-S-R-LTi-90: Final predicted response for selected TiAB bonding conditions, footing interface rotations, and over-strength

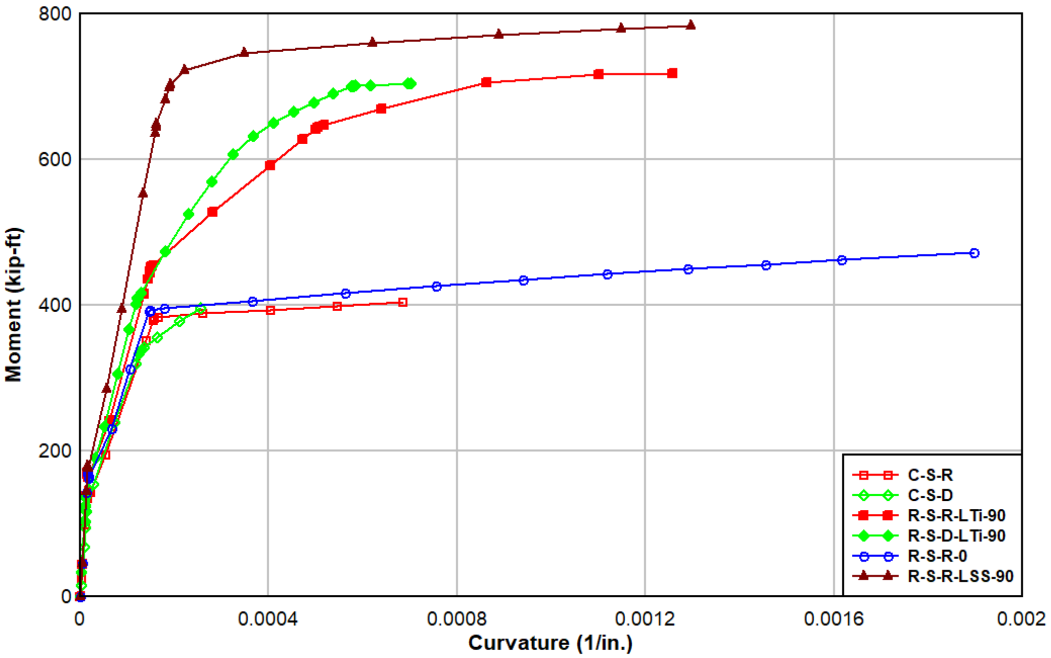

Figure 4.69: Example moment-curvature responses for short columns for selected parameters

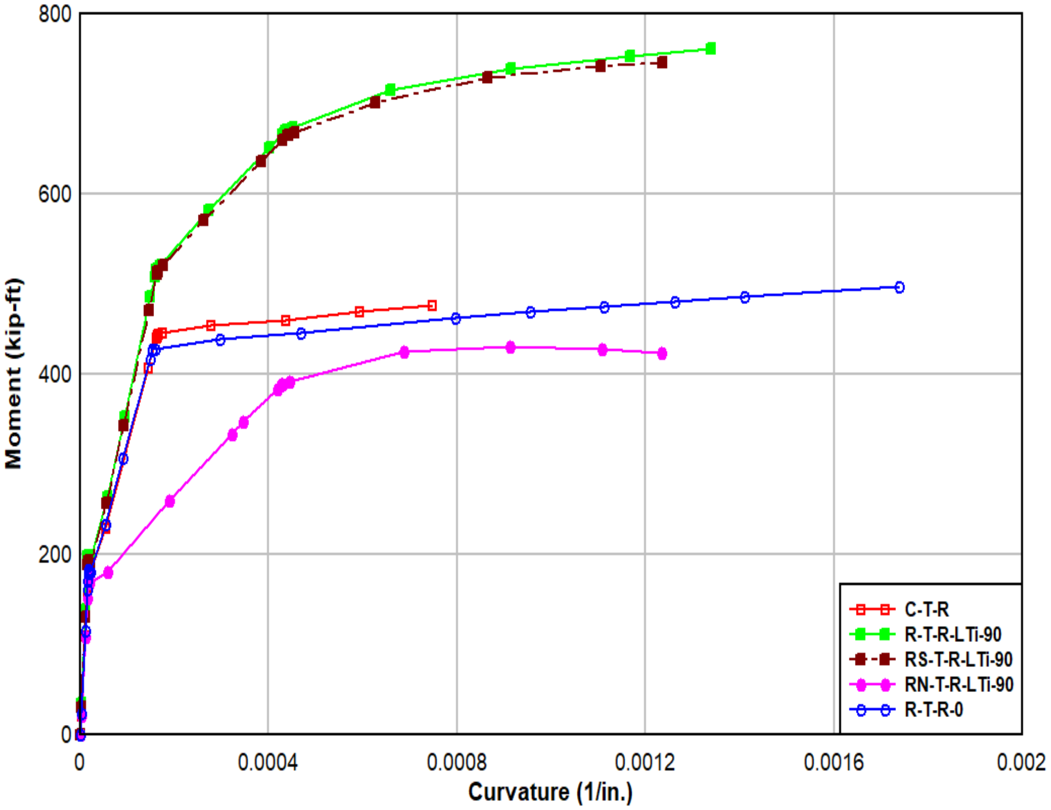

Figure 4.70: Example moment-curvature responses for tall columns for selected parameters

Table 4.11: EI from Moment-Curvature Analysis with Nominal Material Properties

No.	Specimen Name	Uncracked EI [x106],		EI / EI, control (Uncracked)	Cracked EI [x106]		EI / EI, control (Cracked)	EI, cracked / EI, uncracked
		kip-in2	(kN-m2)		kip-in2	(kN-m2)		
1	C-S-R	112	(158)	1.00	30	(43)	1.00	0.27
2	C-S-D	113	(160)	1.00	34	(48)	1.00	0.30
3	R-S-R-LTi-90	138	(194)	1.23	37	(52)	1.21	0.27
4	R-S-D-LTi-90	138	(195)	1.22	41	(58)	1.21	0.30
5	R-S-R-LTi-135	138	(194)	1.23	41	(58)	1.34	0.30
6	R-S-R-0	137	(193)	1.22	33	(46)	1.07	0.24
7	R-S-R-LSS-90	142	(200)	1.27	49	(69)	1.61	0.34
8	R-S-R-LTi-90-Spread	138	(194)	1.23	37	(52)	1.21	0.27
9	R-S-R-LTi-90-Pile	138	(194)	1.23	37	(52)	1.21	0.27
10	C-T-R	113	(159)	1.00	32	(45)	1.00	0.29
11	R-T-R-LTi-90	138	(195)	1.23	39	(55)	1.20	0.28
12	RS-T-R-LTi-90	138	(195)	1.23	39	(55)	1.20	0.28
13	RN-T-R-LTi-90	125	(176)	1.11	11	(15)	0.34	0.09
14	R-T-R-0	137	(194)	1.22	35	(49)	1.08	0.25

Table 4.12: EI from Moment-Curvature Analysis with Measured Material Properties

No.	**Specimen Name**	**Uncracked EI [x10^6],**		**EI / EI, control (Uncracked)**	**Cracked EI [x10^6],**		**EI / EI, control (Cracked)**	**EI, cracked / EI, uncracked**
		kip-in^2			**kip-in^2**			
		(kN-m^2)			**(kN-m^2)**			
1	C-S-R	108	(152)	1.00	29	(41)	1.00	0.27
2	C-S-D	107	(151)	1.00	32	(45)	1.00	0.30
3	R-S-R-LTi-90	137	(194)	1.28	36	(51)	1.23	0.26
4	R-S-D-LTi-90	143	(202)	1.34	41	(57)	1.28	0.28
5	R-S-R-LTi-135	133	(187)	1.23	36	(50)	1.21	0.27
6	R-S-R-0	139	(196)	1.29	32	(45)	1.09	0.23
7	R-S-R-LSS-90	143	(202)	1.33	48	(68)	1.65	0.34
8	R-S-R-LTi-90-Spread	143	(202)	1.33	36	(52)	1.25	0.25
9	R-S-R-LTi-90-Pile	146	(206)	1.36	37	(52)	1.25	0.25
10	C-T-R	128	(181)	1.00	32	(45)	1.00	0.25
11	R-T-R-LTi-90	150	(211)	1.16	38	(54)	1.19	0.26
12	RS-T-R-LTi-90	143	(202)	1.11	38	(53)	1.17	0.26
13	RN-T-R-LTi-90	126	(178)	0.98	11	(15)	0.34	0.09
14	R-T-R-0	132	(187)	1.03	34	(47)	1.04	0.25

4.6 STRENGTH DEGRADATION

The loading profile for both sets of columns comprised of three (3) cycles up to 2% drift and two (2) cycles for the remaining drift levels. The degradation of peak load capacity in terms of column shear and base moment capacity from first to the following cycles were plotted for each drift level versus actual effective column drift in both push (towards North) and pull (towards South) cycles. It was observed that the degradation was not significant for lower drift levels and were prominent as the drift level increased.

Cycle-to-cycle flexural strength degradation within each drift levels were evaluated for both push and pull cycles. Figure 4.71 to Figure 4.84 give a visual representation of strength degradation in each drift level for push-cycles in the negative quadrant and pull-cycles in the positive quadrant. The values of peak loads in each cycle of drift levels are tabulated in Appendix C. For each drift level, each specimen attained maximum capacity in the first cycle and the capacity gradually dropped in the subsequent cycles. Tables comparing the strength degradation in subsequent cycles as compared to the first cycle are also given in Appendix C.

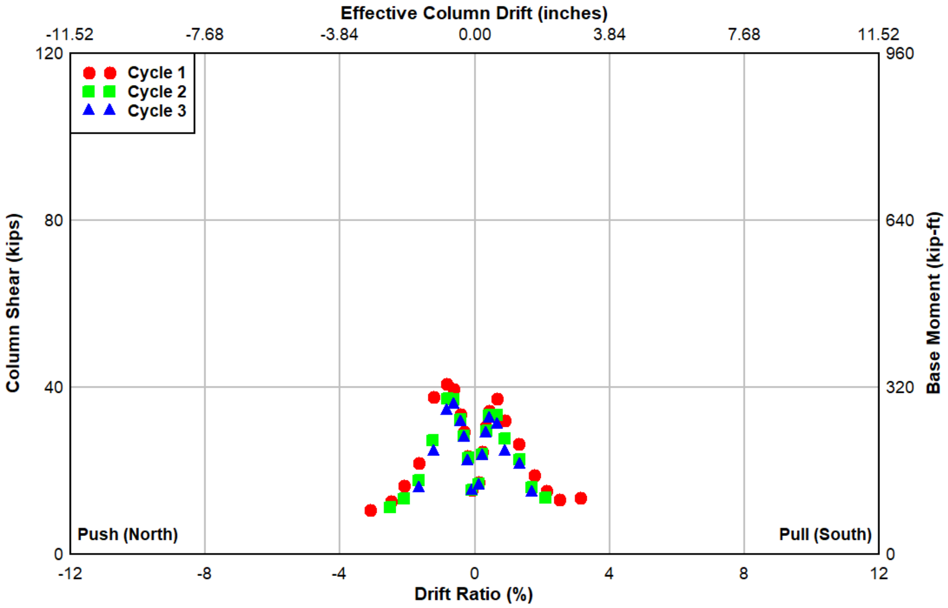

Figure 4.71: Specimen C-S-R: Strength degradation in each cycle

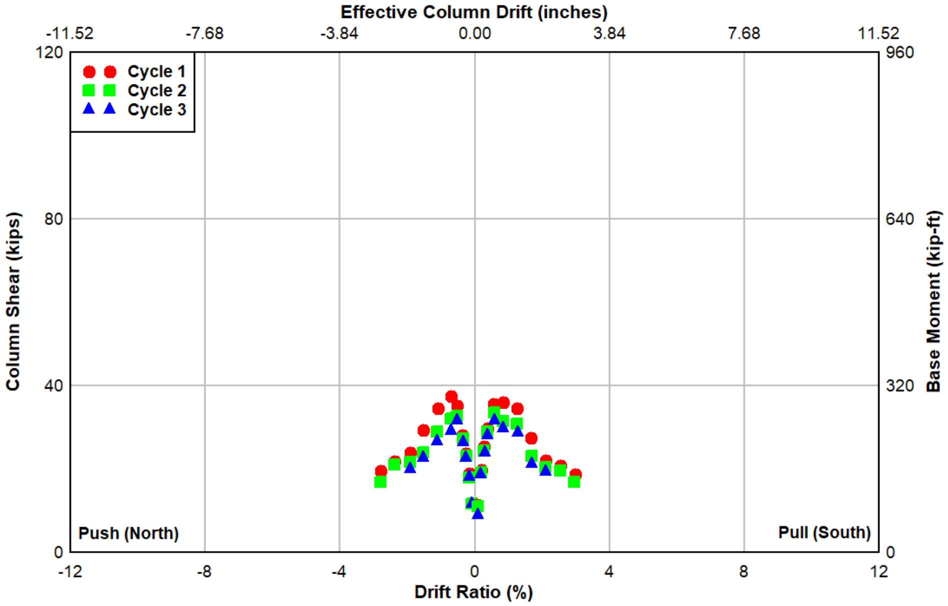

Figure 4.72: Specimen C-S-D: Strength degradation in each cycle

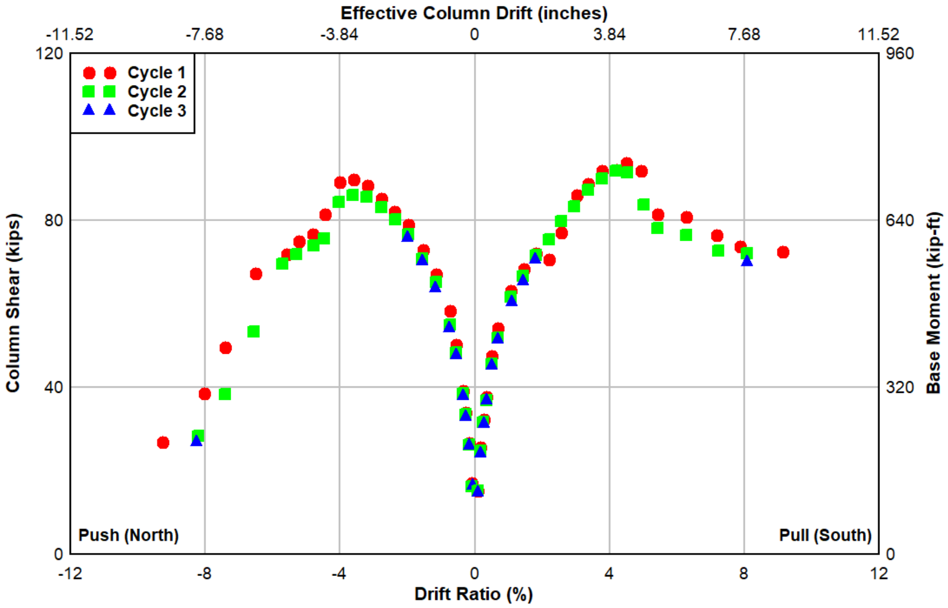

Figure 4.73: Specimen R-S-R-LTi-90: Strength degradation in each cycle

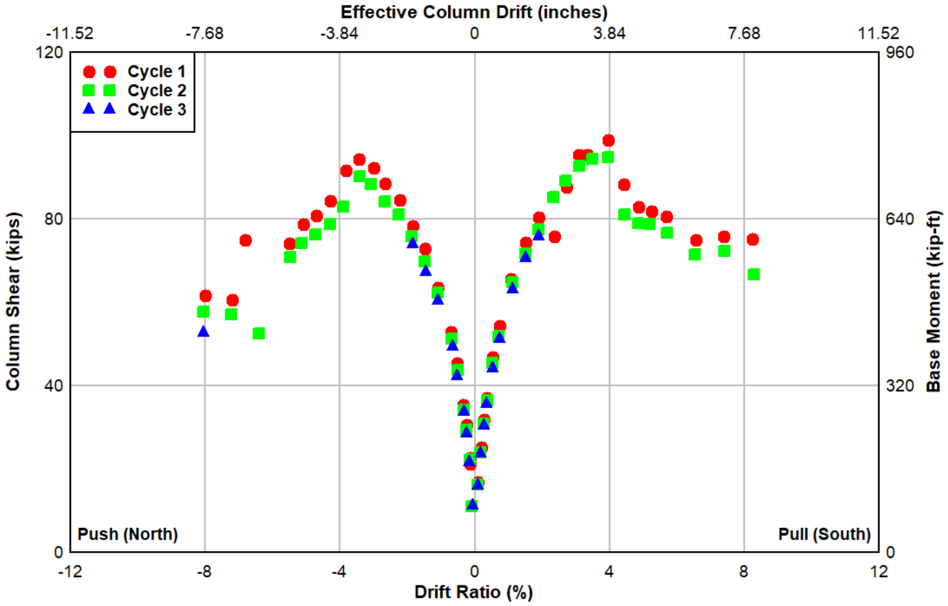

Figure 4.74: Specimen R-S-D-LTi-90: Strength degradation in each cycle

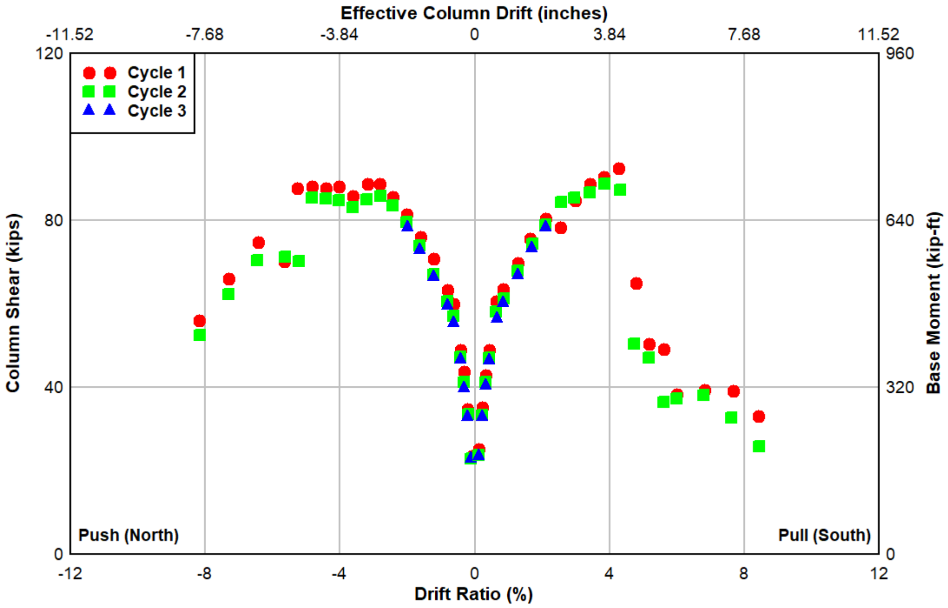

Figure 4.75: Specimen R-S-R-LTi-135: Strength degradation in each cycle

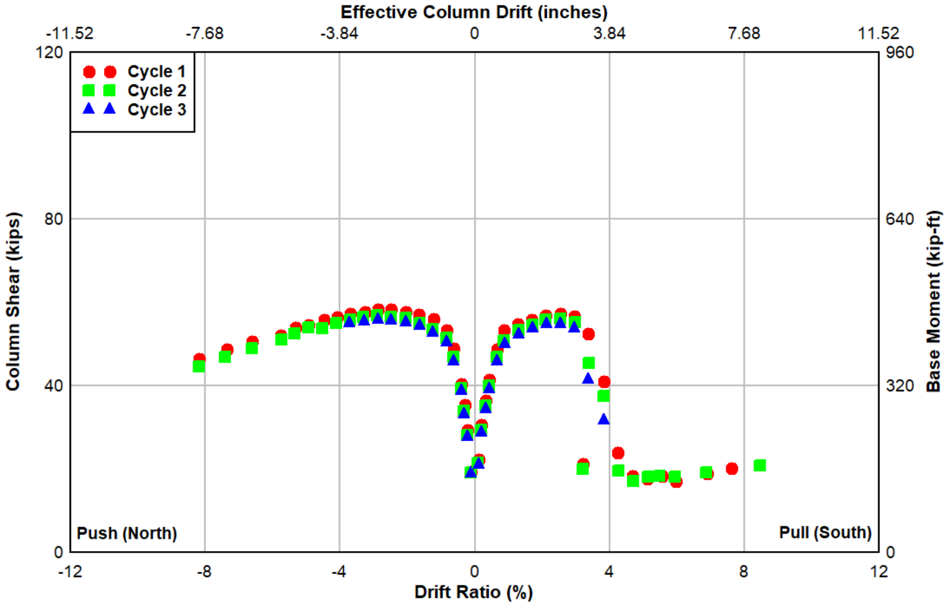

Figure 4.76: Specimen R-S-R-0: Strength degradation in each cycle

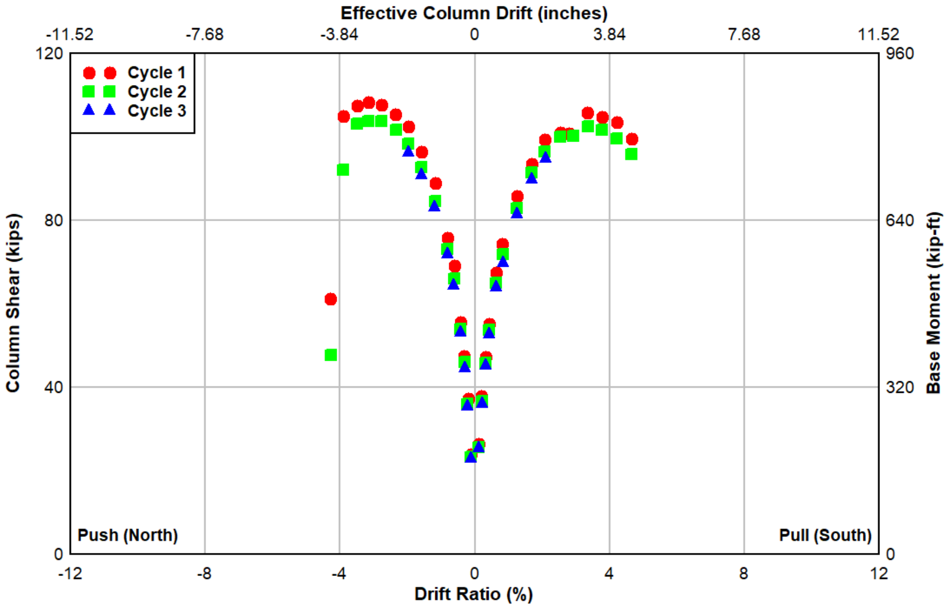

Figure 4.77: Specimen R-S-R-LSS-90: Strength degradation in each cycle

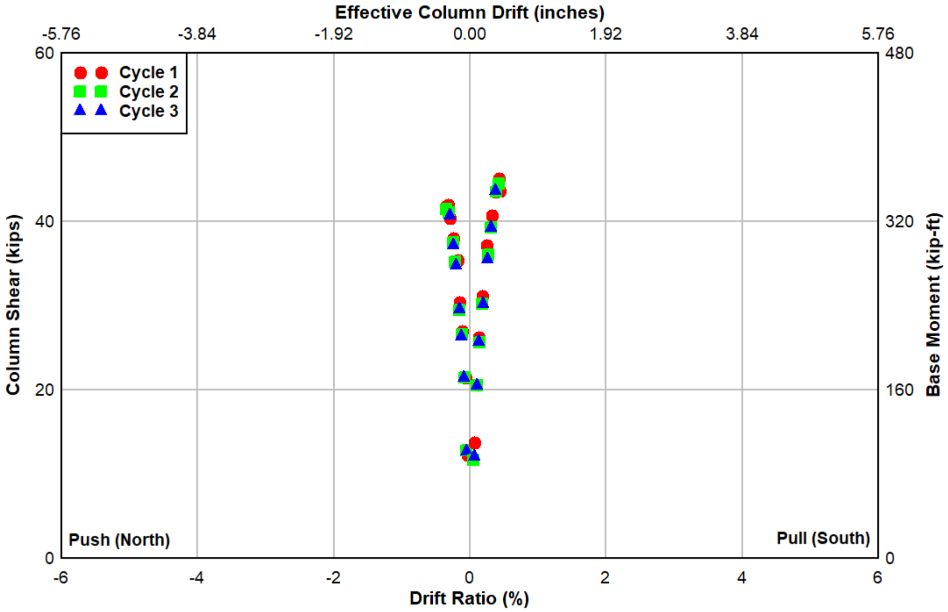

Figure 4.78: Specimen R-S-R-LTi-90-Spread: Strength degradation in each cycle

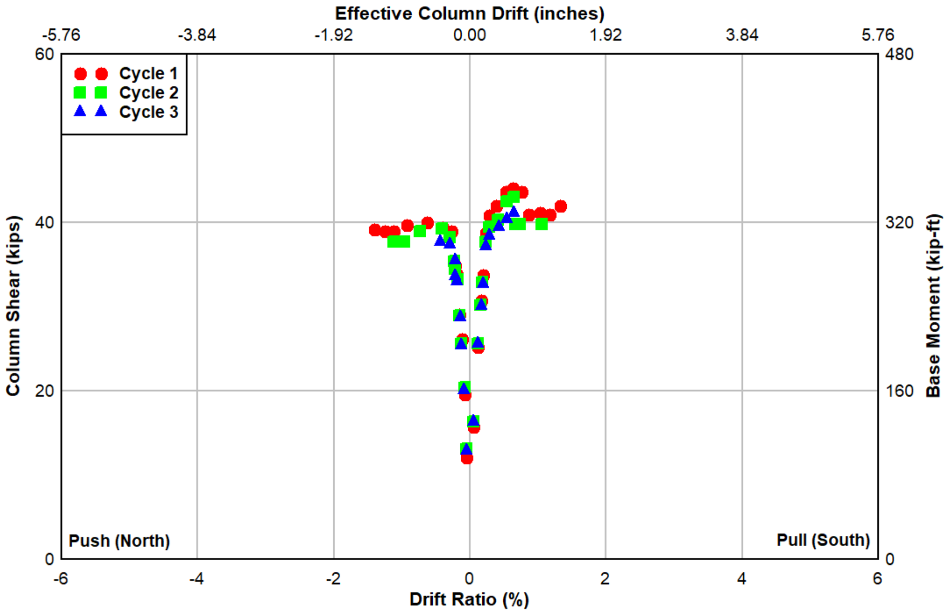

Figure 4.79: Specimen R-S-R-LTi-90-Pile: Strength degradation in each cycle

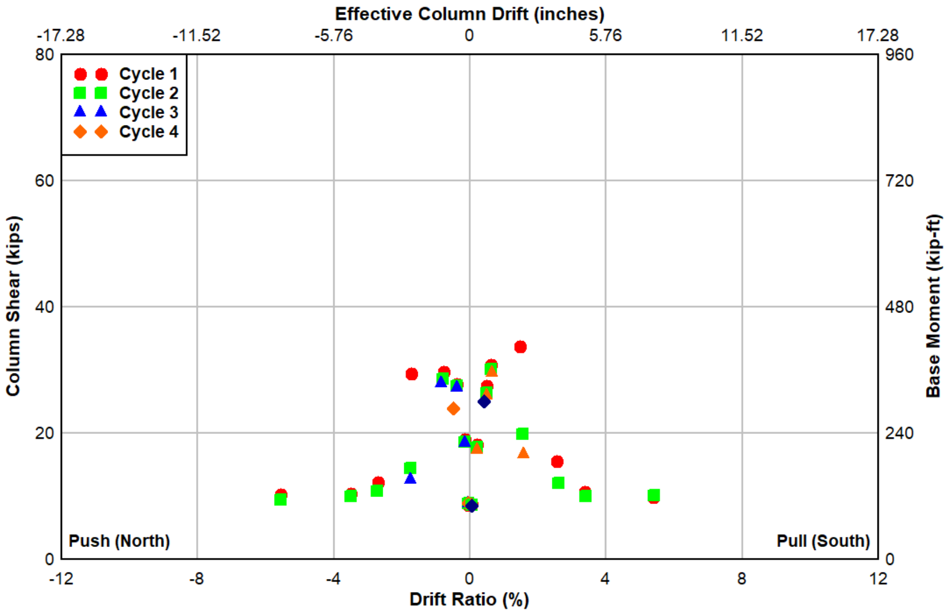

Figure 4.80: Specimen C-T-R: Strength degradation in each cycle

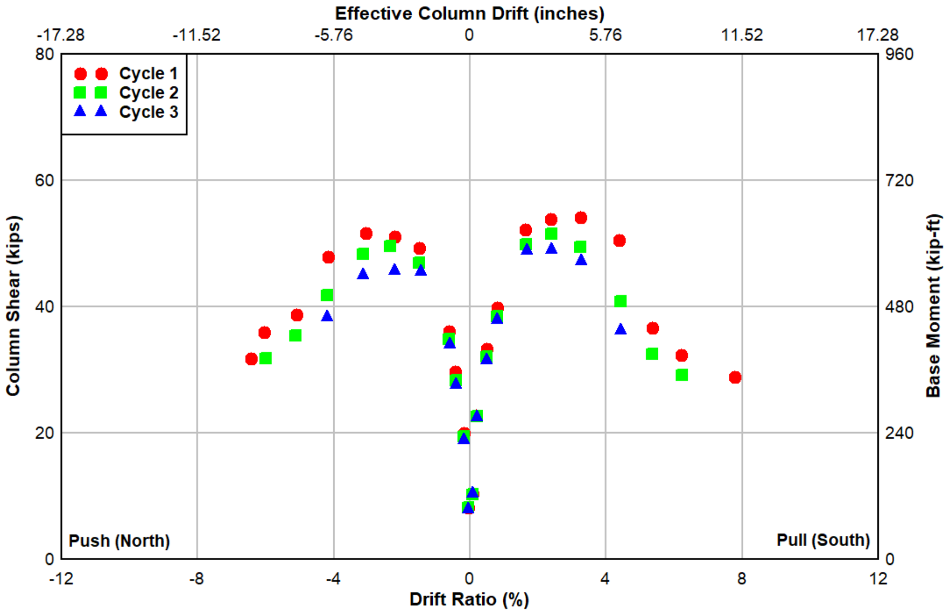

Figure 4.81: Specimen R-T-R-LTi-90: Strength degradation in each cycle

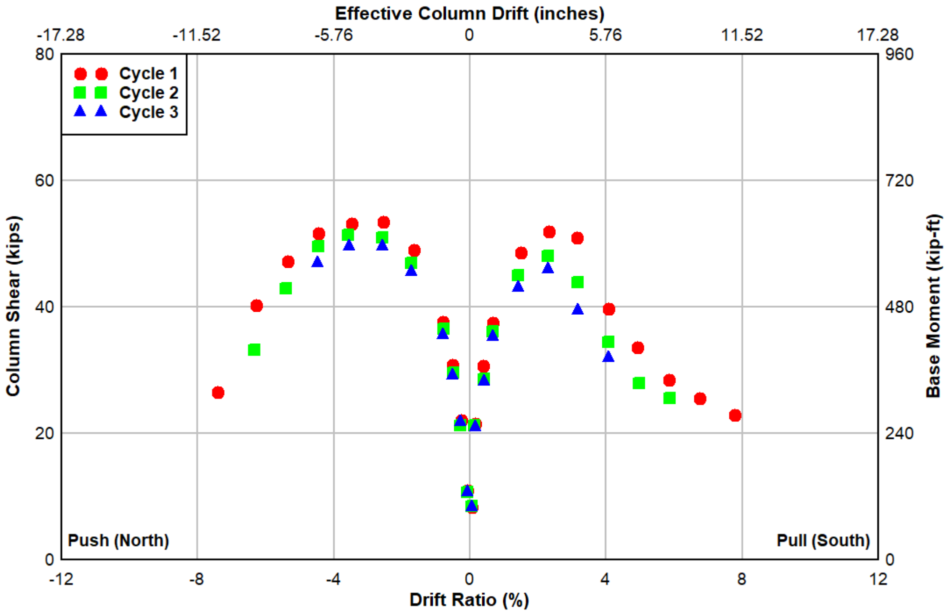

Figure 4.82: Specimen RS-T-R-LTi-90: Strength degradation in each cycle

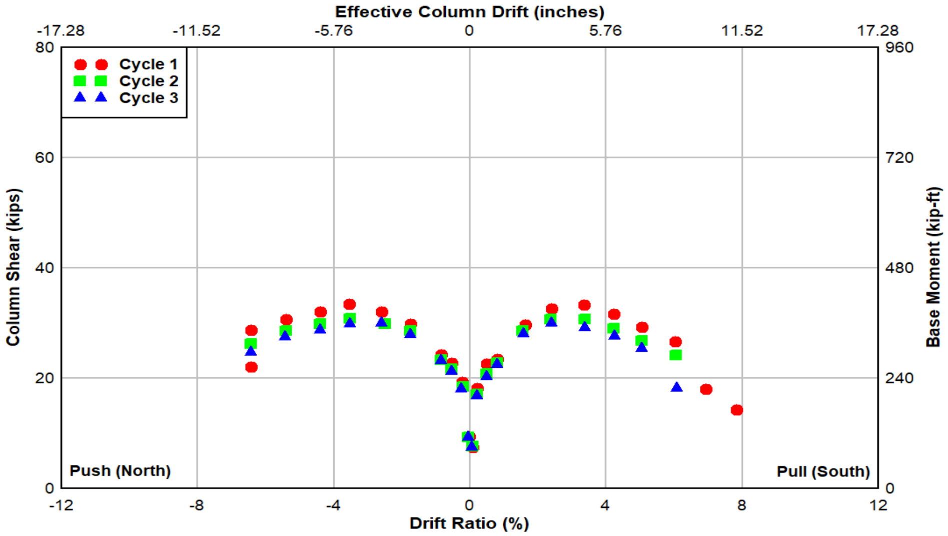

Figure 4.83: Specimen RN-S-R-LTi-90: Strength degradation in each cycle

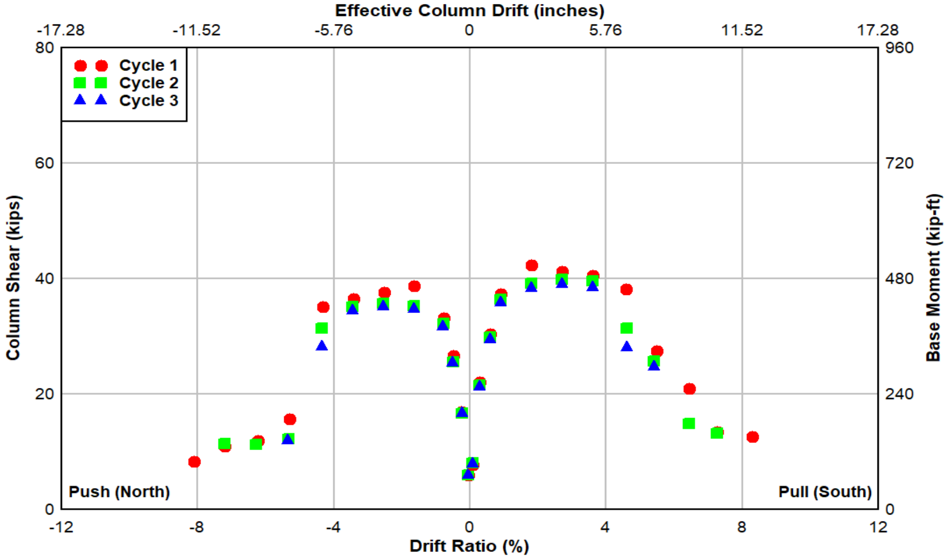

Figure 4.84: Specimen R-T-R-0: Strength degradation in each cycle

4.7 ENERGY DISSIPATION

Energy dissipated by column specimens in each displacement cycle was calculated as the area in the complete loop of each drift cycle obtained by integrating the corrected lateral load-top drift displacement response. The total energy dissipated at each drift level was then calculated as the sum of the total energy dissipated in each cycle at that drift level. Cumulative energy dissipated at each drift level were also compared for the short columns and tall columns as seen in Figure 4.85 and Figure 4.86, respectively. Table 4.13 and Table 4.14 list the cumulative energy dissipation values for each column specimen. Detailed information is given in tables in Appendix C.

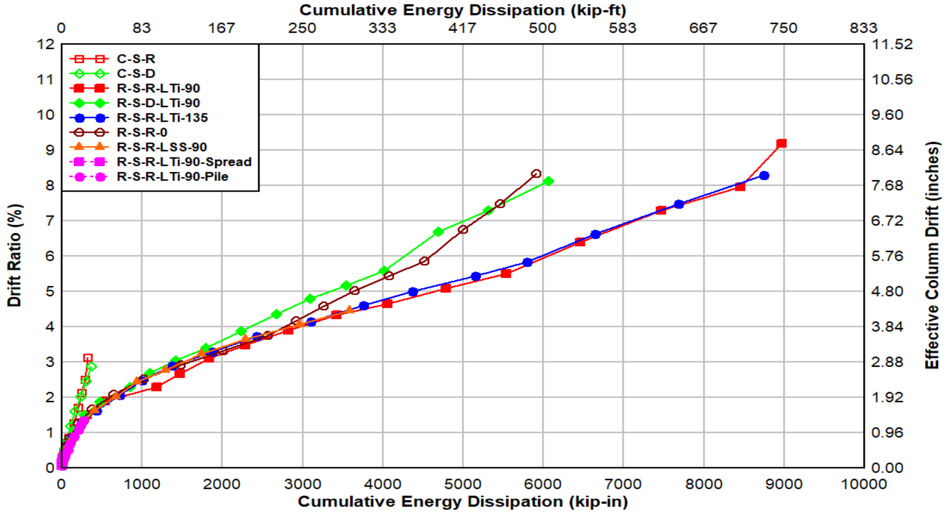

Figure 4.85: Short (8 ft.) specimens: Cumulative energy dissipated

Table 4.13: Short (8 ft.) Specimens: Cumulative Energy Dissipation

Target Drift Cycle,	Cumulative Energy Dissipated, kip-ft. (kN-m)									
in (mm)	C-S-R		C-S-D		R-S-R-LTi-90		R-S-D-LTi-90		R-S-R-LTi-135	
0.1 (2.54)	0.15	(0.21)	0.06	(0.09)	0.19	(0.26)	0.20	(0.27)	0.30	(0.41)
0.2 (5.08)	0.55	(0.75)	0.29	(0.40)	0.65	(0.89)	0.53	(0.72)	0.96	(1.31)
0.3 (7.62)	1.14	(1.55)	0.69	(0.93)	1.45	(1.96)	1.17	(1.58)	2.03	(2.76)
0.4 (10.2)	1.97	(2.67)	1.27	(1.72)	2.49	(3.38)	2.10	(2.85)	3.48	(4.72)
0.6 (15.2)	4.11	(5.58)	2.58	(3.50)	4.40	(5.97)	3.89	(5.28)	6.16	(8.35)
0.8 (20.3)	7.24	(9.81)	4.98	(6.75)	7.28	(9.88)	6.52	(8.84)	10.1	(13.7)
1.2 (30.5)	12.4	(16.8)	8.86	(12.0)	14.08	(19.09)	12.8	(17.4)	19.7	(26.6)
1.6 (40.6)	17.2	(23.3)	13.8	(18.7)	26.0	(35.2)	23.6	(32.0)	35.8	(48.5)
2.0 (50.8)	20.8	(28.2)	19.5	(26.5)	44.5	(60.3)	39.4	(53.4)	60.1	(81.5)
2.4 (60.9)	23.9	(32.5)	24.7	(33.4)	98.3	(133)	70.6	(95.8)	83.6	(113)
2.8 (71.1)	26.6	(36.1)	30.8	(41.8)	122	(166)	91.1	(124)	115	(156)
3.2 (81.3)	-	(-)	-	(-)	153	(208)	118	(159)	156	(212)
3.6 (91.4)	-	(-)	-	(-)	191	(258)	149	(203)	202	(274)
4.0 (102)	-	(-)	-	(-)	235	(319)	186	(252)	259	(351)
4.4 (112)	-	(-)	-	(-)	285	(387)	222	(301)	313	(424)
4.8 (122)	-	(-)	-	(-)	338	(459)	257	(349)	364	(493)
5.2 (132)	-	(-)	-	(-)	399	(540)	295	(399)	429	(581)
5.6 (142)	-	(-)	-	(-)	461	(626)	334	(453)	483	(654)
6.4 (163)	-	(-)	-	(-)	538	(730)	391	(530)	553	(750)
7.2 (183)	-	(-)	-	(-)	623	(844)	443	(600)	640	(868)
8.0 (203)	-	(-)	-	(-)	704	(955)	505	(685)	729	(989)
9.0 (229)	-	(-)	-	(-)	747	(1013)	-	(-)	-	(-)

Table 4.13: Short (8 ft.) Specimens: Cumulative Energy Dissipation (Continued)

Target Drift Cycle,	Cumulative Energy Dissipated, kip-ft. (kN-m)							
in (mm)	R-S-R-0		R-S-R-LSS-90		R-S-R-LTi-90-Spread		R-S-R-LTi-90-Pile	
0.1 (2.54)	0.22	(0.29)	0.25	(0.34)	0.01	(0.02)	0.01	(0.01)
0.2 (5.08)	0.73	(1.00)	0.86	(1.16)	0.06	(0.08)	0.03	(0.04)
0.3 (7.62)	1.55	(2.10)	1.84	(2.50)	0.18	(0.25)	0.16	(0.22)
0.4 (10.2)	2.61	(3.53)	3.31	(4.49)	0.41	(0.56)	0.31	(0.42)
0.6 (15.2)	4.76	(6.46)	5.99	(8.12)	0.79	(1.07)	0.56	(0.75)
0.8 (20.3)	8.10	(11.0)	10.0	(13.5)	1.30	(1.77)	0.92	(1.25)
1.2 (30.5)	16.7	(22.7)	18.7	(25.4)	2.28	(3.09)	2.11	(2.86)
1.6 (40.6)	31.6	(42.9)	33.9	(45.9)	3.10	(4.20)	3.71	(5.03)
2.0 (50.8)	54.0	(73.2)	56.2	(76.2)	3.61	(4.90)	5.92	(8.02)
2.4 (60.9)	84.8	(115)	77.9	(106)	-	(-)	8.48	(11.5)
2.8 (71.1)	123	(167)	107	(145)	-	(-)	12.2	(16.5)
3.2 (81.3)	167	(226)	145	(196)	-	(-)	16.6	(22.5)
3.6 (91.4)	214	(290)	191	(258)	-	(-)	19.1	(26.0)
4.0 (102)	243	(329)	247	(334)	-	(-)	22.3	(30.3)
4.4 (112)	272	(369)	298	(405)	-	(-)	-	(-)
4.8 (122)	304	(413)	-	(-)	-	(-)	-	(-)
5.2 (132)	340	(460)	-	(-)	-	(-)	-	(-)
5.6 (142)	376	(510)	-	(-)	-	(-)	-	(-)
6.4 (163)	417	(565)	-	(-)	-	(-)	-	(-)
7.2 (183)	455	(617)	-	(-)	-	(-)	-	(-)
8.0 (203)	493	(668)	-	(-)	-	(-)	-	(-)
9.0 (229)	-	(-)	-	(-)	-	(-)	-	(-)

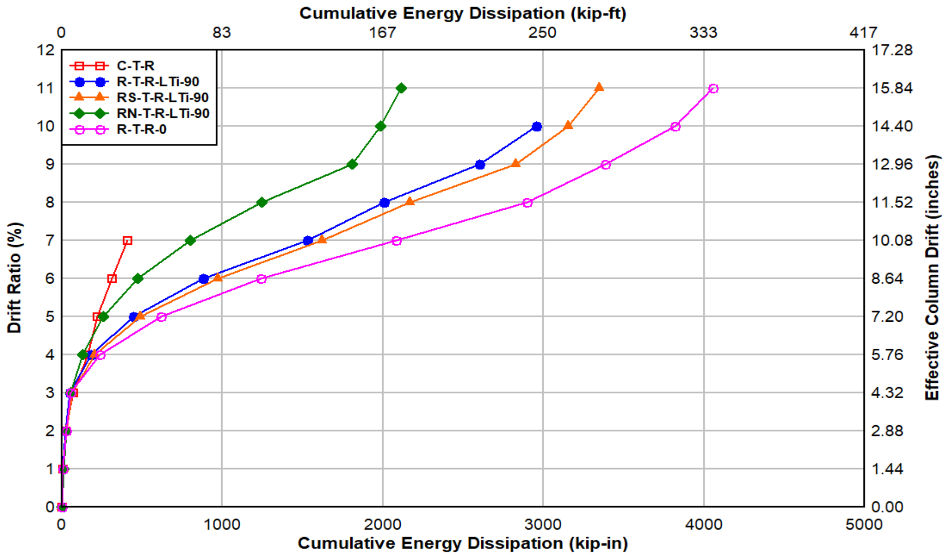

Figure 4.86: Tall (12 ft.) specimens: Cumulative energy dissipated

Table 4.14: Tall (12 ft.) Specimens: Cumulative Energy Dissipation

Target Drift Cycle,	Cumulative Energy Dissipated, kip-ft. (kN-m)									
in (mm)	C-T-R		R-T-R-LTi-90		RS-T-R-LTi-90		RN-T-R-LTi-90		R-T-R-0	
0.144 (3.66)	0.07	(0.09)	0.05	(0.07)	0.12	(0.16)	0.10	(0.13)	0.07	(0.09)
0.43 (10.9)	0.35	(0.47)	0.42	(0.56)	0.69	(0.93)	0.71	(0.96)	0.52	(0.71)
0.86 (21.8)	1.86	(2.53)	1.68	(2.28)	2.40	(3.25)	2.27	(3.08)	2.03	(2.75)
1.30 (33.0)	5.81	(7.88)	3.95	(5.36)	5.16	(7.00)	4.38	(5.94)	4.47	(6.06)
2.59 (65.8)	13.3	(18.1)	15.2	(20.7)	16.9	(22.9)	10.8	(14.6)	19.7	(26.7)
3.89 (98.8)	18.4	(24.9)	37.2	(50.4)	40.9	(55.4)	21.3	(28.8)	51.4	(69.7)
5.18 (131)	25.8	(35.0)	73.3	(99.3)	80.9	(110)	39.1	(53.1)	103	(140)
6.50 (165)	33.8	(45.8)	127	(173)	135	(183)	66.5	(90.1)	173	(235)
7.80 (198)	-	(-)	167	(227)	181	(245)	104	(141)	242	(328)
9.10 (231)	-	(-)	217	(294)	235	(319)	151	(204)	282	(382)
10.4 (264)	-	(-)	246	(334)	263	(356)	165	(224)	318	(431)
11.8 (300)	-	(-)	-	(-)	279	(378)	176	(239)	338	(458)

Looking at the energy dissipation of short column specimens with tied footings, the total energy dissipation for control specimens C-S-R and C-S-D was 26.6 kip-ft. (36.1 kN-m) and 30.8 kip-ft. (41.8 kN-m) respectively which were the lowest values when compared to the rest of the specimens. These values were lower even when compared to the cumulative energy dissipation values of other specimens at 2.8 in (71.1 mm) drift level when the testing of the control specimens was terminated. Ignoring one extra cycle at 9.0 in (229 mm) drift level for specimen R-S-R-LTi-90, the highest energy dissipation was 729 kip-ft. (989 kN-m) for specimen R-S-R-LTi-135 followed by 704 kip-ft. (111 kN-m) for specimen R-S-R-LTi-90. Total energy dissipated by specimen R-S-R-0 was 493 kip-ft. (668 kN-m) which was lower than the specimen with TiAB ligaments having foam insulation located under the shell. This shows that effective confinement with just the retrofit shell can be effective in improving the overall performance of the column specimen, which can be further improved by the addition of TiAB ligaments. The energy dissipated by standard retrofitted specimen with TiAB ligaments: R-S-R-LTi-90 and stainless steel ligaments: R-S-R-LTi-90 were comparable at each drift level. However, over-strength of the stainless steel ligaments resulted in failure of the column above the retrofit shell.

For every column specimen, it was observed that the energy dissipated in the first cycle of each drift level was highest and then it gradually decreased in the subsequent cycles. The drift levels were expressed as the ratio of the lateral drift to the reference yield drift.

4.8 EQUIVALENT VISCOUS DAMPING

Equivalent viscous damping, ξ, is typically assumed as 5% for most concrete structures in seismic design and evaluation. The equivalent viscous damping produced by each of the specimens was established by considering the amount of energy stored and dissipated in each cycle. For a symmetric cyclic behavior of a structure or component as illustrated in Figure 4.87, the equivalent viscous damping is calculated as:

$$\textbf{Viscous Damping, } \xi = \frac{1}{4\pi}\frac{\textbf{Energy Stored}}{\textbf{Energy Dissipated}} \tag{4-21}$$

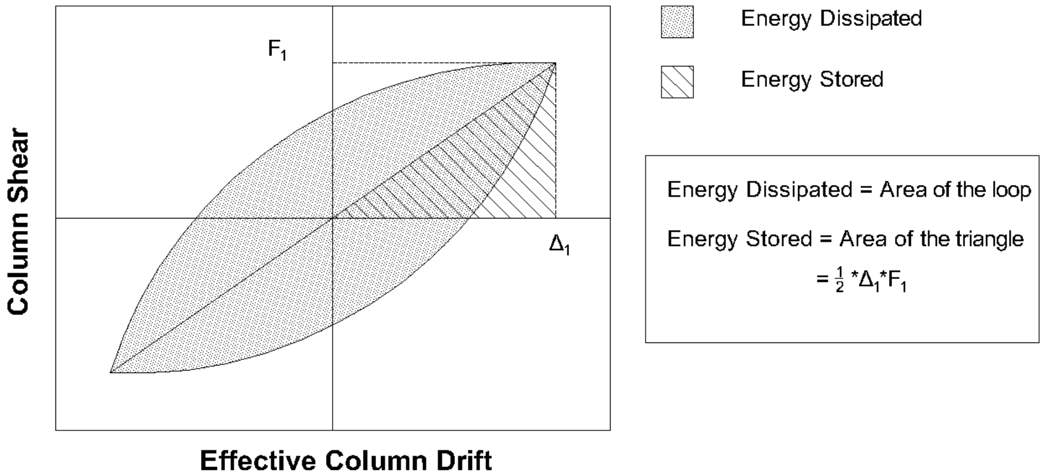

Figure 4.87: Parameters used to compute equivalent viscous damping

For the specimens tested, the cyclic behaviors were not exactly symmetrical for push- and pull-cycles. Thus, the energy stored (area of the right triangle made by the peak point with the origin) was calculated for both push- and pull-cycle separately. The equivalent viscous damping was then compared for each drift level in both push- and pull-cycles.

Figure 4.88 through Figure 4.101 show the evolution of equivalent viscous damping for the test specimens in each cycle at different drift levels. The viscous damping values ranged on average from 5% to 15% for all specimens, with larger values at higher cycles. The equivalent viscous damping distribution of each specimen demonstrated a similar trend. The values of viscous damping of all specimens with tied footings were seen to be approximately 10% initially and then gradually drop to about 5% at approximately 0.6% drift level (estimated first yield of the longitudinal bars) and then were seen to pick up to about 15%. Some specimens showed even higher damping beyond 4% drift level due to larger energy dissipation. Lower values of equivalent viscous damping were observed in the case of specimen R-S-R-LTi-90-Spread which are the result of elastic behavior of the column without any significant damage.

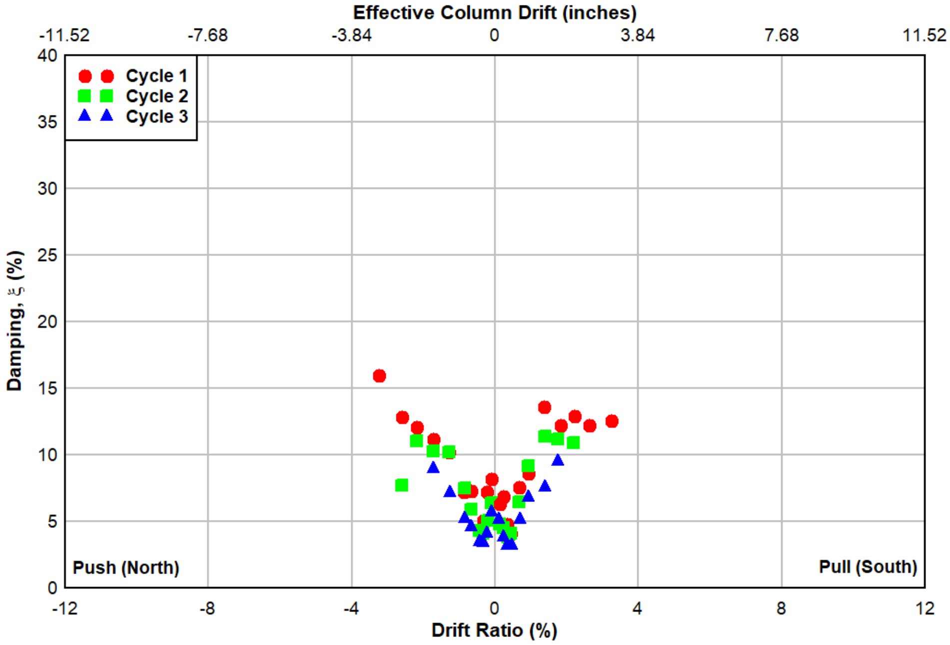

Figure 4.88: Specimen C-S-R: Equivalent viscous damping in each cycle

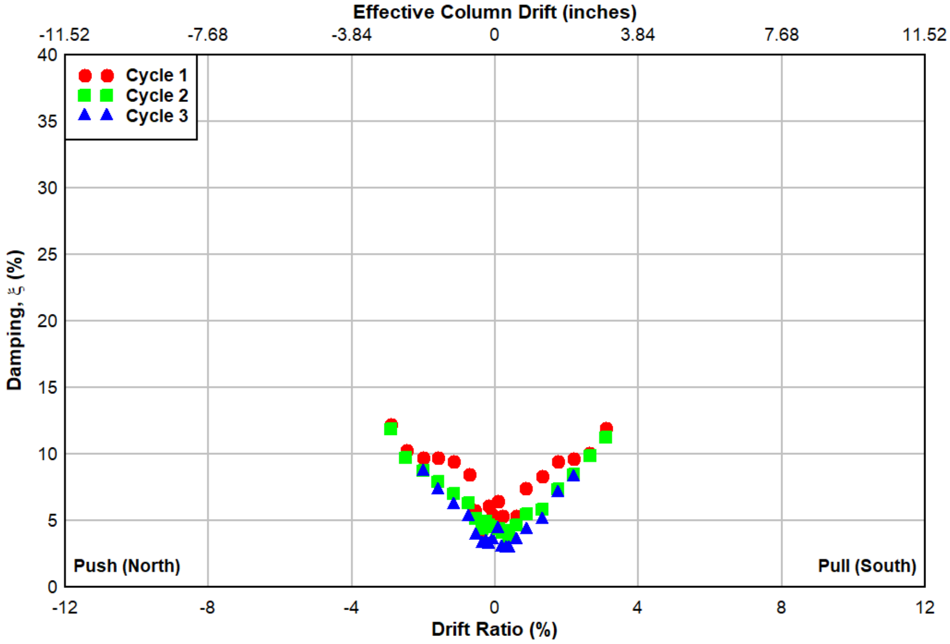

Figure 4.89: Specimen C-S-D: Equivalent viscous damping in each cycle

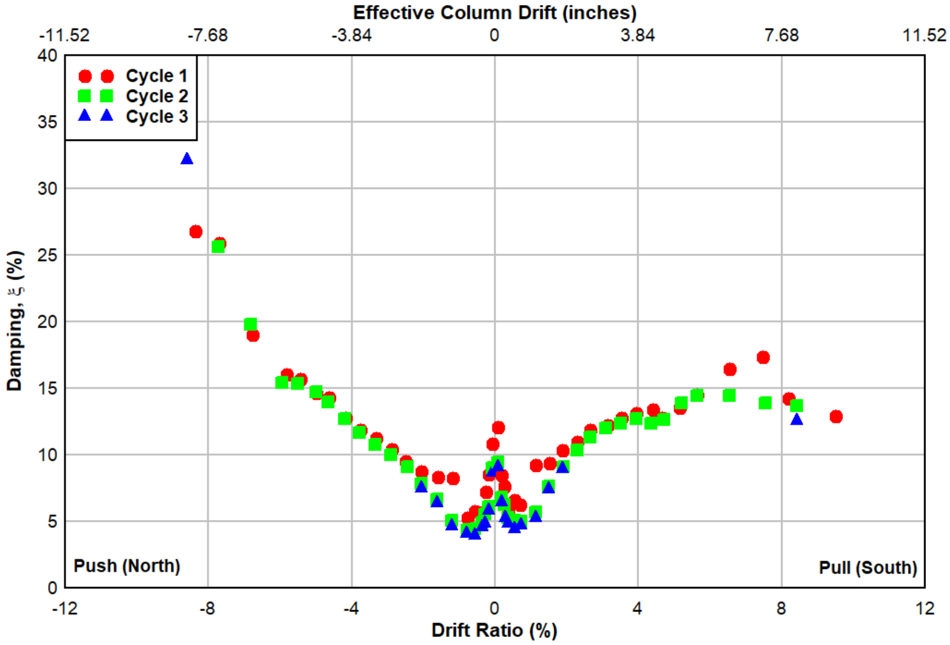

Figure 4.90: Specimen R-S-R-LTi-90: Equivalent viscous damping in each cycle

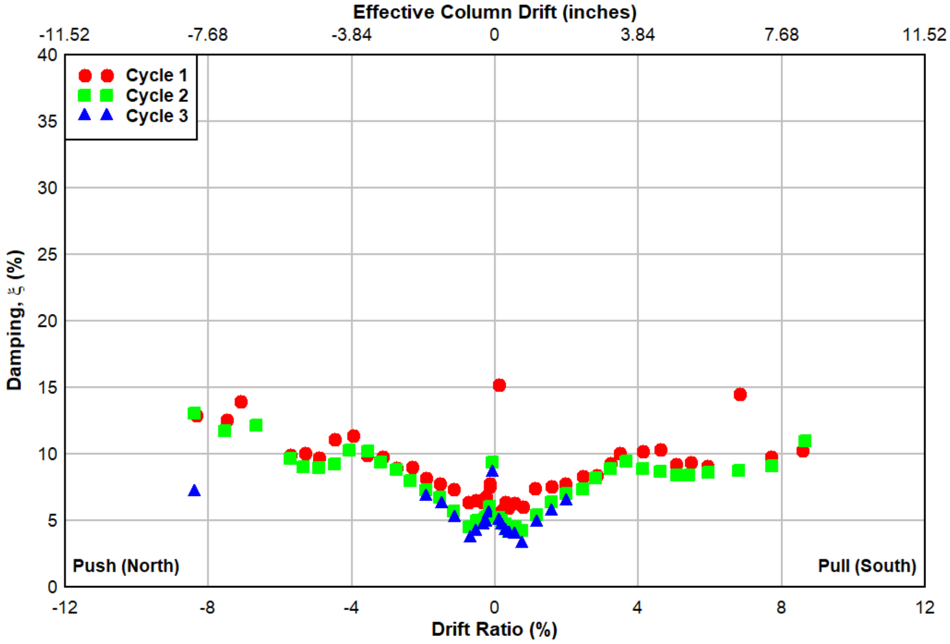

Figure 4.91: Specimen R-S-D-LTi-90: Equivalent viscous damping in each cycle

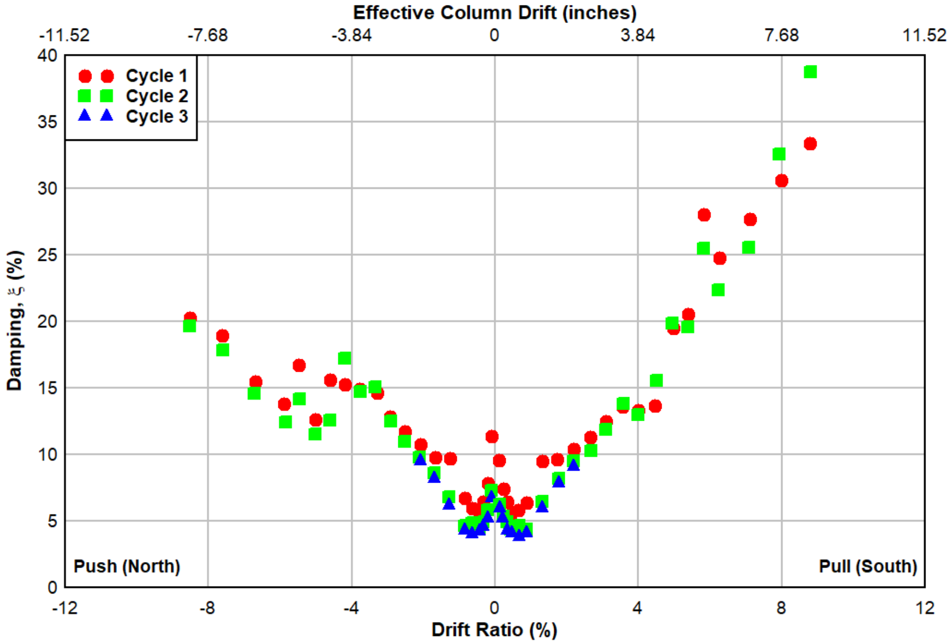

Figure 4.92: Specimen R-S-R-LTi-135: Equivalent viscous damping in each cycle

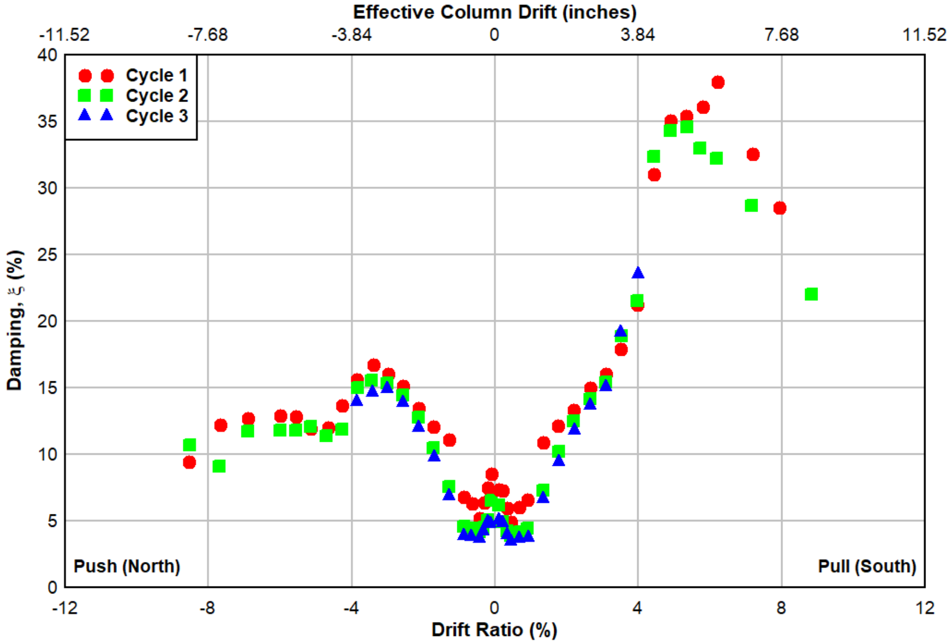

Figure 4.93: Specimen R-S-R-0: Equivalent viscous damping in each cycle

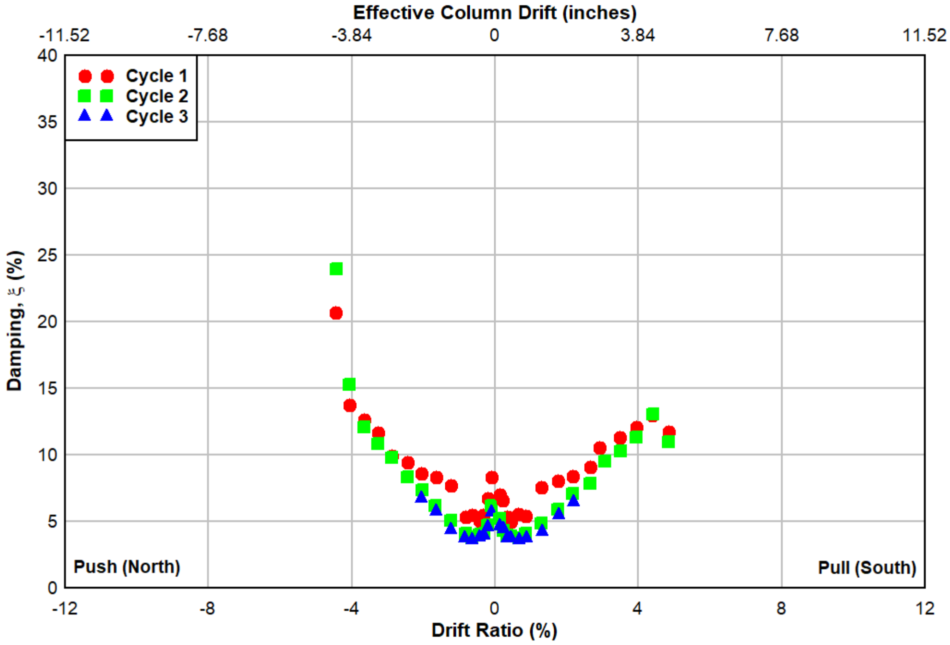

Figure 4.94: Specimen R-S-R-LSS-90: Equivalent viscous damping in each cycle

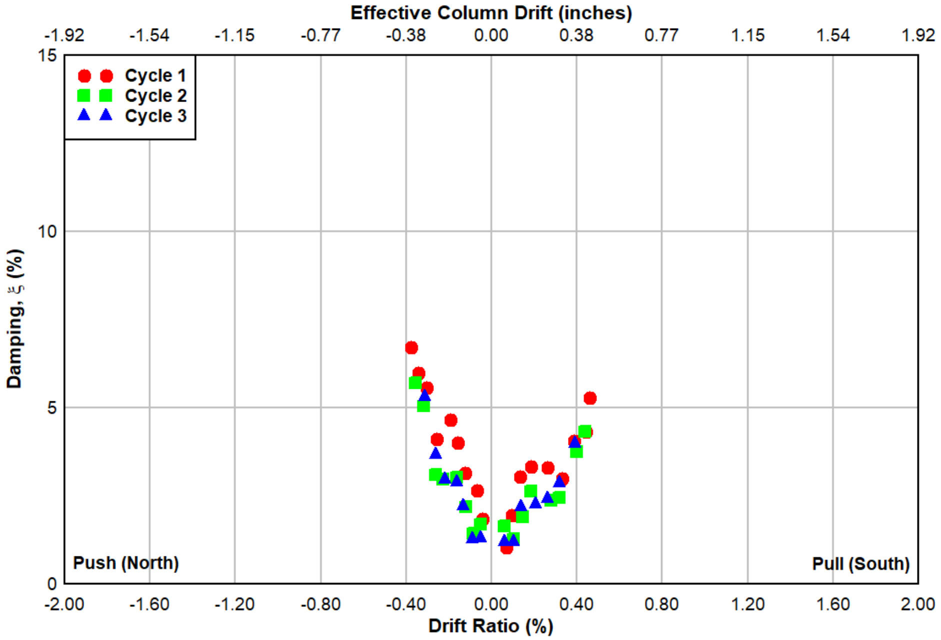

Figure 4.95: Specimen R-S-R-LTi-90-Spread: Equivalent viscous damping in each cycle

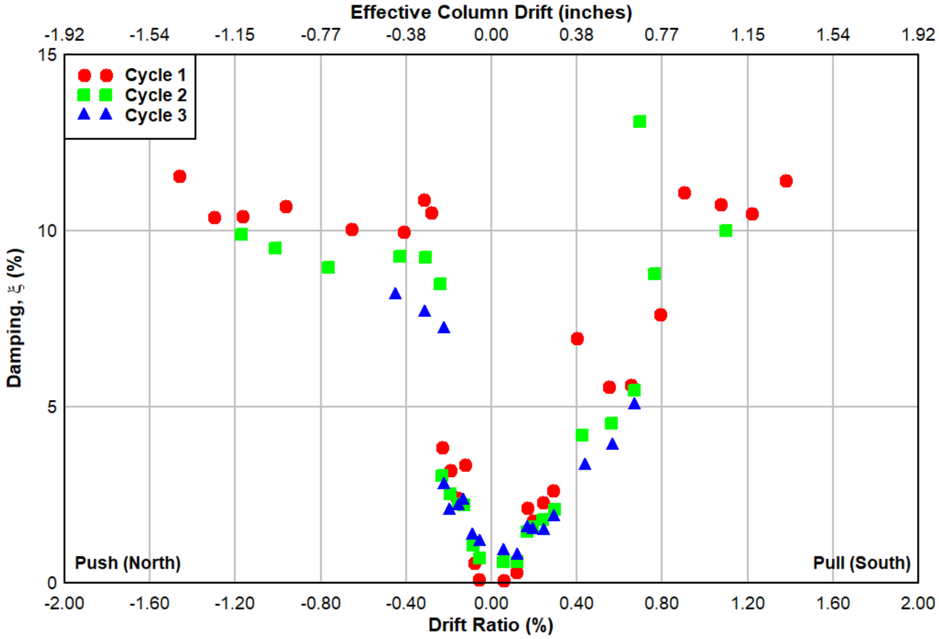

Figure 4.96: Specimen R-S-R-LTi-90-Pile: Equivalent viscous damping in each cycle

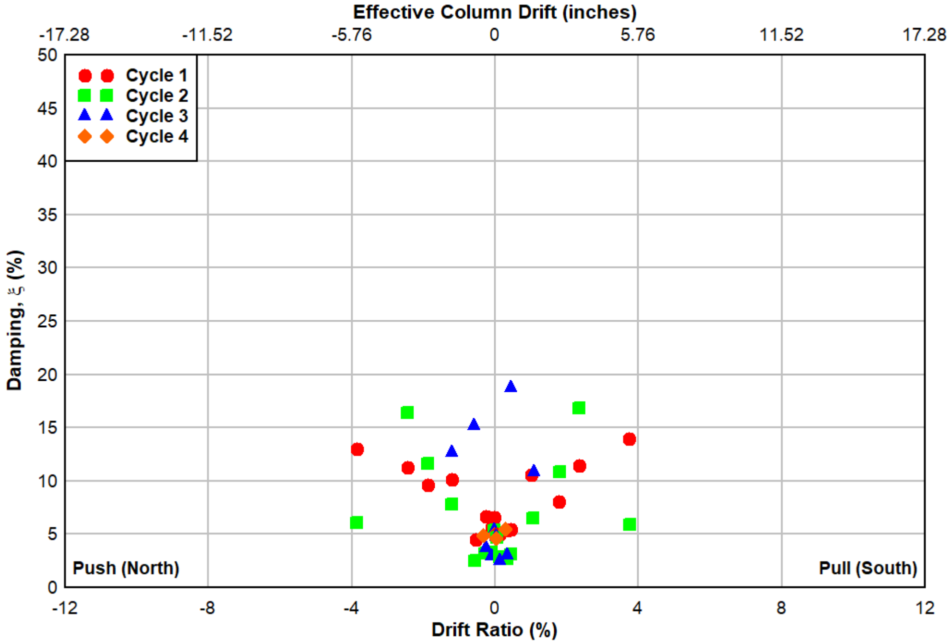

Figure 4.97: Specimen C-T-R: Equivalent viscous damping in each cycle

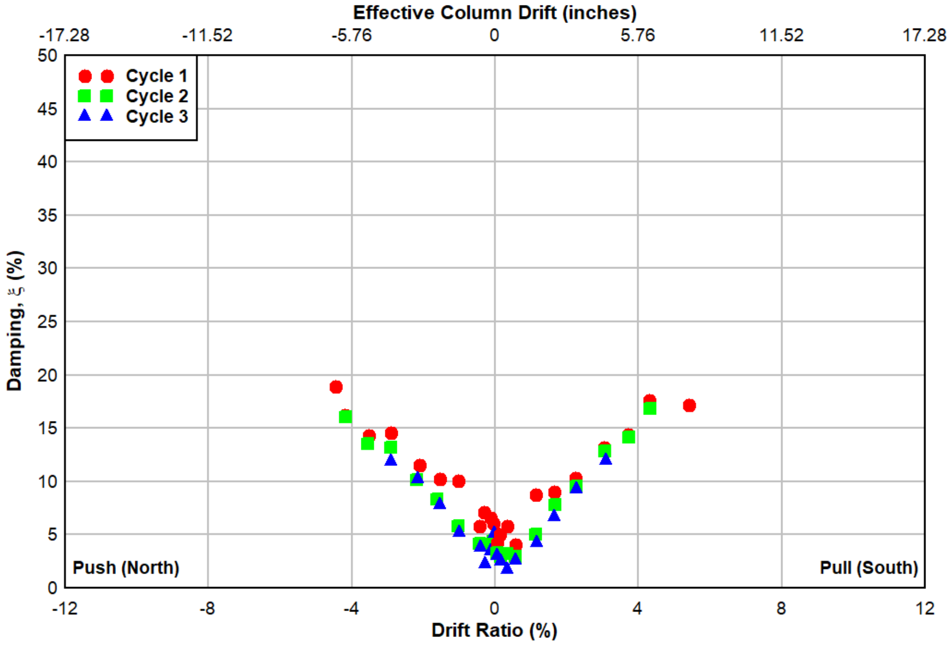

Figure 4.98: Specimen R-T-R-LTi-90: Equivalent viscous damping in each cycle

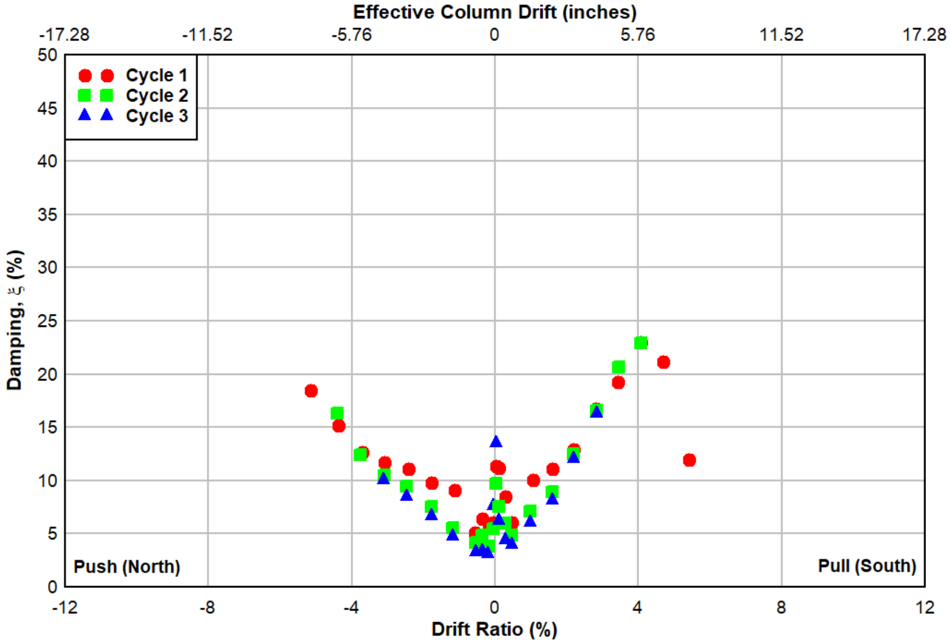

Figure 4.99: Specimen RS-T-R-LTi-90: Equivalent viscous damping in each cycle

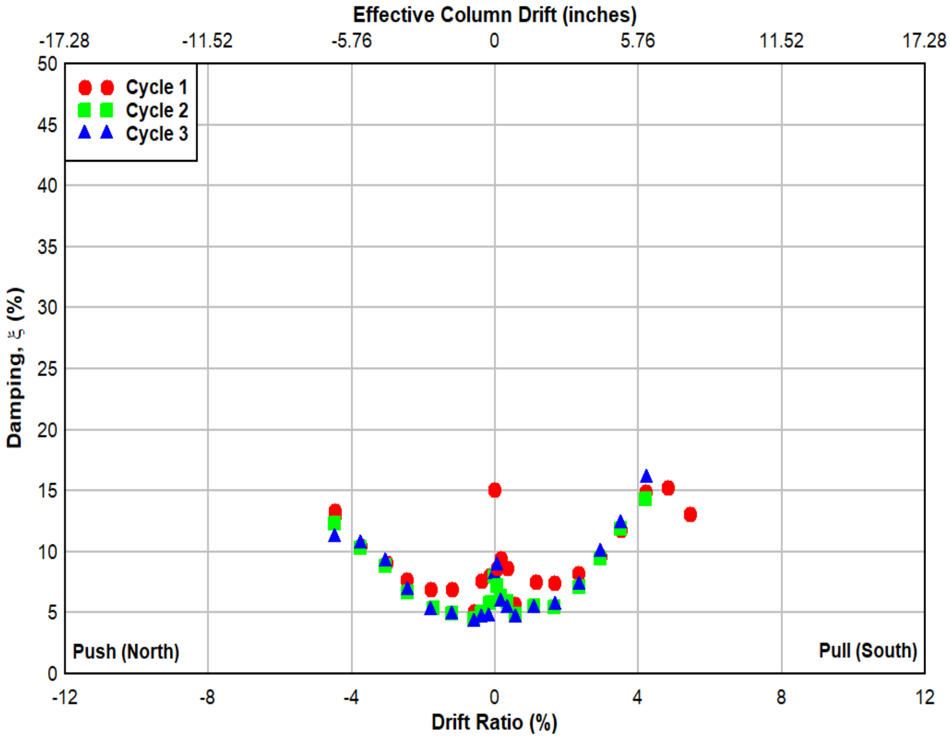

Figure 4.100: Specimen RN-T-R-LTi-90: Equivalent viscous damping in each cycle

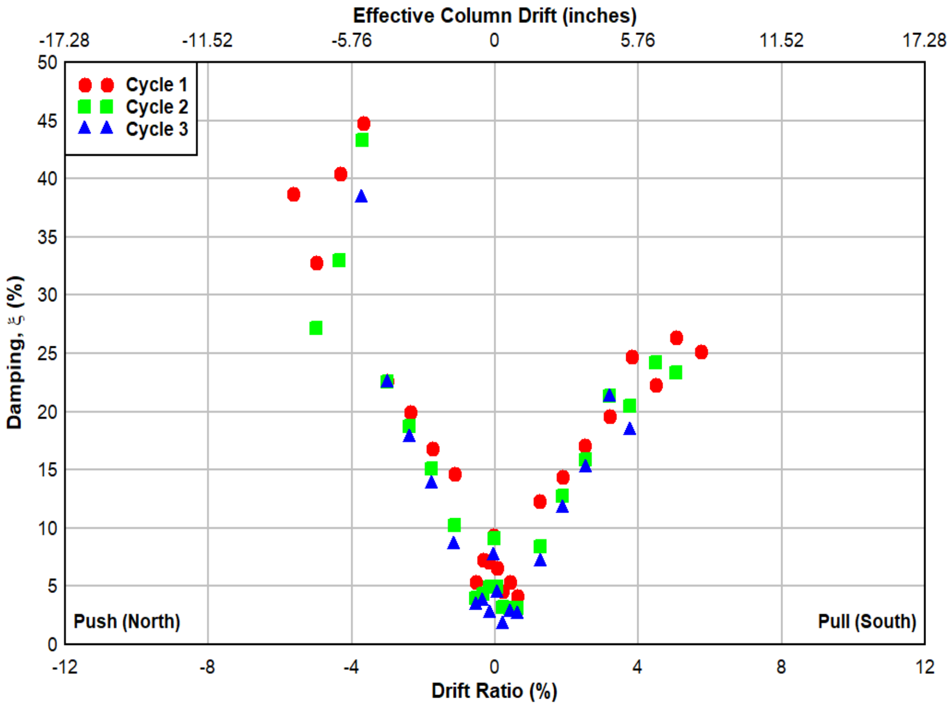

Figure 4.101: Specimen R-T-R-0: Equivalent viscous damping in each cycle

4.9 STIFFNESS DEGRADATION

The secant and tangent stiffness of each specimen were calculated from the backbone of the cyclic response for each column. The backbone curve for the effective column drift versus the column shear capacity was differentiated with respect to the effective column drift to get the tangent stiffness variation at different drift levels. The slope of lines connecting the origin to the points on the backbone were calculated to obtain the secant stiffness. The tangent and secant stiffness of each column was plotted to compare their variation. The tangent stiffness and secant stiffness were compared for all short column specimens and tall column specimens, separately.

The tangent and secant stiffness for short specimens are shown in Figure 4.102 and Figure 4.103, respectively. The tangent and secant stiffness for tall specimens are shown in Figure 4.104 and Figure 4.105, respectively. The results show similar evolution over a test, with stiffness remaining high in the elastic region and transitioning to softer response at larger drifts due to concrete cracking, and slip and/or yielding of the reinforcing. The stiffness of the stainless steel specimen was larger than the other specimens. The tangent stiffness tended toward zero at drifts of about 4% for the short columns, and about 3% for the tall columns. The control specimens lost stiffness at much smaller drifts compared to the retrofitted specimens.

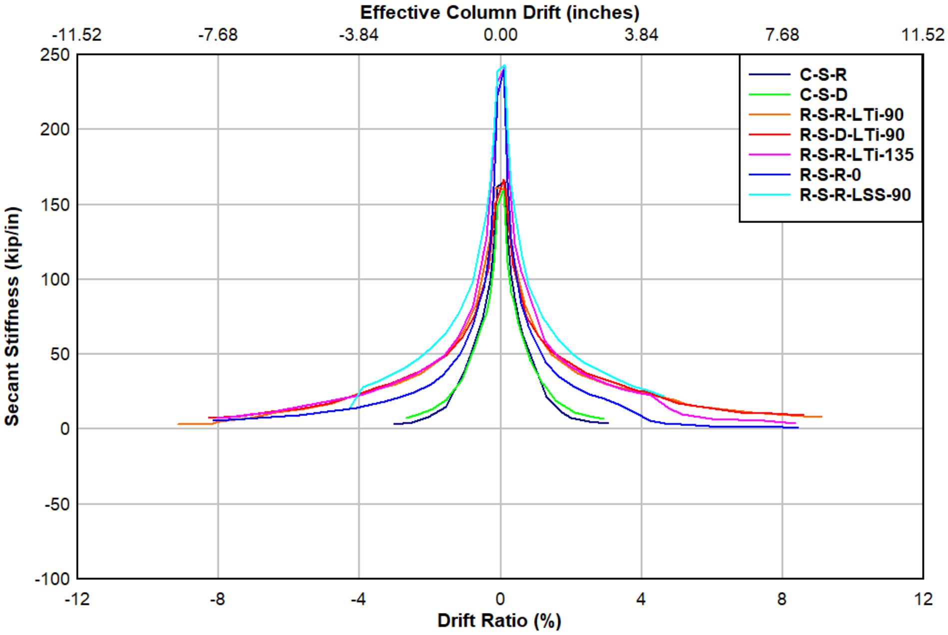

Figure 4.102: Short (8 ft.) specimens: Evolution of secant stiffness

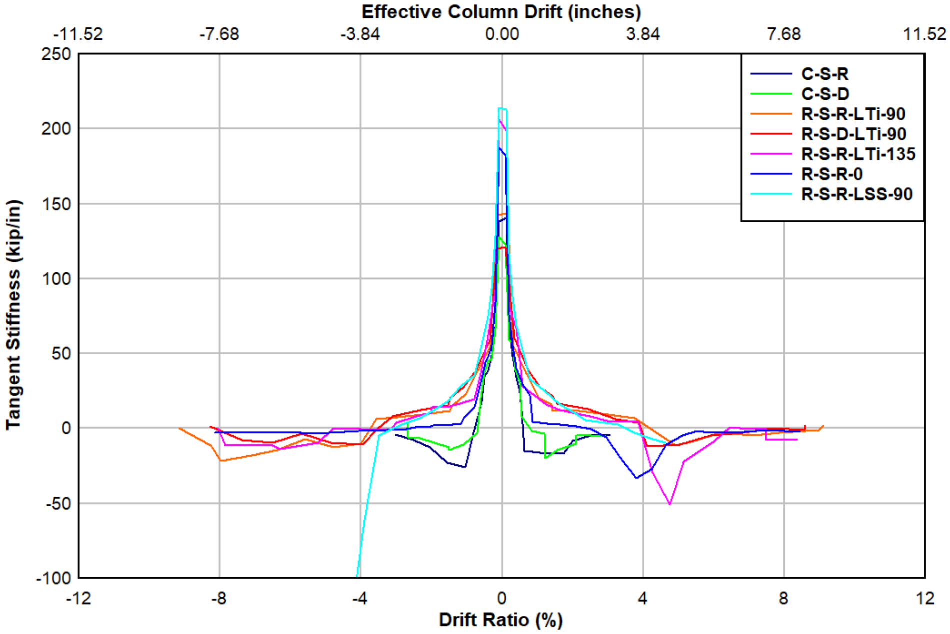

Figure 4.103: Short (8 ft.) specimens: Evolution of tangent stiffness

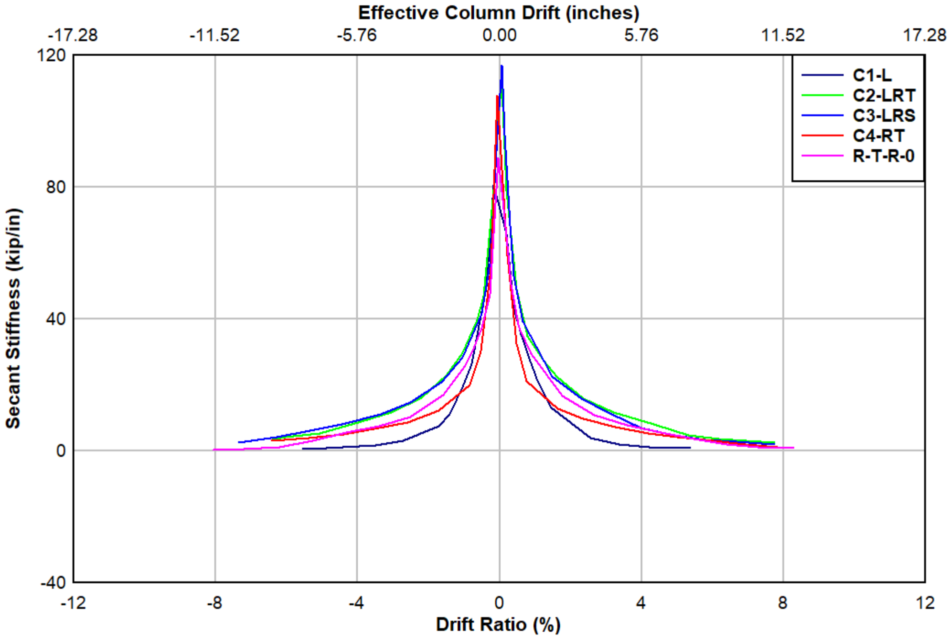

Figure 4.104: Tall (12 ft.) specimens: Evolution of secant stiffness

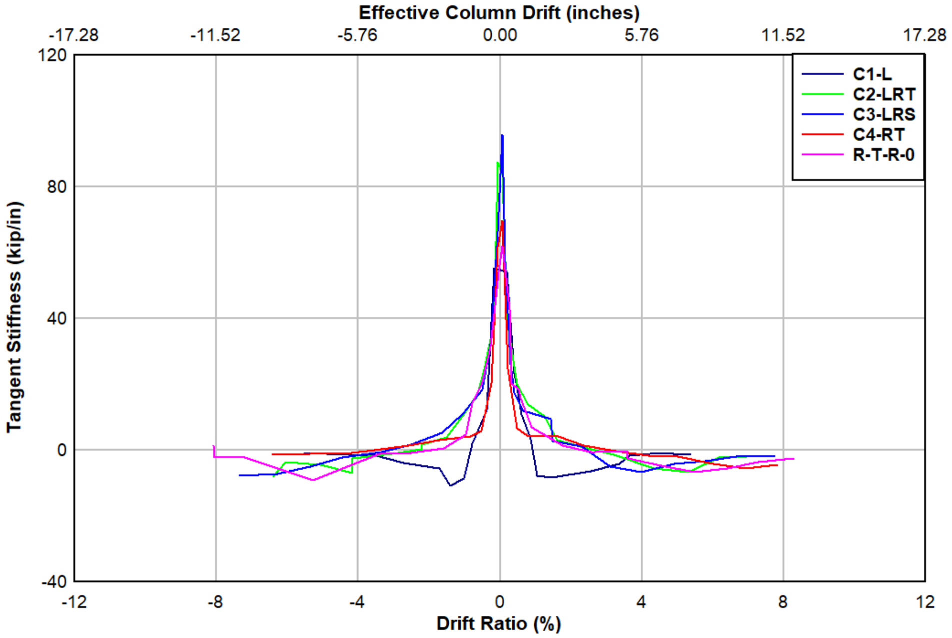

Figure 4.105: Tall (12 ft.) specimens: Evolution of tangent stiffness

Table summarizing the initial stiffness of each specimen can be found in Appendix C.

4.10 DISPLACEMENT DUCTILITY

Displacement ductility for each specimen was calculated by dividing the ultimate drift capacity, defined as the drift magnitude when the lateral load capacity reduced to 80% of peak capacity, by their respective yield drift. The experiments were conducted using an imposed lateral displacement history for a given yield displacement value calculated based on nominal material properties and assumed rigid foundation. The same displacement history was imposed on all specimens within a specified height (short and tall). Based on the calibrated moment-curvature analysis conducted in Section 4.3, the yield displacement at the lateral load point was computed using the actual specimen material properties and assuming the column was non-composite with the spiral reinforced shell, the TiAB ligaments were fully bonded along their length, and the entire square concrete column section was confined according the Mander *et al.* (1989). The yield displacement was computed as:

$$\Delta_y = \frac{1}{3}\varphi_y {H_L}^2 \tag{4-22}$$

Where:

Δ_y = yield displacement (in),

ϕ_y = yield curvature (1/in), and

H_L = height of the column from the top of the footing to the lateral load point (in).

This assumed a triangular curvature distribution and ignores the change in curvature in the small uncracked region of the column near the load point. These values allow better estimation of displacement ductility relative to the computed yield drift for all specimens. Results are shown in Table 4.15. The ductility levels relative to the backbone global response are shown in Figure 4.106 and Figure 4.107, for the short and tall specimens, respectively. As seen in the table, the TiAB retrofitted columns exceed the minimum required displacement ductility level of 3 for newly designed columns as prescribed in Section 3 of Seismic Design Criteria Version 1.7 (Caltrans, 2013). The conventional TiAB retrofits (not including the specimens with insulation board under the shell) meet the preferred ductility level of 5, even as it is recognized that it is more difficult to achieve large displacement ductility for elements with large length/width ratios. Even so, the TiAB retrofits of vintage detailed columns provided displacement ductility performance that exceeds modern requirements for new design.

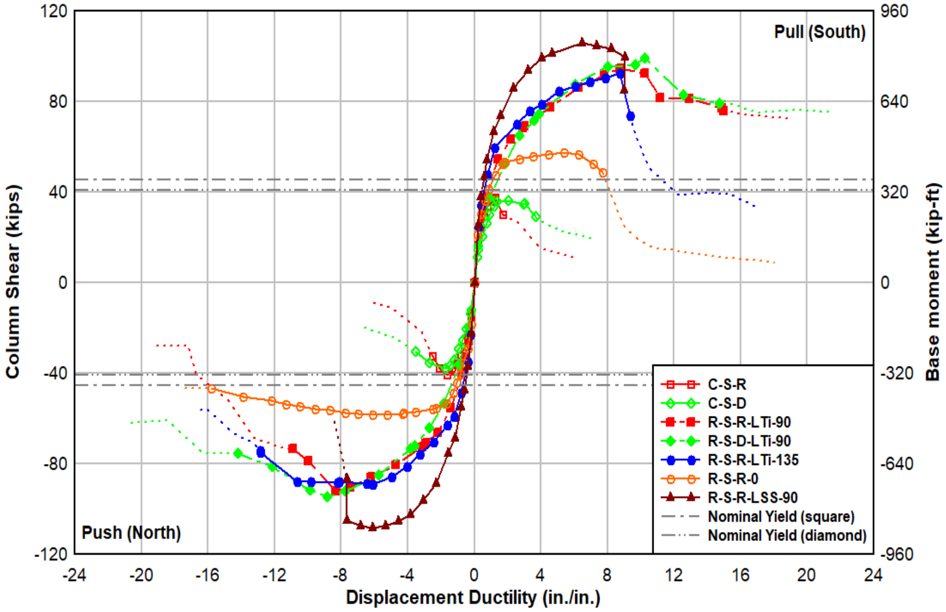

Figure 4.106: Short columns: Displacement ductility - backbone overlay

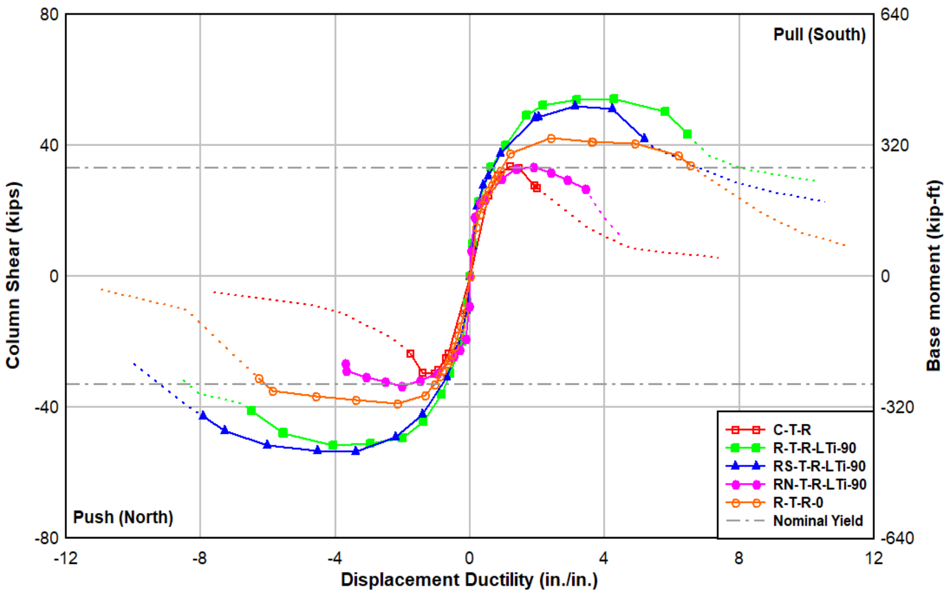

Figure 4.107: Tall columns: Displacement ductility - backbone overlay

Displacement ductility did not apply to the control specimens because they failed at or below the yield strength. It also did not apply to the spread footing or pile cap specimens, as the retrofitted columns remained elastic as the simulated foundation components accumulated damage due to soil-structure interactions. It should be noted that had the realistic foundation specimens not been retrofitted, the column above the footing would have failed instead of the soil/piles by comparing the capacity shown by the control specimen.

In the displacement ductility plots shown in Figure 4.106 and Figure 4.107, the complete backbone response is shown, even beyond the defined ultimate (i.e. reduction of lateral load capacity to 80% of peak capacity). It can be seen from these plots that the capacity of retrofitted columns beyond their defined ultimate capacity is still above the capacity of the control column specimens even for larger drift levels.

It is worth noting that the yield drift was calculated for specimen RN-T-R-LTi-90 (tall column with purposely cut longitudinal steel at the footing level) considering only the contribution of TiABs which produces a much larger yield drift (2.51 in) while the yield drift for other tall columns was approximately 1 in. Therefore, if the ductility of this specimen is expressed in terms of a nominal yield drift corresponding to the steel yield, the ductility would be much higher.

Table 4.15: Computed Displacement Ductility for all Specimens

No.	Specimen Name	Yield Drift, Δ_y in (mm)	Ultimate Drift, Δ_u (at 80% peak load) in (mm) North cycle	Ultimate Drift, Δ_u (at 80% peak load) in (mm) South cycle	Displacement Ductility (Δ_u/Δ_y) North cycle	Displacement Ductility (Δ_u/Δ_y) South cycle
1	C-S-R	0.48 (1.22)	- (-)	- (-)	-	-
2	C-S-D	0.39 (0.99)	- (-)	- (-)	-	-
3	R-S-R-LTi-90	0.46 (1.17)	5.01 (12.73)	6.89 (17.49)	10.9	15.0
4	R-S-D-LTi-90	0.37 (0.94)	5.25 (13.34)	5.45 (13.84)	14.2	14.7
5	R-S-R-LTi-135	0.47 (1.19)	6.05 (15.36)	4.12 (10.48)	12.9	8.8
6	R-S-R-0	0.45 (1.14)	7.10 (18.04)	3.20 (8.13)	15.8	7.1
7	R-S-R-LSS-90	0.49 (1.24)	3.74 (9.50)	4.41 (11.21)	7.6	9.0
8	R-S-R-LTi-90-Spread	0.46 (1.17)	- (-)	- (-)	-	-
9	R-S-R-LTi-90-Pile	0.46 (1.17)	- (-)	- (-)	-	-
10	C-T-R	1.05 (2.67)	- (-)	- (-)	-	-
11	R-T-R-LTi-90	1.08 (2.74)	6.04 (15.34)	6.20 (15.76)	5.6	5.7
12	RS-T-R-LTi-90	1.06 (2.69)	7.78 (19.77)	4.55 (11.56)	7.3	4.3
13	RN-T-R-LTi-90	2.51 (6.38)	9.29 (23.59)	7.27 (18.47)	3.7	2.9
14	R-T-R-0	1.06 (2.69)	6.29 (15.96)	6.54 (16.62)	5.9	6.2

4.11 CURVATURE DUCTILITY

Curvature ductility is the ratio of ultimate curvature to yield curvature. It is as important as the displacement capacity indicator for ductile columns. Unlike displacement ductility, it is insensitive to column height and is popularly used to compare performance of similar columns with different heights. This makes it an important parameter for column design.

Total column drift is the sum contribution of flexural deformation, shear deformation and the inelastic rotation at the base of the column. In flexure dominated columns, the contribution of shear deformation to column drift is comparatively minimal and is often neglected. In columns with fully anchored longitudinal bars, the inelastic rotation in these columns is due to plastic curvature along a definite plastic hinge length and the column is assumed to undergo rigid body rotation about the center of the plastic hinge. In such columns, the total column drift for a given flexural demand can be calculated from the curvature distribution alone along the column height. However, in columns with spliced longitudinal bars at the column base, the inelastic deformation at the column base is the result of relative slip in the spliced bars along with strain penetration. Hence, the phenomenon of conventional plastic hinging does not apply to columns with lap-spliced bars at the base of the column.

To facilitate the calculation of curvature ductility for the retrofitted column specimens to use in retrofit design, an equivalent plastic curvature model was proposed which accounts for the lumped inelastic rotation behavior at the base of column due both relative slip in the bars and strain-penetration. This model was used to calculate equivalent curvature ductility of each retrofitted column specimen. It should be noted that this equivalent plastic curvature model did not apply to the unretrofitted column specimens as they demonstrated a brittle behavior with no ductility.

4.11.1 Equivalent Plastic Curvature

Equivalent plastic curvature for each column specimen was calculated from the ultimate displacement capacity assuming an equivalent plastic hinge length equal to the width of the column. The ultimate displacement is defined as the displacement corresponding to the point when the column loses 20% of its peak capacity. Since the overall force-deformation responses for most of the column specimens were not symmetric in push and pull cycles, ultimate displacement capacity from both cycles were used to calculate plastic curvature as described in the following section. The equivalent plastic curvature was then taken as the average of the push and pull value. This is reasonable for a multi-column bent where there is a frame action in the bent under lateral deformation.

For a column with fixed-fixed connection, the total column drift can be estimated by considering two cantilever sections as shown in the Figure 4.108 above. All the column specimens tested represent the lower half portion of the column assuming the point of inflection at the mid-height of the column. Considering only lower half cantilever portion of the column as shown in Figure 4.109, ultimate top drift of column is given by,

$$\boldsymbol{\Delta_u = \Delta_y + \Delta_p}$$

(4-23)

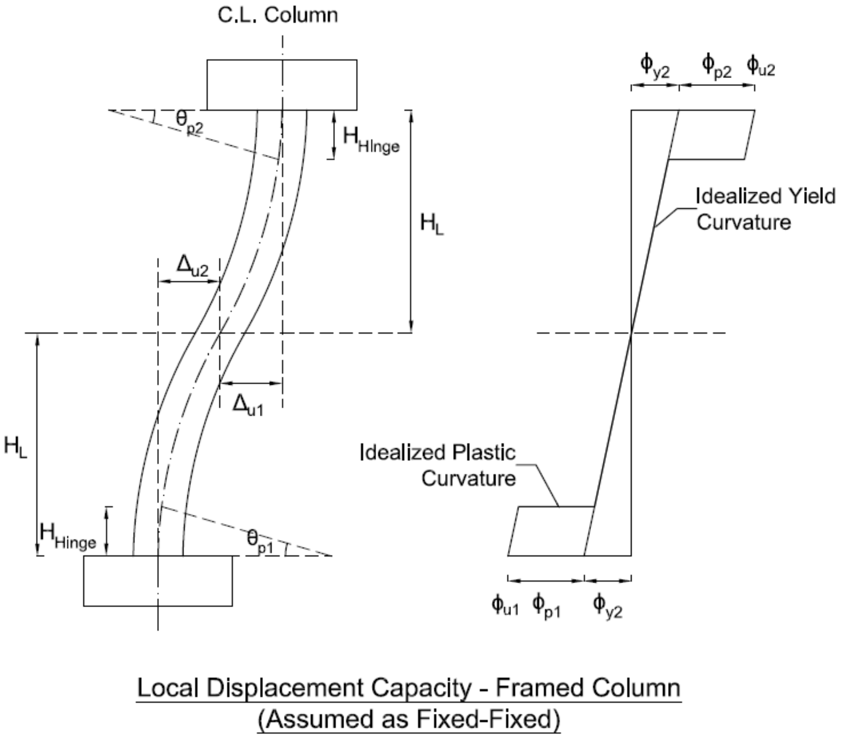

Figure 4.108: Local displacement capacity – framed column, assumed as fixed-fixed (Source: Seismic Design Criteria Version 1.7 (Caltrans, 2013))

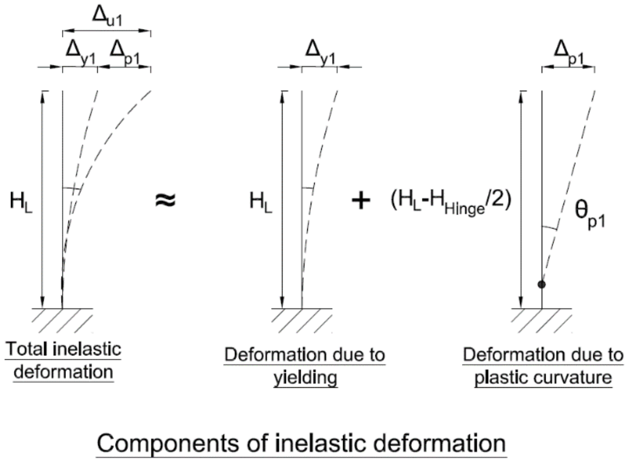

Figure 4.109: Components of inelastic deformation of a cantilevered column

In which, the yield drift,

$$\boldsymbol{\Delta_y = \frac{1}{3}\phi_y H_L{}^2} \tag{4-24}$$

and the top drift due to inelastic curvature at the base is:

$$\boldsymbol{\Delta_p = \phi_P . H_{Hinge} . \left(H_L - \frac{H_{Hinge}}{2}\right)}$$

(4-25)

Where:

ϕ_y = yield curvature calculated from moment curvature analysis of the column section with fully-anchored longitudinal reinforcing steel bars (for initial approximation).

H_L = Height of lower half cantilever portion of the column (i.e. distance between the base of the column to the point of inflection)

H_{Hinge} = Length of equivalent plastic hinge taken equal to the width of the column (i.e. $H_{Hinge} = h_{column}$ = 24 in)

Then, the equivalent plastic curvature (ϕ_P) and the equivalent curvature ductility (μ_ϕ) can be calculated for both push and pull cycles for each column specimen as shown below:

$$\boldsymbol{\phi_P = \frac{\Delta_u - \Delta_y}{H_{Hinge} . \left(H_L - \frac{H_{Hinge}}{2}\right)}}$$

(4-26)

$$\boldsymbol{\mu_\phi = \frac{\phi_y + \phi_P}{\phi_y}}$$

(4-27)

Table 4.16 shows the values of equivalent plastic curvature and curvature ductility calculated for the retrofitted column specimens. The unretrofitted columns failed in a brittle manner before reaching their yield capacities, therefore, curvature ductility does not apply to them.

Table 4.16: Equivalent Curvature Ductility Calculation

No.	Specimen Name	Yield Curvature, ϕ_y	Top Drift due to elastic flexure, Δ_y	Total effective ultimate top drift, Δ_u		Top Drift due to base rotation, Δ_θ		Plastic curvature for 24 in hinge length, ϕ_p		Curvature ductility for 24 in hinge length	
				Push cycle	Pull cycle	Push cycle	Pull cycle	Push cycle	Pull cycle	Push cycle	Pull cycle
		(1/in)	(in)	(in)	(in)	(in)	(in)	(1/in)	(1/in)		
1	C-S-R	0.00016	-	-	-	-	-	-	-	-	-
2	C-S-D	0.00013	-	-	-	-	-	-	-	-	-
3	R-S-R-LTi-90	0.00015	0.46	5.01	6.89	4.55	6.42	0.00226	0.00318	15.9	22.1
4	R-S-D-LTi-90	0.00012	0.37	5.25	5.45	4.88	5.08	0.00242	0.00252	20.9	21.7
5	R-S-R-LTi-135	0.00015	0.47	6.05	4.12	5.58	3.66	0.00277	0.00181	19.1	12.9
6	R-S-R-0	0.00015	0.45	7.10	3.20	6.65	2.75	0.00330	0.00136	23.4	10.3
7	R-S-R-LSS-90	0.00016	0.49	3.74	4.41	3.25	3.92	0.00161	0.00194	11.1	13.1
8	R-S-R-LTi-90-Spread	0.00015	-	-	-	-	-	-	-	-	-
9	R-S-R-LTi-90-Pile	0.00015	-	-	-	-	-	-	-	-	-
10	C-T-R	0.00017	-	-	-	-	-	-	-	-	-
11	R-T-R-LTi-90	0.00016	1.12	6.04	6.20	4.92	5.08	0.00155	0.00160	10.6	10.9
12	RS-T-R-LTi-90	0.00016	1.13	7.78	4.55	6.65	3.42	0.00210	0.00108	13.8	7.6
13	RN-T-R-LTi-90	0.00043	2.95	9.29	7.27	6.33	4.32	0.00200	0.00136	5.7	4.2
14	R-T-R-0	0.00015	1.06	6.29	6.54	5.23	5.49	0.00165	0.00173	11.8	12.3

4.11.2 Displacement Ductility Estimation

The average plastic curvature values for TiAB retrofitted columns in each height group were used to calculate the design plastic curvature value for each of these height groups as shown in Table 4.17.

Table 4.17: Average Equivalent Plastic Curvature

No.	Specimen Name	Clear Column Height, $2H_L$	Plastic curvature for 24 in hinge length, ϕ_p		Average plastic curvature, $\phi_{p,avg}$	Average plastic curvature, $\phi_{p,avg}$	Standard Deviation	Coefficient of variation
			Push cycle	Pull cycle				
		(ft.)	(1/in)	(1/in)	(1/in)	(1/in)	(1/in)	(%)
1	R-S-R-LTi-90	16	0.00226	0.00318	0.00272	0.00245	0.00019	7.9
2	R-S-D-LTi-90	16	0.00242	0.00252	0.00247			
3	R-S-R-LTi-135	16	0.00277	0.00181	0.00229			
4	R-S-R-0	16	0.00330	0.00136	0.00233			
5	R-T-R-LTi-90	24	0.00155	0.00160	0.00158	0.00163	0.00006	3.6
6	RS-T-R-LTi-90	24	0.00210	0.00108	0.00159			
7	RN-T-R-LTi-90	24	0.00200	0.00136	0.00168			
8	R-T-R-0	24	0.00165	0.00173	0.00169			

Since the coefficients of variation for two height groups were different, maximum standard deviation from either height group (0.0019) was used to calculate 95% and 99% confidence values of plastic curvature to use in design. Design plastic curvature curves for a range of height was derived as shown in the Figure 4.110 by assuming the maximum plastic curvature not to exceed that of 16 ft. (4.88 m) columns and the curvature values for columns taller than 16 ft. (4.88 m) interpolated or extrapolated as shown in the Figure 4.110. It should be noted that the curvature values for tall columns may be conservative as the standard deviation for tall columns is less than half the standard deviation used in the calculation.

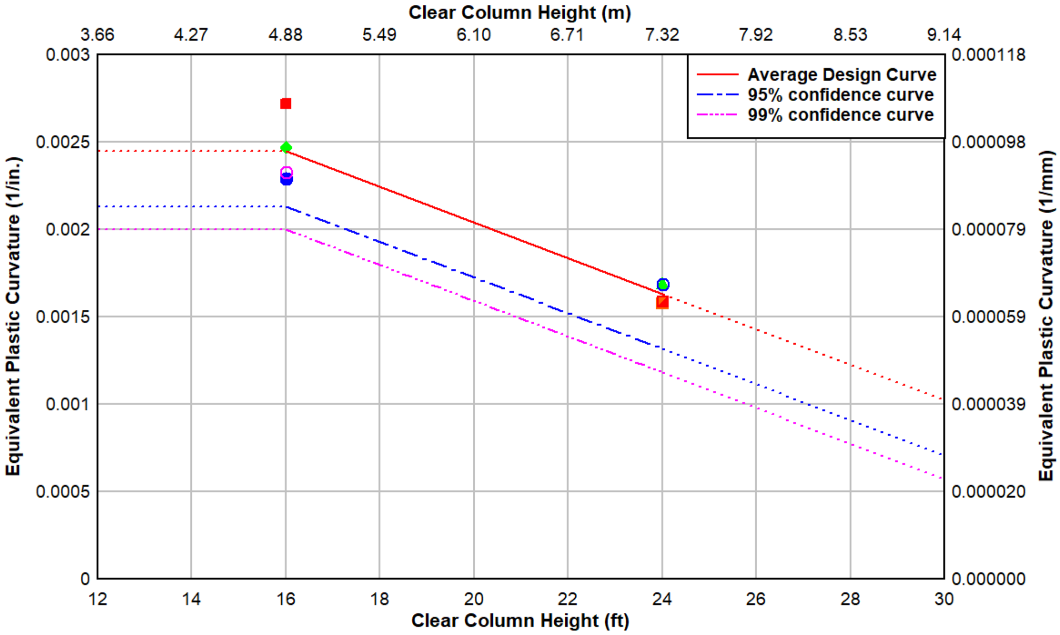

Figure 4.110: Equivalent plastic curvature design curve

Using these values of plastic curvature, displacement ductility (μ_{Δ}) of TiAB retrofitted columns of different heights can be calculated as follows:

Displacement ductility,

$$\mu_{\Delta} = \frac{\Delta_y + \Delta_P}{\Delta_y}$$

(4-28)

Where:

Δ_y and Δ_P are yield and plastic deformation as described above.

As an example, displacement ductility values of TiAB retrofitted columns reinforced with 4-#10 (#32M) ASTM Gr. 60 bars are calculated for four different height groups are given in Table 4.18.

Table 4.18: Displacement Ductility Estimation from Equivalent Plastic Curvature Model

Clear column height	Yield curvature	Yield Displacement	Plastic Curvature	Plastic Displacement	Ultimate Displacement	Curvature Ductility	Displacement Ductility
$2H_L$	ϕ_y	Δ_y	ϕ_p	Δ_p	Δ_u	μ_ϕ	μ_Δ
(ft.)	(1/in)	(in)	(1/in)	(in)	(in)		
For 95% confidence							
12	0.000218	0.38	0.00213	3.1	3.4	10.8	9.2
16	0.000218	0.67	0.00213	4.3	5.0	10.8	7.4
24	0.000218	1.51	0.00132	4.2	5.7	7.0	3.8
For 99% confidence							
12	0.000218	0.38	0.00200	2.9	3.3	10.2	8.6
16	0.000218	0.67	0.00200	4.0	4.7	10.2	7.0
24	0.000218	1.51	0.00118	3.7	5.3	6.4	3.5

From Table 4.18, it can be seen that more than 99% of TiAB retrofitted columns of height less than or equal to 24 ft. (7.32 m) are expected to have displacement ductility of greater than 3 (minimum recommended by Caltrans (Seismic Design of Concrete Bridges (Caltrans, 2015)) assuming fixed-fixed restraints. This shows that this retrofit can be effectively used for this height group to provide minimum recommended displacement ductility. There is also a trend of decrease in plastic curvature and hence, the displacement ductility value as the column gets taller. Further study is recommended to validate the application of this retrofit for columns taller than 24 ft.

4.11.3 Definition of ductility

Column ductility is defined in terms of the ultimate capacity which is popularly taken as the post-peak capacity after 20% reduction in the peak capacity. This definition of ultimate capacity of columns was used for calculating the ductility of standard retrofit columns by taking the reduction in 20% of the peak capacity of the retrofitted column. It can be seen from Figure 4.106 and Figure 4.107 that the ultimate capacity of standard retrofit columns were well above the nominal capacity of column with fully-anchored longitudinal bars. This is because the TiAB ligaments pick up when the lap-splice fails and the ligaments were designed to provide the nominal strength of column with fully-anchored longitudinal bars. So if the failure of the column is defined in terms of the 20% reduction in nominal capacity of the column with fully-anchored bars instead of the peak capacity attained by the standard retrofit column, the ductility calculated for these columns would be much higher. Hence, the definition of failure or the ultimate capacity of retrofitted columns greatly influences the ductility capacity of these columns.

Since there is no additional strength increase in the columns retrofitted with TiAB spirals only, the ductility definition for the spiral-only confined column is similar to the unretrofitted columns.

5.0 FINITE ELEMENT ANALYSIS

In this chapter, a phenomenological model was developed that accounts for the effects of bond-slip in the lap-splice region of the column where the footing starter bars overlap with the column bars. The phenomenological model is based on existing models in the literature and was validated using the tall control column (specimen C-T-R) experimental dataset presented in the previous chapter. After bond-slip model development, a nonlinear modeling approach is proposed for columns retrofitted using TiABs (specimen R-T-R-LTi-90). The conventional retrofit strategy used in the analysis consisting of longitudinal TiABs externally mounted on the RC columns, which are epoxy anchored into holes drilled into the foundation and the column, and a TiAB spiral reinforced shell that wraps the region of the steel lap-splice.

In the second part of this chapter, ten (10) different bridge models were analyzed as case studies, including five bridge geometries: two regular and three irregular geometries, considering response if not retrofitted and retrofitted. For each case study a three-dimensional (3-D) nonlinear finite element model was developed using OpenSees as the analysis software (McKenna, Scott, & Fenves, 2010). In the non-retrofitted cases, the case studies deployed the phenomenological model which accounted for the effects of bond-slip of lap-splice region. In the retrofitted case studies, the modeling approach developed using the TiABs was deployed. In addition, other components typically considered in bridge modeling such as springs to account for the expected response of bridge abutments were also modeled. For each bridge case study, a database of 64 ground motions was used to assess the effects of ground motion duration on the structural behavior. In this work 3-D structural models of bridges were subjected to orthogonal horizontal short- and long-duration ground motion records. The selection of bi-directional ground motion records was performed following the approach proposed in Belejo, Barbosa, and Bento (2017), where the spectral matching of ground motion records in both orthogonal directions was performed. In total, 32 long- and 32 short-duration bi-directional ground motion records with similar 5% equivalent viscous damped linear response spectra were selected. An earthquake record was classified as a “long-duration” record when at least one of its orthogonal ground acceleration components had a significant duration (D5-75) greater than 25 seconds (Belejo et al., 2017).

Lastly, in this chapter, damage index-based fragility curves that indicate the probability of reaching a determined damage level based on the classification proposed by Ang, Kim, and Kim (1993) are computed. These functions are based on: (1) the Park and Ang damage index (DIP&A), and (2) the Reinhorn and Valles damage index (DIR&V).

5.1 MODIFIED LAP-SPLICE BOND STRESS-SLIP MODEL FOR USE IN FIBER SECTIONS

This model was developed to model the reinforcing steel lap-splice response as characterized by the control column experimental response (specimen C-T-R). The bond stress-slip model was developed to be used as part of a fiber cross-section for a displacement-based distributed plasticity finite element implemented in OpenSees. The bond stress-slip model was integrated at the end of the element along the length of the lap-splice. The material model for the bond-slip relationship was applied to the fibers using the *Pinching4* model (Lowes, Mitra, & Altoontash, 2003) available in OpenSees.

5.2 BOND STRESS-SLIP MODEL PARAMETER CALIBRATION

A methodology was developed to reproduce the stress-strain backbone curve of the lap-splice model (specimen C-T-R). The model used the measured material properties for the concrete, steel, and TiABs. The methodology consisted in the following steps:

Step 1: *Adopt a bond stress–slip relationship.* The bond stress–slip relationship used here follows the model proposed by Harajli et al. (2004), which is represented in Figure 5.1. The backbone curve is defined by:

$$u = u_m \left(\frac{s}{s_1} \right)^{0.3}$$

(5-1)

Where:

$$u_m = 2.57\sqrt{f_c'}$$

(5-2)

With u_m equal to the maximum bond stress that corresponds to pullout failure and

s_1 the maximum slip mobilized by unconfined concrete that is defined as 15% of the clear distance between the ribs of the reinforcing bar.

The model follows the relationship defined in:

$$u_{sp} = 0.78\sqrt{f_c'} \left(\frac{c + K_c}{d_b} \right)^{2/3} \leq u_m$$

(5-3)

$$u_p = u_{sp}\left(0.5 + K_{cs}\right)$$

(5-4)

$$s_{sp} = s_1 e^{3.3 ln(u_s/u_m)} + 0.4 ln\left(\frac{u_m}{u_{sp}}\right)$$

(5-5)

Where:

u_{sp} is the splitting bond stress,

u_p is the post-splitting strength, and

s_{sp} is level of slip corresponding to the splitting bond stress.

The parameters K_c and K_{cs} are confinement parameters that depend on the number of spliced tension bars in the section, cover, spacing between bars, and transverse steel area and c is the minimum of the side cover, bottom cover, or half the clear spacing between the bars. Expressions for K_c and K_{cs} are given in Harajli et al. (2004). According to this model, the bond-slip model follows Eqn. 5-1 until the initial splitting bond stress u_{spi} is reached, which corresponds to $0.7u_{sp}$, then followed by a linear segment until the u_{sp}. Beyond the s_{sp} level of slip corresponding to u_{sp}, the bond stress drops to the post-splitting strength u_p, defined in Equation 5-4, and then decays until the maximum slip s_{max} is reached, which corresponds to a level of slip at which the bond stress reduces to zero. In this model, s_{max} is equal to the total clear distance between the ribs of the reinforcing steel bars.

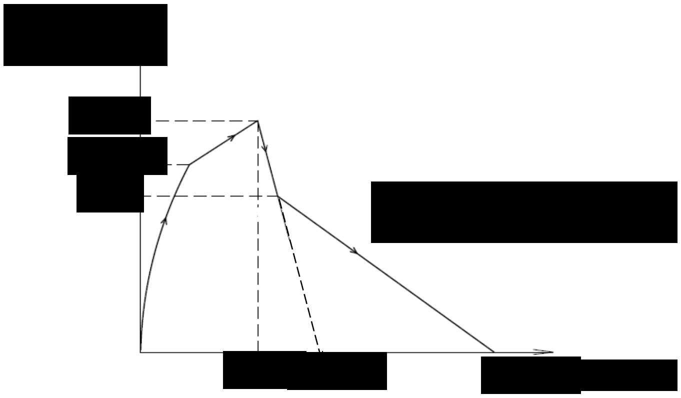

Figure 5.1: Bond stress – slip relationship

Step 2: *Convert the bond stress–slip relationship to a force–deformation constitutive model.* To convert the bond stress–slip relationship to a force–slip relation, the bond force per unit length, f_B, which can be transferred without the assistance of special transverse reinforcement confining the splice is given by:

$$f_B = p \cdot u$$

(5-6)

Where:

> u is the bond stress and p is the perimeter of the characteristic block defined by the rupture path observed when the splitting rupture mode occurs.

The peak force in each bar is given by:

$$F_{bar} = \int_0^{l_s} f_B dx = \frac{2}{3} u_{max} \cdot p \cdot l_s \tag{5-8}$$

Where:

> as shown in Figure 5.2, the shear stress distribution is assumed to follow a semi-parabola from the maximum stress towards zero stress condition at the reinforcing steel bar tip. The perimeter p of the characteristic block is defined as shown in Figure 5.3.

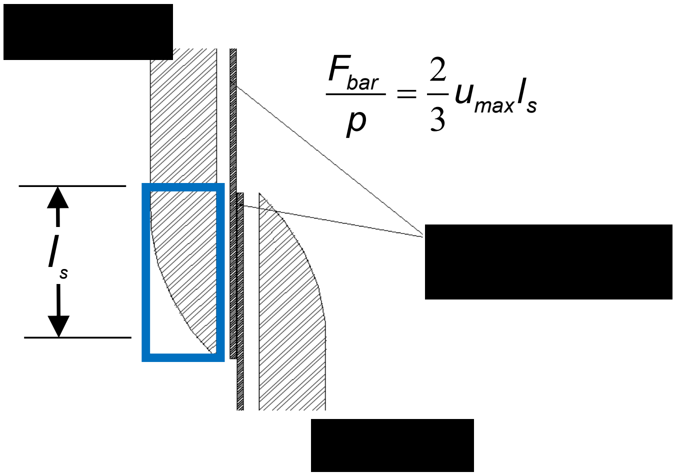

Figure 5.2: Stress distribution along spliced longitudinal bars

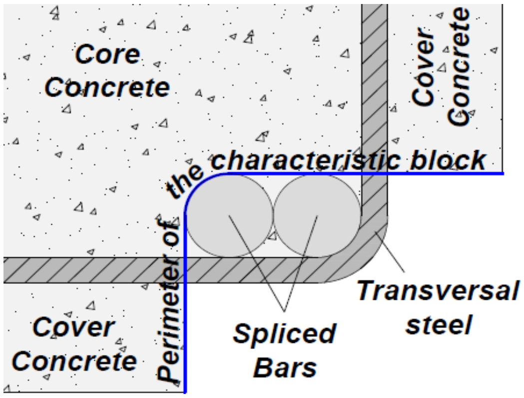

Figure 5.3: Perimeter of characteristic block spliced longitudinal bars

Step 3: *Determine the modified fiber lap-splice bond stress-strain model.* A model was first developed to capture the combined effects of bond-slip as well as reinforcing steel bar strength and stiffness. The model consisted of: (1) a zero-length element where a bond force-slip spring is assigned, and (2) a truss element where the reinforcing steel bar properties are assigned. These two components are assembled in series. Here, the truss element is assigned an area equal to the effective reinforcing steel area and the Menegotto-Pinto model, with modifications by Filippou, Popov, and Bertero (1983) is assigned to the truss element. Displacement-controlled nonlinear static analysis was performed by applying a unit pulling force to the free node of the truss element along the axis of the bar. Finally, the modified lap-splice bond stress-strain model was obtained by dividing the forces and displacements obtained from the nonlinear static analysis by the area of the bars and lap-splice length, respectively.

5.3 CALIBRATION OF THE HYSTERETIC PARAMETERS FOR THE BOND STRESS-SLIP MODEL

The cyclic behavior for the lap-splice was modeled based on the work by Harajli (2009), which was implemented as a *Pinching4* relationship in OpenSees. Four additional calibrated parameters must be defined for the *Pinching4* model: (1) the ratio of deformation at which reloading begins to the peak deformation, which was set to 0.48; (2) the ratio of the force at which reloading begins to the force on the backbone curve corresponding to peak deformation achieved on a previous cycle, which was set to 1.0; (3) the ratio of strength developed upon unloading from negative load to the minimum strength developed under monotonic loading that was set to -0.2; (4) the cyclic degradation model parameters for unloading and reloading stiffness degradation, which were set to 0.5. The definition of these four parameters follows the recommendations in Harajli (2009), except for the third parameter that was calibrated to match the experimental column response as described in the next section.

5.4 VALIDATION OF COLUMN MODELING CONSIDERING THE INFLUENCE OF THE LAP-SPLICE

The column model described here was used to model specimen C-T-R (tall control column). The column was discretized as a fiber-section displacement-based beam-column element, in which the modified lap-splice bond stress-strain model was assigned to the fiber section. Non-retrofitted columns were divided into five (5) elements: one element along the lap-splice length, and four elements above the lap-splice. For all elements, three Gauss-Legendre integration points were defined, and at each integration point the fiber-section was discretized using 144 (12 x 12) concrete fibers and 4 steel fibers. Two different uniaxial concrete models were used for the cover and core concrete. The first model used for the cover concrete was based on the Kent-Scott-Park (Scott, Park, & Priestley, 1982) model with modifications proposed by Yassin (1994) assigned to the unconfined concrete (*Concrete02* in OpenSees). While the Kent-Scott-Park model is useful and has been shown to be robust, it does not allow for explicit definition of the initial tangent stiffness. Thus, a second model was used to capture the response of the core concrete, which follows a compressive stress-strain envelope that is based on the Fujii concrete model (Hoshikuma, Kawashima, Nagaya, & Taylor, 1997). This model in OpenSees is known as “Concrete with beta” and is a uniaxial concrete material that considers the effect of the strain normal to the axis of the element. This material model has two options regarding the strength degradation in tension: (a) tri-linear model or (b) nonlinear model based on the tension stiffening relation of Stevens, Uzumeri, Collins, & Will (1991). Here the nonlinear tension stiffening model by Stevens et al. (1991)was used and the adopted model for softening behavior in compression was tri-linear. The Menegotto-Pinto (*Steel02* in OpenSees) material model as proposed in F.C. Filippou et al. (1983) was assigned to the reinforcing steel bars above the lap-splice. For the reinforcing steel fibers within the lap-splice region, calibrated hysteretic parameters for the bond stress-slip model were used.

From inspection of Figure 5.4a, the results obtained from numerical analysis are compared to the experimental response of specimen C-T-R. The markers shown on the load–displacement plot are reference points where the energy dissipated by yielding were calculated. From analysis of Figure 5.4a it can be seen that both experiment and numerical model show similar results in terms of initial stiffness, peak capacity for both positive and negative directions of the load, and overall pattern of strength degradation. The energy dissipated by yielding during the numerical analysis and the experiment are shown in Figure 5.4b. It can be seen that there is a good correlation between the energy dissipated during the analysis and that dissipated during testing. The numerical model for the specimen is thus able to reasonably capture the response of non-retrofitted column subjected to reversed cyclic loads and the fact that similar energies are dissipated are important here since the dissipated energy plays an important role when performing assessments of ground motion duration effects on the structural response (Dutta & Mander, 2001; Manfredi, Polese, & Cosenza, 2003; Oyarzo-vera & Chouw, 2008; Barbosa, Ribeiro, & Neves, 2017).

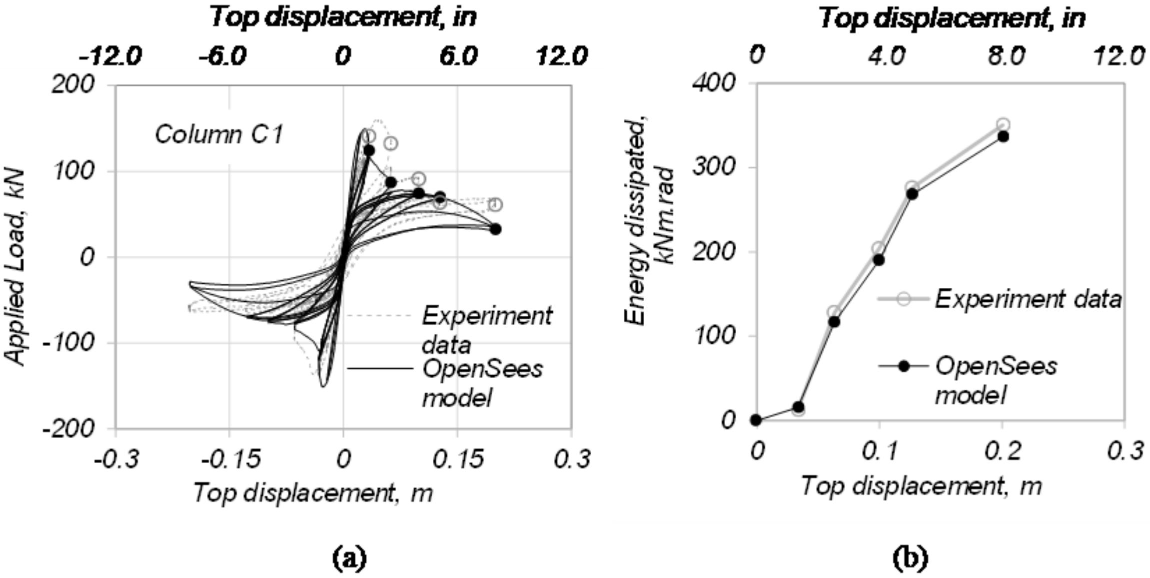

Figure 5.4: Calibration of analytical model for specimen C-T-R a) global force-drift response and b) cumulative energy dissipated with drift

5.5 RETROFIT COLUMN MODELING, CALIBRATION, AND VALIDATION

As a first step to modelling the TiAB retrofitted RC column specimens, specimen RN-T-R-LTi-90 was modeled and calibrated. This specimen was designed and constructed to isolate the effects of the TiAB ligaments and shell retrofit solution. Thus, the main internal longitudinal column reinforcing steel bars of the specimen were not anchored into the footing, starting immediately above the footing. In other words, the flexural tension produced by the over-turning moment in the specimen at the footing was provided by the TiABs only.

Since the internal reinforcing steel was not anchored into the footing, the contribution of the reinforcing steel bars was neglected. Nonetheless, since the titanium spiral and concrete shell provide additional confinement, the concrete square column was modeled as confined. The confining concrete parameters were calculated following Mander et al. (1988). The vertical TiABs were modeled as truss elements, which are connected to the displacement-based finite element of the concrete column through rigid links as shown Figure 5.5. The *Pinching4* model in OpenSees was used to model the hysteretic properties of the TiABs. The calibration of the hysteretic parameters was performed through trial-and-error to correlate the experimental results with the numerical counterparts. The experimental and numerical results obtained from the final calibrated model is shown in Figure 5.6, where it can be seen that the model shows good overall correlation with the experiment, capturing the degradation, but slightly underestimating capacity.

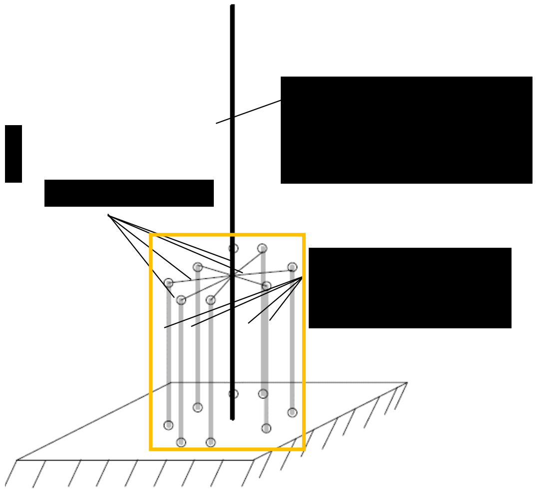

Figure 5.5: Model of column with TiAB ligaments

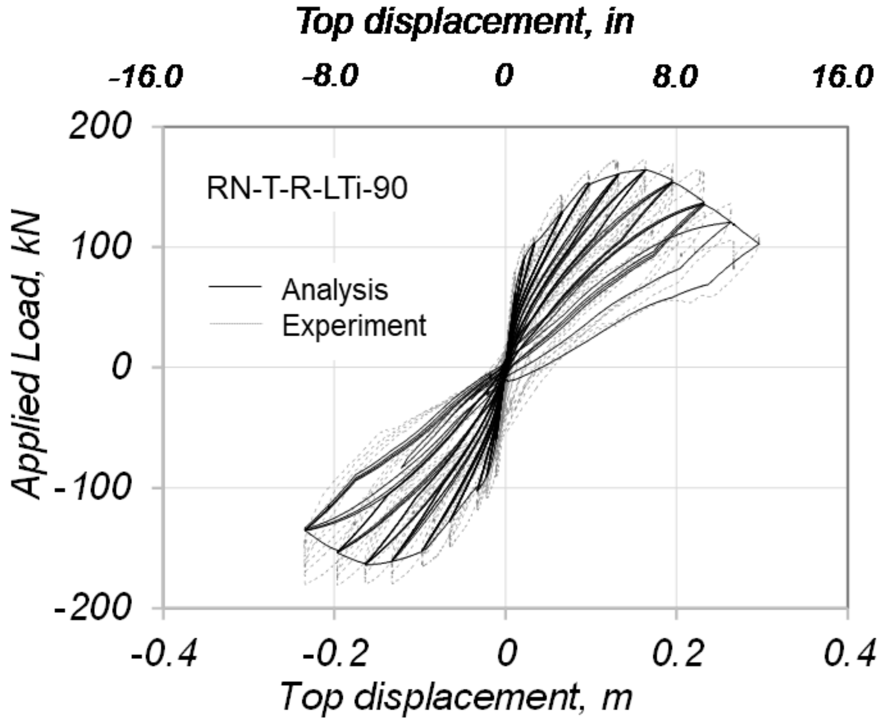

Figure 5.6: Calibrated model with experimental response for specimen RN-T-R-LTi-90 (tall retrofitted specimen with cut flexural steel at footing), solid line is model and dashed line is experiment.

A numerical model was developed for specimen R-T-R-LTi-90 (tall column with conventional TiAB retrofit). The numerical model aggregated the lap-splice and the TiAB retrofit modeling approaches described previously. The load-displacement relationships obtained from the numerical analysis and from the experiment data of the specimen is shown in Figure 5.7a. It can be seen that the model captures well the initial stiffness and the peak capacity. The evolution of the hysteretic energy dissipated is shown in Figure 5.7b, in which a good correlation between model and test results can be observed. In summary, the numerical model of specimen R-T-R-LTi-90 reasonably captured the reversed cyclic behavior of the TiAB retrofitted column.

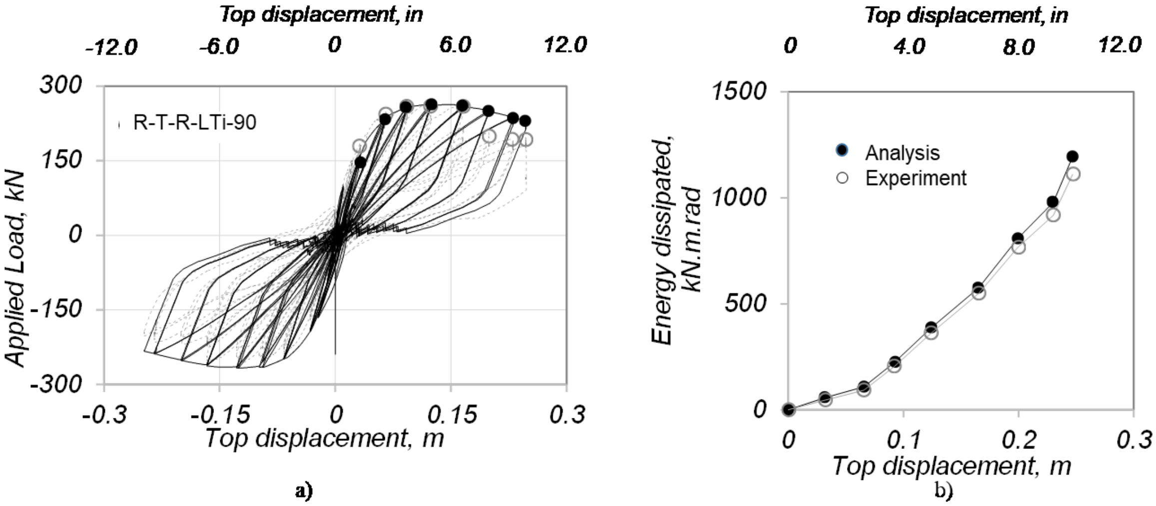

a)

b)

Figure 5.7: Calibration of analytical model for specimen R-T-R-LTi-90 (tall retrofitted specimen with flexural steel at footing) a) global force-drift response and b) cumulative energy dissipated with drift

5.6 APPLICATION EXAMPLES

Case studies were developed to evaluate how TiAB retrofits influence the seismic performance of vintage RC deck-girder bridges over a range of conditions. Bridge models were developed to represent the most common characteristics of existing RC deck-girder bridges constructed in Oregon over the period ranging from 1950 to 1970 based on the database review of Chapter 3. Two different span configurations were considered: three-span, and four-span continuous bridges as shown in Figure 5.8a and Figure 5.8b. The geometry and dimensions for the bridge cross sections, girders, and bents are shown in Figure 5.8c, Figure 5.8d, and Figure 5.8e. The first bridge used in the study, named RB1, simulates a previously existing bridge over the Mackenzie River located on Highway Interstate 5 near Eugene, Oregon. The RB1 bridge model is a 3-span bridge, with equal 15.2 m (50 ft.) long spans, and two bridge bents consisting of two columns with a clear height of 6.71 m (22 ft.). The second bridge case study, RB2, is a prototype design representing the median bridge geometry of 1950-1970 RC bridges from Oregon's DOT database. The prototype design corresponds to a 4-span bridge, with equal 15.2 m (50 ft.) long spans. The column lengths for bents 1, 2, and 3 all correspond to the median length of columns for all the bridges from Oregon DOT bridge database, with a 4.88 m (16 ft.) clear height above the footing. Columns with this length are designated as the "median column." The other three bridge designs considered in this study consist of designs with varying column lengths. The shortest and longest columns, here after labeled as "short column" and "long column", respectively, are defined by the 16th and 84th percentiles of the height of all bridge columns found in the Oregon DOT bridge database. Thus, the clear height of a short column, median column, and long columns are 3.05 m (10 ft.), 4.88 m (16 ft.), and 6.71 m (22 ft.), respectively.

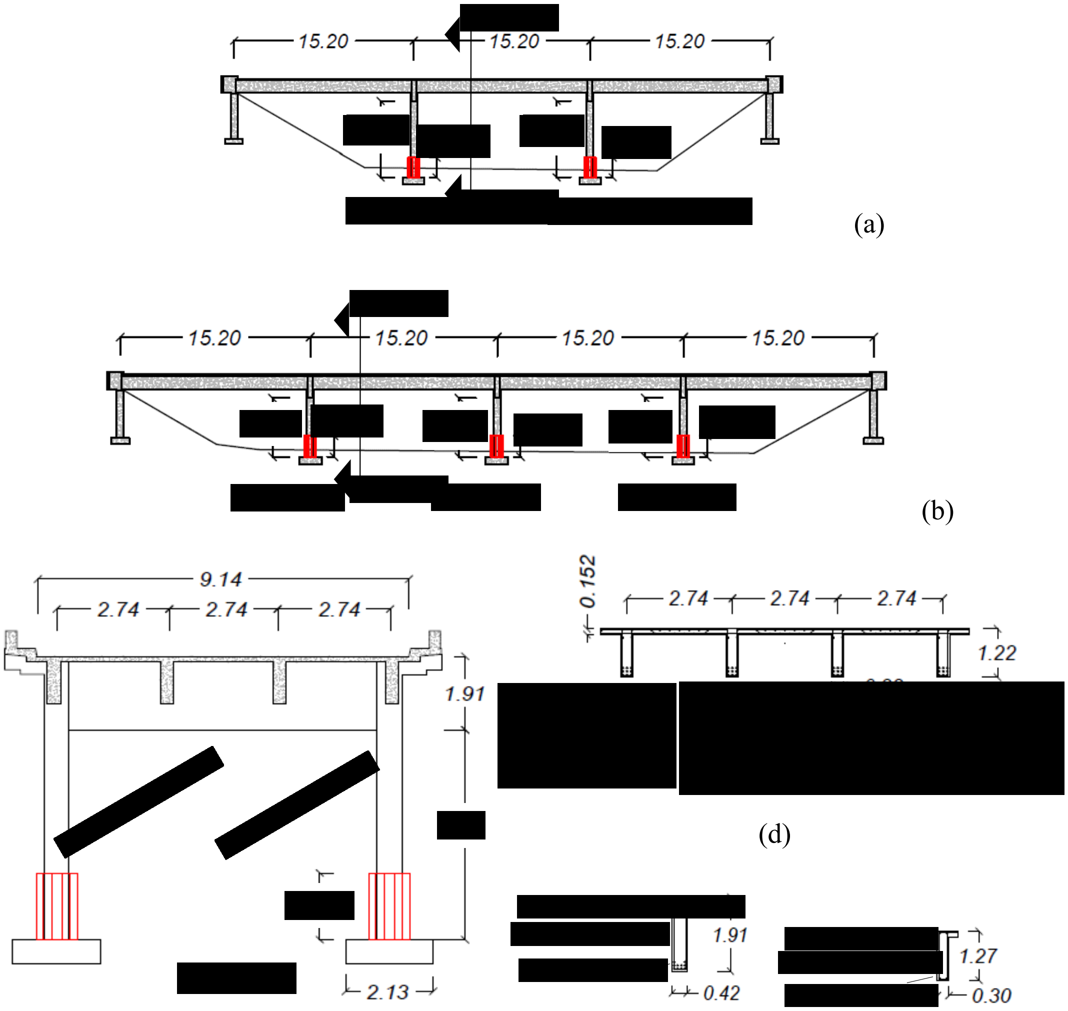

(a)

(b)

(c)

(d)

(e)

Bridge	H_1 (m)	H_{11} (m)	H_2 (m)	H_{21} (m)	H_3 (m)	H_{31} (m)
RB1	6.65	-	6.65	-	-	-
RB1R	6.65	1.52	6.65	1.52	-	-
RB2	4.85	-	4.85	-	4.85	-
RB2R	4.85	1.52	4.85	1.52	4.85	1.52
IB1	3.00	-	4.85	-	6.65	-
IB1R	3.00	1.52	4.85	1.52	6.65	1.52
IB2	3.00	-	6.65	-	4.85	-
IB2R	3.00	1.52	6.65	1.52	4.85	1.52
IB3	4.85	-	3.00	-	6.65	-
IB3R	4.85	1.52	3.00	1.52	6.65	1.52

(f)

Figure 5.8: Case study model bridge configurations

The 10 model configurations are shown in Figure 5.8 Apart from the column lengths, all dimensions and detailing of the original Mackenzie River Bridge were used to define the prototype bridges used in this study, namely: (1) column sections are 0.61m (2 ft.) wide square columns with four ASTM 305 Gr. 40 #36M (#11) longitudinal reinforcing steel bars with the nominal yield stress f_y equal to 276 kPa (40 ksi), a lap-splice length equal to 0.91 m (3 ft.), and #10M (#3) hoops spaced at 0.30 m (12 in) on center; (2) the section of the girders of the superstructure are 1.22 x 0.37 m (4 ft. x 1ft-2.5 in), with ASTM 305 Gr. 40 #36M (#11) longitudinal bars and #13M (#4) stirrups shown in Figure 5.8e. The cap beams are 1.91 m (6 ft. – 3in) high and 0.42 m (1 ft. – 4.5 in) wide, reinforced with #36M (#11) longitudinal bars and #16M (#5) stirrups. The cap beams over the abutment bents are 1.27 m x 0.30m (4 ft. – 2 in x 1 ft.) reinforced with #25M (#8) longitudinal bars and #13M (#4) stirrups.

Each of the five bridge types was used to generate models of bridges retrofitted with TiAB longitudinal bars and TiAB spirals. In all retrofitted bridge models developed, the length of the TiAB longitudinal bars was taken as 1.52 m (5 ft.), measured from the top face of the footing. These models all have an R at the end of the model name.

5.6.1 Bridge Models

The main components considered in the bridge models included: (1) the superstructure, modeled using linear elastic beam-column elements, with its stiffness reduced 50% due to typical cracking that is often observed in these 1950s – 1970s existing bridges, following recommendations of ACI 318-14 (2014); (2) connections between the columns and bent caps were considered to be monolithic and rigid; (3) the bent caps were modeled as rigid elements; (4) the columns were fixed at the base, not considering soil-structure interaction effects in this study; (5) at the abutments, zero-length elements were connected to the abutment cap beam elements, which provide the passive resistance of the soil in contact with the cap beam modeled through a HyperbolicGap material (Duncan & Mokwa, 2001). The model is illustrated in Figure 5.9. The parameters defining the HyperbolicGap model are initial stiffness, unloading/reloading stiffness, ultimate (maximum) passive resistance, initial gap, and failure ratio. The failure ratio, R_f, is defined as the ratio between the ultimate passive pressure load and the hyperbolic asymptotic value of passive resistance. The parameters assigned to the zero-length elements connected to the abutment cap beams were assigned considering the tributary area of each element. The passive resistance material model initial stiffness was obtained following Douglas and Davis (1964). The ultimate passive resistance was calculated based on the Rankine theory. The abutment soil characteristics were obtained from the report SSRP-05/02 by Earth Mechanics (2005) where field investigation for abutment backfill characterization was performed. Among the typical backfills, medium dense silty sand was the one assumed for the abutment backfill. A failure ratio of 0.7 and an initial gap of 0.025m were assigned to the zero-length elements along the longitudinal direction, and no gap was assigned to the elements resisting along the transverse direction. The initial gap along the longitudinal direction and the failure ratio values were defined according to abutment stiffness models proposed for bridge simulations by Wilson and Elgamal (2006) which are based on large-scale abutment tests performed at UC San Diego.

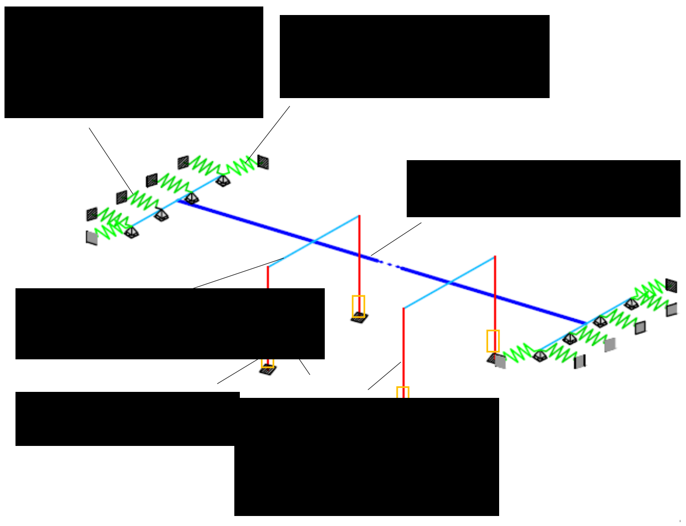

[redacted]
[redacted]
[redacted]
[redacted]
[redacted]
[redacted]

Figure 5.9: Components of case study bridge models

5.7 GROUND MOTION SELECTION

Since the different bridge models have different column lengths, the bridges studied here have different fundamental periods of vibration. The same set of long-duration ground motions was applied for all bridges. However, a selection procedure described in Belejo et al. (2017) was used to select the short-duration ground motions and two different sets were selected. First, one short-duration ground motion set was selected for the study of the three-span bridges (RB1 and RB1R) in which the fundamental period ranged from 1.25 sec $\leq T_1 <$ 1.30 sec. Second, a separate set of short duration ground motions were developed for the four-span bridges (RB2, RB2R, IB1, IB1R, IB2, IB2R, IB3 and IB3R), in which the fundamental periods ranged between 0.74 sec and 0.85 sec. The pairs of long-duration and short-duration earthquake records selected for the three-span bridges and four-span bridges with information regarding to scale factors and rotation angles are listed in Table 5.1 and Table 5.2, respectively, while Table 5.3, Table 5.4 and Table 5.5 show information regarding significant duration D_{5-75}, rupture distance, peak ground acceleration (PGA), moment magnitude (M_W), and the 5% damped linear elastic spectral acceleration at the fundamental period of the structure $S_a(T_1)$.

Table 5.1: Long-duration Set and Short-duration Set (Bridges RB1 and RB1R) of the Ground Motions with Respective Scale Factor and Rotation Angle Applied to the Short-duration Earthquake Records

Pair	**Long-duration earthquake record**			**Short-duration earthquake record**			**θ**	**SF**
Number	**Earthquake**	**Year**	**Station**	**Earthquake**	**Year**	**Station**	**[degrees]**	**[-]**
1	Tohoku (Japan)	2011	Towadako	Parkfield-02_CA	2004	Coalinga-Priest Valley	100	0.38
2	Tohoku (Japan)	2011	Nagawa	El Mayor-Cucapah_Mexico	2010	El Centro-Imperial & Ross	80	0.26
3	Tohoku (Japan)	2011	Taksato	Northridge-01	1994	LA-Century City CC North	105	1.07
4	Tohoku (Japan)	2011	Fukushima	Hector Mine		Hector	90	2.71
5	Tohoku (Japan)	2011	Ichinohe	Loma Prieta	1989	Coyote Lake Dam-Southwest Abutment	0	0.87
6	Tohoku (Japan)	2011	Shizukuishi	Coalinga-01	1983	Parkfield-Fault Zone 15	105	0.72
7	Tohoku (Japan)	2011	Hanamaki	Big Bear-01	1992	Morongo Valley Fire Station	10	1.65
8	Tohoku (Japan)	2011	Kanegasaki	Victoria_Mexico	1980	Chihuahua	175	3.16
9	Tohoku (Japan)	2011	Ichinoseki	Corinth_Greece	1981	Corinth	90	1.6
10	Tohoku (Japan)	2011	Iwanuma	Northern Calif-03	1954	Ferndale City Hall	105	0.73
11	Tohoku (Japan)	2011	Shiroishi	Northridge-01	1994	Hollywood-Willoughby Ave.	5	1.38
12	Tohoku (Japan)	2011	Shizugawa	Chuetsu-oki_Japan	2007	Sanjo Shinbori	160	0.82
13	Tohoku (Japan)	2011	Tedou	Chuetsu-oki_Japan	2007	Joetsu Kita	0	1.42
14	Tohoku (Japan)	2011	Yamagata	El Mayor-Cucapah_Mexico	2010	Michoacan De OCampo	5	0.38
15	Maule (Chile)	2010	Constituition	Chuetsu-oki_Japan	2007	JoetsuYasuzukaku Yasuzuka	170	2.4
16	Maule (Chile)	2010	Curico	Chalfant Valley-02	1986	Long Valley Dam ((L Abut)	85	3.77
17	Maule (Chile)	2010	Hualele	Morgan Hill	1984	Hollister Differential Array #3	80	1.57
18	Maule (Chile)	2010	Talca	Loma Prieta	1989	Anderson Dam (Downstream)	175	1.7
19	Valparaiso (Chile)	1985	Llolleo	Duzce_Turkey	1999	Bolu	0	2.27
20	Valparaiso (Chile)	1985		Joshua Tree_CA	1992	Indio-Jackson Road	165	1.37
21	Valparaiso (Chile)	1985	San Isisdro	Loma Prieta	1989	Gilroy Array #7	175	2.31
22	Valparaiso (Chile)	1985	Vina del Mar	Joshua Tree_CA	1992	Morongo Valley Fire Station	85	2.12

Pair Number	Long-duration earthquake record			Short-duration earthquake record			θ [degrees]	SF [-]
	Earthquake	Year	Station	Earthquake	Year	Station		
23	ChiChi (Taiwan)	1999	CHY004	Superstition Hills-02	1987	Imperial Valley Wildlife Liquefaction Array	95	0.39
24	ChiChi (Taiwan)	1999	CHY076	Darfield_New Zealand	2010	Styx Mill Transfer Station	0	2.06
25	ChiChi (Taiwan)	1999	CHY082	Parkfield-02_CA	2004	Parkfield-Fault Zone 3	80	0.55
26	ChiChi (Taiwan)	1999	CHY107	San Simeon_CA	2003	San Luis Obispo-Lopez Lake Grounds	80	0.82
27	ChiChi (Taiwan)	1999	CHY012	Imperial Valley-06	1979	Westmorland Fire Sta	95	0.3
28	Kocacli (Turkey)	1999	Bursa Tofas	Tabas_Iran	1978	Boshrooyeh	95	1.02
29	Denali (Alaska)	2002	Fairbanks Geophysic. Obs. CIGO	Chuetsu-oki_Japan	2007	Joetsu Yanagishima paddocks	10	0.26
30	Landers (US)	1992	Downey – Co. Maint. Bldg.		2008	Yuzawa Town	85	0.28
31	Landers (US)	1992	Mission Creek Fault	Darfield_New Zealand	2010	Christchurch Cashmere High School	95	0.76
32	Niigata (Japan)	2004	NIG010	Coalinga	1983	Parkfield-Stone Corral 4E	85	0.63

Table 5.2: Long-duration Set and Short-duration Set (Bridges RB2, RB2R, IB1, IB1R, IB2, IB2R, IB3 and IB3R) of the Ground Motions with Respective Scale Factor and Rotation Angle Applied

Pair Number	Long-duration earthquake record			Short-duration earthquake record			θ degrees	SF [-]
	Earthquake	Year	Station	Earthquake	Year	Station		
1	Tohoku (Japan)	2011	Towadako	Imperial Valley-06	1979	El Centro Array #12	100	0.38
2	Tohoku (Japan)	2011	Nagawa	El Mayor-Cucapah_Mexico	2010	El Centro-Imperial & Ross	80	0.26
3	Tohoku (Japan)	2011	Taksato	El Mayor-Cucapah_Mexico	2010	Calexico Fire Station	105	1.07
4	Tohoku (Japan)	2011	Fukushima	Darfield_New Zealand	2010	Christchurch Cashmere High School	90	2.71
5	Tohoku (Japan)	2011	Ichinohe	Northridge-01	1994	LA-Brentwood VA Hospital	0	0.87
6	Tohoku (Japan)	2011	Shizukuishi	Darfield_New Zealand	2010	WSFC	105	0.72
7	Tohoku (Japan)	2011	Hanamaki	Northridge-01	1994	Canyon Country-W Lost Cany	10	16.5
8	Tohoku (Japan)	2011	Kanegasaki	Northridge-01	1994	LA-W 15th ST	175	3.16
9	Tohoku (Japan)	2011	Ichinoseki	Northridge-01	1994	LA-N Faring Rd	90	1.6
10	Tohoku (Japan)	2011	Iwanuma	Superstition Hills-02	1987	El Centro Imp. Co. Cent.	105	0.73
11	Tohoku (Japan)	2011	Shiroishi	Northridge-01	1994	Sunland-Mt Gleason Ave	5	1.38
12	Tohoku (Japan)	2011	Shizugawa	Northridge-01	1994	LA-Century City CC north	160	0.82
13	Tohoku (Japan)	2011	Tedou	Loma Prieta	1989	Sunnyvale-Colton Ave.	0	1.42
14	Tohoku (Japan)	2011	Yamagata	El Mayor-Cucapah_Mexico	2010	Michoachan De OCampo	5	0.38
15	Maule (Chile)	2010	Constituition	Chuetsu-oki_Japan	2007	Joetsu Ysuzukaku Yasuzuka	170	2.4
16	Maule (Chile)	2010	Curico	Umbria Marche_Italy	1997	Castelnuovo-Assisi	85	3.77
17	Maule (Chile)	2010	Hualele	Morgan Hill	1984	Hollister Differential Array #3	80	1.57
18	Maule (Chile)	2010	Talca	Imperial Valley-06	1979	Cerro Prieto	175	1.7
19	Valparaiso (Chile)	1985	Llolleo	Basso Tirreno_Italy	1978	Patti-Cabina Prima	0	2.27
20	Valparaiso (Chile)	1985		N. Palm Springs	1986	Whitewater Trout Farm	165	1.37

Pair Number	**Long-duration earthquake record**			**Short-duration earthquake record**			**θ degrees**	**SF [-]**
	Earthquake	**Year**	**Station**	**Earthquake**	**Year**	**Station**		
21	Valparaiso (Chile)	1985	San Isisdro	Joshua Tree_CA	1992	Indo-Jackson Road	175	2.31
22	Valparaiso (Chile)	1985	Vina del Mar	Spitak_Armenia	1988	Gukasian	85	2.12
23	ChiChi (Taiwan)	1999	CHY004	Victoria_Mexico	1980	Chihuahua	95	0.39
24	ChiChi (Taiwan)	1999	CHY076	Darfield_New Zealand	2010	Styx Mill Transfer Station	0	2.06
25	ChiChi (Taiwan)	1999	CHY082	Iwate_Japan	2008	Yuzawa Town	80	0.55
26	ChiChi (Taiwan)	1999	CHY107	Chuetsu-oki_Japan	2007	Joetsu Kita	80	0.82
27	ChiChi (Taiwan)	1999	CHY012	Imperial Valley-06	1979	Westmorland Fire Station	95	0.30
28	Kocacli (Turkey)	1999	Bursa Tofas	Chuetsu-oki_Japan	2007	Sanjo Shimbori	95	1.02
29	Denali (Alaska)	2002	Fairbanks Geophysic. Obs. CIGO	Chuetsu-oki_Japan	2007	Joetsu Yanagishima paddocks	10	0.26
30	Landers (US)	1992	Downey – Co. Maint. Bldg.	Parkfield-02_CA	2004	Coalinga-Priest Valley	85	0.28
31	Landers (US)	1992	Mission Creek Fault	Northridge-01	1994	Inglewood-Union Oil	95	0.76
32	Niigata (Japan)	2004	NIG010	Big Bear-01	1992	San Benadino-2nd & Arrowhead	85	0.63

Table 5.3: Characteristics of the Long-duration Ground Motions

Record (#, comp.)	Earthquake	Station	Filename	D_{5-75} [sec]	M_w	Rupture Distance [km]	PGA [g]	$S_a(T_1)$ [g]
1_{H1}	Tohoku_Japan	Towadako	KR_AOMH121103111446EW2	53	9	312	0.11	0.173
1_{H2}			KR_AOMH121103111446NS2	55			0.12	
2_{H1}	Tohoku_Japan	Nagawa	KR_AOMH171103111446EW2	53	9	292	0.14	0.204
2_{H2}			KR_AOMH171103111446NS2	53			0.11	
3_{H1}	Tohoku_Japan	Takasato	KR_FKSH031103111446EW2	64	9	279	0.12	0.273
3_{H2}			KR_FKSH031103111446NS2	66			0.13	
4_{H1}	Tohoku_Japan	Fukushima	KR_FKSH161103111446EW2	77	9	221	0.21	0.276
4_{H2}			KR_FKSH161103111446NS2	77			0.33	
5_{H1}	Tohoku_Japan	Ichinohe	KR_IWTH111103111446EW2	52	9	263	0.14	0.359
5_{H2}			KR_IWTH111103111446NS2	54			0.15	
6_{H1}	Tohoku_Japan	Shizukuishi	KR_IWTH161103111446EW2	61	9	238	0.12	0.325
6_{H2}			KR_IWTH161103111446NS2	61			0.16	
7_{H1}	Tohoku_Japan	Hanamaki	KR_IWTH201103111446EW2	54	9	209	0.41	0.61
7_{H2}			KR_IWTH201103111446NS2	54			0.37	
8_{H1}	Tohoku_Japan	Kanegasaki	KR_IWTH241103111446EW2	58	9	202	0.17	0.354
8_{H2}			KR_IWTH241103111446NS2	65			0.19	
9_{H1}	Tohoku_Japan	Ichinoseki	KR_IWTH261103111446EW2	56	9	188	0.53	0.707
9_{H2}			KR_IWTH261103111446NS2	54			0.52	
10_{H1}	Tohoku_Japan	Iwanuma	KR_MYGH081103111446EW2	70	9	177	0.26	0.415
10_{H2}			KR_MYGH081103111446NS2	66			0.29	
11_{H1}	Tohoku_Japan	Shiroishi	KR_MYGH091103111446EW2	70	9	198	0.33	0.638
11_{H2}			KR_MYGH091103111446NS2	70			0.32	
12_{H1}	Tohoku_Japan	Shizugawa	KR_MYGH121103111446EW2	58	9	137	0.53	0.271
12_{H2}			KR_MYGH121103111446NS2	56			0.46	
13_{H1}	Tohoku_Japan	Tendou	KR_YMTH011103111446EW2	71	9	219	0.2	0.214
13_{H2}			KR_YMTH011103111446NS2	64			0.18	
14_{H1}	Tohoku_Japan	Yamagata	KR_YMTH021103111446EW2	78	9	229	0.14	0.38
14_{H2}			KR_YMTH021103111446NS2	84			0.14	

Record (#, comp.)	**Earthquake**	**Station**	**Filename**	**D_{5-75} [sec]**	**M_w**	**Rupture Distance [km]**	**PGA [g]**	**$S_a(T_1)$ [g]**
15_{H1}	Maule_Chile	Constituition	CONSTITUTION_EW	32	8.8	39	0.53	1.619
15_{H2}			CONSTITUTION_NS	32			0.65	
16_{H1}	Maule_Chile	Curico	CURICO_EW	38	8.8	65	0.48	0.587
16_{H2}			CURICO_NS	37			0.41	
17_{H1}	Maule_Chile	Hualele	HUALANE_EW	35	8.8	50	0.38	0.856
17_{H2}			HUALANE_NS	34			0.48	
18_{H1}	Maule_Chile	Talca	TALCA_EW	51	8.8	59	0.46	0.604
18_{H2}			TALCA_NS	52			0.45	
19_{H1}	Valparaiso_Chile	Llolleo	LLOLLEO_EW	28	7.8	N/A	0.39	0.924
19_{H2}			LLOLLEO_NS	27			0.68	
20_{H1}	Valparaiso_Chile	Valparaiso Elmandral	VALPARAISO_EW	31	7.8	N/A	0.16	0.629
20_{H2}			VALPARAISO_NS	37			0.29	
21_{H1}	Valparaiso_Chile	San Isisdro	SANISIDRO_EW	30	7.8	N/A	0.7	0.914
21_{H2}			SANISIDRO_NS	24			0.7	
22_{H1}	Valparaiso_Chile	Vina del Mar	VINADELMAR_EW	32	7.8	N/A	0.32	0.857
22_{H2}			VINADELMAR_NS	32			0.22	
23_{H1}	ChiChi_Taiwan	CHY004	CHICHI_CHY004-W	36	7.62	47	0.1	0.169
23_{H2}			CHICHI_CHY004-N	30			0.1	
24_{H1}	ChiChi_Taiwan	CHY076	CHICHI_CHY076-E	31	7.62	42	0.07	0.162
24_{H2}			CHICHI_CHY076-n	26			0.07	
25_{H1}	ChiChi_Taiwan	CHY082	CHICHI_CHY082-E	26	7.62	36	0.06	0.122
25_{H2}			CHICHI_CHY082-N	30			0.06	
26_{H1}	ChiChi_Taiwan	CHY107	CHICHI_CHY107-W	32	7.62	51	0.09	0.23
26_{H2}			CHICHI_CHY107-N	27			0.1	
27_{H1}	ChiChi_ AfterShock_Taiwan	CHY012	CHICHI.06_CHY012W	41	6.3	89	0.06	0.105
27_{H2}			CHICHI.06_CHY012N	32			0.04	
28_{H1}	Kocaeli_Turkey	Bursa Tofas	KOCAELI_BUR000	26	7.51	60	0.1	0.293
28_{H2}			KOCAELI_BUR090	22			0.1	
29_{H1}	Denali_Alaska	Geophysic. Obs CIGO,	DENALI_FAIGO-90	22	7.9	141	0.09	0.185

Record (#, comp.)	**Earthquake**	**Station**	**Filename**	**D_{5-75} [sec]**	**M_w**	**Rupture Distance [km]**	**PGA [g]**	**$S_a(T_1)$ [g]**
29_{H2}			DENALI_FAIGO360	28			0.07	
30_{H1}	Landers	Downey - Maint Bldg	LANDERS_DWN000	22	7.28	158	0.05	0.095
30_{H2}			LANDERS_DWN090	29			0.04	
31_{H1}	Landers	Mission Creek Fault	LANDERS_MCF000	23	7.28	27	0.13	0.207
31_{H2}			LANDERS_MCF090	31			0.13	
32_{H1}	Niigata_Japan	NIG010	NIIGATA_NIG010EW	11	6.63	58	0.11	0.108
32_{H2}			NIIGATA_NIG010NS	29			0.07	

Table 5.4: Characteristics of the Short-duration Ground Motions Selected for Bridges RB1 and RB1R

Record (#, comp.)	Earthquake	Station	Filename	D_{5-75} [sec]	M_w	Rupture Distance [km]	PGA [g]	$S_a(T_1)$ [g]
1_{H1}	Parkfield-02_ CA	COALINGA - PRIEST VALLEY	RSN4150_PARK2004_46174-90.AT2	9	6	22.02	0.02	0.05
1_{H2}			RSN4150_PARK2004_46174360.AT2	10			0.03	
2_{H1}	El Mayor-Cucapah_ Mexico	El Centro - Imperial & Ross	RSN5837_SIERRA.MEX_01711360.AT2	15	7.2	20.08	0.37	0.41
2_{H2}			RSN5837_SIERRA.MEX_01711-90.AT2	15			0.38	
3_{H1}	Northridge-01	LA - Century City CC North	RSN988_NORTHR_CCN090.AT2	7	6.69	23.41	0.26	0.25
3_{H2}			RSN988_NORTHR_CCN360.AT2	7			0.22	
4_{H1}	Hector Mine	Hector	RSN1787_HECTOR_HEC000.AT2	6	7.13	11.66	0.27	0.45
4_{H2}			RSN1787_HECTOR_HEC090.AT2	8			0.33	
5_{H1}	Loma Prieta	Coyote Lake Dam - Southwest Abutment	RSN755_LOMAP_CYC195.AT2	6	6.93	20.34	0.15	0.20
5_{H2}			RSN755_LOMAP_CYC285.AT2	4			0.48	
6_{H1}	Coalinga-01	Parkfield - Fault Zone 15	RSN339_COALINGA.H_H-Z15000.AT2	5	6.36	29.38	0.19	0.17
6_{H2}			RSN339_COALINGA.H_H-Z15090.AT2	10			0.12	
7_{H1}	Big Bear-01	Morongo Valley Fire Station	RSN6059_BIGBEAR_MVH045.AT2	8	6.46	29.06	0.15	0.19
7_{H2}			RSN6059_BIGBEAR_MVH135.AT2	8			0.12	
8_{H1}	Victoria_ Mexico	Chihuahua	RSN266_VICT_CHI102.AT2	8	6.33	18.96	0.15	0.20
8_{H2}			RSN266_VICT_CHI192.AT2	11			0.10	
9_{H1}	Corinth_ Greece	Corinth	RSN313_CORINTH_COR--L.AT2	5	6.6	10.27	0.24	0.18
9_{H2}			RSN313_CORINTH_COR--T.AT2	5			0.30	
10_{H1}	Northern Calif-03	Ferndale City Hall	RSN20_NCALIF.FH_H-FRN044.AT2	7	6.5	27.02	0.16	0.35
10_{H2}			RSN20_NCALIF.FH_H-FRN314.AT2	6			0.20	
11_{H1}	Northridge-01	Hollywood - Willoughby Ave	RSN978_NORTHR_WIL090.AT2	7	6.69	23.07	0.14	0.22
11_{H2}			RSN978_NORTHR_WIL180.AT2	6			0.25	
12_{H1}		Sanjo Shinbori	RSN4860_CHUETSU_65033NS.AT2	11	6.8	23.18	0.26	0.35

Record (#, comp.)	**Earthquake**	**Station**	**Filename**	**D$_{5-75}$ [sec]**	**M$_w$**	**Rupture Distance [km]**	**PGA [g]**	**S$_a$(T$_1$) [g]**
12$_{H2}$	Chuetsu-oki_ Japan		RSN4860_CHUETSU_65033EW.AT2	10			0.32	
13$_{H1}$	Chuetsu-oki_ Japan	Joetsu Kita	RSN4840_CHUETSU_65003NS.AT2	11	6.8	29.45	0.18	0.21
13$_{H2}$			RSN4840_CHUETSU_65003EW.AT2	20			0.09	
14$_{H1}$	El Mayor-Cucapah_ Mexico	MICHOACAN DE OCAMPO	RSN5827_SIERRA.MEX_MDO000.AT2	20	7.2	15.91	0.54	0.46
14$_{H2}$			RSN5827_SIERRA.MEX_MDO090.AT2	23			0.41	
15$_{H1}$	Chuetsu-oki_ Japan	Joetsu Yasuzukaku Yasuzuka	RSN4841_CHUETSU_65004NS.AT2	6	6.8	25.52	0.22	0.15
15$_{H2}$			RSN4841_CHUETSU_65004EW.AT2	7			0.15	
16$_{H1}$	Chalfant Valley-02	Long Valley Dam (L Abut)	RSN554_CHALFANT.A_A-LVL000.AT2	5	6.19	21.12	0.08	0.10
16$_{H2}$			RSN554_CHALFANT.A_A-LVL090.AT2	8			0.07	
17$_{H1}$	Morgan Hill	Hollister Differential Array #3	RSN464_MORGAN_HD3255.AT2	12	6.19	26.43	0.08	0.13
17$_{H2}$			RSN464_MORGAN_HD3345.AT2	10			0.08	
18$_{H1}$	Loma Prieta	Anderson Dam (Downstream)	RSN739_LOMAP_AND250.AT2	5	6.93	20.26	0.25	0.16
18$_{H2}$			RSN739_LOMAP_AND340.AT2	5			0.24	
19$_{H1}$	Duzce_ Turkey	Bolu	RSN1602_DUZCE_BOL000.AT2	3	7.14	12.04	0.74	0.53
19$_{H2}$			RSN1602_DUZCE_BOL090.AT2	1			0.80	
20$_{H1}$	Joshua Tree_ CA	Indio - Jackson Road	RSN6877_JOSHUA_5294180.AT2	3	6.1	25.53	0.41	0.27
20$_{H2}$			RSN6877_JOSHUA_5294090.AT2	5			0.21	
21$_{H1}$	Loma Prieta	Gilroy Array #7	RSN993_NORTHR_FLE144.AT2	5	6.93	22.68	0.23	0.07
21$_{H2}$			RSN993_NORTHR_FLE234.AT2	4			0.32	
22$_{H1}$	Joshua Tree_ CA	Morongo Valley Fire Station	RSN6875_JOSHUA_5071045.AT2	6	6.1	22.3	0.13	0.13
22$_{H2}$			RSN6875_JOSHUA_5071135.AT2	8			0.07	
23$_{H1}$	Superstition Hills-02	Imperial Valley Wildlife Liquefaction Array	RSN729_SUPER.B_B-IVW090.AT2	19	6.54	23.85	0.18	0.31
23$_{H2}$			RSN729_SUPER.B_B-IVW360.AT2	13			0.21	

Record (#, comp.)	**Earthquake**	**Station**	**Filename**	**$D_{5\text{-}75}$ [sec]**	**M_w**	**Rupture Distance [km]**	**PGA [g]**	**$S_a(T_1)$ [g]**
24_{H1}	Darfield_ New Zealand	Styx Mill Transfer Station	RSN6969_DARFIELD_SMTCN88W.AT2	11	7	20.86	0.18	0.19
24_{H2}			RSN6969_DARFIELD_SMTCS02W.AT2	14			0.17	
25_{H1}	Parkfield-02_ CA	Parkfield - Fault Zone 3	RSN4108_PARK2004_COH090.AT2	3	6	2.73	0.38	0.18
25_{H2}			RSN4108_PARK2004_COH360.AT2	4			0.40	
26_{H1}	San Simeon_ CA	San Luis Obispo - Lopez Lake Grounds	RSN3994_SANSIMEO_36153090.AT2	8	6.52	48.11	0.13	0.08
26_{H2}			RSN3994_SANSIMEO_36153360.AT2	10			0.12	
27_{H1}	Imperial Valley-06	Westmorland Fire Sta	RSN192_IMPVALL.H_H-WSM090.AT2	14	6.53	15.25	0.08	0.07
27_{H2}			RSN192_IMPVALL.H_H-WSM180.AT2	13			0.11	
28_{H1}	Tabas_ Iran	Boshrooyeh	RSN138_TABAS_BOS-L1.AT2	15	7.35	28.79	0.11	0.14
28_{H2}			RSN138_TABAS_BOS-T1.AT2	15			0.08	
29_{H1}	Chuetsu-oki_ Japan	Joetsu Yanagishima paddocks	RSN4846_CHUETSU_65009NS.AT2	4	6.8	31.43	0.28	0.13
29_{H2}			RSN4846_CHUETSU_65009EW.AT2	3			0.33	
30_{H1}	Iwate_ Japan	Yuzawa Town	RSN5806_IWATE_55461NS.AT2	8	6.9	25.56	0.19	0.31
30_{H2}			RSN5806_IWATE_55461EW.AT2	9			0.24	
31_{H1}	Darfield_ New Zealand	Christchurch Cashmere High School	RSN6890_DARFIELD_CMHSN10E.AT2	8	7	17.64	0.23	0.23
31_{H2}			RSN6890_DARFIELD_CMHSS80E.AT2	9			0.25	
32_{H1}	Coalinga-01	Parkfield - Stone Corral 4E	RSN358_COALINGA.H_H-SC4000.AT2	5	6.36	31.58	0.07	0.12
32_{H2}			RSN358_COALINGA.H_H-SC4090.AT2	6			0.07	

Table 5.5: Characteristics of the Short-duration Ground Motions Selected to be used in Bridges RB2, RB2R, IB1, IB1R, IB2, IB2R, IB3 and IB3R

Record (#, comp.)	Earthquake	Station	Filename	D_{5-75} [sec]	M_w	Rupture Distance [km]	PGA [g]	$S_a(T_1)$ [g]
1_{H1}	Imperial Valley-06	El Centro Array #12	RSN175_IMPVALL.H_H-E12140.AT2	10	6.53	17.94	0.14	0.16
1_{H2}			RSN175_IMPVALL.H_H-E12230.AT2	10			0.12	
2_{H1}	El Mayor-Cucapah_ Mexico	El Centro - Imperial & Ross	RSN5837_SIERRA.MEX_01711360.AT2	15	7.2	20.08	0.37	0.87
2_{H2}			RSN5837_SIERRA.MEX_01711-90.AT2	15			0.38	
3_{H1}	El Mayor-Cucapah_ Mexico	Calexico Fire Station	RSN5975_SIERRA.MEX_CXO360.AT2	18	7.2	20.46	0.27	0.43
3_{H2}			RSN5975_SIERRA.MEX_CXO090.AT2	19			0.26	
4_{H1}	Darfield_ New Zealand	Christchurch Cashmere High School	RSN6890_DARFIELD_CMHSN10E.AT2	8	7	17.64	0.23	0.30
4_{H2}			RSN6890_DARFIELD_CMHSS80E.AT2	9			0.25	
5_{H1}	Northridge-01	LA - Brentwood VA Hospital	RSN986_NORTHR_BVA195.AT2	6	6.69	22.5	0.19	0.33
5_{H2}			RSN986_NORTHR_BVA285.AT2	6			0.16	
6_{H1}	Darfield_ New Zealand	WSFC	RSN6988_DARFIELD_WSFCN38W.AT2	15	7	26.93	0.07	0.11
6_{H2}			RSN6988_DARFIELD_WSFCS52W.AT2	14			0.07	
7_{H1}	Northridge-01	Canyon Country - W Lost Cany	RSN960_NORTHR_LOS000.AT2	3	6.69	12.44	0.40	0.52
7_{H2}			RSN960_NORTHR_LOS270.AT2	3			0.47	

Record (#, comp.)	**Earthquake**	**Station**	**Filename**	**$D_{5\text{-}75}$ [sec]**	**M_w**	**Rupture Distance [km]**	**PGA [g]**	**$S_a(T_1)$ [g]**
8_{H1}	Northridge-01	LA - W 15th St	RSN1008_NORTHR_W15090.AT2	10	6.69	29.74	0.10	0.21
8_{H2}			RSN1008_NORTHR_W15180.AT2	9			0.17	
9_{H1}	Northridge-01	LA - N Faring Rd	RSN996_NORTHR_FAR000.AT2	5	6.69	20.81	0.28	0.33
9_{H2}			RSN996_NORTHR_FAR090.AT2	6			0.26	
10_{H1}	Superstition Hills-02	El Centro Imp. Co. Cent	RSN721_SUPER.B_B-ICC000.AT2	7	6.54	18.2	0.36	0.29
10_{H2}			RSN721_SUPER.B_B-ICC090.AT2	9			0.26	
11_{H1}	Northridge-01	Sunland - Mt Gleason Ave	RSN1083_NORTHR_GLE170.AT2	7	6.69	13.35	0.13	0.26
11_{H2}			RSN1083_NORTHR_GLE260.AT2	5			0.16	
12_{H1}	Northridge-01	LA - Century City CC North	RSN988_NORTHR_CCN090.AT2	7	6.69	23.41	0.26	0.36
12_{H2}			RSN988_NORTHR_CCN360.AT2	7			0.22	
13_{H1}	Loma Prieta	Sunnyvale - Colton Ave.	RSN806_LOMAP_SVL270.AT2	10	6.93	24.23	0.21	0.27
13_{H2}			RSN806_LOMAP_SVL360.AT2	10			0.21	
14_{H1}	El Mayor-Cucapah_ Mexico	MICHOACAN DE OCAMPO	RSN5827_SIERRA.MEX_MDO000.AT2	20	7.2	15.91	0.54	0.80
14_{H2}			RSN5827_SIERRA.MEX_MDO090.AT2	23			0.41	
15_{H1}	Chuetsu-oki_ Japan	Joetsu Yasuzukaku Yasuzuka	RSN4841_CHUETSU_65004NS.AT2	6	6.8	25.52	0.22	0.35

Record (#, comp.)	**Earthquake**	**Station**	**Filename**	**D_{5-75} [sec]**	**M_w**	**Rupture Distance [km]**	**PGA [g]**	**$S_a(T_1)$ [g]**
15_{H2}			RSN4841_CHUETSU_65004EW.AT2	7			0.15	
16_{H1}	Umbria Marche_ Italy	Castelnuovo-Assisi	RSN4348_UBMARCHE.P_A-CSA000.AT2	8	6	17.28	0.17	0.15
16_{H2}			RSN4348_UBMARCHE.P_A-CSA270.AT2	9			0.11	
17_{H1}	Morgan Hill	Hollister Differential Array #3	RSN464_MORGAN_HD3255.AT2	12	6.19	26.43	0.08	0.15
17_{H2}			RSN464_MORGAN_HD3345.AT2	10			0.08	
18_{H1}	Imperial Valley-06	Cerro Prieto	RSN164_IMPVALL.H_H-CPE147.AT2	17	6.53	15.19	0.17	0.26
18_{H2}			RSN164_IMPVALL.H_H-CPE237.AT2	20			0.16	
19_{H1}	Basso Tirreno_ Italy	Patti-Cabina Prima	RSN4285_BTIRRENO.P_PTT000.AT2	5	6	17.4	0.07	0.13
19_{H2}			RSN4285_BTIRRENO.P_PTT090.AT2	4			0.16	
20_{H1}	N. Palm Springs	Whitewater Trout Farm	RSN540_PALMSPR_WWT180.AT2	2	6.06	6.04	0.48	0.40
20_{H2}			RSN540_PALMSPR_WWT270.AT2	2			0.63	
21_{H1}	Joshua Tree_ CA	Indio - Jackson Road	RSN6877_JOSHUA_5294180.AT2	3	6.1	25.53	0.41	0.33
21_{H2}			RSN6877_JOSHUA_5294090.AT2	5			0.21	
22_{H1}	Spitak_ Armenia	Gukasian	RSN730_SPITAK_GUK000.AT2	6	6.77	23.99	0.20	0.29
22_{H2}			RSN730_SPITAK_GUK090.AT2	4			0.17	

Record (#, comp.)	Earthquake	Station	Filename	D_{5-75} [sec]	M_w	Rupture Distance [km]	PGA [g]	$S_a(T_1)$ [g]
23$_{H1}$	Victoria_ Mexico	Chihuahua	RSN266_VICT_CHI102.AT2	8	6.33	18.96	0.15	0.22
23$_{H2}$			RSN266_VICT_CHI192.AT2	11			0.10	
24$_{H1}$	Darfield_ New Zealand	Styx Mill Transfer Station	RSN6969_DARFIELD_SMTCN88W.AT2	11	7	20.86	0.18	0.31
24$_{H2}$			RSN6969_DARFIELD_SMTCS02W.AT2	14			0.17	
25$_{H1}$	Iwate_ Japan	Yuzawa Town	RSN5806_IWATE_55461NS.AT2	8	6.9	25.56	0.19	0.25
25$_{H2}$			RSN5806_IWATE_55461EW.AT2	9			0.24	
26$_{H1}$	Chuetsu-oki_ Japan	Joetsu Kita	RSN4840_CHUETSU_65003NS.AT2	11	6.8	29.45	0.18	0.21
26$_{H2}$			RSN4840_CHUETSU_65003EW.AT2	20			0.09	
27$_{H1}$	Imperial Valley-06	Westmorland Fire Sta	RSN192_IMPVALL.H_H-WSM090.AT2	14	6.53	15.25	0.08	0.11
27$_{H2}$			RSN192_IMPVALL.H_H-WSM180.AT2	13			0.11	
28$_{H1}$	Chuetsu-oki_ Japan	Sanjo Shinbori	RSN4860_CHUETSU_65033NS.AT2	11	6.8	23.18	0.18	0.21
28$_{H2}$			RSN4860_CHUETSU_65033EW.AT2	20			0.09	
29$_{H1}$	Chuetsu-oki_ Japan	Joetsu Yanagishima paddocks	RSN4846_CHUETSU_65009NS.AT2	4	6.8	31.43	0.28	0.39
29$_{H2}$			RSN4846_CHUETSU_65009EW.AT2	3			0.33	
30$_{H1}$	Parkfield-02_ CA	COALINGA - PRIEST VALLEY	RSN4150_PARK2004_46174-90.AT2	9	6	22.02	0.02	0.05

Record (#, comp.)	**Earthquake**	**Station**	**Filename**	**$D_{5\text{-}75}$ [sec]**	**M_w**	**Rupture Distance [km]**	**PGA [g]**	**$S_a(T_1)$ [g]**
30_{H2}			RSN4150_PARK2004_46174360.AT2	10			0.03	
31_{H1}	Northridge-01	Inglewood - Union Oil	RSN981_NORTHR_ING000.AT2	12	6.69	42.2	0.09	0.12
31_{H2}			RSN981_NORTHR_ING090.AT2	10			0.10	
32_{H1}	Big Bear-01	San Bernardino - 2nd & Arrowhead	RSN930_BIGBEAR_SB2270.AT2	12	6.46	33.79	0.11	0.13
32_{H2}			RSN930_BIGBEAR_SB2360.AT2	10			0.10	

5.8 FINITE ELEMENT ANALYSIS RESULTS

5.8.1 Modal analysis results

The fundamental modes of vibration were determined and the deformed shapes and periods for the two first modes of bridge models RB1/RB1R and RB2/RB2R are shown in Figure 5.10a and Figure 5.10b, respectively. The mode shapes and periods of bridges IB1/IB1R, IB2/IB2R and IB3/IB3R are displayed in Figure 5.10c, Figure 5.10d, and Figure 5.10e. In all cases, the first mode was characterized by translation along the longitudinal direction, while in the second mode the bridge deforms in the transverse direction. Bridge model RB1 was the most flexible with its mode shapes showing pure translation in both directions. Bridge model RB2 also shows pure translation in both mode shapes with higher fundamental period when compared with the irregular bridges. It is interesting to note that bridge model IB3 shows a smaller second period when compared to bridge models IB1 and IB2 due to the fact that, in bridge model IB3, the short column located at the centerline of the bridge restrained the modal displacement of the deck due to the greater stiffness of the short columns. On the other hand, in bridges IB1 and IB2 the short column is located at one of the bridge ends, thereby restraining the motion of the spans closest to the short column and inducing some twisting.

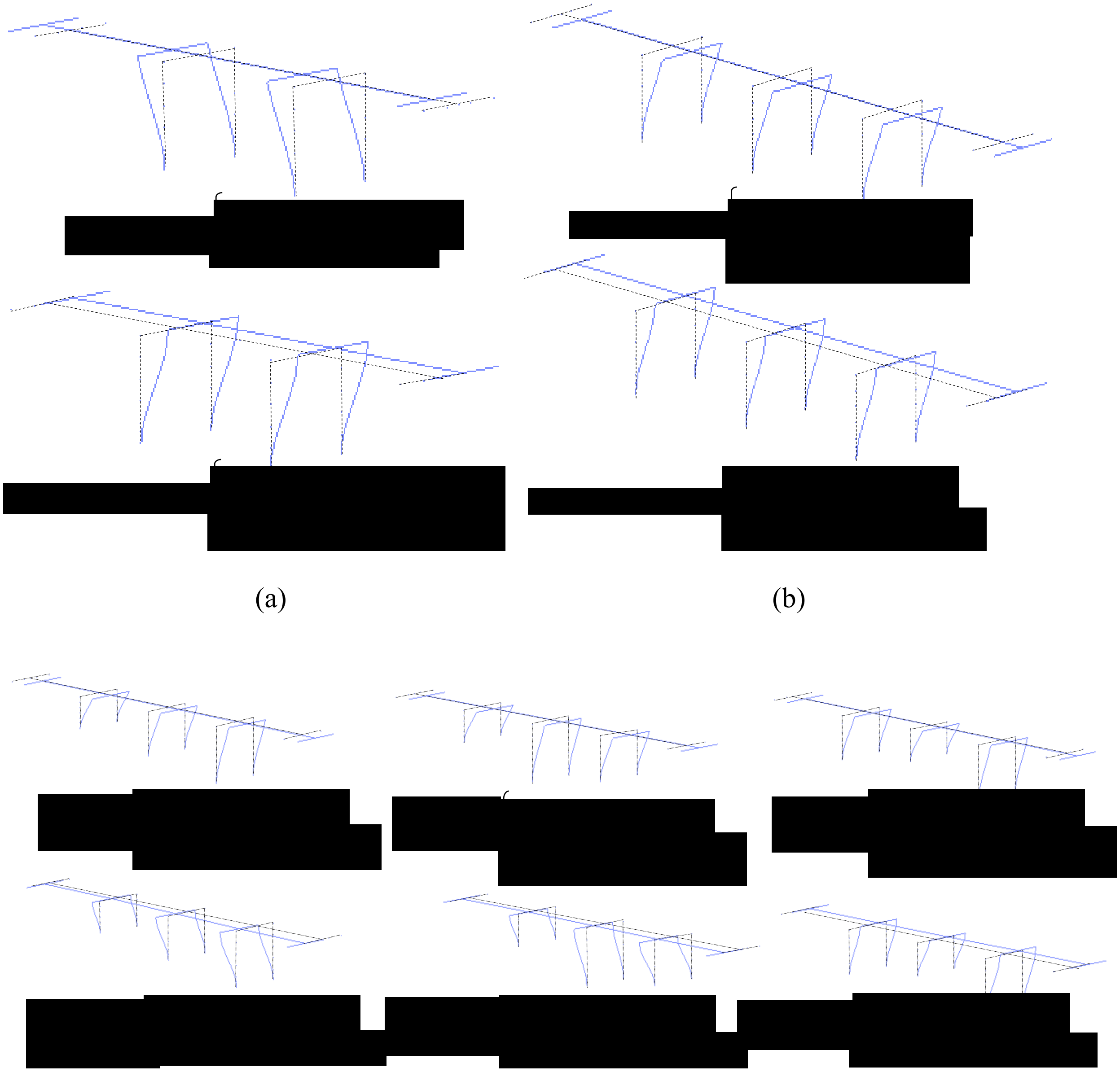

[redacted] [redacted] [redacted] [redacted]

(a) (b)

[redacted] [redacted] [redacted] [redacted] [redacted] [redacted]

(c) (d) (e)

Figure 5.10: Fundamental mode shapes and respective periods: (a) Bridge RB1/RB1R; (b) Bridge RB2/RB2R; (c) Bridge IB1/IB1R; (d) Bridge IB2/IB2R; (e) Bridge IB3/IB3R

5.8.2 Time-history response analysis

Example time-history response analysis results for drift ratios at the top of the bent column at the end of the first span with and without TiAB retrofit for three (3) ground motions for the regular bridge models and for one (1) of the irregular bridge models. Figure 5.11(a), Figure 5.11(c), and Figure 5.11(e) show longitudinal responses, while Figure 5.11(b), Figure 5.11(d), and Figure 5.11(f) show transverse responses of the bridge models. Several salient features can be qualitatively observed from these figures. First, it can be seen that for all bridges, the initial cycles were similar, which was due to the non-retrofitted and retrofitted bridges having essentially the same periods of vibration. As the motions increase, it can be seen that the non-retrofitted bridges showed responses with period elongation compared to the retrofitted counterparts due to softening and period elongation. In addition, for example in Figure 5.11(b), it can be seen that the non-retrofitted bridge shows considerable residual drift while the retrofitted case does not.

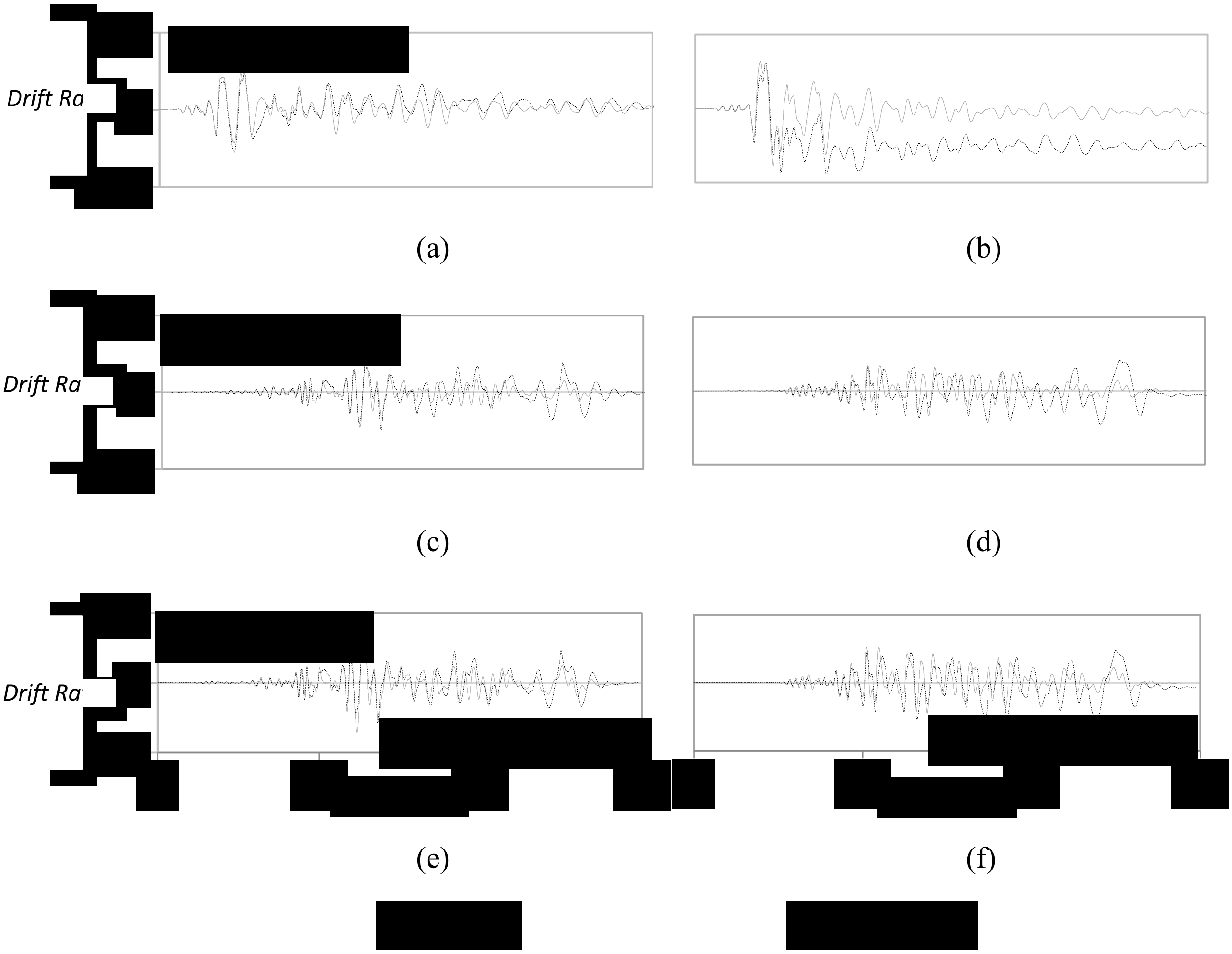

Figure 5.11: Example time-history response analysis results of the non-retrofitted and retrofitted bridge models: (a) Longitudinal direction drift ratios of bridges RB1 and RB1R; (b) transverse direction drift ratios of bridges RB1 and RB1R; (c) Longitudinal direction drift ratios of bridges RB1 and RB1R; (d) transverse direction drift ratios of bridges RB1 and RB1R; (e) Longitudinal direction drift ratios of bridges RB2 and RB2R; (f) transverse direction drift ratios of bridges IB1 and IB1R

The influence of the TiAB retrofit was also evaluated by comparing the hysteretic response in terms of column shear versus column drift ratio for a short column and a median column in the same bridge model configuration, IB1and IB1R. The response of the unretrofitted columns in IB1 are shown in Figure 5.12. It can be seen that, as expected, there are significant differences between the force and deformation demands between the short and long columns, with the shorter column having higher demands.

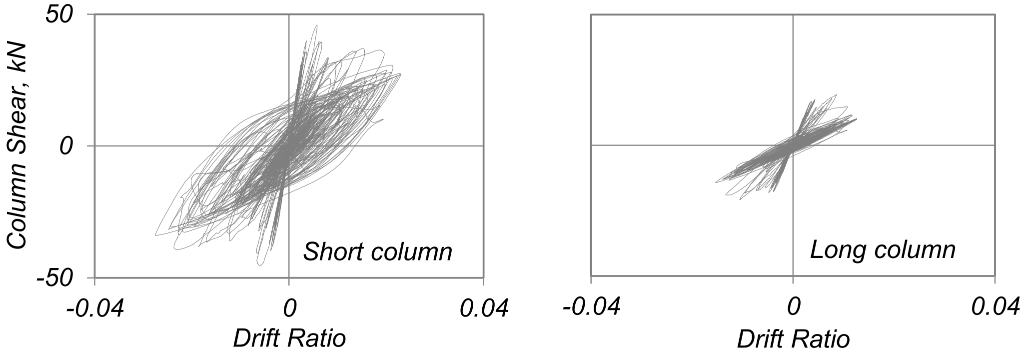

(a) (b)

Figure 5.12: Column shear vs drift ratio time-history response along the longitudinal direction of bridge IB1: (a) column position “1” (short column); (b) column position “3” (long column) for earthquake Pair #6

The hysteretic energies dissipated for short and the median column for the three irregular bridges analyzed are shown in Figure 5.13. As seen in the figure, for higher seismic intensities, the non-retrofitted bridge model showed evidence of higher levels of nonlinearity, while the TiAB retrofitted column showed greater ductility, and produced greater amounts of dissipated energy. For the irregular bridge models, the short columns were subjected to greater forces due to their larger stiffness and larger drift demands. The results of Figure 5.13 also show that the location of the shorter column along the bridge did not greatly affect the column structural behavior in terms of energy demands. The small differences reveal that: (1) the energy dissipated at the short column is a little higher when located at the middle of the bridge, and (2) the energy dissipated at the median column is slightly higher when positioned two spans away from the short column. However, the differences between the irregular bridges IB1 and IB1R, IB2 and IB2R and IB3 and IB3R were minimal. Therefore results for bridges IB1 and IB1R were used to highlight the performance differences due to irregular column heights along the span.

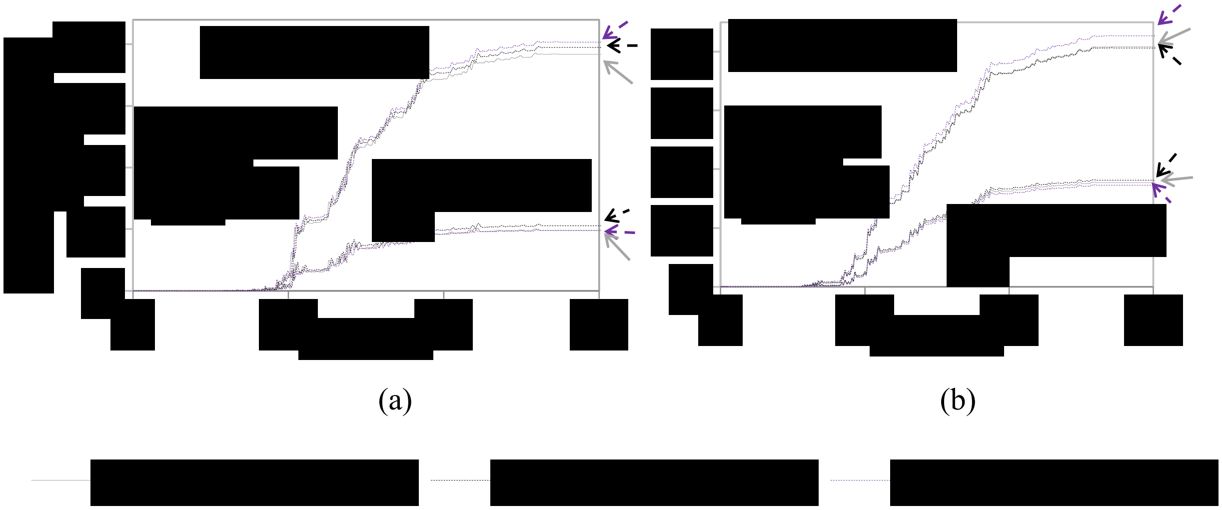

(a) (b)

Figure 5.13: Energy dissipated in the column top along longitudinal direction: (a) Different positions of short "1" and median length columns "2" (Bridges IB1, IB2 and IB3) for *$S_a(T_1)$* = 0.4g; (b) Different positions of short "1" and median length columns "2" (Bridges IB1R, IB2R and IB3R) for *$S_a(T_1)$* = 0.8g

5.8.3 Statistical assessment of the ground motion duration effects

A statistical analysis of damage indicators including: peak drift ratio, Park & Ang damage index ($DI_{P\&A}$), and Reinhorn & Valles damage index ($DI_{R\&V}$) were estimated. All the unscaled ground motions (64 x 2=128 points) were used to assess the role of ground motion duration effects on the bridge models. The damage indicators versus acceleration at the fundamental period $S_a(T_1)$ and significant duration $D_{5\text{-}75}$ are shown in Figure 5.14, Figure 5.15, and Figure 5.16. A multiple linear regression surface that best fit the data is also shown in the figures, along with a horizontal line which caps the limit of the peak response measured. From the data fit, a slight tendency for $DI_{P\&A}$ to increase as duration parameter $D_{5\text{-}75}$ increased, while $DI_{R\&V}$ showed a relationship with duration for non-retrofitted bridge models. Overall, the results indicated that ground motion duration did not play a strong role for low intensities of ground motion. However, for large ground motion intensities, longer ground motion duration increased the values of the damage indices.

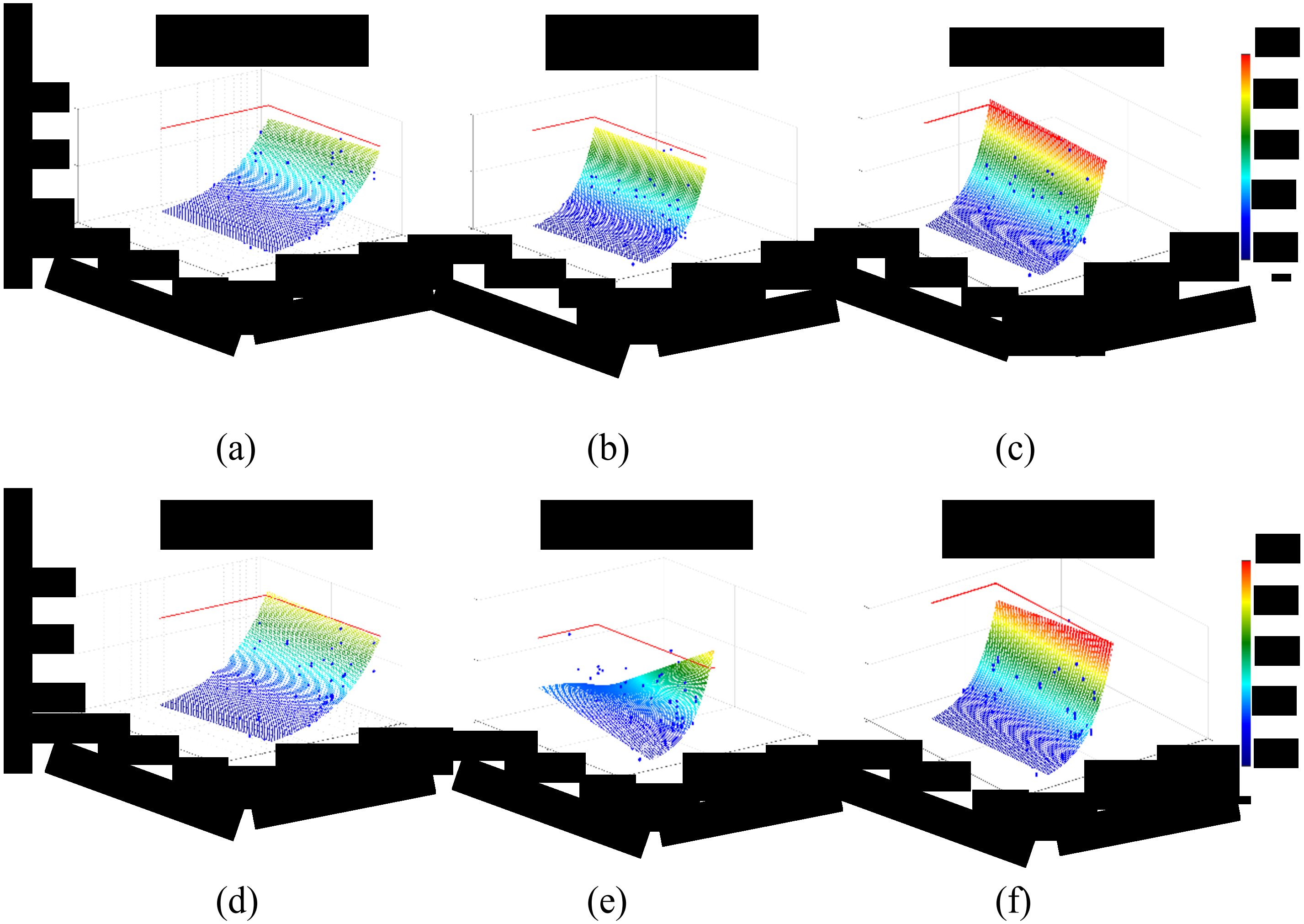
(a) (b) (c)

(d) (e) (f)

Figure 5.14: Surface plots that relate D$_{5-75}$, $S_a(T_1)$ to peak drift ratio: (a) Bridge RB1; (b) Bridge RB2 (c) Bridge IB1; (d) Bridge RB1R; (e) Bridge RB2R; (f) Bridge IB1R

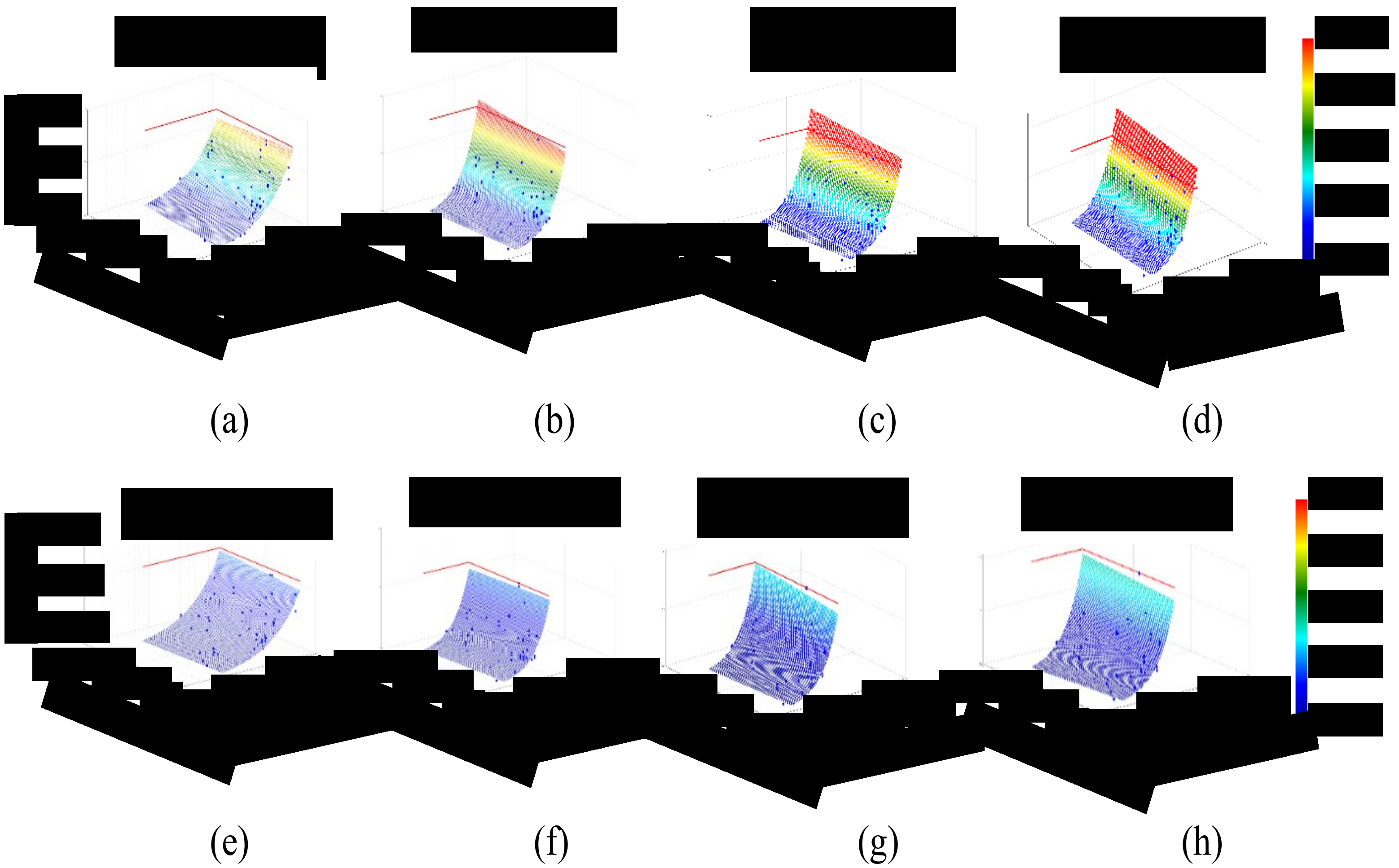

Figure 5.15: Surface plots that relate D_{5-75}, $S_a(T_1)$ Park and Ang Damage Index: (a) Bridge RB1; (b) Bridge RB2 (c) Bridge IB1; (d) Most damaged element of Bridge IB1; (e) Bridge RB1R; (f) Bridge RB2R (g) Bridge IB1R; (h) Most damaged element of Bridge IB1R

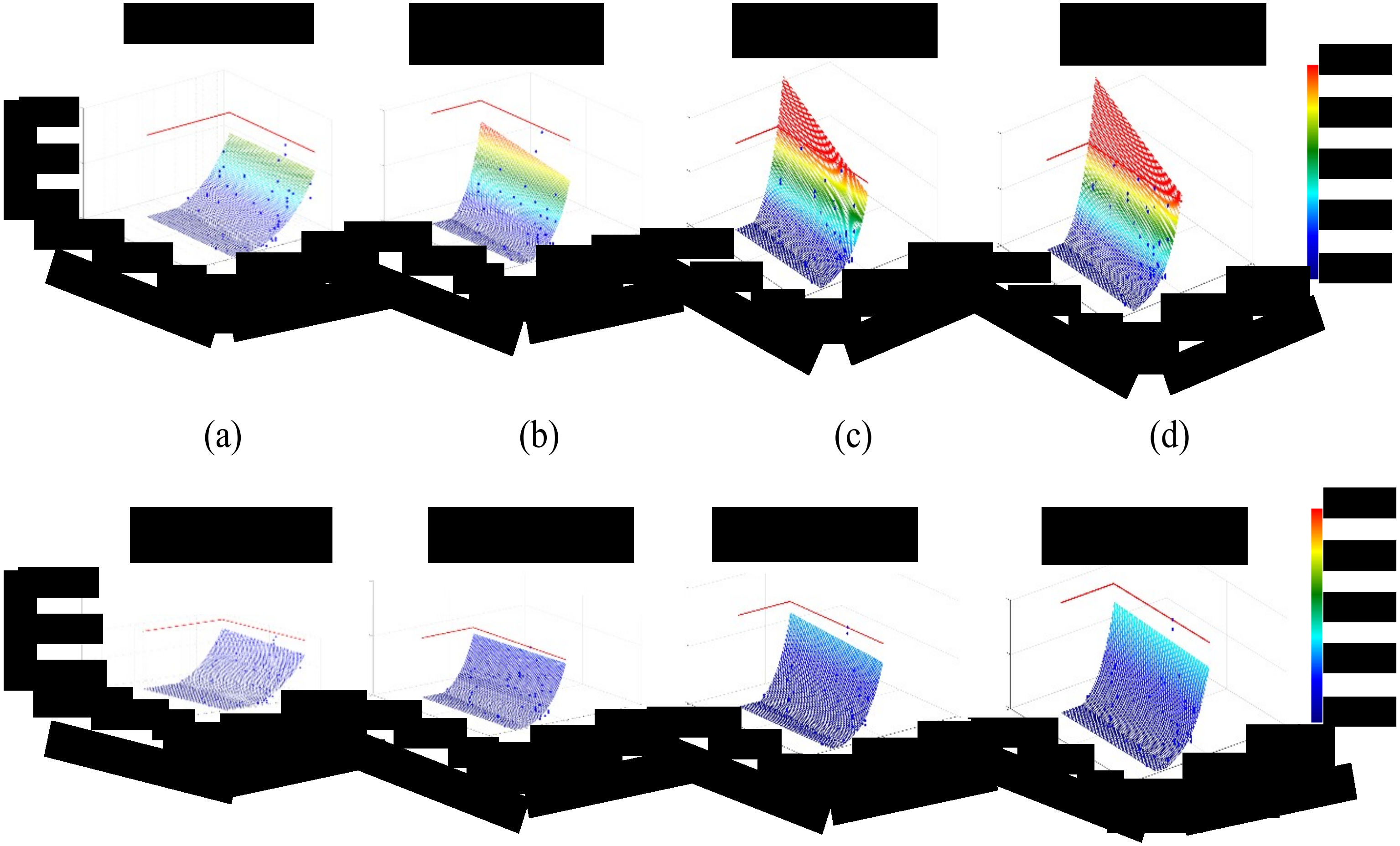

(a) (b) (c) (d)

(e) (f) (g) (h)

Figure 5.16: Surface plots that relate $D_{5\text{-}75}$, $S_a(T_1)$ and Reinhorn and Valles Damage Index: (a) Bridge RB1; (b) Bridge RB2 (c) Bridge IB1; (d) Most damaged element of Bridge IB1; (e) Bridge RB1R; (f) Bridge RB2R (g) Bridge IB1R; (h) Most damaged element of Bridge IB1R.

5.9 DAMAGE ASSESSMENT BASED ON INCREMENTAL DYNAMIC ANALYSIS

Incremental dynamic analysis (IDA) was performed for bridge models RB1 and RB1R, RB2 and RB2R, as well as IB1 and IB1R to assess the role of the retrofit on expected seismic performance of the bridge models. The median IDA curves for peak drift ratio of the bridge models are shown in Figure 5.17a, Figure 5.17b, and Figure 5.17c for RB1 and RB1R, RB2 and RB2R, and IB1 and IB1R, respectively. In these plots, the median peak deformation observed was defined as the vector sum of peak deformations (square root of sum of squares, SRSS) in both orthogonal directions of the bridges. The damage-index based IDA curves are plotted in Figure 5.18 with the first row of figures showing results relative to Park & Ang damage index, while the second row shows the Reinhorn and Valles damage index. As seen in these figures, the TiAB retrofitted cases substantially reduced drift and damage, with greater improvements for regular bridges.

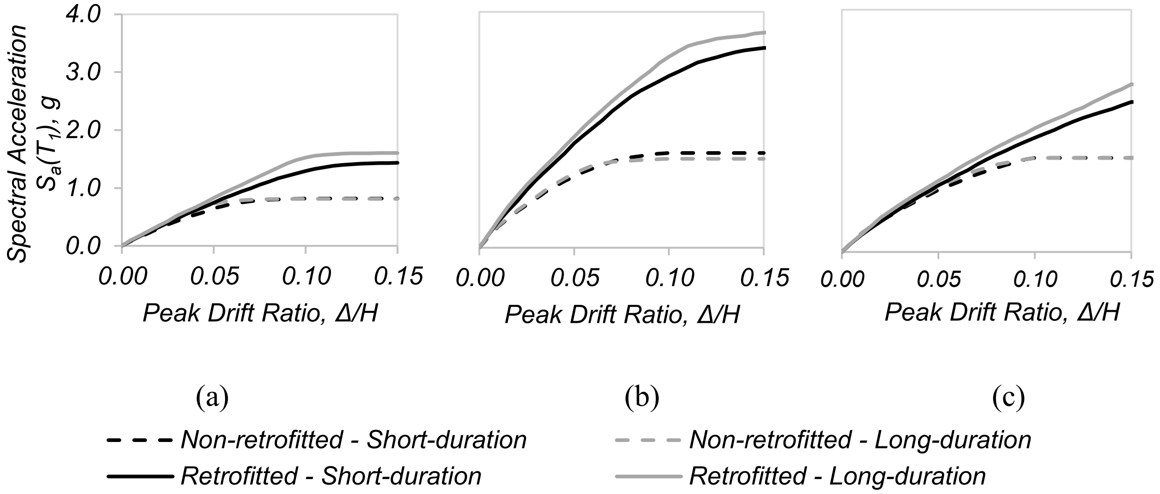

Figure 5.17: Median incremental dynamic analysis curves for vector sum of peak drift ratios in longitudinal and transverse directions based on results from bridge models: (a) RB1 and RB1R; (b) RB2 and RB2R; and (c) IB1 and IB1R

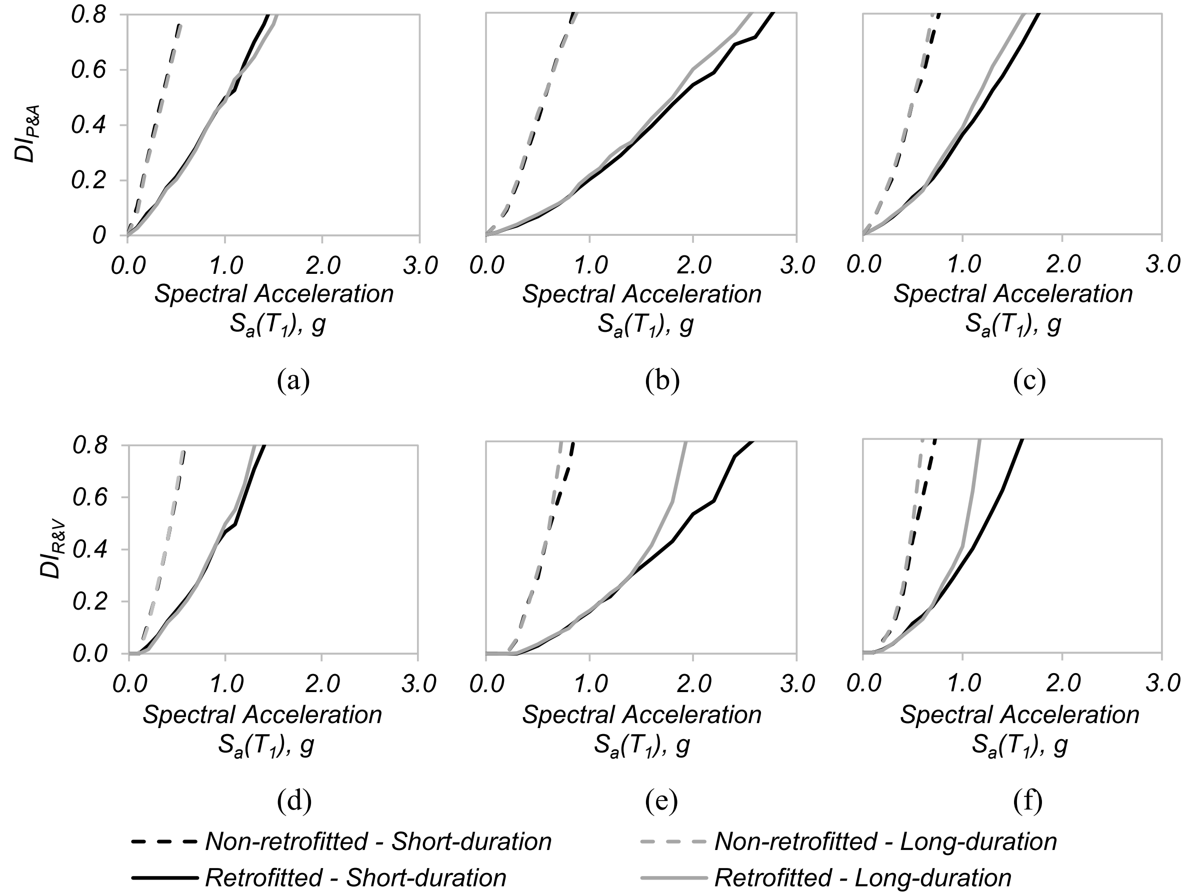

Figure 5.18: Median incremental dynamic analysis damage curves: (a) $DI_{P\&A}$ curves for RB1 and RB1R; (b) $DI_{P\&A}$ curves for RB2 and RB2R; (c) $DI_{P\&A}$ curves for IB1 and IB1R; (d) $DI_{R\&V}$ curves for RB1 and RB1R; (e) $DI_{R\&V}$ curves for RB2 and RB2R; and (f) $DI_{R\&V}$ curves for IB1 and IB1R

Fragility functions that capture the probability of reaching a specific value of drift or damage state (defined by reaching a specific value of damage index) are shown in Figure 5.19. For drift ratio, the fragility functions represent the probability of reaching a threshold peak drift ratio (pdr). The threshold values considered were different for the non-retrofitted bridges (RB2 and IB1) and retrofitted bridges (RB2R and IB1R). In the results shown for peak drift ratios, a threshold value of 4% was considered for the non-retrofitted bridges, while 10% was assumed for the retrofitted cases. The peak drift ratios considered are not indicative of bridge collapse, however, comparison of pdr-based fragility functions with damage-index fragility functions showed similar trends. The experimental results demonstrated the ability of the retrofitted specimens to achieve very large drift ratios without loss of self-centering. Damage index-based fragility functions were computed for the probability of reaching the collapse limit state. The "collapse" qualification is based on a damage index greater than 0.8 as suggested in Ang et al. (1993) and the results are shown in Figure 5.19b and Figure 5.19c. As seen in these figures, all TiAB retrofitted cases greatly reduced the probability of collapse.

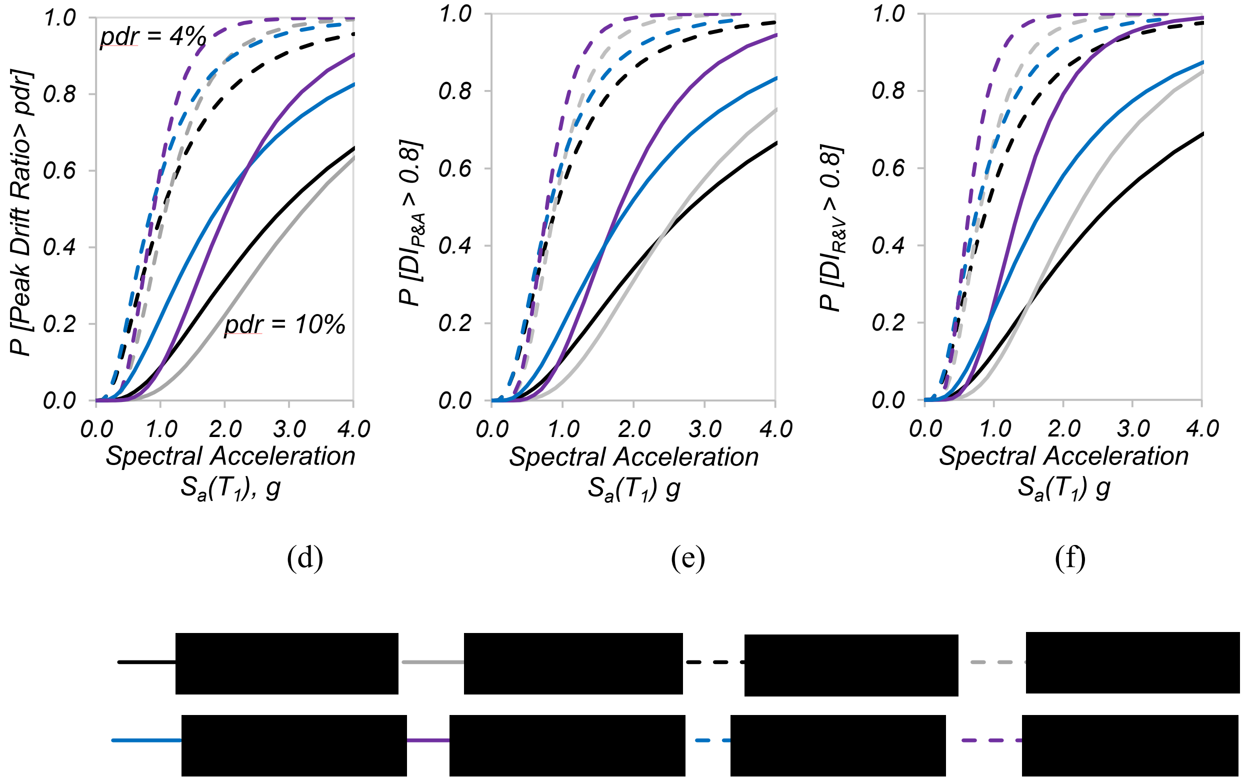

(d) (e) (f)

[redacted] [redacted] [redacted] [redacted]

[redacted] [redacted] [redacted] [redacted]

Figure 5.19: (a) Fragility curves for probability of exceeding a prescribed drift ratio (4% for the non-retrofitted bridges and 10% for the retrofitted bridges); (b) Fragility curves that compute probability of reaching collapse (DI > 0.8) based on the Park and Ang damage index $DI_{P\&A}$; and (b) Fragility curves that compute probability of reaching collapse (DI>0.8) based on the Reinhorn and Valles damage index $DI_{R\&V}$.

5.10 DISCUSSION

Based on the analysis results described above, the TiAB retrofit solution for square vintage RC columns on bridge performance, increased the deformation capacities and energy dissipation. The performance enhancements were better for regular bridges compared to irregular bridges. Short columns tended to have increased demands, and the retrofitted experimental results were shown to produce greater improvements for displacement ductility in the shorter columns. From the IDA curves observed in Figure 5.18, the performance of the retrofitted bridges RB1R, RB2R and IB1R is enhanced, with a capacity increase of approximately twice that of non-retrofitted bridge models. The same figure shows that the unretrofitted bridge RB1 had the capacity to deform up to 5% drift ratio and handle shaking intensities of $S_a(T_1)$ = 0.75g. After applying the TiAB retrofit, the bridge could deform up to 10% drift ratio at $S_a(T_1)$ = 1.5g. Unretrofitted bridge models RB2 and IB1 had lower fundamental periods with more strength and deformation capacities reaching values around 7% of peak drift ratio and $S_a(T_1)$ of 1.5g. The retrofitted bridge RB2R reaches intensities greater than $S_a(T_1)$ of 3.0g for values of peak drift ratio of 10%. Similar increases in capacity can be observed for the IB1R bridge model results, regarding peak drift ratios.

Considering the results shown in Figure 5.19b and Figure 5.19c, the damage indices for the non-retrofitted bridges, indicate structural collapse at: (1) $S_a(T_1)$ of approximately 0.5g for RB1; (2) $S_a(T_1) \approx 0.8$g for RB2, and (3) $S_a(T_1) \approx 0.75$g for IB1. For the retrofitted bridge models the collapses are observed at: (1) $S_a(T_1) \approx 1.5$g for RB1R, (b) $S_a(T_1) > 2.0$g for RB2R, and (3) $S_a(T_1) > 1.2$g for IB1R. In summary, the results highlight the highly beneficial outcome for the TiAB retrofitted solution on the structural capacity, increasing their capacity 2 to 3 times independent of the damage indicator used. The fragility curve shown in Figure 5.19a shows the direct benefit of retrofitting the bridge columns by demonstrating that the probability of reaching a drift level, and thereby damage state, is reduced dramatically when the columns were retrofitted with TiABs using the approach described in this report, for any large earthquake.

6.0 SUMMARY AND CONCLUSIONS

6.1 SUMMARY

Oregon is situated near the Cascadia Subduction Zone (Cascadia fault) which is now known to produce great earthquakes. However, many existing RC bridges in the Oregon Department of Transportation bridge inventory were not designed to resist earthquake forces. Two of the most common seismic deficiencies in older RC columns are inadequate transverse reinforcement and poorly detailed lap lengths in the column above the footing (in the expected hinge location). These poor details can result in non-ductile behavior during an earthquake which can negatively impact the resilience of the transportation system. Replacement of all seismically deficient bridges is not practical due to limited resources and rehabilitation is a feasible approach. Many alternative materials and techniques are available to retrofit deficient RC columns. Presently available retrofitting techniques all have some drawbacks that provide an incentive to develop an effective and economical alternative.

The well-defined material properties of TiABs are advantageous for retrofitting RC columns with seismic deficiencies, but no experimental data on the use of TiABs for seismic retrofitting was available. To establish the viability of using TiABs for seismic retrofitting, to advance analytical tools and design approaches, experimental studies were undertaken.

This research reports on the experimental tests of fourteen (14) full-scale square RC columns constructed and retrofitted to simulate the application of TiAB retrofits on vintage substructures that are seismically deficient. The performances of the TiAB retrofitted columns were compared to unretrofitted columns. To ensure the specimens were representative of the inventory, the details, proportions, and materials were selected based on a detailed review of ODOT's inventory of bridges on key lifeline corridors: I-5, US-97 and OR-58. All of the columns consisted of the same cross sectional dimensions and were detailed according to mid-20th century design standards that included short lap splices and widely spaced transverse steel. Two columns heights were considered (8 ft and 12 ft) and three different footing connections were investigated to consider soil-structure influences on the performance of the retrofits (rigid, realistic spread footing, and realistic timber pile cap). The specimens were tested under reversed cyclic loading. The response of each specimen was measured during tests and described in terms of overall structural behavior, force-deformation response, strength degradation, displacement ductility, energy dissipation, viscous damping, and stiffness degradation.

Analytical models of retrofitted and unretrofitted column specimens were developed based on a phenomenological approach of the measured experimental response. The individual column model was validated using the experimental results and was adapted into a bridge bent system to study the system behavior in regular and irregular bridges. Column bases were fixed to simulate rigid foundations. The retrofit was applied uniformly to all columns in a bridge system regardless of the column height and the performance was compared with that of a similar bridge model with unretrofitted columns.

6.2 CONCLUSIONS

Based on the experimental and analytical findings, the following conclusions are presented:

1. The most common substructure features in the ODOT inventory were 24 in x 24 in square columns with clear height between 15 ft to 18 ft The concrete has a characteristic compressive strength of 3300 psi with 1.5 in cover concrete. The longitudinal reinforcement details were 4-#11 round or square intermediate grade (equivalent to Gr. 40) bars in each corner. Average shear reinforcement was 0.09% with intermediate grade #3 hoops at 12 in on-center. The vertical column bars were spliced with the footing starter bars without extra confining hoops along the splice length. In the columns with Gr. 40 #11 bars, the average splice length was found to be 30 times the diameter of the bar. Most square columns rest on RC spread footings and the remainder on pile foundations with most piles being timber. Both spread footings and pile caps have a single mesh of reinforcement at the bottom. Average service-level axial load per column was calculated to be approximately 0.06 f'_cA_g. For the tests conducted in this research program, axial load was maintained at 200 kips (0.1 f'_cA_g) for 12 ft tall columns and 150 kips (0.08 f'_cA_g) for 8 ft short columns. Specimens were designed and constructed to reflect the salient features of the inventory.

2. The flexibility and light-weight of the TiAB spiral allows it to be continuously wrapped around a large column by a single person without specialized equipment or training.

3. Similarly, the flexibility of the TiAB ligament allows the long straight tail to be placed into the relatively deep footing hole at the same time the 90° hook or 135° hook is placed into the column face. The stainless steel bars used in this program were at or almost at yield in order to place the ligament into the specimens, and required significant effort to place them.

4. The control specimens without TiABs exhibited non-ductile response with no displacement ductility, limited energy dissipation, and overall poor performance.

5. Short column specimens exhibited larger displacement ductility than tall column specimens.

6. Specimens strengthened with TiAB ligaments demonstrated that both the steel and ligaments combine to resist overturning at the beginning of the test and splice failure is delayed to drift ratios of about 4%. Afterwards, the specimen strength begins to reduce as the TiABs become the main source of moment resistance at the footing-column interface and P-Delta effects contribute negative stiffness.

7. Typical TiAB retrofitted specimens (consisting of TiAB spiral and TiAB ligaments without foam insulation under the shell) exhibited an average displacement ductility of 11.1 with the lowest being 5.6. This exceeds the Caltrans minimum displacement

ductility of 3 and even the preferred displacement ductility of 5 (Caltrans, 2006), which was considered for new construction.

8. The TiAB retrofitted specimens exhibited greatly improved energy dissipation, higher viscous damping, and self-centering capacity (less residual drift at neutral position) compared to control specimens.

9. Some TiAB ligaments exhibited ductile hook withdrawal from the column face. Others remained well anchored. The TiAB ligaments with 135 degree hooks exhibited the least amount of hook withdrawal. Tighter spacing of the TiAB spiral over the hooks also helped reduce hook withdrawal.

10. The TiAB reinforced shell was effectively debonded from the square column using plastic wrapped around the column. Displacement sensors measured relative movement between the shell and concrete indicating non-composite behavior.

11. The TiAB spiral reinforced shell provided excellent confinement and delayed bond failure of the reinforcing steel splice. After removal of the shell, only limited cracking was observed along the column height. Column damage was concentrated at the interface of the column and footing.

12. Debonding the upper 5 in of the TiAB ligament at the top of the footing prevented the formation of concrete pullout cones and eliminated localized TiAB buckling. This was compared to the tall specimens which had 2 in debonded length at the top of the footing and exhibited pullout cones that left the TiABs unsupported.

13. The foam insulation between the top of the footing and shell for two tall specimens resulted in buckling and eventual fracture of the TiAB ligaments in the area around the foam. Foam is not recommended for use in the future.

14. Strain gages on the TiAB ligaments indicated they reached yield.

15. The specimen with purposefully cut steel starter bars at the top of the footing demonstrated that the TiAB ligaments alone could provide ductile response at specifically controlled moment magnitude. This demonstrated the ability of the TiABs to provide flexural resistance and member ductility capacity.

16. The over-strength of the stainless steel ligaments used resulted in failure of the column above the TiAB retrofit shell. By comparison, none of the specimens with TiAB ligaments failed in such a way. The well controlled TiABs material properties allow better estimation of maximum strength which can prevent overloading of other bridge details.

17. The TiAB spirals remained elastic with strains in the lowest part of the column only about ¼ of yield.

18. Cracking in the TiAB reinforced spiral shell at the corners is an indicator of the level of drift imposed on the specimen. This can be used as a reference during inspection

after an earthquake. Cracking over the entire shell height was observed at drifts corresponding to 3 times yield drift. Initial spalling of the corners was generally observed at approximately 4 times yield drift.

19. The small number of starter bars passing through the column-footing interface increases the likelihood of sliding failure when the concrete degrades inside the shell over the interface of the column and footing (low amount of dowel action). This was observed for two of the TiAB retrofitted specimens (short with shell only and short with 135 hooks). Sliding behavior resulted in exceptionally good performance on one half of the cycle and poor performance on the other half cycle.

20. For retrofit designs that only use a shell (including steel plate, CFRP, etc.), sliding failures should be prevented. For the present retrofit, a second spiral could be added over the bottom of the column (a height equal to the column dimension) that anchors on the opposite face of the column from the first spiral. Alternatively some additional dowel reinforcement could be considered. Unretrofitted columns are not likely to slide because they fail due to bond slip before the concrete can be crushed and reduced to powder at the interface.

21. Soil-structure interactions reduced damage in the retrofitted columns, but produced damage in the pile cap and soil. The beneficial and deleterious effects of soil-structure interactions on retrofit performance require additional study.

22. Without the TiAB retrofits, an unretrofitted column would have failed above the footing for the spread footing and pile cap specimens.

23. The column shear-drift response for the retrofitted specimens was well captured assuming confined concrete in the square column with reinforcing steel and TiABs both reaching yield (assuming the TiAB is fully bonded to the concrete) with a 10% over-strength factor to account for the partial composite nature of the TiAB spiral reinforced shell.

24. Analytical models were developed that were able to reasonably capture the phenomenological cyclic response of the control specimens and TiAB retrofitted specimens.

25. Analysis of bridge models using the calibrated column element models showed increased deformation capacity and energy dissipation for models with retrofitted columns.

26. Seismic performance enhancements were better for regular bridges compared to irregular bridges because shorter columns in irregular bridge configurations tended to concentrate demands.

27. Incremental dynamic analysis (IDA) demonstrated that the retrofitted bridges exhibited a capacity increase of approximately 2 to 3 times that of unretrofitted bridge models, independent of the damage indicator used. As an example, IDA showed that an unretrofitted bridge could deform up to 5% drift ratio with shaking intensities of

$S_a(T_1)$ = 0.75g, but after applying the TiAB retrofit, the bridge could deform up to 10% drift ratio at $S_a(T_1)$ = 1.5g.

28. Fragility curves demonstrated that the probability of reaching a specific drift level for any large earthquake, and thereby damage state, was reduced dramatically when the columns were retrofitted with TiAB ligaments and spiral reinforced shell.

29. The overall excellent performance, ease of construction, and simple design make TiABs a viable option for upgrading the seismic performance of vintage and deficient RC column substructures. The performance achieved exceeds the standards for modern designs, and the retrofit provides advantageous self-centering capacity not possible with conventional alternatives. The retrofit is not as susceptible to environmental effects compared to polymer materials and allows post-earthquake inspection to assess damage and correlate to drift history.

6.3 DESIGN RECOMMENDATIONS

Based on the experimental results and observations, the following design recommendations are provided:

6.3.1 Ligaments

- The average height for the shell should correspond to the AASHTO-LRFD prescribed development length for the column bars. The average ligament length was about 10 in shorter than the shell height. The intent is that if splice failure should occur, the column bar can develop sufficient capacity within the confined column to resist the moment magnitude at the top of the splice. The TiAB ligaments provide an alternative load path to resist overturning moment at the footing-column interface equal to the starter bar capacity.

- The area of the ligaments should be proportioned to provide the same nominal yield force of the reinforcing steel starter bars at the footing-column interface. In general, it takes about two #5 TiABs (F_y=0.3 in^2 *130 ksi*2=80 kips) to replace one #11 Grade 40 reinforcing bar (F_y=1.56 in^2* 40 ksi=62.4 kips).

- Stainless steel ligaments, produced to present ASTM standards, are not recommended, as there is a high likelihood of over-strength that can produce unintended damage.

- Holes in the column and footing are to be hammer drilled and cleaned to remove dust and debris. The holes in the column must be radiused to allow the hook to sit flush against the column.

- Holes in the footing should be drilled as close as practical to the face of the column. In the laboratory, this was around 1 in.

- High quality epoxy should be used to anchor the ends of all TiABs.

- Anchorage of the ligaments in the footing should include a 5 in debonded length measured below the top of the footing. This debonded length reduces the likelihood for concrete pullout cones to form around the TiABs. The bonded length of 15 in (plus 5 in debonded length on a smooth TiAB surface at the top) was sufficient to develop the tensile strength of the #5 TiAB ligaments.

- No foam should be used between the concrete shell and footing. The shell is adequately debonded from the column by wrapping plastic sheeting around the column before placement of the concrete shell.

- 135° hooks on the ends of the ligaments can be used to reduce or delay hook withdrawal from the column. However, these are harder to produce as they required diamond core drilling to produce the desired angle in the column face.

6.3.2 Spiral shell

- The spiral design is presently applied to square cross sections.

- No surface preparation is required other than placing plastic around the column.

- The upper end of the spiral shall be anchored at the neutral axis of the column. The length of the tail on the 90° hook was 8 in.

- The hooks for the spiral can be field heated and bent.

- At least two tight turns should be placed at the top of the shell the ensure anchorage of the spiral.

- The spiral should be pulled tight against the corners of the column during placement.

- The spiral size (3/8 in diameter) and pitch is prescriptive. The intent is to keep the spiral elastic and was designed to provide a level of confinement to the square concrete column sufficient to achieve ultimate concrete strains of at least 0.005.

- The spiral pitch should be 1.5 inches over the region of the TiAB ligament hooks.

- Outside the ligament hook region, the spiral pitch should be 2.5 in. This spacing allows uniform confining pressure to develop with overlapping concrete wedges at the spliced steel reinforcing corner bars as illustrated in Figure 6.1.

- At the bottom of the column, two tight spirals shall be placed at the level of the footing and end of the spiral anchored into the footing. The length of the hook is 8 in (205 mm).

- A second spiral should be added over the lowest part of the column, equal to the column dimension. The upper end of this spiral should be anchored into the column at the neutral axis and the bottom end of the spiral should be anchored into the footing on the opposite face from that of the continuous spiral. This configuration is illustrated in Figure 6.2

- Smaller diameter bars are not recommended for the TiAB spiral, as the material cost is higher, and part of the function of the large diameter is to effectively engage the concrete shell.
- The maximum aggregate size used for the concrete shell should be at least 3/8 in diameter.
- Polycarbonate formwork allows the progress of concrete placement to be observed and ensures no voids remain in the shell.

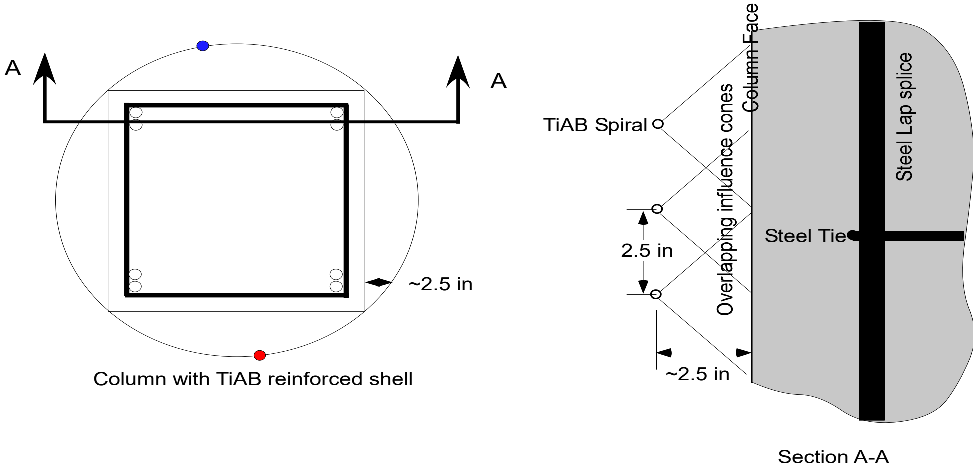

Figure 6.1: Intent of spiral pitch to form overlapping influence cones at concrete column surface

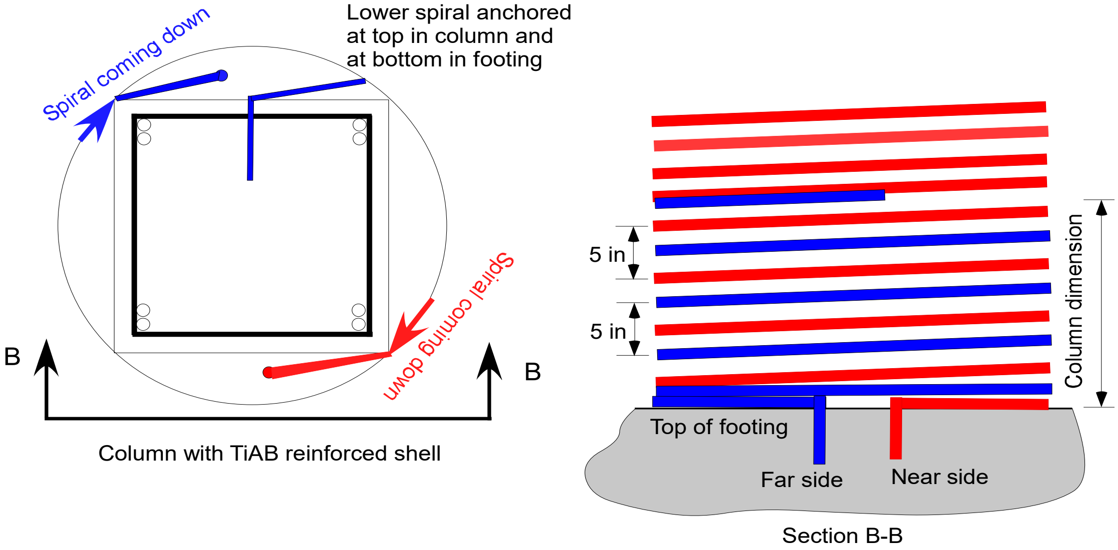

Figure 6.2: Pair of spirals in lower portion of column and anchored on opposite faces of the column to prevent sliding of column relative to top of footing

6.4 FUTURE RESEARCH

Future work could be undertaken to further advance the retrofit design details, improve performance, eliminate undesirable modes of failure, and address other variables relevant for adoption. Some future research could include the following:

Evaluate the effectiveness of smaller diameter TiABs for spirals, or of wider pitch.

Confirm beneficial effect of two spirals in lowest portion of column to prevent sliding.

Repeat test of short specimen with 135° hooked TiAB ligaments to confirm beneficial effects of the anchor detail (specimen failed due to sliding).

Because the specimens were dominated by flexural behavior, the shear strength of TiAB spirally reinforced section should be investigated. This would be more relevant for shorter columns.

Consider the interactions of columns within a bent, considering 2 and 4 column bent configurations.

Conduct additional soil-structure interaction tests including real soil and driven piles.

Advance analytical models that include realistic-soil structural interactions on performance of seismic retrofitted bridge columns and systems.

Optimize retrofits for irregular bridges.

Locate an in-service bridge as a candidate for field implementation of the proposed retrofit.

Consider full-scale shake table studies to further validate the retrofit performance under characteristic earthquake motions.

7.0 REFERENCES

Abedi, K., Afshin, H., & Shirazi, M. R. N. (2010). Numerical Study on the Seismic Retrofitting of Reinforced Concrete Columns Using Rectified Steel Jackets. *Asian Journal of Civil Engineering (Building and Housing)*, *11*(2), 219–240.

ACI Committee 374. (2013). *ACI 374.2R-13: Guide for Testing Reinforced Concrete Structural Elements under Slowly Applied Simulated Seismic Loads*. Detroit, MI.

ACI Committee 318. (2014). *Building code requirements for structural concrete (ACI 318-14) : an ACI standard : commentary on building code requirements for structural concrete (ACI 318R-14), an ACI report*. Farmington Hills, MI: American Concrete Institute.

ACI Committee 440. (2017). *ACI 440.2R-17: Guide for the Design and Construction of Externally Bonded FRP Systems for Strengthening Concrete Structures*. *ACI 440.2R-17*. Detroit, MI.

Adkins, J., & George, W. (2017). Titanium Finds a Home in Civil Engineering. *Concrete International*, *39*(12), 51–55.

American Association of State Highway and Transportation Officials,. (2017). *AASHTO LRFD bridge design specifications, Part I: Sections 1-6*.

Amneus, D. (2014). *Methods for Strengthening Flexural Steel Details in Reinforced Concrete Bridge Girders using a Near-Surface Mounted Retrofitting Technique* (Master's thesis). Oregon State University, Corvallis, OR.

Ang, A. H.-S., Kim, W. J., & Kim, S. B. (1993). Damage Estimation of Existing Bridge Structures. In *Structural Engineering in Natural Hazards Mitigation* (pp. 1137–1142). Irvine, CA.

Apostolou, M., Gazetas, G., & Garini, E. (2007). Seismic Response of Slender Rigid Structures with Foundation Uplifting. *Soil Dynamics and Earthquake Engineering*, *27*(7), 642–654. https://doi.org/10.1016/j.soildyn.2006.12.002

American Society of Civil Engineers,, & Structural Engineering Institute,. (2013). *ASCE/SEI 41-13 : American Society of Civil Engineers: Seismic Evaluation and Retrofit of Existing Buildings*. Reston, VA: American Society of Civil Engineers.

American Society for Testing and Materials. (2018) Standard Specification for Titanium and Titanium Alloy Bars and Billets. (Standard No. B1009 - 18). West Conshohocken, PA. https://doi.org/10.1520/B0348-13.2

Barbosa, A. R., Ribeiro, F. L. A., & Neves, L. C. (2017). Influence of Earthquake Ground-Motion Duration on Damage Estimation: Application to Steel Moment Resisting Frames. *Earthquake Engineering and Structural Dynamics*, *46*(1), 27–49. https://doi.org/10.1002/eqe.2769

Barker, L. (2014). *Flexural Anchorage Performance and Strengthening on Negative Moment Regions Using Near-Surface Mounted Retrofitting in Reinforced Concrete Bridge Girders* (Master's thesis). Oregon State University, Corvallis, OR.

Belejo, A., Barbosa, A. R., & Bento, R. (2017). Influence of Ground Motion Duration on Damage Index-based Fragility Assessment of a Plan-Asymmetric Non-Ductile Reinforced Concrete Builing. *Engineering Structures*, *151*, 682–703.

Belejo, A., Barbosa, A. R., & Higgins, C. C. (2019). Damage-Based Seismic Fragility Assessment of RC Bridges Retrofitted with Titanium Alloy Bars. *Being Prepared for Submission to the ASCE Journal of Bridge Engineering*.

Bournas, D. A., & Triantafillou, T. C. (2009). Flexural Strengthening of Reinforced Concrete Columns with Near-Surface-Mounted FRP or Stainless Steel. *ACI Structural Journal*, *106*(4), 495–505. https://doi.org/10.14359/56615

Breña, S., & Schlick, B. (2007). Hysteretic Behavior of Bridge Columns with FRP-Jacketed Lap Splices Designed for Moderate Ductility Enhancement. *Journal of Composites for Construction*, *11*(December), 565–574. https://doi.org/10.1061/(ASCE)1090-0268(2007)11:6(565)

Buckle, I., Friedland, I., Mander, J., Geoffrey, M., Nutt, R., & Power, M. (2006). *Seismic Retrofitting Manual for Highway Structures : Part 1 – Bridges*. *FHWA-HRT-06-032*. McLean, VA 22101-2296.

Cairns, J., & Arthur, P. D. (1979). Strength of Lapped Splices in Reinforced Concrete Columns. *ACI Journal Proceedings*, *76*(2). https://doi.org/10.14359/6947

Caltrans. (2013). *Seismic Design Criteria Version 1.7*. California Department of Transportation: Sacramento, CA, U.S.

Caltrans. (2015). Seismic Design of Concrete Bridges. In *Bridge Design Practice* (p. 21–(1–144)).

Chai, Y. H., Priestley, M. J. N., & Seible, F. (1994). Analytical Model for Steel-Jacketed RC Circular Bridge Columns. *ASCE Journal of Structural Engineering*, *120*(8), 2358–2376.

Chai, Y. H., Priestley, M. J. N., & Seible, F. (2008). Seismic Retrofit of Rectangular Bridge Columns by Steel Jacketing. In *Third Bridge Engineering Conference: Papers Presented at the Third Bridge Engineering Conference, March 10-13, 1991, Denver, Colorado* (pp. 95–103).

Chowdhury, S. R., & Orakcal, K. (2012). An analytical model for reinforced concrete columns with lap splices. *Engineering Structures*, *43*, 180–193. https://doi.org/10.1016/j.engstruct.2012.05.019

Daudey, X., & Filiatrault, A. (2000). Seismic Evaluation and Retrofit with Steel Jackets of Reinforced Concrete Bridge Piers Detailed with Lap-Splices. *Canadian Journal of Civil Engineering*, *27*(1), 1–16.

Douglas, D. J., & Davis, E. H. (1964). The Movement of Buried Footings due to Moment and Horizontal Load and the Movement of Anchor Plates. *Géotechnique*, *14*(2), 115–132. https://doi.org/https://doi.org/10.1680/geot.1964.14.2.115

Duncan, J. M., & Mokwa, R. L. (2001). Passive Earth Pressures: Theories and Tests. *ASCE Journal of Geotechnical and Geoenvironmental Engineering*, *127*(3), 248–257.

Dutta, A., & Mander, J. B. (2001). Energy Based Methodology for Ductile Design of Concrete Columns. *ASCE Journal of Structural Engineering*, *127*(12), 1374–1381.

Earth Mechanics, I. (2005). *Field Investigation Report for Abutment Backfill Characterization. UCSD Report No. SSRP-05/02*. La Jolla, CA.

ElGawady, M., Endeshaw, M., McLean, D., & Sack, R. (2010). Retrofitting of Rectangular Columns with Deficient Lap Splices. *Journal of Composites for Construction*, *14*(1), 22–35. https://doi.org/10.1061/(asce)cc.1943-5614.0000047

Filippou, F. C., Popov, E. P., & Bertero, V. V. (1983). *Effects of Bond Deteroriation on Hysteretic Behavior of Reinforced Concrete Joints. Report to the National Science Foundation. Earthquake Engineering Research Center*. Berkeley, CA.

Galal, K., Arafa, A., & Ghobarah, A. (2005). Retrofit of RC Square Short Columns. *Engineering Structures*, *27*(5), 801–813. https://doi.org/10.1016/j.engstruct.2005.01.003

Girard, C., & Bastien, J. (2002). Finite-Element Bond-Slip Model for Concrete Columns under Cyclic Loads. *ASCE Journal of Structural Engineering*, *128*(12), 1502–1510. https://doi.org/10.1061/(ASCE)0733-9445(2002)128:12(1502)

Goksu, C., Yilmaz, H., Chowdhury, S. R., Orakcal, K., & Ilki, A. (2014). The Effect of Lap Splice Length on the Cyclic Lateral load Behavior of RC Members with Low-Strength Concrete and Plain Bars. *Advances in Structural Engineering*, *17*(5), 639–658. https://doi.org/10.1260/1369-4332.17.5.639

Goldfinger, C., Nelson, C. H., Morey, A. E., Johnson, J. E., Patton, J. R., Karabanov, E., … Vallier, T. (2012). *Turbidite Event History-Methods and Implications for Holocene Paleoseismicity of the Cascadia Subduction Zone*. US Geological Survey Profesional Paper 1661-F. Reston, VA. https://doi.org/10.3133/pp1661f

Harajli, M. H. (2004). Comparison of Bond Strength of Steel Bars in Normal- and High-Strength Concrete. *Journal of Materials in Civil Engineering*, *16*(4), 365–374. https://doi.org/10.1061/(ASCE)0899-1561(2004)16:4(365)

Harajli, M. H. (2008). Seismic Behavior of RC Columns with Bond-Critical Regions: Criteria for Bond Strengthening Using External FRP Jackets. *Journal of Composites for Construction*, *12*(1), 69–79. https://doi.org/10.1061/(ASCE)1090-0268(2008)12:1(69)

Harajli, M. H. (2009). Bond Stress–Slip Model for Steel Bars in Unconfined or Steel , FRC , or FRP Confined Concrete. *Journal of Structural Engineering*, *135*(5), 509–518. https://doi.org/10.1061/(ASCE)0733-9445(2009)135:5(509)

Harajli, M. H., Rteil, A. A., & Hamad, B. S. (2004). Effect of Confinement on Bond Strength Between Steel Bars and Concrete. *ACI Structural Journal*, *101*(5), 595–603. https://doi.org/10.14359/13381

Haroun, M. A., & Elsanadedy, H. M. (2005). Fiber-Reinforced Plastic Jackets for Ductility Enhancement of Reinforced Concrete Bridge Columns with Poor Lap-Splice Detailing. *ASCE Journal of Bridge Engineering*, *10*(6), 749–757. https://doi.org/10.1061/(ASCE)1084-0702(2005)10:6(749)

Harries, K. A. ., Ricles, J. R. ., Pessiki, S., & Sause, R. (2006). Seismic Retrofit of Lap Splices in Non-ductile Columns Using CFRP Jackets. *ACI Structural Journal*, *103*(6), 874–884. https://doi.org/10.14359/18242

Higgins, C. C. (2018). *Guide for Design and Construction of Near-Surface Mounted Titanium Alloy Bars for Strengthening Concrete Structures*. Corvallis, OR 97331.

Higgins, C. C., Knudtsen, J., Amneus, D., & Barker, L. (2017). Shear and Flexural Strengthening of Reinforced Concrete Beams with Titanium Alloy Bars. *Proceedings of the 2nd World Congress on Civil, Structural, and Environmental Engineering (CSEE'17)*, 1–8. https://doi.org/10.11159/icsenm17.141

Hoshikuma, B. J., Kawashima, K., Nagaya, K., & Taylor, A. W. (1997). Stress-Strain Model for Confined Reinforced Concrete in Bridge Piers. *Journal of Materials in Civil Engineering*, *123*(1992), 624–633.

Hung, H. H., Liu, K. Y., Ho, T. H., & Chang, K. C. (2011). An Experimental Study on the Rocking Response of Bridge Piers with Spread Footing Foundations. *Earthquake Engineering and Structural Dynamics*, *40*(7), 749–769. https://doi.org/10.1002/eqe.1057

Ilki, A., Tezcan, A., KOC, V., & Kumbasar, N. (2004). Seismic Retrofit of Non-Ductile Rectangular Reinforced Concrete Columns by CFRP Jacketing. *13th World Conference on Earthquake Engineering* Vancouver, B.C., Canada August 1-6, 2004 Paper No. 2236, (August).

Isaković, T., & Fischinger, M. (2011). Applicability of Pushover Methods to the Seismic Analyses of an RC Bridge, Experimentally Tested on Three Shake Tables. *Journal of Earthquake Engineering*, *15*(2), 303–320. https://doi.org/10.1080/13632461003802009

Karthik, M. M., & Mander, J. B. (2011). Stress-Block Parameters for Unconfined and Confined Concrete Based on a Unified Stress-Strain Model. *ASCE Journal of Structural*

Engineering, *137*(2), 270–273. https://doi.org/10.1061/(ASCE)ST.1943-541X.0000294

Kawashima, K., & Nagai, T. (2006). Effectiveness of Rocking Seismic Isolation on Bridges. *4th International Conference on Earthquake Engineering*, (086), 12–13.

Kent, D. C., & Park, R. (1971). Flexural Members with Confined Concrete. *ASCE Journal of Structural Division*, *97*(7), 1969–1990.

Knudtsen, J. (2016). *Shear Strengthening Reinforced Concrete Bridge Girders Using Near-Surface Mounted Titanium Alloy Bars* (Master's thesis). Oregon State University, Corvallis, OR.

LeBorgne, M. R., & Ghannoum, W. M. (2014). Analytical Element for Simulating Lateral-Strength Degradation in Reinforced Concrete Columns and Other Frame Members. *ASCE Journal of Structural Engineering*, *140*(7), 04014038. https://doi.org/10.1061/(ASCE)ST.1943-541X.0000925

Lostra, M. M. W. (2016). *Seismic Performance of Square Reinforced Concrete Columns Retrofitted with Titanium Alloy Bars* (Master's thesis). Oregon State University.

Lowes, L. N., Mitra, N., & Altoontash, A. (2003). *A beam-column joint model for simulating the earthquake response of reinforced concrete frames*. Pacific Earthquake Engineering Research Center, College of Engineering, University of California Berkeley.

Lukose, K., Gergely, P., & White, R. N. (1982). Behavior of Reinforced Concrete Lapped Splices for Inelastic Cyclic Loading. *Journal of American Concrete Institute*, *79*(5), 355–365.

Lynn, A. C., Moehle, J. P., Mahin, S. A., & Holmes, W. T. (1996). Seismic Evaluation of Existing Reinforced Concrete Building Columns. *Earthquake Spectra*, *12*(4), 715–739. https://doi.org/10.1193/1.1585907

Mander, J. B., Priestley, M. J. N., & Park, R. (1988). Observed Stress-Strain Behavior of Confined Concrete. *ASCE Journal of Structural Engineering*, *114*(8), 1827–1849.

Mander, J. B., Priestley, M. J. N., & Park, R. (1988). Theoretical Stress-Strain Model for Confined Concrete. *ASCE Journal of Structural Engineering*, *114*(8), 1804–1826.

Manfredi, G., Polese, M., & Cosenza, E. (2003). Cumulative Demand of the Earthquake Ground Motions in the Near Source. *Earthquake Engineering & Structural Dynamics*, *32*(10), 1853–1865. https://doi.org/10.1002/eqe.305

McKenna, F., Scott, M. H., & Fenves, G. L. (2010). Nonlinear Finite-Element Analysis Software Architecture Using Object Composition. *ASCE Journal of Computing in Civil Engineering*, *24*(1), 95–107. https://doi.org/10.1061/(asce)cp.1943-5487.0000002

Melek, M., & Wallace, J. W. (2004). Performance of Columns with Short Lap Splices. In *13th World Conference on Earthquake Engineering* Vancouver, B.C., Canada August 1-6, 2004

Paper No. 1034 (pp. 1–15). https://doi.org/10.1002/eqe.4290180114

Miranda, E. (2000). Inelastic Displacement Ratios for Displacement-Based Earthquake Resistant Design. In *12WCEE* (pp. 1–8). Auckland, New Zealand.

Mirmiran, A., Shahway, M., Samaan, M., Echary, H. El, Mastrapa, J. C., & Pico, O. (1998). Effect of Column Parameters on FRP-Confined Concrete. *Journal of Composites for Construction*, *2*(November), 175–185.

Oyarzo-vera, C., & Chouw, N. (2008). Effect of Earthquake Duration and Sequences of Ground Motions on Structural Responses. In *Proceedings of the 10th International Symposium on Structural Engineering of Young Experts*.

Ozcan, O., Binici, B., & Ozcebe, G. (2008). Improving Seismic Performance of Deficient Reinforced Concrete Columns Using Carbon Fiber-Reinforced Polymers. *Engineering Structures*, *30*(6), 1632–1646. https://doi.org/10.1016/j.engstruct.2007.10.013

Ozcebe, G., & Saatcioglu, M. (1987). Confinement of Concrete Columns for Seismic Loading. *ACI Structural Journal*. https://doi.org/10.14359/1660

Park, Y. J., Ang, A. H., & Wen, Y. K. (1987). Damage-Limiting Aseismic Design of Buildings. *Earthquake Spectra*, *3*(1), 1–26. https://doi.org/https://doi.org/10.1193/1.1585416

Paulay, T. (1982). Lapped Splices in Earthquake-Resisting Columns. *Journal of American Concrete Institute*, *79*(6), 458–469.

Priestley, M. J. N., Seible, F., & Calvi, G. M. (1996). *Seismic Design and Retrofit of Bridges*. New York: John Wiley & Sons, Inc. https://doi.org/10.1002/9780470172858

Priestley, M. J. N., Verma, R., & Xiao, Y. (1995). Seismic Shear Strength of Reinforced Concrete Columns. *ASCE Journal of Structural Engineering*, *120*(8), 2310–2329.

Razvi, S. W. N., & Shaikh, M. G. (2018). Effect of Confinement on Behavior of Short Concrete Column. *Procedia Manufacturing*, *20*(01), 563–570. https://doi.org/10.1016/j.promfg.2018.02.084

Saatcioglu, M., & Ozcebe, G. (1989). Response of Reinforced Concrete Columns to Simulated Seismic Loading. *ACI Structural Journal*, *86*(1), 3–12.

Scott, B. D., Park, R., & Priestley, M. J. N. (1982). Stress-Strain Behavior of Concrete Confined by Overlapping Hoops at Low and High Strain Rates. *ACI Journal Proceedings*, *79*(1), 13–27.

Sheikh, S. A., & Uzumeri, S. M. (1982). Analytical Model for Concrete Confinement in Tied Columns. *ASCE Journal of Structural Division*, *108*(12), 2703–2722.

Stevens, N. J., Uzumeri, S. M., Collins, M. P., & Will, G. T. (1991). Constitutive Model for

Reinforced Concrete Finite Element Analysis. *ACI Structural Journal*, *88*(1). https://doi.org/10.14359/3105

Takahashi, Y., Muto, I., Hitoshi, S., Tadokoro, Y., & Tagomori, N. (1994). Application of Titanium to Construction and Civil Engineering. https://doi.org/UDC669.295.7:624/627

The European Standard. (2004). *Eurocode 8 : Design of Structures for Earthquake Resistance - Part 1: General Rules, Seismic Actions and Rules for Buildings*. British Standard. Brussels.

Todeschini, C. E., Bianchini, A. C., & Kesler, C. E. (1964). Behavior of Concrete Columns Reinforced with High Strength Steels. *ACI Journal Proceedings*, *61*(6), 701–716.

Valluvan, R., Kreger, M. E., & Jirsa, J. O. (1993). Strengthening of Column Splices for Seismic Retrofit on Non-ductile Reinforced Concrete Frames. *ACI Structural Journal*, *90*(4), 432–433.

Vavra, E. (2016). *Application of Titanium Alloy Bars for Strengthening Reinforced Concrete Bridge Girders in Flexure* (Master's thesis). Oregon State University, Corvallis, OR.

Wang, D., Wang, Z., Yu, T., & Li, H. (2018). Seismic Performance of CFRP-Retrofitted Large-Scale Rectangular RC Columns Under Lateral Loading in Different Directions. *Composite Structures*, *192*(3), 475–488. https://doi.org/10.1016/j.compstruct.2018.03.029

Watson, S., Zahn, F. A., & Park, R. (1994). Confining Reinforcement for Concrete Columns. *ASCE Journal of Structural Engineering*, *120*(6), 1798–1824.

Wilson, P., & Elgamal, A. (2006). Large Scale Measurement of Lateral Earth Pressure on Bridge Abutment Back-Wall Subjected to Static and Dynamic Loading. *Proceedings of the New Zealand Workshop on Geotechnical Earthquake Engineering*, (December), 307–315.

Xiao, Y., & Ma, R. (1997). Seismic Retrofit of RC Circular Columns Using Prefabricated Composite Jacketing. *ASCE Journal of Structural Engineering*, *123*(10), 1357–1364. https://doi.org/10.1061/(ASCE)0733-9445(1997)123:10(1357)

Yalcin, C., & Saatcioglu, M. (2000). Inelastic Analysis of Reinforced Concrete Columns. *Computers and Structures*, *77*(5), 539–555. https://doi.org/10.1016/S0045-7949(99)00228-X

Yassin, M. H. M. (1994). *Nonlinear Analysis of Prestressed Concrete Structures under Monotonic and Cyclic Loads* (PhD dissertation). University of California, Berkeley.

Yavari, S., Elwood, K. J., & Wu, C. (2009). Collapse of a Non-ductile Concrete frame: Evaluation of Analytical Models. *Earthquake Engineering and Structural Dynamics*, *38*(October 2008), 225–241. https://doi.org/10.1002/eqe.855

Zahn, F. A., Park, R., & Priestley, M. J. N. (1989). Strength and Ductility of Square Reinforced Concrete Column Sections Subjected to Biaxial Bending. *ACI Structural*

Journal.

Zhao, J., & Sritharan, S. (2007). Modeling of strain penetration effects in fiber-based analysis of reinforced concrete structures. *ACI Structural Journal*, *104*(2), 133–141. https://doi.org/10.14359/18525